Universidad del País Vasco
Euskal Herriko Unibertsitatea

UNIVERSITY OF THE BASQUE COUNTRY

Holistic approach for the development of high-performing, safe, and long-cycle life prototype lithium-sulfur batteries

Julen Castillo Ruiz de Azua, 2024

Universidad del País Vasco
Euskal Herriko Unibertsitatea

Facultad de Ciencia y Tecnología
Zientzia eta Teknologia Fakultatea

Departamento de Ingeniería Química
Ingeniaritza Kimikoa Saila

Holistic approach for the development of high-performing, safe, and long-cycle life prototype lithium-sulfur batteries

By
Julen Castillo Ruiz de Azua

Thesis supervisors:
Prof. José Antonio González Marcos
Dr. Alexander Santiago Sánchez

A thesis submitted in fulfillment of the requirements
for the degree of Doctor in Chemical Engineering

"*Las cosas difíciles requieren un largo tiempo,*
las cosas imposibles un poco más"
André A. Jackson

Acknowledgments/Agradecimientos

Llegado el final del trabajo de estos últimos años, solo me queda agradecer a todas las personas que han sido parte fundamental en este proyecto, contribuyendo así a hacer realidad esta tesis doctoral. Este trabajo, plagado de desafíos, ha sido posible gracias al apoyo de todos y cada uno de vosotros, y antes de entrar en más detalles, me gustaría agradecéroslo de todo corazón.

En primer lugar, me gustaría expresar mi profunda gratitud a mis supervisores de tesis **José Antonio** y **Alex**, por el apoyo invaluable que me habéis ofrecido durante estos años. **Jose Antonio**, gracias por la oportunidad que me diste en 2019 para empezar a trabajar contigo, así como todos los consejos y orientación que me has proporcionado durante mi trabajo de fin de máster y esta tesis doctoral. Y a ti, **Alex** (alías "puto gafas"), es imposible expresar toda mi gratitud por todo lo que has hecho por mí a lo largo de estos años. Esta tesis no habría sido posible sin tu enorme esfuerzo, dedicación y dirección, incluso cuando inicialmente no tenías ese rol oficial, y afortunadamente, al final, se te va a reconocer. Espero poder seguir trabajando a tu lado durante muchos años y que sigamos liándola en el futuro.

A pesar de que los continuos cambios en el equipo de Li-S hayan sido todo un desafío para el trabajo diario, me han permitido conocer y trabajar con personas excepcionales que han contribuido enormemente a que esta tesis salga adelante. Quiero agradecer especialmente a **Garbayo** y a **Xabi** por toda la enseñanza, ayuda, supervisión, correcciones, orientación, etc., durante mis primeros años y que de tanta ayuda me han servido. A **Amaia** por toda la ayuda y por crear un tan buen ambiente en el equipo. A **Jose Coca** por siempre tener una sonrisa y el buen rollo que transmitías. A **Chunmei** por darme la oportunidad de llevar a cabo esta tesis y la confianza que depositaste en mí. A **Dani** y **Aitor**, agradezco toda la ayuda, consejos y el apoyo que me habéis ofrecido para impulsar este proyecto. A los últimos en llegar, **Asier** y **Adrián**, gracias por toda la ayuda que me habéis ofrecido en el último año y por contribuir al buen ambiente actual del equipo. Y a **Jokin** por todos los consejos que me has ofrecido.

Gracias a todos mis compañeros de trabajo, especialmente al grupo del café y del ping-pong, por los buenos momentos y por hacer que el día a día sea más llevadero. Me gustaría agradecer a dos personas que considero que han sido claves para mi día a día en el CIC. A **Silvia**, por siempre tener una sonrisa, ser tan detallista y

siempre preocuparte por mí y mi rodilla. A **Añastro**, por los buenos momentos compartiendo mesa y por las terapias cuando las cosas no iban tan bien. Sin ti, el día a día habría sido mucho más difícil. También a mis compañeros del piso 0, por el buen ambiente que siempre hemos tenido.

I'm deeply grateful for the enriching experiences I gained during my stay in Goteborg with Prof. Aleksandar Matic's group. I would like to give special thanks to **Alex** and **Matt** for their warm acceptance into their group, their kindness, mentorship, and for creating an exceptional working environment. I also extend my sincere thanks to the Italian duo, **Eu** and **Matteo**, and **Marita**, whose companionship not only made my stay in Goteborg bearable but also filled it with good moments outside of work. In a broader sense, I extend my gratitude to the entire **Materials Physics** department at Chalmers for the excellent working atmosphere and for the warm welcome I received during the three months I spent with you. Tack så mycket!

A mi **cuadrilla de Lagran**, gracias por estar siempre ahí para ayudarme a desconectar y por los buenos momentos que siempre tenemos cada vez que nos juntamos. Especialmente, el tiempo que paso con vosotros en Lagran ha sido fundamental para poder encontrar cierta paz y encarar siempre con ganas este proyecto.

Por último, un agradecimiento especial a toda mi familia. Comienzo con mi **tío Alberto**, sin cuya dirección y ayuda fundamentales hace algunos años, estoy seguro de que todo esto no habría sido posible. A mis **tíos de Maturana**, Isma y Jesu, gracias por todos los buenos momentos que compartimos cada viernes comiendo en el pueblo, momentos que tanto me ayudan a desconectar, y, por supuesto, por los buenos kalimotxos y patxaranes que disfrutamos juntos. Finalmente, no puedo olvidar agradecer a mis **padres** por dármelo todo, por el enorme esfuerzo que habéis hecho siempre por mí, por apoyarme incondicionalmente y facilitarme enormemente este trabajo.

Y, por supuesto, **Amaia**, creo que tendría que escribir otra tesis solo para agradecerte toda la ayuda, tanto para hacer posible esta tesis como para todo en la vida. Gracias por estar a mi lado cada día, por conseguir sacarme siempre una sonrisa, apoyarme en los momentos más difíciles, aguantarme (que no es nada fácil) y por ser una parte tan importante en mi vida. "*Iraun dezala zerua erori artean*"

ABSTRACT

Lithium-sulfur batteries (LSBs) represent a compelling alternative in pursuing advanced energy storage systems, with the potential to surpass conventional lithium-ion batteries. This appeal stems from their commendable practical gravimetric energy density, surpassing 400 Wh kg^{-1}, with further improvement on the horizon. Despite these promising characteristics, the successful integration of LSBs into the market relies on overcoming a range of challenges inherent to this technology. Given the multifaceted nature of these challenges, this thesis adopts a holistic approach, developing individualized strategies for each cell component to deploy a unified final device. Beyond component-level innovations, this work places significant emphasis on the systematic evaluation of the upscaling process associated with the developed approach, recognizing its pivotal role in leading to practical advancements and facilitating the broader application of this technology.

Within the objective of optimizing the sulfur cathode, the integration of graphene-based activated carbons as sulfur hosts has offered remarkable results, with the ResFArGO material standing out as particularly effective. The outstanding intrinsic properties of ResFArGO contributed to an enhanced compatibility with lithium polysulfides (LiPS), effectively trapping and mitigating the shuttle effect's adverse impact. This, coupled with the improved electronic conductivity attributed to the presence of graphene, enhances the overall performance of LSBs under different operational conditions, highlighting the material's effectiveness.

Given the promising potential of ResFArGO and in a concerted effort to uphold the cost-effective advantage of Li-S batteries, a strategic additive approach was systematically explored to ensure the practical and economic viability of this material. Notably, even minimal quantities of ResFArGO, when combined with a commercial carbonaceous material, harnessed the intrinsic properties of ResFArGO, significantly improving the compatibility with the LiPS. Moreover, the presence of ResFArGO demonstrated its efficacy as an electrocatalyst, actively promoting the sulfur redox reactions intrinsic to the operation of Li-S batteries, thereby resulting in commendable cell performance.

In the pursuit of optimizing the sulfur cathode through the use of ResFArGO, it became evident that the conventional electrolyte, often employed as a reference in LSBs, fell short of ensuring long-term and stable cycling. In response to this limitation,

the investigation shifted towards exploring gel polymer electrolytes as a potential solution to the challenges posed by the conventional electrolyte. The result of this investigation, denoted as GPE_20, exhibited commendable individual properties and demonstrated promising performance in lithium iron phosphate (LFP)-based lithium metal batteries. However, despite these positive attributes, the GPE_20 was unable to mitigate the dissolution of LiPS and manage the reaction of the polymer matrix and the lithium metal anode, regrettably resulting in unsuitable battery performance.

At this point, successfully implementing tailored sparingly solvating electrolytes for application in LSBs proved pivotal to achieving the defined objectives. The strategic incorporation of the lithium bis(fluorosulfonyl)imide (LiFSI) salt within the electrolyte formulation was key to harnessing the benefits conferred by the distinctive solvation structure of this family of electrolytes. This inclusion was instrumental in ensuring long-term compatibility with the lithium metal anode. Moreover, the absence of free solvent molecules, a characteristic feature of this electrolyte family, emerged as a critical factor in mitigating the dissolution of LiPS in the electrolyte. Additionally, this attribute, coupled with well-selected electrolyte components, contributed to solidifying the non-flammable nature of this electrolyte, fundamental for guaranteeing the safety of the battery system. This electrolyte not only met the essential criteria for an optimal electrolyte in Li-S technology but also demonstrated outstanding compatibility with graphene-based sulfur cathodes. This synergistic combination yielded impressive cell performances, showcasing remarkable sulfur utilization and long-term cycle life.

The concluding chapter, dedicated to a comprehensive evaluation of the LSBs upscaling process, provided fundamental insights. The developed energy density calculation model facilitated the identification of the most influential operational parameters and established the necessary operating conditions to achieve high energy density LSBs. Furthermore, as an intermediate step in the scale-up process, the analysis of the monolayer pouch cells revealed substantial differences when compared to the performances observed in small coin cells, particularly in terms of cyclability. Notably, systems employing the conventional DME/DOL electrolyte experienced a noteworthy reduction in cyclability attributed to poor compatibility with the lithium metal anode. In stark contrast, the holistic system emerged as the sole configuration capable of ensuring cyclability comparable to coin cells. Finally, 1.1 Ah multilayer pouch cells were adeptly assembled and tested, demonstrating the

scalability of the strategies designed throughout the thesis in cells closely aligned to practical applications. Notably, these cells reiterated the cyclability issues of the conventional electrolyte, despite achieving remarkable energy density values, exceeding the impressive barrier of 300 Wh kg^{-1}. Conversely, despite facing new operational challenges arising from the upscaling process, the holistic system demonstrated its commendable cell stability and sustained long-term cycling even under Ah-level prototype cells.

Consequently, the obtained results underscore the substantial improvement achieved in the performance and stability of the Li-S cells through implementing the holistic approach, even at the prototype scale. This work establishes a robust groundwork for future improvements and optimizations of the system, with the overarching objective of further enhancing the performance of prototype cells.

Resumen

La transición hacia un modelo de producción de energía renovable y sostenible, así como la electrificación del transporte, son pasos fundamentales para combatir los problemas medioambientales actuales vinculados al uso extensivo de combustibles fósiles. En ambos ámbitos, el desarrollo de sistemas de almacenamiento electroquímico eficientes se presenta como un componente fundamental para alcanzar estos objetivos. En este contexto, las baterías de litio-ion (BLI) han transformado completamente la perspectiva de la electrónica portátil y han propiciado el inicio de la transición hacia la movilidad eléctrica, consolidándose como solución de uso generalizado comercialmente. No obstante, esta tecnología está alcanzando sus límites teóricos de rendimiento, lo que la incapacita para satisfacer los requerimientos energéticos de las aplicaciones emergentes.

Para superar esta limitación, resulta fundamental explorar nuevas tecnologías de batería, destacando aquellas denominadas “de siguiente generación”. En este contexto, la tecnología de litio-azufre emerge debido a su excepcional densidad energética. Estas baterías se fundamentan en la incorporación del azufre como material activo en lugar de los óxidos metálicos complejos como el fosfato de hierro y litio (LFP) o el óxido de manganeso cobalto y níquel (NMC) empleados en las BLI, junto con la incorporación de un ánodo de litio metálico. El azufre se distingue por ser un material económico, sostenible medioambientalmente y con una elevada capacidad teórica de 1675 mAh g^{-1}, incrementando en 10 veces la capacidad de las actuales BLI. Estas características confieren a esta tecnología de batería la capacidad de proporcionar un almacenamiento energético por unidad de masa considerablemente superior por un precio inferior al de los óxidos metálicos complejos, convirtiéndose así en un candidato idóneo para aplicaciones en las que la masa del dispositivo es un factor crítico.

A pesar de las prometedoras propiedades teóricas anteriormente mencionadas, la tecnología de Li-S se enfrenta a múltiples desafíos operacionales que han obstaculizado hasta la fecha su comercialización. Por un lado, se destacan los problemas intrínsecos de la tecnología, entre los que se incluye la naturaleza aislante del azufre, las variaciones de volumen durante el ciclado de la batería, debido a la diferencia de densidad entre los productos de partida y los finales de la reacción de conversión, la disolución y, por consiguiente, la pérdida de los compuestos

intermedios de la reacción (conocido como “efecto shuttle”) y la degradación del ánodo de litio metálico. Por otro lado, se encuentran los problemas operacionales asociados con el proceso de escalado de la tecnología al tratar de ajustar las condiciones de operación a las necesarias para aplicaciones prácticas. En la última década, en el mundo académico se han dedicado considerables esfuerzos de investigación para resolver los desafíos inherentes de la tecnología, dando lugar a avances pioneros que han mejorado sustancialmente su rendimiento. Sin embargo, es importante señalar que gran parte de estos estudios se han llevado a cabo en condiciones de operación ideales, alejadas de los requisitos necesarios para aplicaciones prácticas. Esta disparidad, junto con la limitada atención al estudio del proceso de escalado, ha generado una brecha sustancial entre la investigación académica y la industria en el ámbito de las baterías de Li-S (BLS). Con el objetivo de reducir esta brecha, para impulsar la futura comercialización de las BLS, resulta crucial intensificar la investigación centrada en el proceso de escalado en prototipos con condiciones cercanas a los requerimientos industriales.

En este contexto, considerando la naturaleza multidisciplinar de los desafíos que enfrenta la tecnología de Li-S, esta tesis aborda la implantación de un enfoque holístico para las BLS. Con este enfoque en mente, la tesis fue planteada como el desarrollo de estrategias individualizadas para cada uno de los componentes de la celda, con el objetivo final de unificar todas las mejoras en un dispositivo final. Asimismo, dada la importancia de cerrar la brecha entre el mundo industrial y el académico anteriormente explicada, se dedicó un especial énfasis en el proceso de escalado, poniendo el foco en el desarrollo de materiales con viabilidad industrial y profundizando el estudio del rendimiento de las estrategias desarrolladas a escala prototipo.

El **Capítulo I** de la tesis doctoral se centró en el estudio bibliográfico del estado del arte de la tecnología. En dicha búsqueda bibliográfica, se investigaron las diferentes problemáticas de la tecnología de Li-S, así como las posibles estrategias viables para su desarrollo.

Posteriormente, los primeros pasos prácticos de este proyecto de tesis, dado su carácter fundamental y su papel diferenciador en la tecnología de Li-S, se centraron en la optimización del cátodo de azufre. Esta optimización puede ser seguida a lo largo de los **Capítulos II** y **III** de la tesis. En el **Capítulo II**, basándose en una tecnología ya

consolidada como los condensadores electroquímicos y aprovechando los requisitos coincidentes entre ambas tecnologías referentes a los materiales carbonosos a utilizar, se seleccionaron diversos componentes carbonosos en base al conocimiento de una tecnología consolidada y madura como los supercondensadores. En este sentido, se estudió de forma pionera la implementación de carbones activados basados en grafeno como alternativa prometedora para servir como "anfitriones" de azufre. En esta investigación, se sintetizaron e incorporaron a la fórmula del cátodo de azufre dos carbones activados de distintas fuentes, denominados rGOCaf y ResFArGO. Los materiales resultantes, especialmente el ResFArGO, demostraron una destacada combinación de propiedades tanto texturales, agrupadas en una estructura plana bidimensional, alta área superficie específica y adecuada microporosidad, como una química superficial de naturaleza polar. Esta combinación de propiedades favoreció la compatibilidad del cátodo de azufre con los polisulfuros de litio generados por las reacciones de conversión del sistema, mitigando parcialmente los problemas asociados al "efecto shuttle". Además, la mejorada conductividad electrónica, debida a la presencia de grafeno, contribuyó a lograr excelentes rendimientos de celda bajo diferentes protocolos de ciclado.

Impulsados por los excelentes resultados demostrados por el ResFArGO en el **Capítulo II**, el siguiente capítulo se centró en la evaluación de su viabilidad práctica y económica, con el objetivo final de escalar el sistema. Para ello, se investigó la incorporación del ResFArGO como aditivo, al porcentaje de material carbonoso del sistema, completado por un material comercial de bajo coste conocido como Ketjenblack KJ600. A pesar de la reducción en su contenido, la combinación entre el carbón comercial y el ResFArGO mantuvo las excelentes propiedades inherentes del ResFArGO. Además, se determinó que la inclusión de este material como aditivo en la receta del cátodo permitió mejorar altamente la cinética de las reacciones redox correspondientes al funcionamiento de las BLS, destacando la función del ResFArGO como electrocatalizador. Estas propiedades favorables posibilitaron que el sistema basado en ResFArGO como aditivo exhibiera rendimientos de celda comparables a los observados en el **Capítulo II** cuando el ResFArGO se utilizó como fuente única de carbón estando en mayores proporciones. Estos resultados corroboraron la eficacia de la estrategia implementada, logrando un equilibrio exitoso entre aplicabilidad y rendimiento.

La optimización del cátodo de azufre evidenció simultáneamente la limitación del electrolito líquido convencional de la tecnología de Li-S para garantizar un ciclado de batería a largo plazo, resultando en una capacidad máxima de ciclado de tan solo 50 ciclos. Esta limitación en la ciclabilidad, combinada con los desafíos de seguridad inherentes de la utilización de electrolitos líquidos inflamables junto con litio metálico, subraya la necesidad de explorar nuevas soluciones de electrolito con el fin de cumplir con los objetivos marcados para este trabajo. Los **Capítulos IV** y **V** se enfocaron en abordar estas limitaciones de ciclabilidad y seguridad, consideradas como el principal desafío de la tecnología. El **Capítulo IV** se centró en la aplicación de electrolitos de geles poliméricos como una alternativa viable para baterías de Li-S. En este caso, se empleó un proceso de fabricación fácilmente escalable para desarrollar los electrolitos. Estos electrolitos demostraron un balance satisfactorio de propiedades individuales, como su adecuada integridad estructural, su alta estabilidad térmica, su naturaleza ignífuga y las notables propiedades electroquímicas como por ejemplo su alta conductividad iónica a temperatura ambiente. No obstante, a pesar de estas cualidades tan prometedoras, la falta de mitigación de la disolución de polisulfuros de litio, combinada con la incontrolada reactividad de la matriz polimérica con el ánodo de litio metálico, dieron lugar a una serie de reacciones parasitarias, resultando en un pobre rendimiento en celdas de Li-S.

Estos resultados adversos fueron fundamentales para identificar a la supresión de la disolución polisulfuros de litio y la compatibilidad entre el electrolito y el ánodo de litio metálico como aspectos claves a tener en cuenta en el desarrollo de un electrolito ideal para su aplicación en BLS. Con esto en mente, el **Capítulo V** se adentró en el desarrollo de electrolitos pobremente solventes como candidatos para su utilización en la tecnología de Li-S de alto rendimiento. En este sentido, la estratégica incorporación de la sal de litio LiFSI permitió explotar las propiedades de solvatación únicas de esta familia de electrolitos, gracias al papel fundamental que desempeña el anión de la sal empleado en su formulación. De esta forma, se logró una excelente compatibilidad con el ánodo de litio metálico evidenciado en el comportamiento en la deposición de litio metálico y la formación de capas protectoras ricas en LiF sobre el ánodo. Asimismo, la ausencia de moléculas libres de disolvente, característica de esta familia de electrolitos, contribuyó a mitigar la disolución de los polisulfuros de litio, uno de los aspectos claves anteriormente mencionado. Además, la seguridad de la batería fue asegurada por la naturaleza no inflamable del electrolito desarrollado caracterizada mediante diversas pruebas de flamabilidad llevados a cabo

durante la presente tesis. Por último y no por ello menos importante, este electrolito no solo cumplió con los requisitos clave para ser una alternativa idónea identificados en el **Capítulo IV**, sino que también presentó una excelente compatibilidad con los cátodos de azufre que incorporan ResFArGO. Esta sinérgica relación se tradujo en una mejora de la mojabilidad del sistema que resultó en rendimientos de celda extraordinarios, ofreciendo tasas elevadas de utilización de azufre al mismo tiempo que garantiza un ciclado estable a largo plazo. Por lo tanto, estos resultados ejemplificaron la eficacia del enfoque holístico de batería implementado en este trabajo de tesis.

Finalmente, motivados por los resultados obtenidos en los capítulos anteriores de la tesis, el **Capítulo VI** presenta una evaluación detallada del proceso de escalado de las diversas estrategias desarrolladas en celdas prototipo a nivel de Ah con relevancia industrial. Inicialmente, el desarrollo y estudio del modelo de densidad energética permitieron identificar los parámetros operacionales más influyentes y establecer, con ello, las condiciones necesarias para alcanzar los tan necesarios altos valores de densidad energética en el dispositivo final. Debido a la gran diferencia entre las celdas a escala de laboratorio con las industriales, se determinó la realización de un paso intermedio realizando con ello el análisis del rendimiento de las celdas tipo pouch monocapa. Estas celdas monocapa evidenciaron una notable reducción de la ciclabilidad en comparación con los resultados obtenidos a escala laboratorio con las celdas de tipo botón debido a los problemas inherentes del uso de láminas de litio metálico de mayor superficie. Sin embargo, en esta etapa intermedia, el sistema holístico demostró ser capaz de garantizar un ciclado notable, reforzando así la eficacia evidenciada a escala laboratorio. Finalmente, el paso final de la tesis doctoral tuvo como objetivo el estudio de las celdas prototipo a nivel de Ah. Estas celdas volvieron a evidenciar los problemas del ciclado largo del electrolito convencional a pesar de los remarcables valores tanto de capacidad como de densidad energética, superior a 300 Wh kg^{-1}. Por el contrario, el sistema holístico, a pesar de enfrentar nuevos desafíos operacionales derivados del proceso de escalado, mantuvo su característica estabilidad y ciclado a largo plazo incluso en las desafiantes condiciones de las celdas prototipo, volviendo a evidenciar la buena compatibilidad del electrolito desarrollado con el ánodo de litio incluso en estas condiciones tan desafiantes.

En resumen, la implementación del enfoque holístico como estrategia para abordar los desafíos de las BLS, llevado a cabo en este trabajo, ha permitido mejoras

significativas tanto del rendimiento de la celda como, de forma destacada, en su estabilidad de ciclado, incluso a escala prototipo con relevancia industrial. Los resultados presentados se encuentran entre los más destables dentro del estado del arte de la tecnología de Li-S y sientan las bases para futuras mejoras del sistema, enfocadas en la optimización del rendimiento de las celdas prototipo desarrolladas en el proyecto actual.

List of abbreviations

2D	Bidimensional
AC	Activated carbon
AC	Alternating current
AGG	Cation-anion aggregate
ATR-FTIR	Attenuated total reflectance-Fourier transform infrared
CA	Commercial additive
CCD	Critical current density
CE	Coulombic efficiency
CIP	Contact ion pairs
CMC	Carboxymethyl cellulose
CV	Cyclic voltammetry
DC	Direct current
DME	1,2-Dimethoxyethane
DOL	1,3-Dioxolane
e^-	Electrons
EDS	Energy dispersive spectrometry
EES	Electrochemical energy storage
EIS	Electrochemical impedance spectroscopy
EU	European Union
EV	Electric vehicle
eVTOL	Electric vertical take-off and landing
GNP	Graphene nanoplatelets
GO	Graphene oxide
GPE	Gel polymer electrolyte

HAPS	High-altitude pseudo satellites
HCE	Highly concentrated electrolytes
HFE	Hydrofluoroether
KJ600	Ketjenblack® EC-600JD
LCO	Lithium cobalt oxide
LE	Liquid electrolyte
LED	Light-emitting diode
LFP	Lithium iron phosphate
LHCE	Localized high-concentration electrolytes
Li^+	Lithium ions
LIB	Lithium-ion battery
LiDFTFSI	Lithium (difluoromethanesulfonyl)(trifluoromethanesulfonyl)imide
LiFSI	Lithium bis(fluoromethanesulfonyl)imide
LiPS	Lithium polysulfides
LiTFSI	Lithium bis(trifluoromethanesulfonyl)imide
LMA	Lithium metal anode
LMB	Lithium metal battery
LSB	Lithium-sulfur battery
MD	Molecular dynamics
MWCNT	Multiwalled carbon nanotube
NIB	Sodium-ion battery
Ni-MH	Nickel-metal hydride
PEGDME	Poly(ethylene glycol dimethyl ether)
PMMA	Poly(methyl methacrylate)
PSD	Pore size distribution

PVdF	Poly(vinylidene fluoride)
PVdF-HFP	Poly(vinylidene fluoride-co-hexafluoropropylene)
rGO	Reduced graphene oxide
RT	Room temperature
SBR	Styrene butadiene rubber
SEI	Solid electrolyte interphase
SEM	Scanning electron microscopy
SET	Self-extinguishing time
SS	Stainless steel
SSE	Sparingly solvating electrolytes
SSIP	Solvent-separated ion pair
TGA	Thermogravimetric analysis
TTE	1,1,2,2-Tetrafluoroethyl-2,2,3,3-tetrafluoropropylether
XPS	X-ray photoelectron spectroscopy
XRD	X-ray diffraction

CONTENTS

Chapter I

Introduction and Objectives

Chapter II

Graphene-Based Activated Carbons as Sulfur Host for High-Performing Lithium-Sulfur Batteries

Chapter III

Bringing ResFArGO Graphene-Based Activated Carbon toward Practical Lithium-Sulfur Application

Chapter V

Development of Sparingly Solvating Electrolytes for High-Performing, Safe, and Long Cycle Life Li-S Batteries

Chapter VI

From Lab-Scale Coin Cell to Ah-Level Prototype Li-S Cell Performance

CONCLUSIONS

APPENDIX

LIST OF CONTRIBUTIONS

Chapter I

Introduction and Objectives

1.1. Conceptualization and importance of energy storage systems

The economic growth of a country and its human development are strongly linked to its energy consumption. Despite efforts made by developed countries to reduce this dependency, the energy demand is continuously growing (**Figure 1.1a**), particularly in developing countries [1,2]. Primarily, this demand is met by the combustion reaction of fossil fuels, namely coal, oil, and natural gas, collectively accounting for 81% of the overall energy demand (**Figure 1.1a**) [3,4]. However, this notable dependence on fossil fuels entails two major problems. Firstly, fossil fuel reserves are finite and controlled by a limited number of countries, resulting in price volatility and uncertainties, especially affecting import-dependent heavily dependent like the European Union (EU) [5,6]. Secondly, the combustion of fossil fuels contributes significantly to global warming through the emission of greenhouse gasses [7–9].

The Paris Climate Agreement was established during the 2015 United Nations Framework Convention on Climate Change in response to urgent environmental concerns [10,11]. Ratified by 197 countries in 2019, this international agreement committed to restricting the global temperature increase to well below 2 °C. It is evident that meeting the objective outlined in the Paris Agreement, given the current trend of global energy consumption, requires a transition to a more sustainable and highly efficient energy model [12,13].

However, despite the significant technological advancements in renewable energies and their collection systems, their widespread deployment faces a fundamental obstacle: the non-constant and weather-dependent generation [14,15]. In this regard, developing and deploying cost-effective and efficient energy storage systems is crucial to overcome the intermittent nature of renewable energies. Among the available energy storage solutions, electrochemical energy storage (EES), primarily utilizing batteries, has emerged as a standout choice [16–18].

The transportation sector is another key domain that can greatly benefit from EES deployment. The automotive industry, a worldwide leader at the economic, research, and development level, has historically relied on combustion engines, resulting in significant environmental damage through greenhouse gas emissions [19,20]. Consequently, an imperative switch from combustion engines to electric motors is evident. However, challenges such as limited autonomy and high cost are

currently slowing down the widespread display of electric vehicles (EVs) [21–23]. Hence, the effective development of EES holds the key to overcoming these challenges and advancing the decarbonization of the transport sector.

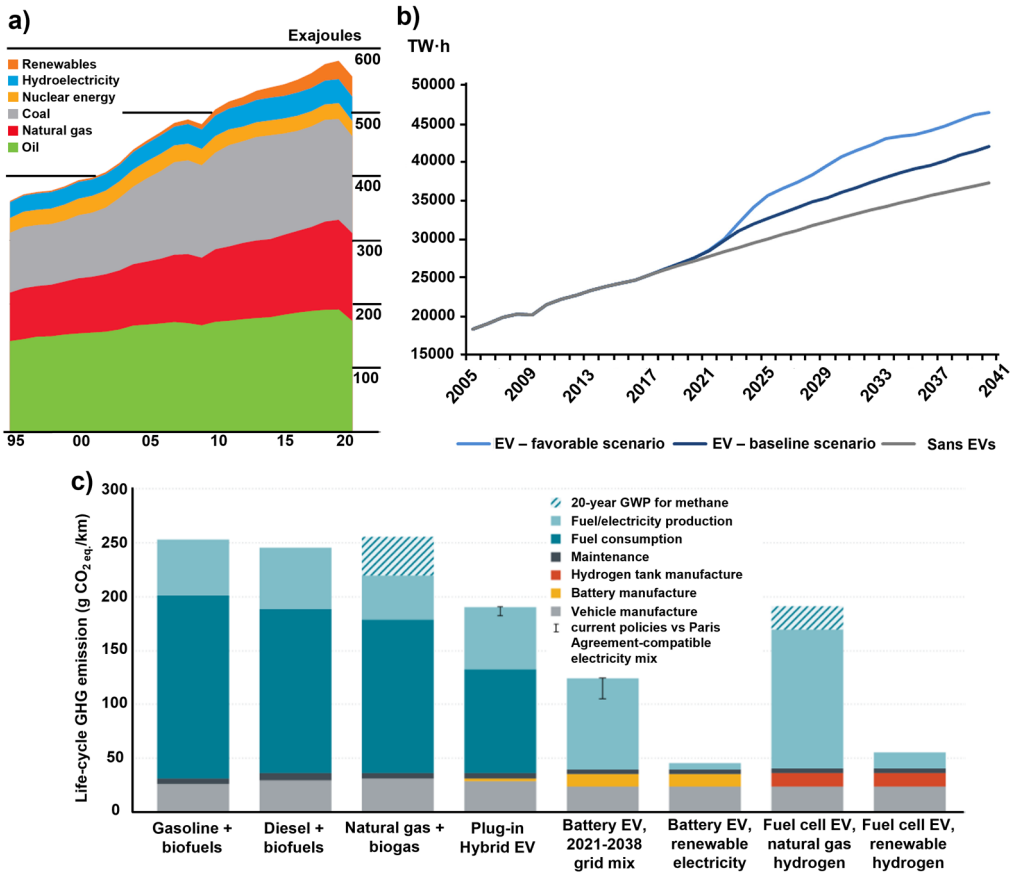

Figure 1.1. a) World primary energy consumption trend until 2021 reflecting the share of each generation source [24]. **b)** Total electricity consumption evolution in the EU. **c)** Life-cycle greenhouse gas emissions for typical medium-sized passenger cars [25].

In the EU, the adoption of EVs is projected to comprise approximately 80% of the total vehicle fleet by 2050, resulting in an estimated 10% rise in total electricity consumption (**Figure 1.1b**) [26,27]. This transition to transport electrification will notably reduce both CO_2 and air pollutants emissions originating from the road transport sector itself [28,29]. However, it is crucial to acknowledge that the power source of EVs is directly linked to the grid. Presently, as previously outlined, a substantial portion of global electricity generation relies on fossil sources.

Consequently, this increased electricity consumption by EVs may directly contribute to an increase in greenhouse gas emissions (**Figure 1.1c**) [27]. Therefore, EVs cannot be considered an environmentally friendly solution until there is a fundamental transition in electricity generation towards clean and sustainable sources.

Indeed, the integration of renewable energies and transport electrification requires a closely interlinked approach, with the development of EES systems as a pivotal and common nexus [30]. In the realm of energy storage systems, critical features such as flexibility, security, high energy density, durability, and environmental compatibility are indispensable requirements. Among the spectrum of EES technology systems, batteries are booming both in industrial applications and everyday life, owing to their high efficiency, straightforward design, portability, and swift installation [31]. However, despite these benefits, batteries face substantial challenges, including high maintenance costs, limited cycle life, and relatively lower power density. Addressing these hurdles is essential for their effective deployment to large-scale facilities.

1.2. Rechargeable Batteries

While the term “battery” is commonly used, it is noteworthy that a battery comprises one or more fundamental electrochemical units referred to as cells. A cell essentially consists of two electrochemically active components known as negative and positive electrodes, separated by an ion-conductive and electronically insulator medium called electrolyte. In most cases, the terms “anode” and “cathode” are conventionally employed to denote the negative and positive electrodes, respectively.

Batteries can be broadly classified into two main categories: primary batteries and secondary batteries [32]. Primary batteries are non-rechargeable devices that come pre-charged and are discarded once their energy is depleted. Examples of primary batteries include zinc-air, zinc-carbon, alkaline, mercury, and molten salt batteries [33,34]. In contrast, secondary batteries, also known as rechargeable batteries, are electrochemical energy conversion and storage devices that are designed for high energy density applications. These batteries store energy in chemical forms, converting electric energy into electrochemical energy, and can be recharged multiple times after being discharged [35]. As a result, in the case of secondary batteries, the terminology of “anode” and “cathode” can be a source of

confusion, as the designation of “anode” and “cathode” need to be aligned with the charge and discharge processes.

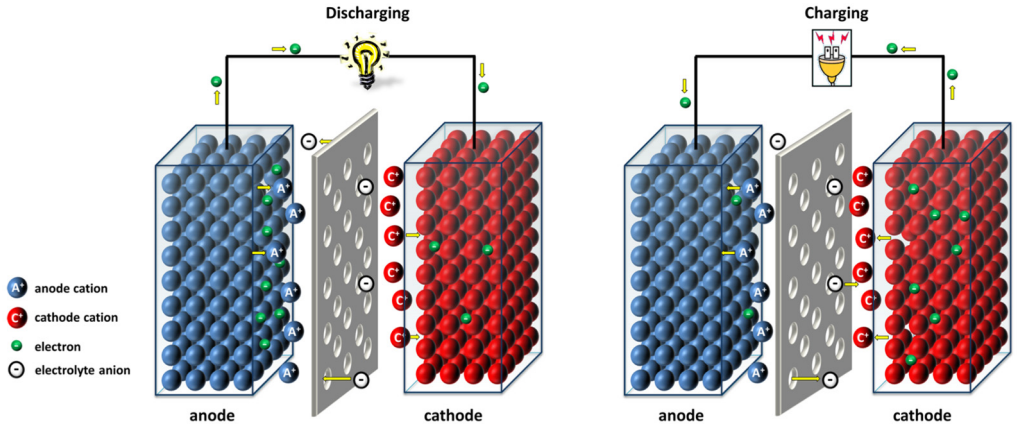

Figure 1.2. Electrochemical operation of a cell during the discharge and charge process (reproduced with permission from Ref. [36]).

Figure 1.2 schematically illustrates the working principle of a common rechargeable cell. During the charging process, when the two electrodes are connected through an external device, the negative electrode undergoes oxidation, releasing metal ions that migrate through the electrolyte toward the positive electrode. Simultaneously, electrons (e^-) are compelled to move from the negative electrode to the positive electrode through the external load, leading to the reduction of the latter. Conversely, during the discharge cycle, the charge flow process is reversed, resulting in the oxidation of the positive electrode, while the negative electrode accepts both the e^- and ions, undergoing reduction.

The amount of electric charge that can be stored in a battery is represented through the concept of capacity, measured in coulombs (1 C = 1 As) or more commonly in ampere-hour (1 Ah = 3600 C). The theoretical capacity, or the maximum obtainable capacity of a given active material, can be determined through Faraday’s law:

$$C_{theo} = \frac{F \cdot n_e}{M_w} \tag{1.1}$$

where F is Faraday’s constant, n_e is the number of electrons involved in the redox reaction and M_w is the molecular weight of the active material. As can be seen

in **Equation 1.1**, the theoretical capacity is generally normalized by the mass of the active material (C_{theo} = Ah g^{-1}).

In practice, the achieved capacity during battery cycling falls short of the theoretical capacity due to different operational constraints, such as side reactions, internal resistances, or component degradation. In this context, a key parameter for evaluating a battery's performance is its Coulombic efficiency (CE), calculated as the ratio between the provided capacity during the discharge process versus the capacity value stored during the charging process:

$$\mathrm{CE} = \frac{\mathrm{C_{dis}}}{\mathrm{C_{ch}}} \times 100 \tag{1.2}$$

This parameter indicates the degree of efficiency of battery operation and is closely linked to battery lifespan. Ideally, its value should approach 100% to ensure optimal efficiency and performance, ultimately leading to extended battery life.

The current density at which a battery is charged and discharged is expressed by the intensity, measured in amperes (A). In the battery research field, the battery cycling current is expressed by the C-rate parameter, which is defined by the following equation:

$$\mathrm{C_{rate}} = \frac{\mathrm{i_{applied}}}{\mathrm{i_{1h}}} \tag{1.3}$$

where $i_{applied}$ is the current applied to the battery and i_{1h} is the current required to charge/discharge the cell in 1 h. As an example, a C-rate of 0.2C or C/5 indicates that it takes 5 hours to either charge or discharge the battery.

The cell voltage, expressed in volts (V), is determined through the potential difference between the two electrodes constituting the cell. The energy a battery possesses (E_{cell}) is directly related to the capacity (C_{cell}) and voltage (V_{cell}) of the cell:

$$\mathrm{E_{cell}} = \mathrm{C_{cell}} \cdot \mathrm{V_{cell}} \tag{1.4}$$

It should be noted that the cell voltage is not a constant parameter and changes during battery operation. Hence, to obtain the capacity value, it is necessary to integrate over the entire voltage range:

$$E_{cell} = \int_{0}^{C_{cell}} V_{cell} \cdot dC \quad (1.5)$$

However, this equation is less commonly used in practice, and instead, an average voltage value is typically employed to determine the energy of a battery. This parameter is generally expressed per unit of mass or volume to facilitate the comparison of battery storage capacity in terms of weight or size. These expressions are denoted as gravimetric or volumetric energy density, respectively.

Finally, an additional key metric in assessing a battery is its electrical power, which refers to the rate at which electrical energy can be released or delivered. This parameter is obtained from the inversely proportional relationship between the energy released by the cell and the time taken for the charge/discharge process (t):

$$P_{cell} = \frac{E_{cell}}{t} \quad (1.6)$$

1.2.1 Lithium-ion batteries (LIBs)

Rechargeable batteries were introduced into the market in the mid-19th century, propelled by the successful invention of lead-acid batteries by French physicist Gaston Planté. Remarkably, this battery technology continues nowadays to find applications in different domains [37]. Over time, other battery technologies emerged, including Nickel-Cadmium (Ni-Cd) and Nickel-metal hydride (Ni-MH) batteries, aimed to enhance battery properties and establish a presence in the market [38].

Nevertheless, despite the great virtues of these technologies, none of them provided a definitive solution to the rechargeable battery landscape, mainly due to significant self-discharge issues. In this context, the emergence of lithium-ion batteries (LIBs) marked a revolutionary breakthrough in the rechargeable battery landscape. Firstly commercialized by SONY company in 1991, LIBs rapidly gained dominance in the market as a power source for portable electronics [39,40]. As a result, LIBs are now emerging as a viable alternative in the EV market and are being actively pursued for grid energy storage applications.

The first commercially available secondary LIBs relied on the intercalation and deintercalation reaction of lithium ions (Li^+), a discovery attributed to the pioneering

research of Professor John Goodenough [41]. This electrochemical reaction involves the movement of Li^+ between the anode and the cathode. As illustrated in **Figure 1.3**, during the charging process, Li^+ are released (deintercalated) from the layered oxide-based positive electrode, traveling through the ion-conductive electrolyte to reach the negative electrode, where they are inserted (intercalated) within its structure. Simultaneously, electrons (e^-) released during the deintercalation process move through an external circuit favored by an external energy supply. Once Li^+ and e^- reach the negative electrode, their insertion (intercalation) into the carbonaceous structure take place. Conversely, during the discharge process, analogous processes occur in reverse, Li^+ is deintercalated from the negative electrode a re-intercalated in the positive one. Concurrently, e^- spontaneously flow to the oxide layer cathode, generating an electrical current that powers an external load.

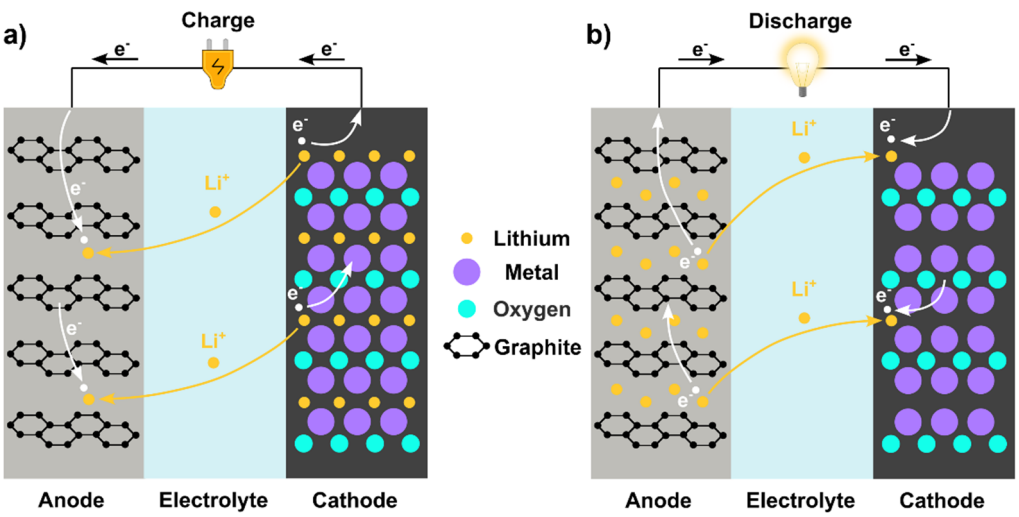

Figure 1.3. Schematic illustration of **a)** charge and **b)** discharge mechanism process in a commercial LIB.

This Li-ion cell operates at 3.7 V and delivers an energy storage capacity and density of 150 mAh g^{-1} and 250 Wh kg^{-1}, respectively. Notably, this energy storage capacity is three times higher than that of previously discussed technologies, making LIBs successful not only in portable electronics but also in EVs and grid energy storage applications [42].

1.2.2. Challenges and opportunities for Li-ion batteries

Nevertheless, the growing demand for new applications requiring higher energy storage capacities has driven the need to develop batteries with increased energy density. For instance, the EV industry mandates batteries with energy values of > 400 Wh kg^{-1} and 800 Wh L^{-1} at the cell level to sustain autonomy levels in alignment with conventional transportation patterns while ensuring cost-effectiveness [43]. In this sense, traditional LIBs are approaching their theoretical limits and would encounter challenges to meet future energy requirements. Consequently, researchers are currently directing their efforts towards enhancing the performance of LIBs by exploring new materials: cathode materials that offer enhanced storage ability and/or anode materials that operate at lower potentials [44–46].

1.2.2.1. New cathode materials

A key strategy to enhance the energy density of LIB involves replacing the traditionally used lithium cobalt oxide ($LiCoO_2$) cathode active material with innovative alternatives [47,48]. One of the early approaches focused on partially replacing cobalt with other transition metals, such as nickel and/or manganese, within the structure of the layer oxide $LiNi_yMn_{1-y-x}Co_x$, commonly referred to as NMC [49,50]. A special focus has been placed on materials with high Ni content ($y > 0.5$) while reducing Co content. This shift is driven by the lower cost, higher theoretical capacity, and increased operational voltage, all while considering the ethical concerns related to the current cobalt mining issues [51,52]. However, this configuration encounters new operational challenges, particularly in terms of cyclability and thermal stability [53,54].

In alignment with this trend, other cathode materials that have gained prominence in recent years are the layered lithium- and manganese-rich oxides (LMROs), represented by the formula $_xLi_2MnO_3{\cdot}(1-x)LiMO_2$ (M = Ni, Co, Mn or combinations). These materials offer high gravimetric capacity and energy density ($\sim$200–300 mAh g^{-1} and $\sim$900 Wh kg^{-1}, respectively) and exhibit high thermal stability [55,56]. However, LMR cathodes still face several technical limitations that need to be addressed before practical application, including capacity loss in the initial cycle, poor rate capability, voltage decay during cycling, and relatively short cycle life [57,58].

Among the different cathode materials studied for LIBs, olivine phosphates have garnered significant attention for industrial applications. Notably, lithium iron phosphate, or $LiFePO_4$ (LFP), stands out as the predominant cathode material widely employed in LIBs [59]. The significant adoption of LFP is notably attributed to the pioneering commitment of the Chinese battery industry [60,61]. This technology offers several advantages, including high-energy density, good cyclability, high thermal stability, low cost, and environmental friendliness, making it an excellent candidate as a battery active material [62,63]. Nowadays, LFP is a commercially available material and can nearly achieve its theoretical capacity (approximately 170 mAh g^{-1}), showing an excellent rate capability and guaranteeing extraordinary safety properties. Nonetheless, its low nominal working potential of 3.2 V restricts its use for high energy density applications, positioning it as a viable alternative for applications where safety, durability, and cost-effectiveness are critical requirements [64,65].

1.2.2.2. New anode materials

Presently, LIBs use graphite as the anode material, resulting in a limited theoretical capacity of 372 mAh g^{-1}. To improve and increase the energy density of future batteries, the replacement of graphite with alternative materials has been recognized [66]. Consequently, extensive research has been dedicated to exploring alternative anode materials. In this sense, silicon (Si) has emerged as an appealing alternative due to its outstanding features, especially for its high reversible capacity of 4200 mAh g^{-1} (over ten times higher than graphite). Furthermore, Si operates at a moderate working potential of approximately 0.4 V vs. Li^+/Li, enabling higher energy storage while enhancing safety issues as lithium plating and dendrite formation are prevented [67]. In addition, as the second most abundant element in the Earth's crust, Si is a cost-effective material [68]. Nevertheless, the implementation of Si as an anode material faces several technical challenges. The primary challenge stems from the significant volume change, approximately 400%, that occurs during battery cycling. This volume change leads to the development of cracks and pulverization of the Si electrode, ultimately compromising the electrochemical performance of the battery [69,70].

Another anode alternative that has gained significant attention is the resurgence of Li metal due to its outstanding electrochemical features. Its low atomic

mass contributes to its outstandingly high theoretical capacity of 3860 mAh g^{-1}, and its high tendency to release electrons from its outer shell results in a low electrochemical voltage (-3.04 V vs. the standard hydrogen electrode) [71,72]. Despite safety concerns that led to its sidelining for several decades in favor of graphite, impressive advancements in electrolyte engineering and the implementation of effective protection strategies have brought lithium metal batteries (LMBs) to the brink of commercialization [73].

While the broken-down solutions for alternative materials for both cathode and anode have provided partial solutions to the energy storage constraints of traditional LIBs, they remain insufficient for meeting the demands of high energy density applications. Notably, these strategies rely on the same cathode materials as traditional LIBs, hindering the potential for increasing cathode capacity and consequently limiting the final battery energy density. Additionally, the dependence on traditional cathode materials further exposes the technology to supply chain vulnerabilities, such as resource shortages and notable price fluctuations, impeding the scalability and/or cost-effectiveness of large battery capacities [48,74]. Moreover, safety concerns and the environmental impact of LIB materials underscore critical challenges that require solutions. Consequently, it is imperative to look beyond the current standard and undertake an intensive search for alternative chemistries or technologies. This imperative has given rise to the concept of "beyond Li-ion" alternative technologies.

1.3. Transitioning beyond lithium-ion batteries

In the domain of the “beyond Li-ion” concept, several alternative technologies have emerged. These alternatives encompass the use of alternative alkali or alkali earth metals such as sodium (Na), potassium (K), or magnesium (Mg), as well as the development of novel cathode materials based on reaction chemistries involving elements like sulfur or oxygen [75,76].

1.3.1. Non-Li metal-based batteries

Ensuring the long-term sustainability of batteries as a viable energy solution necessitates a comprehensive evaluation of the feasibility, cost, and availability of the resources upon which they depend. Nevertheless, the projected increase in lithium demand, coupled with its scarce and geographically concentrated supply, raises

concerns about potential future supply constraints, price fluctuations, and geopolitical conflicts [77]. Relying exclusively on lithium-based batteries for all energy storage requirements could jeopardize their long-term sustainability and hinder the widespread adoption of renewable energies and EV applications. To address this challenge, extensive research has been devoted to exploring alternative electropositive metals that are abundant in nature, aiming to identify viable substitutes for lithium and diversify the resource base.

1.3.1.1. Monovalent-ion batteries

Among the different alternatives, sodium-ion batteries (NIBs) have attracted significant attention from both academia and industry as viable and cost-effective alternatives to LIBs, especially due to the high abundance of Na, ranking as the sixth most abundant element in the Earth's crust [78,79]. The (de)intercalation chemistry of Na-ion is highly comparable to that of lithium-ion, with a slightly lower reduction voltage (-2.7 V of Na compared to -3.04 V for Li). However, due to the larger specific weight and ionic size of Na, NIBs exhibit lower gravimetric and volumetric capacities compared to Li-based batteries [80,81]. Nonetheless, this battery technology holds great potential for applications where overall cost takes precedence over considerations of weight. Consequently, NIBs are well-suited for large-scale grid energy storage applications when coupled with renewable energy sources [82–84] .

In addition to Na, other alkaline alternatives like potassium, which is an abundant and cost-effective metal, have been recently studied as a suitable candidate for beyond LIB battery technologies [85]. K-ion batteries (KIBs) exhibit a relatively low standard reduction potential of K^+/K (-2.936 V vs. the standard hydrogen electrode), which is lower than that of Na^+/Na and closer to Li^+/Li. This exceptional negative potential enables KIBs to operate at higher voltage, being competitive to NIBs in terms of energy density and power density, and a potential alternative to LIBs for high-voltage applications [86]. However, it is important to highlight that these alkaline-based alternative technologies are still in the early stages of development, and additional research efforts are required to address operational challenges and establish themselves as a viable alternative in the energy storage landscape [87,88].

1.3.1.2. Multivalent-ion batteries

In contrast to single-atom alkali metal-based batteries, multivalent-based batteries are gaining prominence as an emerging alternative for higher storage capacity systems. While the gravimetric energy density of LMBs may prove practically unattainable for multivalent-based batteries, they offer a competitive edge in terms of volumetric capacity [89,90]. Multivalent ion-based batteries increase the total charge transfer per ion within a specified electrode volume compared with monovalent ions, resulting in higher volumetric capacities. In this sense, several multivalent electrochemical systems, highlighting magnesium (Mg), calcium (Ca), aluminum (Al), and zinc (Zn), have been subjected to thorough investigation [91]. These metals not only provide the advantage of greater volumetric energy but also exhibit a reduced propensity to dendrite formation. Additionally, due to their inherent stability compared to alkaline metals, they are more manageable and amenable to processing, avoiding the need for highly controlled inert atmospheres during manufacturing [92]. Despite these promising features, it is important to emphasize that these multivalent-based technologies are still in their developmental stages. Extensive research and development efforts are indispensable to overcome the multiple challenges that their practical application presents [93,94].

1.3.2. Conversion-based positive electrodes

As previously described, the use of both Si and Li as anode materials offers the potential to increase the theoretical capacity of the anode. However, this capacity enhancement is limited by the constrained capacity of cathode materials based on traditional layered oxide materials. Additionally, the availability and sustainability of these materials is a paramount challenge. The extensively documented issues surrounding cobalt supply, including health and, particularly, ethical considerations related to child labor in its extraction, underscores the imperative to address these supply chain vulnerabilities [95–97]. Additionally, the scarcity and rising price of nickel, coupled with its negative environmental and health impacts, have surfaced as emerging concerns that require immediate attention [98,99]. For that reason, the exploration of new positive electrode materials is crucial. In this context, batteries based on conversion-type positive electrodes, with a special focus on technologies such as lithium-air (Li-air) and lithium-sulfur (Li-S) technologies, have become a hot

topic. This growing interest is mainly attributed to their availability, cost-effectiveness, and impressive theoretical capacity [100,101].

1.3.2.1. Lithium-air batteries (Li-air)

Lithium-air (Li-air) batteries have become of great interest, particularly as a power source for transportation, primarily due to their remarkably high energy density of 3505 Wh kg^{-1}. This surpasses even the energy density provided by conventional gasoline engines, typically around 1700 Wh kg^{-1} [102,103]. In contrast to many battery designs, Li-air batteries feature a unique structure where the traditional bulky positive electrode is replaced by a porous electrode, facilitating the introduction of oxygen from the ambient air. Among the different types of Li-air batteries, distinguished by the media involved in the reactions, non-aqueous or aprotic batteries are the most extensively studied approach [104]. These batteries are based on the following electrochemical reaction pathway:

$$\text{Anode}: \quad \mathrm{Li} \leftrightarrow \mathrm{Li^+} + \mathrm{e^-} \tag{1.7}$$

$$\text{Cathode}: \quad 2\mathrm{Li^+} + 2\mathrm{e^-} + \mathrm{O_2} \leftrightarrow \mathrm{Li_2O_2} \tag{1.8}$$

$$\text{Cell reaction}: \quad 2\mathrm{Li} + \mathrm{O_2} \leftrightarrow \mathrm{Li_2O_2} \tag{1.9}$$

$$\mathrm{E} = 2.96\ \mathrm{V\ vs\ Li/at\ Li^+}$$

Despite the outstanding properties of Li-air batteries, this technology remains immature and far from practical application. Several technical challenges need to be addressed to boost the viability of the technology. These challenges include low practical energy density due to poor rate capability, low energy efficiencies induced by large voltage hysteresis, limited cycle life resulting from the electrode and electrolyte decomposition by high overpotentials, and the interferences and parasitic reactions related to the other air components, such as CO_2 or H_2O [105,106].

1.3.2.2. Lithium-sulfur batteries (LSBs)

Lithium-sulfur batteries (LSBs) are becoming a promising and practical alternative from both academia and industry to pursue light and environmentally friendly high energy density batteries. This technology leverages the use of Li metal as the negative electrode, which presents a remarkable theoretical capacity of 3861 mAh g^{-1}, and elemental sulfur (S_8) as the electroactive material in the positive

electrode, which offers a theoretical capacity of 1675 mAh g^{-1}. This combination enables a theoretical energy density of 2500 Wh kg^{-1} [107,108].

The energy storage process in Li-S batteries takes place through the following electrochemical reaction:

$$Cell\ reaction: S + 2Li \leftrightarrow Li_2S \quad (1.10)$$

Due to their high theoretical specific energy density, as represented in **Figure 1.4**, LSBs have become a promising and practical alternative to replace LIBs, especially in applications where weight is a key parameter, such as trucks or buses, electric passenger aircraft, electric vertical take-off and landing (eVTOL), or high-altitude long-endurance unmanned pseudo satellites (HAPS) [109,110].

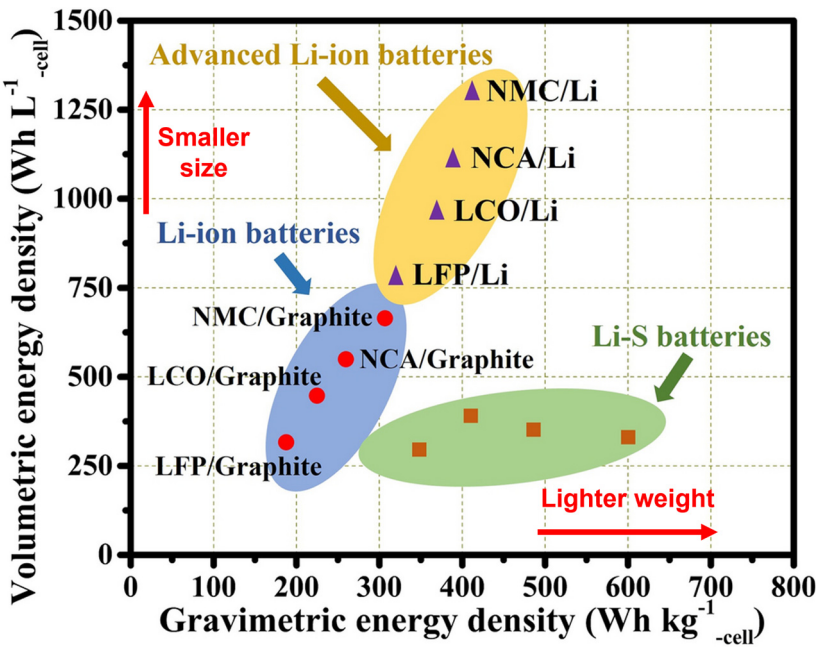

Figure 1.4. Comparison of volumetric energy density and gravimetric energy density of LSBs, LIBs, and advanced LIBs. Advanced LIBs are those that pair high-capacity lithium transition metal oxide cathodes with silicon or Li metal, rather than graphite anode materials (reproduced and modified with permission from Ref. [111])

HAPSs, exemplified by projects like Project Loon, Facebook Aquila, or Airbus Zephyr, represent prominent applications for LSBs [112]. These systems use solar

panels to charge their batteries during the day and rely on the energy storage in their Li-S batteries, with energy densities of 350 Wh kg^{-1}, to power their flights during the night. LSBs are well-suited for this application as they operate efficiently under soft battery rate conditions, typically around C/10. Notably, significant progress has been made in the Li-S technology, resulting in the development of high-capacity batteries of 20 Ah achieving energy densities exceeding 400 Wh kg^{-1} at practical pilot-scale levels. Furthermore, there is potential for LSBs to reach even higher practical values, possibly in the range of 500-600 Wh kg^{-1} shortly, making them strong competitors to traditional LIBs [113,114]. Therefore, as suggested by Fotouhi et al., future LSB applications will depend on further developments in terms of power, cycle life, and the combination of them [115]. However, the commercialization of LSBs encounters several challenges that have hampered their widespread adoption in the industry. These challenges include poor power capability, limited cycle life (particularly under high rates), and high self-discharge. Despite these hurdles, LSBs are distinguished as one of the more mature emerging technologies, benefiting from significant ongoing research aiming to overcome these challenges [112,116].

Consequently, LSB technology can be viewed as a rough diamond that requires proper polish before taking the decisive leap toward practical application, thereby becoming an attractive and viable solution in the eyes of the industry.

1.4. Delving deeper into Li-S Batteries

1.4.1. Elemental sulfur: ideal active material for battery manufacturing

The use of S_8 as an electroactive material provides significant advantages over traditionally employed metal oxide intercalation cathode materials. Firstly, despite the bad reputation of sulfur, it is an environmentally friendly, benign, and safe material [117,118]. These characteristics eliminate the need for precious metals like cobalt or nickel, which suffer from limited availability and high environmental impact. Notably, sulfur can be stored in an open-air environment, either in the form of powder or blocks, as illustrated in **Figure 1.5**, showcasing its stability and low reactivity. Secondly, sulfur is an abundantly available material, ranking as the sixteenth most abundant element in the Earth's crust [119]. This abundance positions sulfur as a cost-effective alternative, mitigating concerns related to material scarcity and contributing to the economic feasibility of battery systems.

From a chemical engineering perspective, it is noteworthy that most of the elemental sulfur is obtained as a by-product of desulfurization processes in refineries. The modified Clauss process for sour gas and the hydrodesulfurization process, followed by the Clauss process for oil, play a pivotal role in reducing the sulfur content in commercial fossil fuels to below 10 ppm requirements. This reduction is essential to comply with stringent environmental restrictions, preventing the formation of sulfur oxides (SO_x) during fuel combustion [120]. Therefore, sulfur's abundance is complemented by its large-scale production as a by-product of industry, contributing to its remarkably low price and making LSBs a real cost-effective alternative to LIBs. Furthermore, the depletion of gas and oil reserves, along with increased demand, has driven the utilization of "sour" resources characterized by higher sulfur content. This trend, alongside the tightening of fuel sulfur content regulations, has led to an involuntary increase in sulfur production [121,122]. This oversupply of sulfur, which cannot be readily absorbed by the sulfuric acid market alone, presents a promising opportunity for LSBs to establish a sustainable balance between demand and supply. This scenario creates a new "industrial symbiosis", fostering a mutually beneficial relationship between unintended sulfur producers and battery manufacturers.

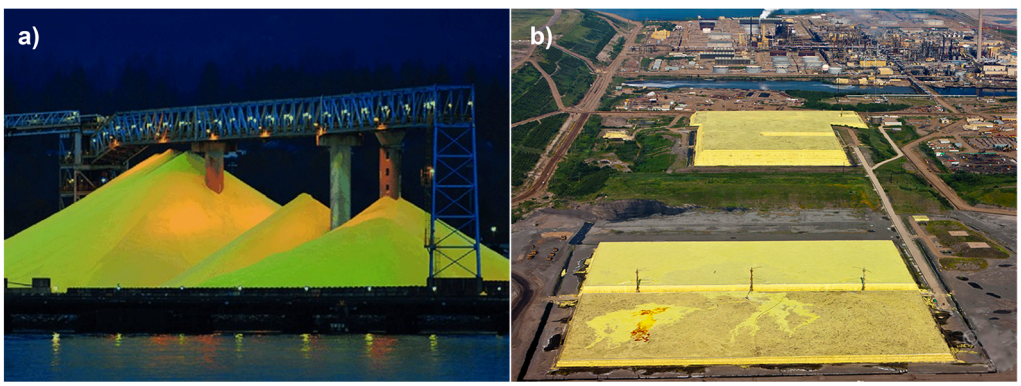

Figure 1.5. Open-air **a)** sulfur powder (reproduced with the permission of Ref. [101]) and **b)** sulfur bricks storage sites resulting from the desulfurization of petroleum by the Clauss process in the refineries.

1.4.2. Working principles of Li-S batteries

Regarding the electrochemistry aspect, as previously outlined, a conventional Li-S battery comprises a lithium metal anode (LMA), an S_8-based composite positive electrode, and a Li^+ conducting electrolyte. It is important to highlight that, contrary

to LIB-based active materials, sulfur initiates in a charged state, and the battery operation starts with a discharge process. In this process, as illustrated in **Figure 1.6**, Li metal is oxidized in the negative electrode, resulting in the formation of Li^+ and e^- (as shown in **Equation 1.7**). These Li^+, facilitated by the electrolyte, and e^-, conducted through an external circuit generating an electrical current, are simultaneously transported to the positive electrode. Subsequently, within the positive electrode, the reduction reaction of S_8 occurs, forming Li_2S by accepting both the e^- and Li^+.

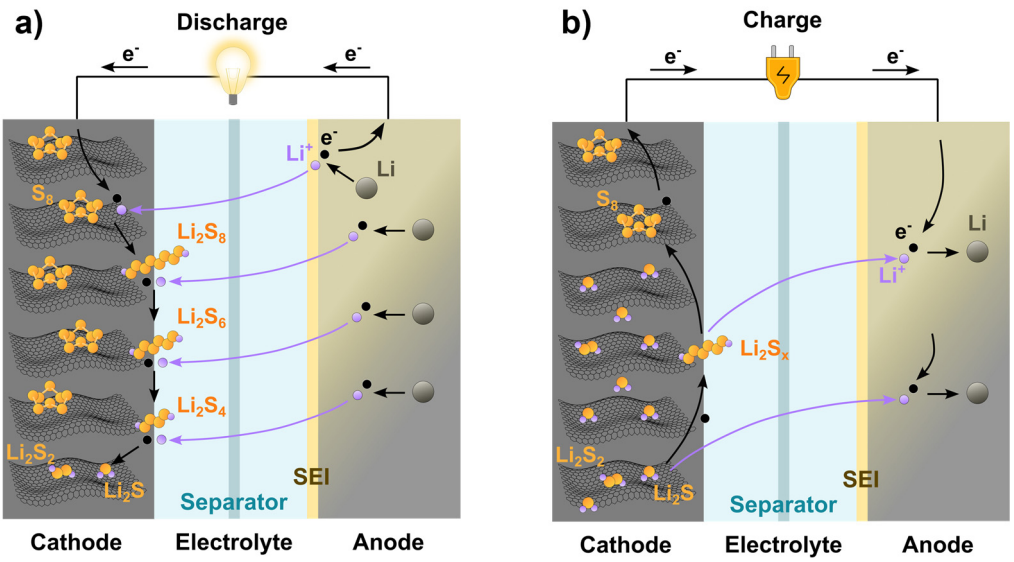

Figure 1.6. Schematic illustration of **a)** discharge and **b)** charge process in LSBs, and the corresponding intermediate products (lithium polysulfides) involved in the sulfur redox reactions.

The electrochemical processes governing the operation of a Li-S battery can be succinctly summarized through the following reactions:

$$\text{Negative electrode: } 16Li \leftrightarrow 16Li^+ + 16e^- \quad (1.11)$$

$$\text{Positive electrode: } S_8 + 16Li^+ + 16e^- \leftrightarrow 8Li_2S \quad (1.12)$$

$$\text{Cell reaction: } S_8 + 16Li \leftrightarrow 8Li_2S \quad (1.13)$$

However, as evidenced in **Figure 1.6**, the operation of LSBs is more complex than previously described. The reaction represented in **Equation 1.13** does not occur

as a single-step reaction but instead follows a multi-step reaction mechanism. In this mechanism, the elemental sulfur is reduced, leading to the opening of its ring structure and the formation of intermediate products known as lithium polysulfides (LiPS), specifically denoted as Li_2S_x ($2 \leq x \leq 8$) [123,124]. To elaborate, when the S_8 ring is opened, high-order LiPS with x ranging from 6 to 8 are formed. Subsequently, as more Li^+ are accepted, lower-ordered polysulfides emerge, with values of x ranging from 2 to less than 6. In more detail, the sulfur reduction mechanism during the discharge process can be broken down into four different stages:

Stage 1: Through a solid-liquid biphasic reaction, elemental sulfur is converted to Li_2S_8:

$$S_8 + 2e^- + 2Li^+ \rightarrow Li_2S_8 \quad (1.14)$$

Stage 2: Through a liquid-liquid monophasic reaction, Li_2S_8 (soluble) is further reduced forming high and low-order LiPS:

$$3Li_2S_8 + 2e^- + 2Li^+ \rightarrow 4Li_2S_6 \quad (1.15)$$

$$2Li_2S_6 + 2e^- + 2Li^+ \rightarrow 3Li_2S_4 \quad (1.16)$$

Stage 3: represents three-quarters of the theoretical capacity (1254 mAh g^{-1}). It is associated with the reduction of the low-order polysulfides to Li_2S_2 and Li_2S by a liquid-solid reaction, being those competing reactions [124]:

$$Li_2S_4 + 2e^- + 2Li^+ \rightarrow 2Li_2S_2 \quad (1.17)$$

$$Li_2S_4 + 6e^- + 6Li^+ \rightarrow 4Li_2S \quad (1.18)$$

Stage 4: Li_2S_2 is reduced to Li_2S by a solid-solid reaction, and, due to the insulator and insoluble nature of both products, this reaction is kinetically slow and commonly suffers from severe polarization:

$$Li_2S_2 + 2e^- + 2Li^+ \rightarrow Li_2S \quad (1.19)$$

Hence, an ideal discharge process follows four-stage profiles characterized by two plateaus. The first upper plateau > 2.3 V (as represented in **Equation 1.14**) is complemented by a lower ranging from 1.9 to 2.1 V (as indicated in **Equation 1.17** and

Equation 1.18). Additionally, two slopping-down regions emerge, one between 2.1-2.3 V (described in **Equation 1.15** and **Equation 1.16**) and another below 1.9 V (explained in **Equation 1.19**). For illustrative purposes, **Figure 1.7** displays a typical voltage profile for a Li-S battery during the discharge process, highlighting these four different stages and their resulting final products. Significant endeavors have been devoted to understanding the intricacies of the reaction mechanism in Li-S batteries to enhance cathode design and composition for enhanced performance. However, it is important to emphasize that discharge and charge processes, along with the resulting voltage profiles, are highly dependent on various factors. These factors include the composition of both electrode and electrolyte, electronic and ionic conductivity, internal cell resistance, as well as the operating rate. Consequently, formulating a universal model that suits the heterogeneity of LSB systems remains an elusive goal [125,126].

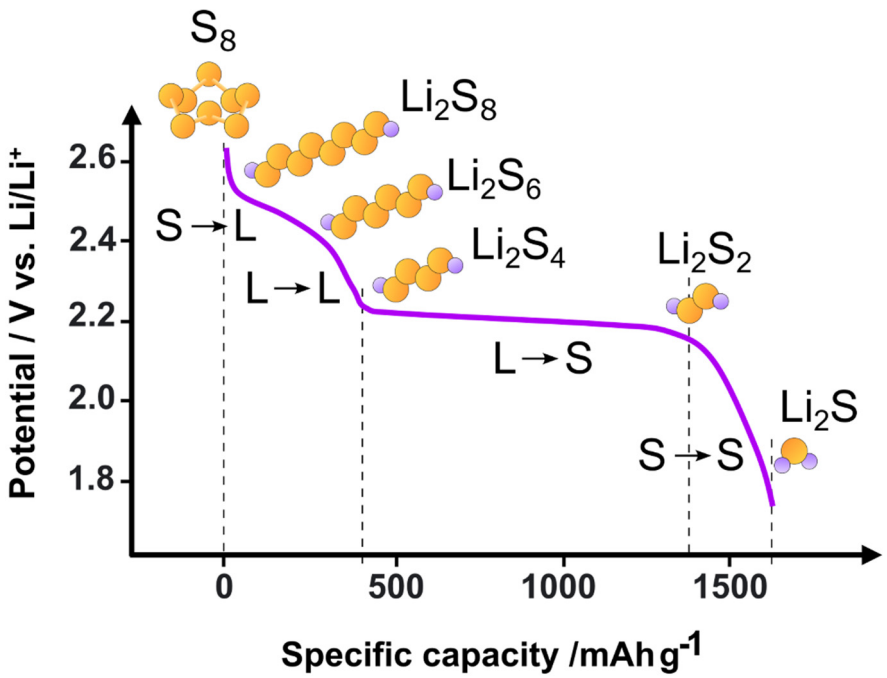

Figure 1.7. Voltage profile of Li-S during discharge, with the four differentiated steps

1.4.3. Challenges of Li-S batteries

Despite the striking properties of LSBs, the journey to commercialization is fraught with challenges, reminding that all that glitters is not gold. As schematically represented in **Figure 1.8**, the practical performance of LSBs falls short of their theoretical potential due to several technical challenges that continue to impede their broad implementation [116,127,128].

Mainly, these challenges can be broadly categorized into two principal groups: i) inherent challenges of the technology and ii) upscaling challenges. The first group is associated with the inherent problems intrinsic to technology and its underlying reaction mechanism. Conversely, the latter group of challenges is related to operational issues arising from the implementation of realistic operating conditions closely mirroring practical applications.

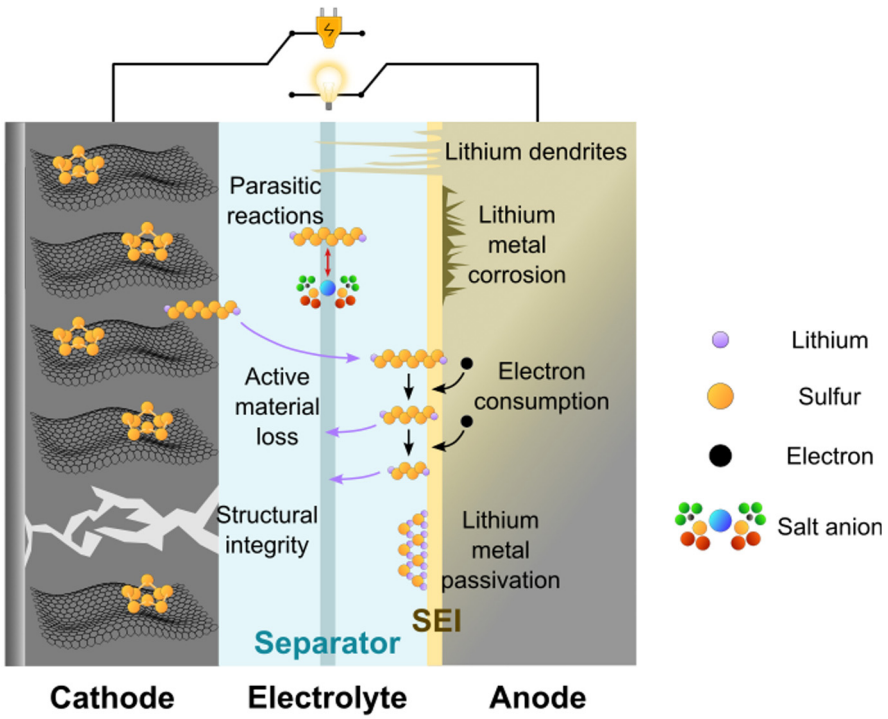

Figure 1.8. Schematic illustration of the different degradation processes encountered during LSB cycling.

1.4.3.1 Li-S technology's inherent challenges

1.4.3.1.1 Insulating nature of initial active material (S_8) and final products (Li_2S and Li_2S_2)

A primary challenge that must be addressed lies in the inherent insulating nature of elemental sulfur (S_8), which has poor electronic conductivity of 5×10^{-30} S cm^{-1} at room temperature. Besides, the end products of the discharge process, namely Li_2S_2 and Li_2S, share similar insulating properties. This inherent limitation gives rise to low sulfur utilization, poor cycle life, and suboptimal cell performance [129,130]. To address this challenge, a higher amount of conductive carbonaceous material (ranging from 20 to 40 wt.%) must be introduced into the sulfur electrode composition in comparison with LIBs. These carbonaceous materials, aside from providing electronic conductivity, must possess a certain level of porosity to host the sulfur, thereby improving the electronic environment of the active material. However, the incorporation of additional non-electrochemically active materials limits the final sulfur content, inevitably leading to a reduction in energy density and specific capacity per electrode mass [128,131].

1.4.3.1.2. Severe volume expansion upon cycling

During the discharge process, the ring structure of elemental sulfur (S_8) undergoes an opening as it accepts e^- and Li^+, giving rise to the formation of Li_2S as the final product. The substantial density difference between the initial product S_8 (2.07 g cm^{-3}) and the final product Li_2S (1.66 g cm^{-3}), induces a severe volume expansion of 78.7% during the discharge process [132,133]. This pronounced volumetric expansion, coupled with morphological changes in the active material upon lithiation, has a detrimental effect on the microstructure and architecture of the electrodes. These consequences seriously influence the LSB performance, leading to a large capacity drop, diminished CEs, and even the potential collapse of the cathode [134,135].

1.4.3.1.3. Shuttle effect

The shuttle effect is indeed the primary and well-known challenge associated with Li-S technology. As mentioned before, intermediate products, particularly high-order LiPS, possess high solubility in organic electrolytes, especially in commonly used ether-based electrolytes (e.g., Li_2S_6 with a solubility of 6 M in a mixture of

1,2-dimethoxyethane (DME) and 1,3-dioxolane (DOL)) [136,137]. Therefore, during the discharge process, a concentration gradient and potential difference emerge, resulting in the diffusion of these LiPS through the electrolyte toward the negative electrode. During the charging process, if the LMA is not adequately protected, LiPS can be reduced unwantedly, accepting e^- and Li^+. Subsequently, if the newly formed LiPS remain soluble, they can diffuse back to the cathode and get oxidized in the following charge. However, if the generated LiPSs are insoluble (i.e., when Li_2S_2 and Li_2S are formed) they irreversible deposit on the anode surface, leading to corrosion and undesired passivation of lithium anode [138,139]. This phenomenon, commonly referred to as the polysulfide "shuttle effect", induces detrimental consequences on the cell performance, including active material loss and anode degradation, resulting in reduced cycle life, low CE, and ineffective use of the sulfur [140,141]. However, the dissolution of LiPS is a double-edged sword. While it presents significant operational problems, it also plays a pivotal role in accelerating mass migration and enhancing electrochemical kinetics during cycling [142]. Hence, controlling the dissolution of LiPS is indeed necessary to mitigate the described issues, ensuring that this process is confined exclusively to the positive electrode while maintaining its essential role in optimizing LSB performance.

1.4.3.1.4. Li dendrite and anode degradation

The use of Li metal as an anode in batteries is regarded as the "holy grail" due to remarkable properties, such as low redox potential and the potential for increased energy density in final devices. However, employing Li metal introduces several challenges related to stability and safety.

A primary concern stems from its high negative redox potential, which renders it highly reactive with commonly used organic solvents. This reactivity results in the formation of a non-suitable and non-homogeneous solid electrolyte interphase (SEI) on the Li metal surface. The irregular SEI leads to uneven current density and conductivity, resulting in a non-uniform plating of Li^+ during the charging process [143]. Cycling exacerbated these issues, placing significant stress on the SEI, thereby inducing cracking and rupture. Consequently, needle-like microstructures, known as "dendrites", begin to grow from the cracks, expanding over time and potentially piercing the separator, causing a short circuit in the cell [144,145]. This issue generates heat and poses a safety risk, including the potential for fire and explosion due to the

large current passing through these microstructures [146]. Furthermore, the repeated rupture of the SEI during cycling continuously exposed fresh Li metal to the electrolyte, leading to its reaction and the depletion of the electrolyte, as well as the corrosion of the anode surface. These factors collectively contribute to low CE, a significant increase in internal resistance, and substantial capacity decay upon cycling [147,148].

The growth of Li dendrite has another significant consequence: the formation of inactive lithium, often referred to as “dead lithium”. Dead lithium originates from the breakdown of Li dendrites at their finest point [149]. Once formed, Li dendrites corrode in the presence of the electrolyte, resulting in the development of a poor electron-conducting SEI. Hence, the broken Li dendrite parts lose electrical contact and become unable to participate in the subsequent reactions. The accumulation of inactive lithium not only hampers Li^+ conductivity but also promotes the formation of new dendrites, ultimately leading to irreversible capacity loss of the cell [150,151].

1.4.3.2. Challenges derived from practical operating conditions

In the past decade, significant scientific efforts have been devoted to addressing the inherent challenges outlined above in the context of LSBs. This remarkable trend is vividly reflected in the exponential growth of publications related to LSBs since 2010, underscoring the widespread interest and the potential for technological advancements in this field. As a result of these fruitful strategies, LSBs have demonstrated remarkable performances, boasting long cycle-life (>1000 cycles) with high specific capacities (> 1000 mAh g^{-1}), and high Coulombic efficiencies (> 99%) [152–155]. However, it is worth noticing that most of these remarkable advancements have been achieved at the small lab cell level, typically employing coin cells or Swagelok cells, and operating under idealized conditions. These idealized conditions include the employment of low active material loading (< 2 mg cm^{-2}), an excess of electrolyte (with an electrolyte-to-sulfur ratio, denoted as E/S ratio, exceeding 10 µL mg_S^{-1}), and a thick lithium anode (often in 20-fold excess) [112,156,157]. Under these non-realistic laboratory conditions, many of the inherent challenges associated with LSB technology can be mitigated or masked, posing challenges in directly extrapolating and scaling up the proposed strategies to meet practical conditions demanded by the industry.

The transition from lab-scale LSBs to practical prototype cells encounters substantial challenges, with current results deviating from the performance achieved at the lab-scale, mainly due to significant cyclability issues. These challenges emerge as accelerated degradation in larger-sized cells, particularly derived from the degradation of the anode and electrolyte depletion when subjected to practical operating conditions [158,159]. Recent investigations into the upscaling of Li-S technology emphasized an evident gap between academic and industrial research, underscoring a lack of effective communication and collaboration between these institutions [107,110,160].

To achieve practical and high-energy LSBs capable of competing with commercial LIBs, three key parameters have been identified as crucial: i) amount of electrolyte, ii) cathode sulfur loading, and iii) the amount or excess of lithium. The amount of electrolyte, as mentioned previously, is commonly expressed as the ratio between the employed amount of electrolyte and the amount of sulfur in the cathode (E/S ratio). Cathode sulfur loading refers to the amount of sulfur per unit area of the electrode (mg cm^{-2}). Finally, the lithium inventory in the anode is quantified by the ratio of negative capacity to positive capacity (N/P), which represents the excess of lithium used in the cell. Certainly, these three parameters direct and significant impact on the energy density of the cells. For achieving practical high-energy density LSBs capable of competing with commercial LIBs, low amount of electrolyte (E/S < 4 µL mg^{-1}), high sulfur loading (> 5 mg cm^{-2}), and limited excess of lithium (N/P < 2) operational conditions must be used [112,161]. However, the implementation of these realistic conditions at the practical level brings new challenges that must be overcome for the long-awaited commercialization of LSBs, especially considering the scalability problems of this technology.

1.4.3.2.1. Challenges arising from lean electrolyte conditions

The electrolyte volume in LSBs is a key parameter that greatly influences their practical energy density, and it is closely linked to the sulfur content in the cathode [162,163]. Sulfur loading is another important parameter that also affects the energy density of the final battery. Increasing sulfur loading leads to a rapid enhancement in the energy until an optimal value is reached. Beyond this point, further increasing sulfur loading results in a gradual decay in the energy density. In contrast, reducing the amount of electrolyte for a fixed sulfur loading value significantly increases the

energy density of the cell, particularly for high sulfur loading values [164]. Therefore, the employment of high and optimal sulfur loading values coupled with low electrolyte amounts (E/S < 5 µL mg^{-1}, often referred to as lean conditions) is essential to obtain practical and competitive energy density values in LSBs.

The quantity of electrolyte in LSBs is not only pivotal for achieving high energy density but also greatly influences the overall battery system. Unlike LIBs, where the cost is predominantly driven by the expensive electrode raw materials, an excessive incorporation of electrolyte in Li-S cells constitutes a significant cost burden for practical LSB. This practice overshadows the inherent cost advantage of sulfur. As depicted in **Figure 1.9a**, the sulfur content has a minimal impact on the total cost of the battery, while an increase in the E/S ratio leads to a linear increase [165,166]. Therefore, a clear consensus exists among researchers regarding the pivotal role of lean electrolyte conditions in realizing practical and cost-effective LSBs.

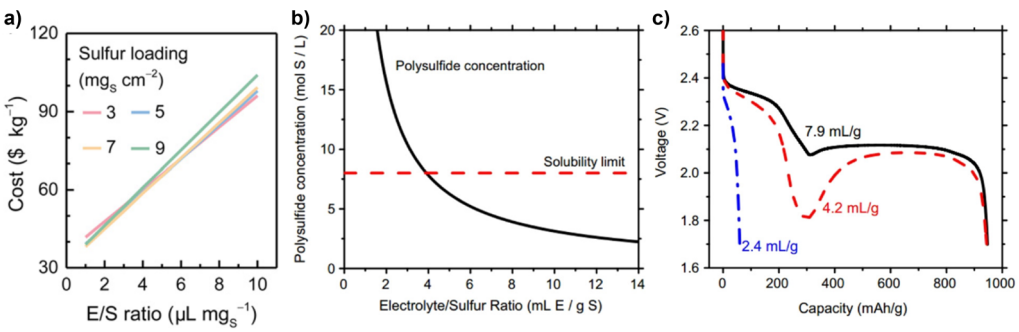

Figure 1.9. a) Influence of the E/S ratio on the overall cost of a practical Li–S package calculated with different areal sulfur loading (reproduced with permission from Ref. [152]). **b)** Polysulfide concentration solubility in correlation with the E/S ratio assuming complete dissolution of sulfur and **c)** galvanostatic discharge curves for Li–S cells influenced by the E/S ratio.

Despite this agreement, a pertinent question arises: why is every research work not conducted under these conditions? The honest answer lies in the inherent challenges associated with minimizing the electrolyte volume, as it introduces several operational problems [161]:

- Damaged ionic conductivity: In conventional ether-based electrolyte composed of the DME/DOL-based mixture, the redox reaction pathway involves the dissolution-precipitation of LiPS in the electrolyte. However, when high sulfur loading and lean electrolyte conditions are combined, LiPS

concentration increases, resulting in poor ionic conductivity and reduced wettability of the electrolyte due to its increased viscosity. In consequence, these effects can sluggish the sulfur redox kinetics, leading to poor sulfur utilization and increased polarization during the second plateau of discharge processes.

- Saturation and untimely precipitation of LiPS: When low E/S ratios are applied, the concentration of LiPS is sharply increased, exceeding their solubility limits and resulting in the saturation and premature precipitation of these soluble species (**Figure 1.9b**). The untimely LiPS precipitation onto the carbonaceous conductive matrix causes the clogging of both electronic and ionic conduction pathways, resulting in irreversible active material loss and sluggish solid-solid reaction kinetics. The premature solid precipitation at a low E/S ratio increases polarization during the second plateau reaching the voltage cut-off, thus resulting in a decreased capacity, and causing cell failure (**Figure 1.9c**) [167,168].

- Instability and degradation of LMA: Low E/S results in a significantly higher concentration of LiPS, which exacerbates the polysulfide shuttle effect. Additionally, the accumulation of dead Li due to the growth of Li dendrite under realistic operating conditions (which will be defined deeper in the next point), increases the contact surface area of the LMA, exacerbating the reactions with the organic electrolyte. This continuous electrolyte consumption, especially manifested when low E/S ratios are employed, can lead to premature cell failure due to electrolyte depletion and battery drying out [169].

1.4.3.2.2. High sulfur loading

Developing LSBs that can compete with the current commercial LIBs indeed requires the employment of high sulfur loading cathodes (≥ 4 mg cm^{-2}) with a remarkable utilization of active material (> 4 mAh cm^{-2}). While the scientific community has shown a strong preference for the research of new materials for the development of new sulfur cathodes to maximize the specific capacity, a limited number of studies included the application of high sulfur loading in their developed cathodes [170,171]. To advance the practical application of LSBs and enable a

meaningful comparison with LIBs, a more comprehensive exploration of high sulfur loading cathodes is imperative [172].

However, the development of high sulfur loading cathodes presents new challenges that need to be faced. Firstly, in the processing step, the conventional solvent drying process used for the preparation of high sulfur loading cathodes often leads to cracks formation and electrode delamination from the current collector. These issues can compromise the structural integrity of the cathode. Furthermore, in terms of electrochemical performance, high-loading cathodes deliver poor cycling performance with significant electrochemical polarization, low cyclability, and inferior rate performance [173]. This non-suitable performance behavior can be ascribed to several operating factors: i) The reaction kinetics are slowed down because of the increased transport distance of electrons and Li^+ within the electrode, worsened by the insulating nature of sulfur. ii) The undesired shuttle effect is exacerbated with high sulfur loadings due to the increase in the sulfur concentration gradient, thus resulting in a higher loss of active material and triggering the consequent cycling problems discussed above.

1.4.3.2.3. Li pulverization

The scientific community has predominantly focused on cathode optimization, addressing challenges related to sulfur's insulating nature and LiPS shuttle, to maximize the electrochemical conversion of sulfur and its practical capacity. However, this intense scientific focus on cathode optimization has inadvertently resulted in neglecting other critical research domains [174].

As mentioned previously, the major challenge for practical LSBs lies in their limited cycle life, primarily stemming from the instability of the LMA during cycling, especially in large-size cells (**Figure 1.10a**). Surprisingly, the significance of this behavior and the key role of the LMA have been largely underestimated in academic research, which has mostly focused on lab-scale conditions [175]. In the case of prototype cells, the amount of sulfur is notably higher compared to a coin cell, resulting in a larger current density on the anode surface and an intensified LiPS shuttle due to the increased concentration gradient. To illustrate this point, a case involving a LSB pouch cell with a total capacity of 2 Ah is considered, a standard capacity of a typical smartphone battery. Charging this cell at a moderate rate of 0.2C would require a current of 560 mA, which is significantly higher than those

corresponding to a coin cell, which typically ranges from 0.1-10 mA. The challenge arises from the uniform distribution of this current across the anode surface, due to the increased probability of encountering imperfections when employing a larger LMA area. These imperfections serve as concentration points for the current, leading to nucleation, dendrite growth, and the degradation of the anode (**Figures 1.10 b** and **c**) [169,177].

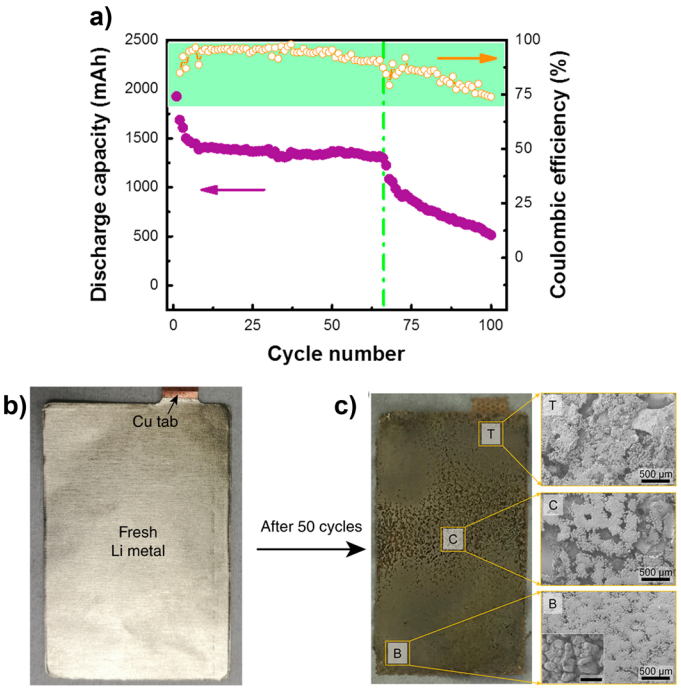

Figure 1.10. **a)** Discharge capacity and Coulombic efficiency of a 2.67 Ah pouch cell at a C-rate of C/10 (reproduced with permission from Ref. [175]). Optical images of top views of the Li foil **b)** before and **c)** after cycling (reproduced with permission from Ref. [176] and Ref. [175], respectively).

Consequently, the major concern affecting the poor cycle life of practical LMBs is the LMA degradation at high current densities. In contrast to conventional understanding, this degradation is not solely caused by short-circuiting but is primarily attributed to the formation and accumulation of a porous interface along the Li metal surface, resulting in Li pulverization and the formation of dead Li [176,178]. Even with the commonly used lithium nitrate ($LiNO_3$) salt additive, a pivotal component of commonly employed LSB additives that has shown remarkable results in coin cells, it proves insufficient in preventing degradation under these conditions. The resultant

formation of powdery Li leads to a larger contact surface, thus resulting in several operational and safety problems. I) Stronger reactivity with the electrolyte is induced, causing the electrolyte depletion issue that has been widely observed in LSB pouch cells. II) Safety issues are worsened due to an increased probability of combustion when exposed to air [178,179].

Hence, to bridge the substantial gap between academic and industrial research in this context, it is imperative to build a stable protective SEI layer on the Li anode surface to prevent Li pulverization and enhance Li ion diffusion.

1.4.3.3. Strategies for addressing LSB challenges

Indeed, the different challenges discussed are fundamental factors hindering the commercialization and industrial application of LSBs. Overcoming these constraints is of key importance in bridging the performance gap between lab-scale cells and prototype battery systems. To address these challenges, different strategies have been proposed for the different cell components. For the sulfur cathode, the development of new carbon hosts with additional functionalities and the introduction of kinetic promoters have emerged as highly promising strategies [180–186]. In the case of the electrolyte, electrolyte engineering involving novel solvation structures to modify the reaction pathway from precipitation-dissolution processes to quasi-solid or solid-solid processes is an appealing alternative that has gathered special attention [187–191]. Finally, on the anode side, the protection of the lithium anode is the main strategy being pursued through both ex-situ and/or in-situ protection techniques [192–197].

In this way, significant progress has been achieved by implementing these strategies in prototype cells. However, it is common to see in the literature the application of these valuable and useful strategies independently. Although each strategy demonstrates improvements when applied individually, they often fall short of meeting the established benchmarks for practical LSBs. This limitation arises from the recognition that the ultimate solution does not rely on the development of a single strategy but requires the integration of multiple strategies into a final unified LSB design, thereby giving rise to the concept of a "holistic LSB approach". In this sense, it is essential to emphasize that the challenges related to one cell component can have indirect repercussions on the rest of the cell components. For instance, addressing problems related to the use of lean electrolyte conditions requires not only electrolyte

modification but also the optimization of the sulfur cathode and the protection of the LMA to ensure effective operation under these conditions. In this sense, there is a consensus among industry and academic researchers on the imperative for a holistic and balanced approach to solving the multidisciplinary challenges of LSBs.

1.4.4. Industrial perspective of Li-S batteries

Despite the challenges associated with the upscaling process of LSBs, there is encouraging news regarding the commercialization of this technology. LSBs have garnered considerable attention from different companies and institutions, particularly in the realms of potential applications in transport and aerospace applications.

Sion Power and BASF have been actively engaged in the research and development of high energy density Li-S prototype cells based on practical applications [198,199]. However, after a long research trajectory in LSBs offering outstanding findings and improvements, Sion Power recently announced its decision to withdraw from this technology due to the operational difficulties associated with the cycle life issues. On the other hand, LG Chem has made significant investments in this next-generation technology and has recently reported successful testing of a 410 Wh kg^{-1} LSB, designed to power a high-altitude, long-endurance unmanned vehicle (EV-3) [200]. The company has explicitly stated its real intention to start commercial production of these cells by the year 2027 [201]. OXIS Energy Ltd. held a distinctive position in the industry as a company exclusively focused on the industrial development and implementation of LSBs. The technology pioneered by OXIS successfully met customer requirements, delivering high-capacity (>15 Ah) LSBs that exceeded 400 Wh kg^{-1} at a technology readiness level of 7–8 [202]. Unfortunately, in 2021, the economic downturn resulting from the COVID-19 pandemic led to OXIS's bankruptcy, orphaning the industrial development of LSB technology at that moment. Despite this setback, a ray of hope persists. Several promising start-ups, including Lyten, Theion, and Zeta Energy, have emerged in recent years, all poised to drive the long-awaited commercialization of LSBs [203–205]. The entry of these new players, coupled with the rise of additional companies in the field, inspires optimism for the future of this technology, anticipating new and outstanding developments in the coming years.

The industrial journey of Li-S technology demonstrates its challenging nature, marked by numerous hurdles that demand overcoming. Consequently, the establishment of close collaboration between industry and academic research stands out as a fundamental cornerstone for advancing the commercialization of LSBs. Bridging the gap between these two entities is imperative for enabling a symbiotic relationship that allows for a holistic approach to addressing the multidisciplinary challenges associated with LSBs.

1.5. Scope and objectives of the thesis

Advancing new battery technologies is pivotal for completing the transition to a sustainable energy model and meeting the energy demands of emerging applications. In this context, LSBs emerge as a promising alternative within the "beyond LIBs", particularly for applications where weight is a critical factor. However, to promote the commercialization of LSBs, establishing a closer and more collaborative relationship between academic research and industry is an imperative task.

Accordingly, the main objective of this thesis will be the development of high-performing, safe, and long cycle-life LSBs. To this end, a holistic approach will be implemented for addressing the multifaceted challenges inherent in Li-S technology. This approach will be characterized by the formulation of individualized strategies for each component of the cell, with the ultimate goal of integrating all advancements into a cohesive final device. Notably, this thesis work would emphasize evaluating the upscaling process of LSBs featuring the developed strategies, aiming to provide crucial insights into the pivotal transition from small coin cells to more practical cell configuration. The results obtained by the implementation of these strategies in Ah-level prototype cells will hold fundamental relevance for subsequent developments implemented at this large scale. For that purpose, the following specific points are identified as the primary objectives guiding the development of this work:

1. The identification and understanding of the principal challenges posed by each cell component of LSBs for tailoring the different improvement strategies. The multifaced nature of the emerging challenges underscores the significance that this study will have in guiding the research work of this thesis.
2. The investigation of the incorporation of graphene-based activated carbons in the sulfur cathode composition aiming to optimize its performance. To

achieve this objective, two different production sources of activated carbons will be analyzed in the synthesis process.

3. The evaluation of the practical and economic feasibility of the synthesized carbonaceous materials, with a specific focus on ensuring scalability within the proposed strategies. For this purpose, the additive strategy will be implemented to strike a balance between applicability and electrochemical performance.
4. The study of the employment of gel polymer electrolytes as an alternative to overcome the operational and safety limitations associated with the conventional electrolyte used in Li-S technology.
5. The exploration of sparingly solvating electrolytes to ensure long-term and safe cycling of LSBs. The objective will be to leverage the unique solvation properties inherent in this electrolyte family to prevent the dissolution of LiPS and promote compatibility with LMA.
6. The development of a comprehensive energy density calculation model to evaluate the prototype cells. This model will serve as a valuable tool for identifying the most influential operational parameters and establishing the optimal operating conditions to achieve high energy density in the developed LSBs.
7. The evaluation of the performance of the different strategies implemented in prototype cells, aiming to determine their viability in cells closely aligning to practical applications. This study will be of fundamental importance for discerning the existing differences between results obtained in laboratory-scale cells and those in prototype cells. This information will be essential for the design of future improvements tailored to optimize the performance of prototype cells, key to be applied in practical applications.

For all this, each chapter of the thesis will focus on a specific component of the battery, with the holistic battery concept progressively taking shape by the incorporation of improvements from earlier chapters into subsequent ones. **Chapter I** sets the stage by providing contextualization, reviewing the current state of the field, and outlining the objectives of the thesis. Subsequently, given the key role of the sulfur cathode Li-S technology, special attention is dedicated to its optimization in two consecutive chapters (**Chapter II** and **Chapter III**). **Chapter II** is dedicated to exploring the use of graphene-based activated carbons as sulfur host, aiming to produce cathodes with high sulfur loading and efficient utilization of the active material.

Building on these concepts, **Chapter III** focuses on improving the economic feasibility and practical application of the cathodes developed in the preceding chapter, without compromising their suitable electrochemical performance. Shifting the focus to the electrolyte and LMA, **Chapter IV** introduces and explores the implementation of gel polymer electrolytes as a promising alternative for the development of safe and high-performing room-temperature LSBs. Along the same line, **Chapter V** aims at the preparation of new liquid electrolytes with low LiPS solubility and suitable compatibility with the LMA to enhance LSB cyclability. **Chapter VI** provides a comprehensive analysis of crucial parameters for the upscaling process of LSBs. It also offers an in-depth evaluation of the results obtained from the prototype cell featuring each developed strategy. Finally, **Chapter VII** presents an analysis and contextualization of the thesis results, summarizing key conclusions drawn from the research work.

1.6. Bibliography

[1] R. Waheed, S. Sarwar, C. Wei, The survey of economic growth, energy consumption and carbon emission, Energy Reports 2019, 5, 1103–1115. https://doi.org/10.1016/j.egyr.2019.07.006.

[2] M.S. Gorus, M. Aydin, The relationship between energy consumption, economic growth, and CO2 emission in MENA countries: Causality analysis in the frequency domain, Energy 2019, 168, 815–822. https://doi.org/10.1016/j.energy.2018.11.139.

[3] J.L. Holechek, H.M.E. Geli, M.N. Sawalhah, R. Valdez, A Global Assessment: Can Renewable Energy Replace Fossil Fuels by 2050?, Sustain. 2022, 14, 4792–4814. https://doi.org/10.3390/su14084792.

[4] A. Kalair, N. Abas, M.S. Saleem, A.R. Kalair, N. Khan, Role of energy storage systems in energy transition from fossil fuels to renewables, Energy Storage 2021, 3, 135–162. https://doi.org/10.1002/est2.135.

[5] M.T. Punzi, The impact of energy price uncertainty on macroeconomic variables, Energy Policy 2019, 129, 1306–1319. https://doi.org/10.1016/j.enpol.2019.03.015.

[6] A. Carfora, R.V. Pansini, G. Scandurra, Energy dependence, renewable energy generation and import demand: Are EU countries resilient?, Renew. Energy 2022, 195, 1262–1274. https://doi.org/10.1016/j.renene.2022.06.098.

[7] M.D. Leonard, E.E. Michaelides, D.N. Michaelides, Energy storage needs for the substitution of fossil fuel power plants with renewables, Renew. Energy 2020, 145, 951–962. https://doi.org/10.1016/j.renene.2019.06.066.

[8] F. Perera, K. Nadeau, Climate Change, Fossil-Fuel Pollution, and Children's Health, N. Engl. J. Med. 2022, 386, 2303–2314. https://doi.org/10.1056/nejmra2117706.

[9] O.A. Towoju, F.A. Ishola, A case for the internal combustion engine powered vehicle, Energy Reports 2020, 6, 315–321. https://doi.org/10.1016/j.egyr.2019.11.082.

[10] M. Jakučionytė-Skodienė, G. Liobikienė, The changes in climate change concern, responsibility assumption and impact on climate-friendly behaviour in EU from the Paris Agreement until 2019, Environ. Manage. 2022, 69, 1–16. https://doi.org/10.1007/s00267-021-01574-8.

[11] P. Goglio, A.G. Williams, N. Balta-Ozkan, N.R.P. Harris, P. Williamson, D. Huisingh, Z. Zhang, M. Tavoni, Advances and challenges of life cycle assessment (LCA) of greenhouse gas removal technologies to fight climate changes, J. Clean. Prod. 2020, 244, 118896-118903. https://doi.org/10.1016/j.jclepro.2019.118896.

[12] M.T. Huang, P.M. Zhai, Achieving Paris Agreement temperature goals requires carbon neutrality by middle century with far-reaching transitions in the whole society, Adv. Clim. Chang. Res. 2021, 12, 281–286. https://doi.org/10.1016/j.accre.2021.03.004.

[13] H.L. van Soest, M.G.J. den Elzen, D.P. van Vuuren, Net-zero emission targets for major emitting countries consistent with the Paris Agreement, Nat. Commun. 2021, 12, 2140. https://doi.org/10.1038/s41467-021-22294-x.

[14] H. Stančin, H. Mikulčić, X. Wang, N. Duić, A review on alternative fuels in future energy system, Renew. Sustain. Energy Rev. 2020, 128, 109927. https://doi.org/10.1016/j.rser.2020.109927.

[15] R. Meenal, D. Binu, K.C. Ramya, P.A. Michael, K. Vinoth Kumar, E. Rajasekaran, B. Sangeetha, Weather forecasting for renewable energy system: A review, Arch. Comput. Methods Eng. 2022, 29 2875–2891. https://doi.org/10.1007/s11831-021-09695-3.

[16] J. Jiang, J. Liu, Iron anode - based aqueous electrochemical energy storage devices : Recent advances and future perspectives, Interdiscip. Mater. 2022, 1, 116–139. https://doi.org/10.1002/idm2.12007.

[17] M.S. Zantye, A. Gandhi, Y. Wang, S.P. Vudata, D. Bhattacharyya, M.M.F. Hasan, Optimal design and integration of decentralized electrochemical energy storage with renewables and fossil plants, Energy Environ. Sci. 2022, 15 4119–4136. https://doi.org/10.1039/d2ee00771a.

[18] D. Solyali, A comprehensive state-of-the-art review of electrochemical battery storage systems for power grids, Int. J. Energy Res. 2022, 46, 17786–17812. https://doi.org/10.1002/er.8451.

[19] P. Ahmadi, Environmental impacts and behavioral drivers of deep decarbonization for transportation through electric vehicles, J. Clean. Prod. 2019, 225, 1209–1219. https://doi.org/10.1016/j.jclepro.2019.03.334.

[20] A.G. Olabi, M.A. Abdelkareem, T. Wilberforce, A. Alkhalidi, T. Salameh, A.G. Abo-Khalil, M.M. Hassan, E.T. Sayed, Battery electric vehicles: Progress, power electronic converters, strength (S), weakness (W), opportunity (O), and threats (T), Int.

J. Thermofluids 2022, 16, 100212. https://doi.org/10.1016/j.ijft.2022.100212.

[21] R. Schmuch, R. Wagner, G. Hörpel, T. Placke, M. Winter, Performance and cost of materials for lithium-based rechargeable automotive batteries, Nat. Energy 2018, 3, 267–278. https://doi.org/10.1038/s41560-018-0107-2.

[22] S. Chen, F. Dai, M. Cai, Opportunities and challenges of high-energy lithium metal batteries for electric vehicle applications, ACS Energy Lett. 2020, 5, 3140–3151. https://doi.org/10.1021/acsenergylett.0c01545.

[23] V. Brescia, G. Degregori, D. Maggi, D. Hadro, An integrated vision of electric vehicles' consumer behaviour: Mapping the practitioners to consolidate the research agenda, J. Clean. Prod. 2023, 410, 137210. https://doi.org/10.1016/j.jclepro.2023.137210.

[24] British Petroleum, Statistical Review of World Energy 2021, 2021. moz-extension://bff414f9-b0c4-4d93-bac4-cff3282ad27d/enhanced-reader.html?openApp&pdf=https%3A%2F%2Fwww.bp.com%2Fcontent%2Fdam%2Fbp%2Fbusiness-sites%2Fen%2Fglobal%2Fcorporate%2Fpdfs%2Fenergy-economics%2Fstatistical-review%2Fbp-stats-review-2021-full-report.pdf (accessed December 16, 2023).

[25] Why are electric vehicles the only way to quickly and substantially decarbonize transport? - International Council on Clean Transportation, https://theicct.org/why-are-electric-vehicles-the-only-way-to-quickly-and-substantially-decarbonize-transport/ (accessed December 16, 2023).

[26] B. Lin, W. Wu, The impact of electric vehicle penetration: A recursive dynamic CGE analysis of China, Energy Econ. 2021, 94, 105086. https://doi.org/10.1016/j.eneco.2020.105086.

[27] N.O. Kapustin, D.A. Grushevenko, Long-term electric vehicles outlook and their potential impact on electric grid, Energy Policy 2020, 137, 111103. https://doi.org/10.1016/j.enpol.2019.111103.

[28] S. Khalili, E. Rantanen, D. Bogdanov, C. Breyer, Global transportation demand development with impacts on the energy demand and greenhouse gas emissions in a climate-constrained world, Energies 2019, 12, 3870. https://doi.org/10.3390/en12203870.

[29] R. Zhang, S. Fujimori, The role of transport electrification in global climate change mitigation scenarios, Environ. Res. Lett. 2020, 15, 034019. https://doi.org/10.1088/1748-9326/ab6658.

[30] L. Zhang, X. Hu, Z. Wang, J. Ruan, C. Ma, Z. Song, D.G. Dorrell, M.G. Pecht, Hybrid electrochemical energy storage systems: An overview for smart grid and electrified vehicle applications, Renew. Sustain. Energy Rev. 2021, 139, 110581. https://doi.org/10.1016/j.rser.2020.110581.

[31] J. Wen, D. Zhao, C. Zhang, An overview of electricity powered vehicles: Lithium-ion battery energy storage density and energy conversion efficiency, Renew. Energy 2020, 162, 1629–1648. https://doi.org/10.1016/j.renene.2020.09.055.

[32] C. Julien, A. Mauger, A. Vijh, K. Zaghib, Lithium Batteries, Springer International Publishing, Cham, 2016. https://doi.org/10.1007/978-3-319-19108-9.

[33] M. Armand, J.-M. Tarascon, Building better batteries, Nature 2008, 451, 652–657. https://doi.org/https://doi.org/10.1038/451652a.

[34] X. Luo, J. Wang, M. Dooner, J. Clarke, Overview of current development in electrical energy storage technologies and the application potential in power system operation, Appl. Energy 2015, 137, 511–536. https://doi.org/10.1016/j.apenergy.2014.09.081.

[35] S. Hemavathi, S. Srirama, A.S. Prakash, Present and future generation of secondary batteries: A review, ChemBioEng Rev. 2023, 10 1123–1145. https://doi.org/10.1002/cben.202200040.

[36] S. Muench, A. Wild, C. Friebe, B. Häupler, T. Janoschka, U.S. Schubert, Polymer-Based Organic Batteries, Chem. Rev. 2016, 116, 9438–9484. https://doi.org/10.1021/acs.chemrev.6b00070.

[37] Y. Zhang, C. gang Zhou, J. Yang, S. chang Xue, H. li Gao, X. hua Yan, Q. yuan Huo, S. wen Wang, Y. Cao, J. Yan, K. zheng Gao, L. xia Wang, Advances and challenges in improvement of the electrochemical performance for lead-acid batteries: A comprehensive review, J. Power Sources 2022, 520, 230800. https://doi.org/10.1016/j.jpowsour.2021.230800.

[38] A. Yoshino, Development of the Lithium-Ion Battery and Recent Technological Trends, Elsevier, 2014. https://doi.org/10.1016/B978-0-444-59513-3.00001-7.

[39] J.B. Goodenough, K.S. Park, The Li-ion rechargeable battery: A perspective, J. Am. Chem. Soc. 2013, 135, 1167–1176. https://doi.org/10.1021/ja3091438.

[40] H.J. Kim, T.N.V. Krishna, K. Zeb, V. Rajangam, C.V.V. Muralee Gopi, S. Sambasivam, K.V.G. Raghavendra, I.M. Obaidat, A comprehensive review of li-ion battery materials and their recycling techniques, Electronics 2020, 9, 1161.

https://doi.org/10.3390/electronics9071161.

[41] A.G. Olabi, Q. Abbas, P.A. Shinde, M.A. Abdelkareem, Rechargeable batteries: Technological advancement, challenges, current and emerging applications, Energy 2023, 266, 126408. https://doi.org/10.1016/j.energy.2022.126408.

[42] G. Zubi, R. Dufo-López, M. Carvalho, G. Pasaoglu, The lithium-ion battery: State of the art and future perspectives, Renew. Sustain. Energy Rev. 2018, 89, 292–308. https://doi.org/10.1016/j.rser.2018.03.002.

[43] C. Yang, Running battery electric vehicles with extended range: Coupling cost and energy analysis, Appl. Energy 2022, 306, 118116. https://doi.org/10.1016/j.apenergy.2021.118116.

[44] A. Masias, J. Marcicki, W.A. Paxton, Opportunities and challenges of lithium Ion batteries in automotive applications, ACS Energy Lett. 2021, 6, 621–630. https://doi.org/10.1021/acsenergylett.0c02584.

[45] J.T. Frith, M.J. Lacey, U. Ulissi, A non-academic perspective on the future of lithium-based batteries, Nat. Commun. 2023, 14, 420. https://doi.org/10.1038/s41467-023-35933-2.

[46] H. Wang, Z. Yu, X. Kong, S.C. Kim, D.T. Boyle, J. Qin, Z. Bao, Y. Cui, Liquid electrolyte: The nexus of practical lithium metal batteries, Joule. 2022, 6, 588–616. https://doi.org/10.1016/j.joule.2021.12.018.

[47] D. Goonetilleke, N. Sharma, W.K. Pang, V.K. Peterson, R. Petibon, J. Li, J.R. Dahn, Structural evolution and high-voltage structural stability of Li(Ni x Mn y Co z)O 2 electrodes, Chem. Mater. 2019, 31, 376–386. https://doi.org/10.1021/acs.chemmater.8b03525.

[48] B.E. Murdock, K.E. Toghill, N. Tapia-Ruiz, A Perspective on the sustainability of cathode materials used in lithium-Ion batteries, Adv. Energy Mater. 2021, 11, 2102028. https://doi.org/10.1002/aenm.202102028.

[49] S. Mahmud, M. Rahman, M. Kamruzzaman, M.O. Ali, M.S.A. Emon, H. Khatun, M.R. Ali, Recent advances in lithium-ion battery materials for improved electrochemical performance: A review, Results Eng. 2022, 15, 100472. https://doi.org/10.1016/j.rineng.2022.100472.

[50] A. Gomez-Martin, F. Reissig, L. Frankenstein, M. Heidbüchel, M. Winter, T. Placke, R. Schmuch, Magnesium substitution in Ni-Rich NMC layered cathodes for high-energy lithium ion batteries, Adv. Energy Mater. 2022, 12, 2103045.

https://doi.org/10.1002/aenm.202103045.

[51] J.U. Choi, N. Voronina, Y.K. Sun, S.T. Myung, Recent progress and perspective of advanced high-energy Co-Less Ni-Rich cathodes for Li-Ion batteries: Yesterday, today, and tomorrow, Adv. Energy Mater. 2020, 10, 2002027. https://doi.org/10.1002/aenm.202002027.

[52] H. Zhang, X. He, Z. Chen, Y. Yang, H. Xu, L. Wang, X. He, Single-crystalline Ni-Rich LiNixMnyCo1−x−yO2 cathode materials: A Perspective, Adv. Energy Mater. 2022, 12, 2202022. https://doi.org/10.1002/aenm.202202022.

[53] M. Jiang, D.L. Danilov, R.A. Eichel, P.H.L. Notten, A Review of degradation mechanisms and recent achievements for Ni-Rich cathode-based Li-Ion batteries, Adv. Energy Mater. 2021, 11, 2103005. https://doi.org/10.1002/aenm.202103005.

[54] S.S. Zhang, Problems and their origins of Ni-rich layered oxide cathode materials, Energy Storage Mater. 2020, 24, 247–254. https://doi.org/10.1016/j.ensm.2019.08.013.

[55] H. Zheng, X. Han, W. Guo, L. Lin, Q. Xie, P. Liu, W. He, L. Wang, D.L. Peng, Recent developments and challenges of Li-rich Mn-based cathode materials for high-energy lithium-ion batteries, Mater. Today Energy 2020, 18, 100518. https://doi.org/10.1016/j.mtener.2020.100518.

[56] B. Wen, F.N. Sayed, W.M. Dose, J.K. Morzy, Y. Son, S. Nagendran, C. Ducati, C.P. Grey, M.F.L. De Volder, Surface reduction in lithium- and manganese-rich layered cathodes for lithium ion batteries drives voltage decay, J. Mater. Chem. A 2022, 10, 21941–21954. https://doi.org/10.1039/d2ta04876k.

[57] S. Liu, B. Wang, X. Zhang, S. Zhao, Z. Zhang, H. Yu, Reviving the lithium-manganese-based layered oxide cathodes for lithium-ion batteries, Matter. 2021, 4, 1511–1527. https://doi.org/10.1016/j.matt.2021.02.023.

[58] W. Hua, S. Wang, M. Knapp, S.J. Leake, A. Senyshyn, C. Richter, M. Yavuz, J.R. Binder, C.P. Grey, H. Ehrenberg, S. Indris, B. Schwarz, Structural insights into the formation and voltage degradation of lithium- and manganese-rich layered oxides, Nat. Commun. 2019, 10, 5365. https://doi.org/10.1038/s41467-019-13240-z.

[59] P.H. Camargos, P.H.J. dos Santos, I.R. dos Santos, G.S. Ribeiro, R.E. Caetano, Perspectives on Li-ion battery categories for electric vehicle applications: A review of state of the art, Int. J. Energy Res. 2022, 46, 19258–19268. https://doi.org/10.1002/er.7993.

[60] D. V. Pelegov, J. Pontes, Main drivers of battery industry changes: Electric vehicles—A market overview, Batteries 2018, 4, 65. https://doi.org/10.3390/batteries4040065.

[61] H. Gong, T. Hansen, The rise of China's new energy vehicle lithium-ion battery industry: The coevolution of battery technological innovation systems and policies, Environ. Innov. Soc. Transitions 2023, 46, 100689. https://doi.org/10.1016/j.eist.2022.100689.

[62] Z. Ahsan, B. Ding, Z. Cai, C. Wen, W. Yang, Y. Ma, S. Zhang, Recent progress in capacity enhancement of LiFePO4 cathode for Li-Ion batteries, J. Electrochem. Energy Convers. Storage 2021, 18, 010801. https://doi.org/10.1115/1.4047222.

[63] H.H. Ryu, H.H. Sun, S.T. Myung, C.S. Yoon, Y.K. Sun, Reducing cobalt from lithium-ion batteries for the electric vehicle era, Energy Environ. Sci. 2021, 14, 844–852. https://doi.org/10.1039/d0ee03581e.

[64] J. Chen, Recent progress in advanced materials for lithium ion batteries, Materials 2013, 6, 156–183. https://doi.org/10.3390/ma6010156.

[65] N. Tolganbek, Y. Yerkinbekova, S. Kalybekkyzy, Z. Bakenov, A. Mentbayeva, Current state of high voltage olivine structured LiMPO4 cathode materials for energy storage applications: A review, J. Alloys Compd. 2021, 882, 160774. https://doi.org/10.1016/j.jallcom.2021.160774.

[66] V. Pellegrini, S. Bodoardo, D. Brandell, K. Edström, Challenges and perspectives for new material solutions in batteries, Solid State Commun. 2019, 303–304, 113733. https://doi.org/10.1016/j.ssc.2019.113733.

[67] P. Li, G. Zhao, X. Zheng, X. Xu, C. Yao, W. Sun, S.X. Dou, Recent progress on silicon-based anode materials for practical lithium-ion battery applications, Energy Storage Mater. 2018, 15, 422–446. https://doi.org/10.1016/j.ensm.2018.07.014.

[68] L. Sun, Y. Liu, R. Shao, J. Wu, R. Jiang, Z. Jin, Recent progress and future perspective on practical silicon anode-based lithium ion batteries, Energy Storage Mater. 2022, 46, 482–502. https://doi.org/10.1016/j.ensm.2022.01.042.

[69] X. Zuo, J. Zhu, P. Müller-Buschbaum, Y.J. Cheng, Silicon based lithium-ion battery anodes: A chronicle perspective review, Nano Energy 2017, 31, 113–143. https://doi.org/10.1016/j.nanoen.2016.11.013.

[70] H. Schmidt, B. Jerliu, E. Hüger, J. Stahn, Volume expansion of amorphous silicon electrodes during potentiostatic lithiation of Li-ion batteries, Electrochem.

Commun. 2020, 115, 106738. https://doi.org/10.1016/j.elecom.2020.106738.

[71] D. Lin, Y. Liu, Y. Cui, Reviving the lithium metal anode for high-energy batteries, Nat. Nanotechnol. 2017, 12, 194–206. https://doi.org/10.1038/nnano.2017.16.

[72] W. Wu, W. Luo, Y. Huang, Less is more: a perspective on thinning lithium metal towards high-energy-density rechargeable lithium batteries, Chem. Soc. Rev. 2023, 52, 2553–2572. https://doi.org/10.1039/d2cs00606e.

[73] X. Judez, G.G. Eshetu, C. Li, L.M. Rodriguez-Martinez, H. Zhang, M. Armand, Opportunities for rechargeable solid-state batteries based on li-intercalation cathodes, Joule. 2018, 2, 2208–2224. https://doi.org/10.1016/j.joule.2018.09.008.

[74] K. Turcheniuk, D. Bondarev, G.G. Amatucci, G. Yushin, Battery materials for low-cost electric transportation, Mater. Today 2021, 42, 57–72. https://doi.org/10.1016/j.mattod.2020.09.027.

[75] H. Aziam, B. Larhrib, C. Hakim, N. Sabi, H. Ben Youcef, I. Saadoune, Solid-state electrolytes for beyond lithium-ion batteries: A review, Renew. Sustain. Energy Rev. 2022, 167, 112694. https://doi.org/10.1016/j.rser.2022.112694.

[76] Y. Gao, Z. Pan, J. Sun, Z. Liu, J. Wang, High-energy batteries: beyond lithium-ion and their long road to commercialisation, Springer Singapore, 2022. https://doi.org/10.1007/s40820-022-00844-2.

[77] G. Martin, L. Rentsch, M. Höck, M. Bertau, Lithium market research – global supply, future demand and price development, Energy Storage Mater. 2017, 6, 171–179. https://doi.org/10.1016/j.ensm.2016.11.004.

[78] H. Ahmad, K.T. Kubra, A. Butt, U. Nisar, F.J. Iftikhar, G. Ali, Recent progress, challenges, and perspectives in the development of solid-state electrolytes for sodium batteries, J. Power Sources 2023, 581, 233518. https://doi.org/10.1016/j.jpowsour.2023.233518.

[79] Z. Li, P. Liu, K. Zhu, Z. Zhang, Y. Si, Y. Wang, L. Jiao, Solid-state electrolytes for sodium metal batteries, Energy and Fuels 2021, 35, 9063–9079. https://doi.org/10.1021/acs.energyfuels.1c00347.

[80] L. Zhao, T. Zhang, W. Li, T. Li, L. Zhang, X. Zhang, Z. Wang, Engineering of sodium-Ion batteries: opportunities and challenges, Engineering 2023, 24, 172–183. https://doi.org/10.1016/j.eng.2021.08.032.

[81] K.M. Abraham, How Comparable Are sodium-Ion batteries to lithium-ion counterparts?, ACS Energy Lett. 2020, 5, 3544–3547. https://doi.org/10.1021/acsenergylett.0c02181.

[82] J.F. Peters, A.P. Cruz, M. Weil, Exploring the economic potential of sodium-ion batteries, Batteries 2019, 5, 10. https://doi.org/10.3390/batteries5010010.

[83] N. Tapia-ruiz, A.R. Armstrong, H. Alptekin, M.A. Amores, H. Au, J. Barker, R. Boston, W.R. Brant, J.M. Brittain, Y. Chen, M. Chhowalla, Y. Choi, S.I.R. Costa, M.C. Ribadeneyra, S.A.M. Dickson, E.I. Eweka, J.D. Forero-saboya, C.P. Grey, Z. Li, S.F.L. Mertens, R. Mogensen, L. Monconduit, D.M.C. Ould, R.G. Palgrave, P. Poizot, A. Ponrouch, S. Renault, E.M. Reynolds, A. Rudola, R. Sayers, D.O. Scanlon, S. Sen, V.R. Seymour, B. Silv, G.S. Stone, C.I. Thomas, M. Titirici, J. Tong, T.J. Wood, D.S. Wright, R. Younesi, 2021 roadmap for sodium-ion batteries, J. Phys. Energy 2021, 3, 031503–031592. https://doi.org/10.1088/2515-7655/AC01EF.

[84] T. Yu, G. Li, Y. Duan, Y. Wu, T. Zhang, X. Zhao, M. Luo, Y. Liu, The research and industrialization progress and prospects of sodium ion battery, J. Alloys Compd. 2023, 958, 170486. https://doi.org/10.1016/j.jallcom.2023.170486.

[85] X. Zou, P. Xiong, J. Zhao, J. Hu, Z. Liu, Y. Xu, Recent research progress in non-aqueous potassium-ion batteries, Phys. Chem. Chem. Phys. 2017, 19, 26495–26506. https://doi.org/10.1039/c7cp03852f.

[86] B. John, V. Anoopkumar, T.D. Mercy, Potassium-ion batteries: Key to future large-scale energy storage?, ACS Appl. Energy Mater. 2020, 3, 9478–9492. https://doi.org/10.1021/acsaem.0c01574.

[87] K. Sada, J. Darga, A. Manthiram, Challenges and prospects of sodium-Ion and potassium-ion batteries for mass production, Adv. Energy Mater. 2023, 13, 2302321. https://doi.org/10.1002/aenm.202302321.

[88] R. Rajagopalan, Y. Tang, X. Ji, C. Jia, H. Wang, Advancements and challenges in potassium ion batteries: A comprehensive review, Adv. Funct. Mater. 2020, 30, 1909486. https://doi.org/10.1002/adfm.201909486.

[89] H. Zhang, L. Qiao, H. Kühnle, E. Figgemeier, M. Armand, G.G. Eshetu, From lithium to emerging mono- and multivalent-cation-based rechargeable batteries: non-aqueous organic electrolyte and interphase perspectives, Energy Environ. Sci. 2022, 16, 11–52. https://doi.org/10.1039/d2ee02998g.

[90] Y. Tian, G. Zeng, A. Rutt, T. Shi, H. Kim, J. Wang, J. Koettgen, Y. Sun, B. Ouyang, T. Chen, Z. Lun, Z. Rong, K. Persson, G. Ceder, Promises and challenges of next-

generation “beyond Li-ion” batteries for electric vehicles and grid decarbonization, Chem. Rev. 2021, 121, 1623–1669. https://doi.org/10.1021/acs.chemrev.0c00767.

[91] A. Ponrouch, J. Bitenc, R. Dominko, N. Lindahl, P. Johansson, M.R. Palacin, Multivalent rechargeable batteries, Energy Storage Mater. 2019, 20, 253–262. https://doi.org/10.1016/j.ensm.2019.04.012.

[92] T.M. Gür, Review of electrical energy storage technologies, materials and systems: Challenges and prospects for large-scale grid storage, Energy Environ. Sci. 2018, 11, 2696–2767. https://doi.org/10.1039/c8ee01419a.

[93] X. Zhang, R. Lv, W. Tang, G. Li, A. Wang, A. Dong, X. Liu, J. Luo, Challenges and opportunities for multivalent metal anodes in rechargeable batteries, Adv. Funct. Mater. 2020, 30, 2004187. https://doi.org/10.1002/adfm.202004187.

[94] Y. Chen, K. Fan, Y. Gao, C. Wang, Challenges and perspectives of organic multivalent metal-Ion batteries, Adv. Mater. 2022, 34, 2200662. https://doi.org/10.1002/adma.202200662.

[95] H. Zhao, W.Y.A. Lam, L. Sheng, L. Wang, P. Bai, Y. Yang, D. Ren, H. Xu, X. He, Cobalt-free cathode materials: Families and their prospects, Adv. Energy Mater. 2022, 12, 2103894. https://doi.org/10.1002/aenm.202103894.

[96] S.S. Sharma, A. Manthiram, Towards more environmentally and socially responsible batteries, Energy Environ. Sci. 2020, 13, 4087–4097. https://doi.org/10.1039/d0ee02511a.

[97] E.A. Olivetti, G. Ceder, G.G. Gaustad, X. Fu, Lithium-ion battery supply chain considerations: Analysis of potential bottlenecks in critical metals, Joule 2017, 1, 229–243. https://doi.org/10.1016/j.joule.2017.08.019.

[98] C.M. Costa, J.C. Barbosa, R. Gonçalves, H. Castro, F.J.D. Campo, S. Lanceros-Méndez, Recycling and environmental issues of lithium-ion batteries: Advances, challenges and opportunities, Energy Storage Mater. 2021, 37, 433–465. https://doi.org/10.1016/j.ensm.2021.02.032.

[99] S. Buxton, E. Garman, K.E. Heim, T. Lyons-Darden, C.E. Schlekat, M.D. Taylor, A.R. Oller, Concise review of nickel human health toxicology and ecotoxicology, Inorganics 2019, 7, 89. https://doi.org/10.3390/inorganics7070089.

[100] W. Cao, J. Zhang, H. Li, Batteries with high theoretical energy densities, Energy Storage Mater. 2020, 26, 46–55. https://doi.org/10.1016/j.ensm.2019.12.024.

[101] S.H. Yu, X. Feng, N. Zhang, J. Seok, H.D. Abruña, Understanding conversion-type electrodes for lithium rechargeable batteries, Acc. Chem. Res. 2018, 51, 273–281. https://doi.org/10.1021/acs.accounts.7b00487.

[102] N. Imanishi, O. Yamamoto, Perspectives and challenges of rechargeable lithium–air batteries, Mater. Today Adv. 2019, 4, 100031. https://doi.org/10.1016/j.mtadv.2019.100031.

[103] Z. Wu, Y. Tian, H. Chen, L. Wang, S. Qian, T. Wu, S. Zhang, J. Lu, Evolving aprotic Li-air batteries, Chem. Soc. Rev. 2022, 51, 8045–8101. https://doi.org/10.1039/d2cs00003b.

[104] X. Zou, Q. Lu, K. Liao, Z. Shao, Towards practically accessible aprotic Li-air batteries: Progress and challenges related to oxygen-permeable membranes and cathodes, Energy Storage Mater. 2022, 45, 869–902. https://doi.org/10.1016/j.ensm.2021.12.031.

[105] J.H. Kang, J. Lee, J.W. Jung, J. Park, T. Jang, H.S. Kim, J.S. Nam, H. Lim, K.R. Yoon, W.H. Ryu, I.D. Kim, H.R. Byon, Lithium-air batteries: Air-breathing challenges and perspective, ACS Nano. 2020, 14, 14549–14578. https://doi.org/10.1021/acsnano.0c07907.

[106] T. Liu, J.P. Vivek, E.W. Zhao, J. Lei, N. Garcia-Araez, C.P. Grey, Current challenges and routes forward for nonaqueous lithium-air batteries, Chem. Rev. 2020, 120, 6558–6625. https://doi.org/10.1021/acs.chemrev.9b00545.

[107] J. Sun, T. Wang, Y. Gao, Z. Pan, R. Hu, J. Wang, Will lithium-sulfur batteries be the next beyond-lithium ion batteries and even much better?, InfoMat 2022, 4, 12359. https://doi.org/10.1002/inf2.12359.

[108] R. Deng, M. Wang, H. Yu, S. Luo, J. Li, F. Chu, B. Liu, F. Wu, Recent advances and applications toward emerging lithium–sulfur batteries: Working principles and opportunities, Energy Environ. Mater. 2022, 5, 777–799. https://doi.org/10.1002/eem2.12257.

[109] S.H. Chung, A. Manthiram, Current status and future Prospects of Metal–Sulfur Batteries, Adv. Mater. 2019, 31, 39–42. https://doi.org/10.1002/adma.201901125.

[110] S. Dörfler, S. Walus, J. Locke, A. Fotouhi, D.J. Auger, N. Shateri, T. Abendroth, P. Härtel, H. Althues, S. Kaskel, Recent progress and emerging application areas for lithium–sulfur battery technology, Energy Technol. 2021, 9, 2000694. https://doi.org/10.1002/ente.202000694.

[111] H. Pan, Z. Cheng, Z. Zhou, S. Xie, W. Zhang, N. Han, W. Guo, J. Fransaer, J. Luo, A. Cabot, M. Wübbenhorst, Boosting lean electrolyte lithium–sulfur battery performance with transition metals: A comprehensive review, Springer Nature Singapore, 2023. https://doi.org/10.1007/s40820-023-01137-y.

[112] S. Dörfler, H. Althues, P. Härtel, T. Abendroth, B. Schumm, S. Kaskel, Challenges and key parameters of lithium-sulfur batteries on pouch cell level, Joule 2020, 4, 539–554. https://doi.org/10.1016/j.joule.2020.02.006.

[113] R. Fang, K. Chen, Z. Sun, G. Hu, D. Wang, F. Li, Realizing high-energy density for practical lithium–sulfur batteries, Interdiscip. Mater. 2023, 2, 761–770. https://doi.org/10.1002/idm2.12118.

[114] J.B. Robinson, K. Xi, R.V. Kumar, A.C. Ferrari, H. Au, M.-M. Titirici, A. Parra-Puerto, A. Kucernak, S.D.S. Fitch, N. Garcia-Araez, Z.L. Brown, M. Pasta, L. Furness, A.J. Kibler, D.A. Walsh, L.R. Johnson, C. Holc, G.N. Newton, N.R. Champness, F. Markoulidis, C. Crean, R.C.T. Slade, E.I. Andritsos, Q. Cai, S. Babar, T. Zhang, C. Lekakou, N. Kulkarni, A.J.E. Rettie, R. Jervis, M. Cornish, M. Marinescu, G. Offer, Z. Li, L. Bird, C.P. Grey, M. Chhowalla, D. Di Lecce, R.E. Owen, T.S. Miller, D.J.L. Brett, S. Liatard, D. Ainsworth, P.R. Shearing, 2021 roadmap on lithium sulfur batteries, J. Phys. Energy 2021, 3, 031501. https://doi.org/10.1088/2515-7655/abdb9a.

[115] A. Fotouhi, D.J. Auger, L. O'Neill, T. Cleaver, S. Walus, Lithium-sulfur battery technology readiness and applications - A review, Energies 2017, 10, 1937. https://doi.org/10.3390/en10121937.

[116] Z. Han, S. Li, Y. Wu, C. Yu, S. Cheng, J. Xie, Challenges and key parameters in exploring the cyclability limitation of practical lithium-sulfur batteries, J. Mater. Chem. A 2021, 9, 24215–24240. https://doi.org/10.1039/d1ta06499a.

[117] S. Dong, H. Liu, Y. Hu, S. Chong, Cathode materials for rechargeable lithium-sulfur batteries: Current progress and future prospects, ChemElectroChem 2022, 9 202101564. https://doi.org/10.1002/celc.202101564.

[118] L. Yang, H. Li, Q. Li, Y. Wang, Y. Chen, Z. Wu, Y. Liu, G. Wang, B. Zhong, W. Xiang, Y. Zhong, X. Guo, Research progress on improving the sulfur conversion efficiency on the sulfur cathode side in lithium-sulfur batteries, Ind. Eng. Chem. Res. 2020, 59, 20979–21000. https://doi.org/10.1021/acs.iecr.0c04960.

[119] X. Yu, A. Manthiram, A progress report on metal–sulfur batteries, Adv. Funct. Mater. 2020, 30, 2004084. https://doi.org/10.1002/adfm.202004084.

[120] J.G. Wagenfeld, K. Al-Ali, S. Almheiri, A.F. Slavens, N. Calvet, Sustainable

applications utilizing sulfur, a by-product from oil and gas industry: A state-of-the-art review, Waste Manag. 2019, 95, 78–89. https://doi.org/10.1016/j.wasman.2019.06.002.

[121] W.J. Chung, J.J. Griebel, E.T. Kim, H. Yoon, A.G. Simmonds, H.J. Ji, P.T. Dirlam, R.S. Glass, J.J. Wie, N.A. Nguyen, B.W. Guralnick, J. Park, Á. Somogyi, P. Theato, M.E. Mackay, Y.E. Sung, K. Char, J. Pyun, The use of elemental sulfur as an alternative feedstock for polymeric materials, Nat. Chem. 2013, 5, 518–524. https://doi.org/10.1038/nchem.1624.

[122] J. Lim, J. Pyun, K. Char, Recent approaches for the direct use of elemental sulfur in the synthesis and processing of advanced materials, Angew. Chemie - Int. Ed. 2015, 54, 3249–3258. https://doi.org/10.1002/anie.201409468.

[123] X. Zhang, H. Xie, C.S. Kim, K. Zaghib, A. Mauger, C.M. Julien, Advances in lithium—sulfur batteries, Mater. Sci. Eng. R Reports 2017, 121, 1–29. https://doi.org/10.1016/j.mser.2017.09.001.

[124] H. Yuan, H.J. Peng, J.Q. Huang, Q. Zhang, Sulfur redox reactions at working interfaces in lithium–sulfur batteries: A perspective, Adv. Mater. Interfaces 2019, 6, 1802046. https://doi.org/10.1002/admi.201802046.

[125] S. Lang, X. Feng, J. Seok, Y. Yang, M.R. Krumov, A. Molina Villarino, M.A. Lowe, S.H. Yu, H.D. Abruña, Lithium–sulfur redox: challenges and opportunities, Curr. Opin. Electrochem. 2021, 25, 100652. https://doi.org/10.1016/j.coelec.2020.100652.

[126] M. Wild, L. O'Neill, T. Zhang, R. Purkayastha, G. Minton, M. Marinescu, G.J. Offer, Lithium sulfur batteries, a mechanistic review, Energy Environ. Sci. 2015, 8, 3477–3494. https://doi.org/10.1039/c5ee01388g.

[127] A. Bhargav, J. He, A. Gupta, A. Manthiram, Lithium-sulfur batteries: Attaining the critical metrics, Joule 2020, 4, 285–291. https://doi.org/10.1016/j.joule.2020.01.001.

[128] B. Liu, R. Fang, D. Xie, W. Zhang, H. Huang, Y. Xia, X. Wang, X. Xia, J. Tu, Revisiting scientific issues for industrial applications of lithium–sulfur batteries, Energy Environ. Mater. 2018, 1, 196–208. https://doi.org/10.1002/eem2.12021.

[129] N. Wang, X. Zhang, Z. Ju, X. Yu, Y. Wang, Y. Du, Z. Bai, S. Dou, G. Yu, Thickness-independent scalable high-performance Li-S batteries with high areal sulfur loading via electron-enriched carbon framework, Nat. Commun. 2021, 12, 4519. https://doi.org/10.1038/s41467-021-24873-4.

[130] H. Chu, H. Noh, Y.J. Kim, S. Yuk, J.H. Lee, J. Lee, H. Kwack, Y.K. Kim, D.K. Yang, H.T. Kim, Achieving three-dimensional lithium sulfide growth in lithium-sulfur batteries using high-donor-number anions, Nat. Commun. 2019, 10, 188. https://doi.org/10.1038/s41467-018-07975-4.

[131] K.R. Kim, K.S. Lee, C.Y. Ahn, S.H. Yu, Y.E. Sung, Discharging a Li-S battery with ultra-high sulphur content cathode using a redox mediator, Sci. Rep. 2016, 6, 32433. https://doi.org/10.1038/srep32433.

[132] W. Guo, Y. Fu, A perspective on energy densities of rechargeable Li-S batteries and alternative sulfur-based cathode materials, Energy Environ. Mater. 2018, 1, 20–27. https://doi.org/10.1002/eem2.12003.

[133] M. Shaibani, M.S. Mirshekarloo, R. Singh, C.D. Easton, M.C. Dilusha Cooray, N. Eshraghi, T. Abendroth, S. Dörfler, H. Althues, S. Kaskel, A.F. Hollenkamp, M.R. Hill, M. Majumder, Expansion-tolerant architectures for stable cycling of ultrahigh-loading sulfur cathodes in lithium-sulfur batteries, Sci. Adv. 2020, 6, 2257. https://doi.org/10.1126/sciadv.aay2757.

[134] X. Chen, H. Ji, Z. Rao, L. Yuan, Y. Shen, H. Xu, Z. Li, Y. Huang, Insight into the fading mechanism of the solid-conversion sulfur cathodes and designing long cycle lithium–sulfur batteries, Adv. Energy Mater. 2022, 12, 2102774. https://doi.org/10.1002/aenm.202102774.

[135] P. Barai, A. Mistry, P.P. Mukherjee, Poromechanical effect in the lithium–sulfur battery cathode, Extrem. Mech. Lett. 2016, 9, 359–370. https://doi.org/10.1016/j.eml.2016.05.007.

[136] W. Ren, W. Ma, S. Zhang, B. Tang, Recent advances in shuttle effect inhibition for lithium sulfur batteries, Energy Storage Mater. 2019, 23, 707–732. https://doi.org/10.1016/j.ensm.2019.02.022.

[137] C. Weller, S. Thieme, P. Härtel, H. Althues, S. Kaskel, Intrinsic shuttle suppression in lithium-sulfur batteries for pouch cell application, J. Electrochem. Soc. 2017, 164, A3766–A3771. https://doi.org/10.1149/2.0981714jes.

[138] J. Wang, H. Wang, S. Jia, Q. Zhao, Q. Zheng, Y. Ma, T. Ma, X. Li, Recent advances in inhibiting shuttle effect of polysulfide in lithium-sulfur batteries, J. Energy Storage 2023, 72, 108372. https://doi.org/10.1016/j.est.2023.108372.

[139] J. Liu, D. Lu, J. Zheng, P. Yan, B. Wang, X. Sun, Y. Shao, C. Wang, J. Xiao, J.G. Zhang, J. Liu, Minimizing polysulfide shuttle effect in lithium-ion sulfur batteries by anode surface passivation, ACS Appl. Mater. Interfaces. 2018, 10, 21965–21972.

https://doi.org/10.1021/acsami.8b02381.

[140] M. Fang, X. Liu, J.C. Ren, S. Yang, G. Su, Q. Fang, J. Lai, S. Li, W. Liu, Revisiting the anchoring behavior in lithium-sulfur batteries: many-body effect on the suppression of shuttle effect, Npj Comput. Mater. 2020, 6, 8. https://doi.org/10.1038/s41524-020-0273-1.

[141] G. Di Donato, T. Ates, H. Adenusi, A. Varzi, M.A. Navarra, S. Passerini, Electrolyte measures to prevent polysulfide shuttle in lithium-sulfur batteries, Batter. Supercaps 2022, 5, 202200097. https://doi.org/10.1002/batt.202200097.

[142] C. Deng, Z. Wang, S. Wang, J. Yu, Inhibition of polysulfide diffusion in lithium-sulfur batteries: Mechanism and improvement strategies, J. Mater. Chem. A 2019, 7, 12381–12413. https://doi.org/10.1039/c9ta00535h.

[143] J.G. Zhang, W. Xu, J. Xiao, X. Cao, J. Liu, Lithium metal anodes with nonaqueous electrolytes, Chem. Rev. 2020, 120, 13312–13348. https://doi.org/10.1021/acs.chemrev.0c00275.

[144] Y. Han, B. Liu, Z. Xiao, W. Zhang, X. Wang, G. Pan, Y. Xia, X. Xia, J. Tu, Interface issues of lithium metal anode for high-energy batteries: Challenges, strategies, and perspectives, InfoMat 2021, 3, 155–174. https://doi.org/10.1002/inf2.12166.

[145] Z. Luo, X. Qiu, C. Liu, S. Li, C. Wang, G. Zou, H. Hou, X. Ji, Interfacial challenges towards stable Li metal anode, Nano Energy. 2021, 79, 105507. https://doi.org/10.1016/j.nanoen.2020.105507.

[146] H. Hong, N.A.R. Che Mohamad, K. Chae, F. Marques Mota, D.H. Kim, The lithium metal anode in Li-S batteries: challenges and recent progress, J. Mater. Chem. A 2021, 9, 10012–10038. https://doi.org/10.1039/d1ta01091c.

[147] H. Ye, Z.J. Zheng, H.R. Yao, S.C. Liu, T.T. Zuo, X.W. Wu, Y.X. Yin, N.W. Li, J.J. Gu, F.F. Cao, Y.G. Guo, Guiding uniform Li plating/stripping through lithium–aluminum alloying medium for long-life Li metal batteries, Angew. Chemie - Int. Ed. 2019, 58, 1094–1099. https://doi.org/10.1002/anie.201811955.

[148] S. Li, Z. Luo, L. Li, J. Hu, G. Zou, H. Hou, X. Ji, Recent progress on electrolyte additives for stable lithium metal anode, Energy Storage Mater. 2020, 32, 306–319. https://doi.org/10.1016/j.ensm.2020.07.008.

[149] R. Zhang, X. Shen, Y.T. Zhang, X.L. Zhong, H.T. Ju, T.X. Huang, X. Chen, J.D. Zhang, J.Q. Huang, Dead lithium formation in lithium metal batteries: A phase field model, J. Energy Chem. 2020, 71, 29–35.

https://doi.org/10.1016/j.jechem.2021.12.020.

[150] G. Yasin, M. Arif, T. Mehtab, X. Lu, D. Yu, N. Muhammad, M.T. Nazir, H. Song, Understanding and suppression strategies toward stable Li metal anode for safe lithium batteries, Energy Storage Mater. 2020, 25, 644–678. https://doi.org/10.1016/j.ensm.2019.09.020.

[151] K.H. Chen, K.N. Wood, E. Kazyak, W.S. Lepage, A.L. Davis, A.J. Sanchez, N.P. Dasgupta, Dead lithium: Mass transport effects on voltage, capacity, and failure of lithium metal anodes, J. Mater. Chem. A. 2017, 5, 11671–11681. https://doi.org/10.1039/c7ta00371d.

[152] M. Zhao, B.Q. Li, H.J. Peng, H. Yuan, J.Y. Wei, J.Q. Huang, Lithium–sulfur batteries under lean electrolyte conditions: challenges and opportunities, Angew. Chemie - Int. Ed. 2020, 59, 12636–12652. https://doi.org/10.1002/anie.201909339.

[153] Q. Pang, L.F. Nazar, Long-life and high-areal-capacity Li-S batteries enabled by a light-weight polar host with intrinsic polysulfide adsorption, ACS Nano. 2016, 10, 4111–4118. https://doi.org/10.1021/acsnano.5b07347.

[154] W. Cai, G. Li, K. Zhang, G. Xiao, C. Wang, K. Ye, Z. Chen, Y. Zhu, Y. Qian, Conductive nanocrystalline niobium carbide as high-efficiency polysulfides tamer for lithium-sulfur batteries, Adv. Funct. Mater. 2018, 28, 1704865. https://doi.org/10.1002/adfm.201704865.

[155] D.R. Deng, F. Xue, Y.J. Jia, J.C. Ye, C.D. Bai, M. Sen Zheng, Q.F. Dong, Co4N nanosheet assembled mesoporous sphere as a matrix for ultrahigh sulfur content lithium-sulfur batteries, ACS Nano. 2017, 11, 6031–6039. https://doi.org/10.1021/acsnano.7b01945.

[156] C.X. Bi, M. Zhao, L.P. Hou, Z.X. Chen, X.Q. Zhang, B.Q. Li, H. Yuan, J.Q. Huang, Anode material options toward 500 Wh kg−1 lithium–sulfur batteries, Adv. Sci. 2022, 9, 2103910. https://doi.org/10.1002/advs.202103910.

[157] H. Ye, Y. Li, Room-temperature metal–sulfur batteries: What can we learn from lithium–sulfur?, InfoMat 2022, 4, 12291. https://doi.org/10.1002/inf2.12291.

[158] L.P. Hou, L.Y. Yao, C.X. Bi, J. Xie, B.Q. Li, J.Q. Huang, X.Q. Zhang, High-valence sulfur-containing species in solid electrolyte interphase stabilizes lithium metal anodes in lithium–sulfur batteries, J. Energy Chem. 2022, 68, 300–305. https://doi.org/10.1016/j.jechem.2021.12.024.

[159] L.P. Hou, X.Q. Zhang, B.Q. Li, Q. Zhang, Challenges and promises of lithium

metal anode by soluble polysulfides in practical lithium–sulfur batteries, Mater. Today 2021, 45, 62–76. https://doi.org/10.1016/j.mattod.2020.10.021.

[160] E. Cha, J.H. Yun, D.K. Kim, Polysulfide regulation vs anode modification: Perspectives on commercializing lithium-sulfur batteries, APL Mater. 2022, 10, 020701. https://doi.org/10.1063/5.0070013.

[161] M. Zhao, B.Q. Li, X.Q. Zhang, J.Q. Huang, Q. Zhang, A perspective toward practical lithium-sulfur batteries, ACS Cent. Sci. 2020, 6, 1095–1104. https://doi.org/10.1021/acscentsci.0c00449.

[162] S.H. Kang, X. Zhao, J. Manuel, H.J. Ahn, K.W. Kim, K.K. Cho, J.H. Ahn, Effect of sulfur loading on energy density of lithium sulfur batteries, Phys. Status Solidi Appl. Mater. Sci. 2014, 211, 1895–1899. https://doi.org/10.1002/pssa.201330569.

[163] Q. Jin, X. Qi, F. Yang, R. Jiang, Y. Xie, L. Qie, Y. Huang, The failure mechanism of lithium-sulfur batteries under lean-ether-electrolyte conditions, Energy Storage Mater. 2021, 38, 255–261. https://doi.org/10.1016/j.ensm.2021.03.014.

[164] Y. Zhang, X. Zhang, S.R.P. Silva, B. Ding, P. Zhang, G. Shao, Lithium–sulfur batteries meet electrospinning: Recent advances and the key parameters for high gravimetric and volume energy density, Adv. Sci. 2022, 9, 2103879. https://doi.org/10.1002/advs.202103879.

[165] Y. Jeoun, M.S. Kim, S.H. Lee, J. Hyun Um, Y.E. Sung, S.H. Yu, Lean-electrolyte lithium-sulfur batteries: Recent advances in the design of cell components, Chem. Eng. J. 2022, 450, 138209. https://doi.org/10.1016/j.cej.2022.138209.

[166] F. Chu, M. Wang, J. Liu, Z. Guan, H. Yu, B. Liu, F. Wu, Low concentration electrolyte enabling cryogenic lithium–sulfur batteries, Adv. Funct. Mater. 2022, 32, 2205393. https://doi.org/10.1002/adfm.202205393.

[167] F.Y. Fan, Y.-M. Chiang, Electrodeposition kinetics in Li-S batteries: Effects of low electrolyte/sulfur ratios and deposition surface composition, J. Electrochem. Soc. 2017, 164, A917–A922. https://doi.org/10.1149/2.0051706jes.

[168] F.Y. Fan, W.C. Carter, Y.M. Chiang, Mechanism and kinetics of Li2S precipitation in lithium-sulfur batteries, Adv. Mater. 2015, 27, 5203–5209. https://doi.org/10.1002/adma.201501559.

[169] L. Kong, Q. Jin, J.Q. Huang, L. Da Zhao, P. Li, B.Q. Li, H.J. Peng, X. Zhang, Q. Zhang, Nonuniform redistribution of sulfur and lithium upon cycling: Probing the origin of capacity fading in lithium–sulfur pouch cells, Energy Technol. 2019, 7,

1900111. https://doi.org/10.1002/ente.201900111.

[170] L. Wang, M. Zhen, Z. Hu, Status and prospects of electrocatalysts for lithium-sulfur battery under lean electrolyte and high sulfur loading conditions, Chem. Eng. J. 2023, 452, 139344. https://doi.org/10.1016/j.cej.2022.139344.

[171] M. Wang, Z. Bai, T. Yang, C. Nie, X. Xu, Y. Wang, J. Yang, S. Dou, N. Wang, Advances in high sulfur loading cathodes for practical lithium-sulfur batteries, Adv. Energy Mater. 2022, 12, 2201585. https://doi.org/10.1002/aenm.202201585.

[172] H. Kwack, J. Lee, W. Jo, Y.J. Kim, H. Noh, H. Chu, H.T. Kim, Rational Design of Highly Packed, Crack-free sulfur electrodes by scaffold-supported drying for ultrahigh-sulfur-loaded lithium-sulfur batteries, ACS Appl. Mater. Interfaces 2019, 11, 29849–29857. https://doi.org/10.1021/acsami.9b08006.

[173] H.J. Peng, J.Q. Huang, X.B. Cheng, Q. Zhang, Review on high-loading and high-energy lithium–sulfur batteries, Adv. Energy Mater. 2017, 7, 1700260. https://doi.org/10.1002/aenm.201700260.

[174] T. Cleaver, P. Kovacik, M. Marinescu, T. Zhang, G. Offer, Perspective—commercializing lithium sulfur batteries: Are we doing the right research?, J. Electrochem. Soc. 2018, 165, A6029–A6033. https://doi.org/10.1149/2.0071801jes.

[175] X.B. Cheng, C. Yan, J.Q. Huang, P. Li, L. Zhu, L. Zhao, Y. Zhang, W. Zhu, S.T. Yang, Q. Zhang, The gap between long lifespan Li-S coin and pouch cells: The importance of lithium metal anode protection, Energy Storage Mater. 2017, 6, 18–25. https://doi.org/10.1016/j.ensm.2016.09.003.

[176] C. Niu, H. Lee, S. Chen, Q. Li, J. Du, W. Xu, J.G. Zhang, M.S. Whittingham, J. Xiao, J. Liu, High-energy lithium metal pouch cells with limited anode swelling and long stable cycles, Nat. Energy 2019, 4, 551–559. https://doi.org/10.1038/s41560-019-0390-6.

[177] Z.X. Chen, M. Zhao, L.P. Hou, X.Q. Zhang, B.Q. Li, J.Q. Huang, Toward practical high-energy-density lithium–sulfur pouch cells: A review, Adv. Mater. 2022, 34, 2201555. https://doi.org/10.1002/adma.202201555.

[178] H. Liu, X. Sun, X.B. Cheng, C. Guo, F. Yu, W. Bao, T. Wang, J. Li, Q. Zhang, Working principles of lithium metal anode in pouch cells, Adv. Energy Mater. 2022, 12, 2202518. https://doi.org/10.1002/aenm.202202518.

[179] C. Jin, T. Liu, O. Sheng, M. Li, T. Liu, Y. Yuan, J. Nai, Z. Ju, W. Zhang, Y. Liu, Y. Wang, Z. Lin, J. Lu, X. Tao, Rejuvenating dead lithium supply in lithium metal anodes

by iodine redox, Nat. Energy. 2021, 6, 378–387. https://doi.org/10.1038/s41560-021-00789-7.

[180] S. Li, B. Jin, X. Zhai, H. Li, Q. Jiang, Review of carbon materials for lithium-sulfur batteries, ChemistrySelect. 2018, 3, 2245–2260. https://doi.org/10.1002/slct.201703112.

[181] M. Wang, X. Xia, Y. Zhong, J. Wu, R. Xu, Z. Yao, D. Wang, W. Tang, X. Wang, J. Tu, Porous carbon hosts for lithium–sulfur batteries, Chem. - A Eur. J. 2019, 25, 3710–3725. https://doi.org/10.1002/chem.201803153.

[182] Z. Wang, X. Xu, S. Ji, Z. Liu, D. Zhang, J. Shen, J. Liu, Recent progress of flexible sulfur cathode based on carbon host for lithium-sulfur batteries, J. Mater. Sci. Technol. 2020, 55, 56–72. https://doi.org/10.1016/j.jmst.2019.09.037.

[183] H. Shin, M. Baek, A. Gupta, K. Char, A. Manthiram, J.W. Choi, Recent progress in high donor electrolytes for lithium–sulfur batteries, Adv. Energy Mater. 2020, 10 2001456. https://doi.org/10.1002/aenm.202001456.

[184] J. He, A. Manthiram, A review on the status and challenges of electrocatalysts in lithium-sulfur batteries, Energy Storage Mater. 2020, 20, 55–70. https://doi.org/10.1016/j.ensm.2019.04.038.

[185] L. Wang, W. Hua, X. Wan, Z. Feng, Z. Hu, H. Li, J. Niu, L. Wang, A. Wang, J. Liu, X. Lang, G. Wang, W. Li, Q.H. Yang, W. Wang, Design rules of a sulfur redox electrocatalyst for lithium–sulfur batteries, Adv. Mater. 2022, 34, 2110279. https://doi.org/10.1002/adma.202110279.

[186] S. Wang, Z. Wang, F. Chen, B. Peng, J. Xu, J. Li, Y. Lv, Q. Kang, A. Xia, L. Ma, Electrocatalysts in lithium-sulfur batteries, Nano Res. 2023, 16, 4438–4467. https://doi.org/10.1007/s12274-022-5215-4.

[187] L. Kong, L. Yin, F. Xu, J. Bian, H. Yuan, Z. Lu, Y. Zhao, Electrolyte solvation chemistry for lithium–sulfur batteries with electrolyte-lean conditions, J. Energy Chem. 2021, 55, 80–91. https://doi.org/10.1016/j.jechem.2020.06.054.

[188] Y. Liu, Y. Elias, J. Meng, D. Aurbach, R. Zou, D. Xia, Q. Pang, Electrolyte solutions design for lithium-sulfur batteries, Joule. 2021, 5, 2323–2364. https://doi.org/10.1016/j.joule.2021.06.009.

[189] M. He, X. Li, X. Yang, C. Wang, M.L. Zheng, R. Li, P. Zuo, G. Yin, X. Sun, Realizing solid-phase reaction in Li–S batteries via localized high-concentration carbonate electrolyte, Adv. Energy Mater. 2021, 11, 2101004.

https://doi.org/10.1002/aenm.202101004.

[190] Z. Jiang, Z. Zeng, W. Hu, Z. Han, S. Cheng, J. Xie, Diluted high concentration electrolyte with dual effects for practical lithium-sulfur batteries, Energy Storage Mater. 2021, 36, 333–340. https://doi.org/10.1016/j.ensm.2021.01.008.

[191] Z. Hou, P.F. Wang, X. Sun, W. Li, C. Sheng, P. He, Protecting Li metal anode while suppressing “shuttle sffect” of Li-S battery through localized high-concentration electrolyte, J. Electron. Mater. 2022, 51, 4772–4779. https://doi.org/10.1007/s11664-022-09751-z.

[192] W. Guo, W. Zhang, Y. Si, D. Wang, Y. Fu, A. Manthiram, Artificial dual solid-electrolyte interfaces based on in situ organothiol transformation in lithium sulfur battery, Nat. Commun. 2021, 12, 3031. https://doi.org/10.1038/s41467-021-23155-3.

[193] J. Yu, L. Zhao, Y. Huang, Y. Hu, L. Chen, Y.B. He, Progress and perspective of constructing solid electrolyte interphase on stable lithium metal anode, Front. Mater. 2020, 7, 71. https://doi.org/10.3389/fmats.2020.00071.

[194] J. Castillo, J.A. Coca-Clemente, J. Rikarte, A. Sáenz De Buruaga, A. Santiago, C. Li, Recent progress on lithium anode protection for lithium-sulfur batteries: Review and perspective, APL Mater. 2023, 11, 010901. https://doi.org/10.1063/5.0107648.

[195] W. Wang, X. Yue, J. Meng, J. Wang, X. Wang, H. Chen, D. Shi, J. Fu, Y. Zhou, J. Chen, Z. Fu, Lithium phosphorus oxynitride as an efficient protective layer on lithium metal anodes for advanced lithium-sulfur batteries, Energy Storage Mater. 2019, 18, 414–422. https://doi.org/10.1016/j.ensm.2018.08.010.

[196] C.X. Bi, L.P. Hou, Z. Li, M. Zhao, X.Q. Zhang, B.Q. Li, Q. Zhang, J.Q. Huang, Protecting lithium metal anodes in lithium–sulfur batteries: A review, Energy Mater. Adv. 2023, 4, 0010. https://doi.org/10.34133/energymatadv.0010.

[197] L. Luo, A. Manthiram, An Artificial Protective Coating toward Dendrite-free lithium-metal anodes for lithium–sulfur batteries, Energy Technol. 2020, 8, 2000348. https://doi.org/10.1002/ente.202000348.

[198] H. Schneider, T. Weiß, C. Scordilis-Kelley, J. Maeyer, K. Leitner, H.J. Peng, R. Schmidt, J. Tomforde, Electrolyte decomposition and gas evolution in a lithium-sulfur cell upon long-term cycling, Electrochim. Acta 2017, 243, 26–32. https://doi.org/10.1016/j.electacta.2017.05.034.

[199] Sion Power delivers next generation battery performance through patented

Licerion® technology. https://www.businesswire.com/news/home/20161003005315/en/Sion-Power-Delivers-Generation-Battery-Performance-Patented (accessed December 16, 2023).

[200] LG Chem tests drone with lithium-sulfur battery - THE ELEC, Korea Electronics Industry Media. https://www.thelec.net/news/articleView.html?idxno=1525 (accessed December 16, 2023).

[201] LG Energy Solution aiming to develop lithium sulfur battery within 3 years - THE ELEC, Korea Electronics Industry Media. https://thelec.net/news/articleView.html?idxno=4368 (accessed December 16, 2023).

[202] OXIS Energy to build world's first Li-S manufacturing plant in Brazil. https://insideevs.com/news/423438/oxis-energy-lis-manufacturing-plant-brazil/ (accessed December 16, 2023).

[203] Zeta Energy demonstrates industry-leading progress in lithium-sulfur batteries. https://www.prnewswire.com/news-releases/zeta-energy-demonstrates-industry-leading-progress-in-lithium-sulfur-batteries-301964964.html (accessed December 16, 2023).

[204] Theion GmbH – Solid-state batteries on lithium-sulfur basis. https://www.theion.de/ (accessed December 16, 2023).

[205] Stellantis buys into Li-S battery developer Lyten. https://www.electrive.com/2023/05/26/stellantis-buys-into-li-s-battery-developer-lyten/ (accessed December 16, 2023).

Chapter II

Graphene-Based Activated Carbons as Sulfur Host for High-Performing Lithium-Sulfur Batteries

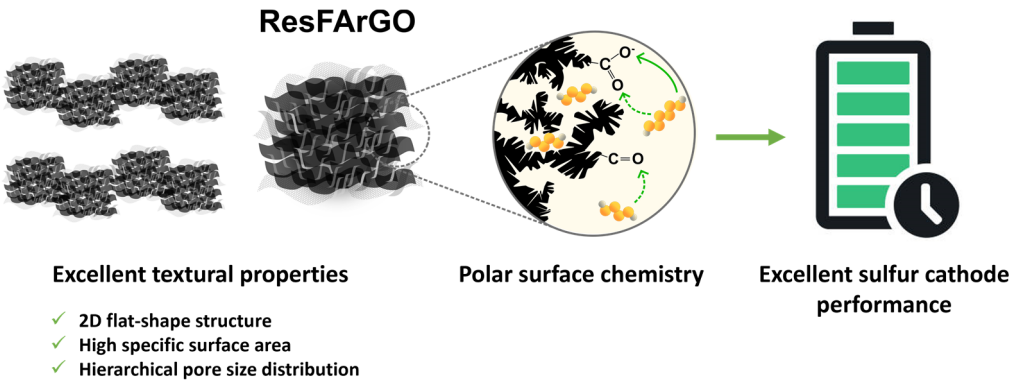

2.1 Introduction

As widely described in the introduction section, Li-S batteries are a promising technology that offers higher energy density compared to conventional Li-ion batteries [1,2]. This improved energy density is directly related to the inherent properties of sulfur as active material and its redox reactions, making it the key distinguishing element of this battery technology. However, several intrinsic challenges, including the insulating nature, volume expansion, or shuttle effect, are still hindered in its commercialization [3,4]. Notably, these issues are primarily related to the active material and can be mitigated through cathode engineering [5].

In this sense, sulfur encapsulation within porous carbonaceous materials has emerged as a feasible and adaptable approach [6]. These materials present a high specific surface area, which allows for the incorporation of a significant amount of sulfur within an electronically conductive framework while also facilitating the physical adsorption and partial retention of polysulfides. Furthermore, their porous structure aids in buffering volume changes during cycling, thus enhancing overall battery performance [6–8]. One commonly employed carbonaceous material for sulfur encapsulation is the commercially available Ketjenblack® EC-600JD (KJ600), known for its high surface area of approximately 1400 m^2 g^{-1} [9]. However, KJ600 exhibits inadequate electronic conductivity for high sulfur utilization, particularly at fast cycling rates and high sulfur loadings [10–12]. Additionally, its predominant pore structure primarily consists of large micropores and mesopores, which are not optimal for LiPS retention [13]. Consequently, investigating new porous carbon nanostructures with customized properties represents a promising avenue for advancing LSBs.

This research has found intriguing similarities between the criteria established for sulfur cathode carbon materials and the electrode materials employed in electrochemical capacitors, commonly known as supercapacitors [14,15]. Supercapacitors represent a well-established and widely adopted energy storage technology, and their performance strongly relies on the characteristics of electrode materials, with carbonaceous materials playing a pivotal role [16–19]. In particular, electric double-layer supercapacitors, which depend on charge accumulation in the electrode/electrolyte interphase for energy storage, require carbon materials with high surface area, accessible pore volume, and a hierarchical pore size distribution

[20,21]. Interestingly, these requirements closely align with the need for a suitable sulfur carbon host [22]. Therefore, implementing knowledge and insights into the design of porous carbonaceous materials from supercapacitor technology can effectively contribute to developing new materials to address the challenges of Li-S technology and maximize its performance.

In this sense, activated carbons (ACs), extensively utilized in the supercapacitors field, offer a compelling alternative as sulfur-hosting material. They exhibit high specific surface area, typically ranging from 500-3000 m^2 g^{-1}, and abundantly available porosity, overcoming the above-described challenges [15,23,24]. Moreover, ACs can be readily synthesized from abundant and easily accessible waste materials, allowing the development of an improved sustainability route for carbon material production [25–27]. However, their electronic conductivity remains insufficient for efficient sulfur utilization during battery cycling, particularly at high sulfur loadings [28–30].

To address the conductivity limitations of ACs, researchers have turned their attention to graphene, a two-dimensional (2D) carbon material with excellent electronic conductivity, high theoretical specific surface area, and superior electrochemical properties [31–33]. However, large-scale production challenges and the non-polar nature of graphene have led to the utilization of graphene oxide (GO) or its reduced counterpart (rGO) as graphene-based materials [34–36]. In addition to their excellent mechanical properties, these materials possess polar nature functional groups that aid in polysulfide retention and enhance the wettability of the electrolyte within the sulfur electrode structure [33,37]. Nevertheless, these graphene-based materials do not present the ideal textural characteristics to become the optimal sulfur host material, mainly due to their low practical specific surface area and insufficient porosity.

Therefore, a promising approach may involve the combination of graphene materials with activated carbons to create hybrid carbon structures. This strategy has shown remarkable results in supercapacitor technology owing to the synergistic effects produced. However, its application in the context of LSBs has been relatively limited. Therefore, this thesis chapter focuses on synthesizing graphene-based activated carbon hybrid materials as sulfur hosts for their implementation into high-performance sulfur cathodes. The study involves the synthesis, physicochemical and

electrochemical characterization, subsequent integration into sulfur cathode composition, and the final performance evaluation in Li-S cells of two newly developed porous carbonaceous materials. To assess the characteristics and potential applicability of the two synthesized carbonaceous materials, the widely used commercial material KJ600 will be used as a reference.

2.2. Graphene-based activated porous carbon for high-performing sulfur cathode

Two different sources were selected for the preparation of these porous carbons. The first carbonaceous material, referred to as rGOCaf, was synthesized using coffee waste in combination with GO. The selection of coffee waste as a precursor aimed to enhance the sustainability and cost-effectiveness of the process by utilizing this abundant biowaste. The second graphene-based activated carbon, named ResFArGO, was prepared through the pyrolysis of high-purity polymers over the GO template. In this case, a phenolic resin derived from the resorcinol/formaldehyde hydrothermal polycondensation reaction was employed as the precursor. This choice was based on the resin's high yield production and versatility in tailoring morphological properties to suit specific requirements.

2.2.1. Carbon material synthesis

For the synthesis of rGOCaf material, GO dispersion with a concentration of 4 mg GO mL^{-1} as a 2D template, obtained from Graphenea company, and coffee waste as a carbon source were used as precursors. In the initial step, the coffee waste and GO dispersion were thoroughly mixed under vigorous stirring, followed by a freeze-drying process to obtain the dry coffee waste/GO precursor. This precursor was then pre-carbonized at 400 °C under Ar atmosphere for 3 hours. To fine-tune its morphological properties, the obtained carbon was ground and mixed with potassium hydroxide (KOH) at a C:KOH ratio of 1:6, to carry out the chemical activation step. The mixture was then heated to 800 °C under Ar atmosphere. The resulting material was neutralized using a diluted hydrochloric acid solution and subsequently purified by a water-washing process. Finally, the material was freeze-dried to obtain the graphene-based activated carbon material.

To synthesize ResFArGO material, resorcinol was dissolved in a mixture of water and ethanol under magnetic stirring. Afterward, the GO suspension was added and thoroughly stirred to ensure complete homogenization. Following that,

formaldehyde and phosphoric acid, serving as catalyst, were subsequently added to the suspension, and the mixture was promptly transferred to an oven at 85 °C for 70 h to carry out the hydrothermal condensation reaction. The resulting resin was then carbonized in a tubular oven at 800 °C under Ar atmosphere, yielding the carbon material. Finally, this material was activated, purified, and dried following the same procedure as in the rGOCaf synthesis. **Scheme 2.1** illustrates the two synthetic routes followed for the preparation of both graphene-based activated carbons.

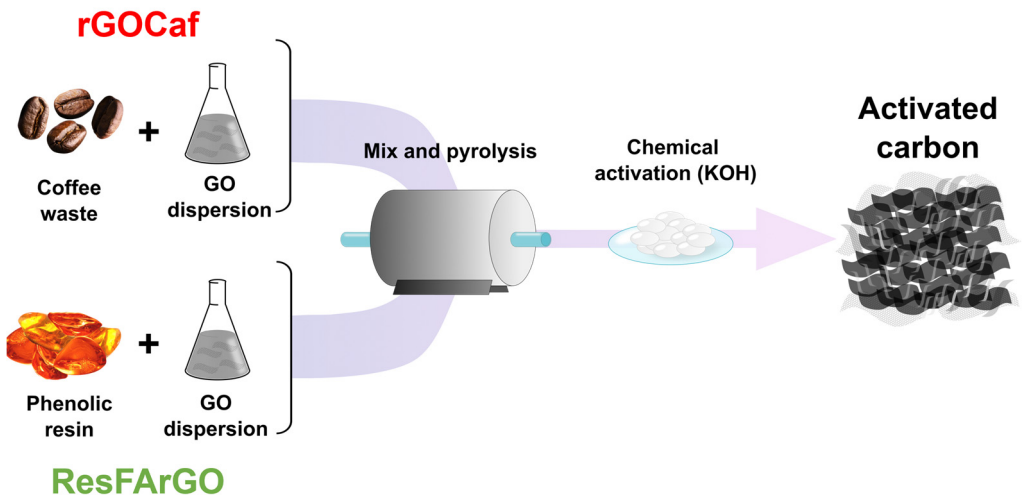

Scheme 2.1. Schematic illustration of the synthesis process of the two graphene-based ACs.

2.2.2. Physicochemical characterization of the porous carbon materials

As previously mentioned, the textural properties of the carbon material used in sulfur cathodes play a pivotal role in addressing the inherent challenges associated with the Li-S technology. Accordingly, conducting a comprehensive study of the inherent properties of carbon material is an essential first step for this endeavor. **Figure 2.1** presents the morphological features of the three different carbon materials: commercial KJ600, and the in-house synthesized rGOCaf and ResFArGO carbon materials. Scanning electron microscopy (SEM) images (**Figures 2.1a**, **b**, and **c**) reveal significant differences in particle structure among the three different carbons analyzed in the study. KJ600 consists of irregularly shaped submicrometer-sized particles with a non-uniform distribution. In contrast, rGOCaf showcases larger particle sizes, characteristic of carbon materials derived from biowaste sources [38].

Notably, these particles are uniformly coated by the rGO laminates, obtained through the thermal reduction of GO. The ResFArGO carbon material showcases an open and uniform 2D flat structure with evenly distributed AC flakes over the rGO template. This 2D structure arises from the templating effect of GO during the phenolic resin yield process [29]. The open structure of both in-house prepared ACs would provide effective buffering of the volume changes characteristic of LSBs during cycling and serve as a potential reservoir for LiPS.

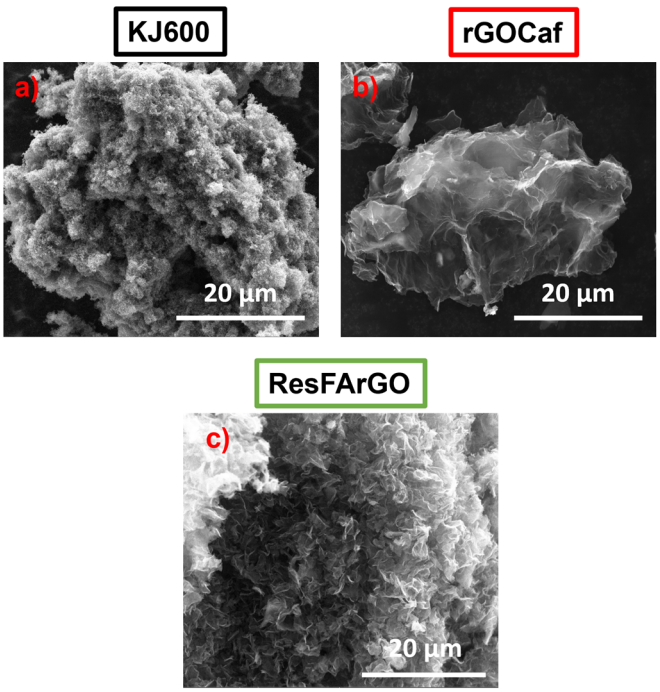

Figure 2.1. SEM images of the morphological properties of **a)** KJ600 commercial, **b)** rGOCaf, and **c)** ResFArGO carbon materials.

To evaluate the textural properties of the different porous carbons, nitrogen adsorption/desorption isotherms at -196 °C. **Figures 2.2a** and **b** collect the isotherms, revealing distinct profile types according to the IUPAC classification, as well as the pore size distribution (PSD) of the studied carbons[39]. KJ600 exhibits a type IV isotherm profile, indicative of a mesoporous nature, accompanied by an H3 type of hysteresis loop, suggesting the presence of slit-shaped pores [40]. In contrast, rGOCaf displays a combination of type I and IV isotherm profiles, reflecting the coexistence of microporous associated with small amounts of mesoporous structures [41]. Lastly,

ResFArGO presents a type I isotherm behavior, characteristic of microporous materials [42]. Importantly, both synthesized ACs show a higher BET-specific surface area (2350 $m^2 g^{-1}$ and 2318 $m^2 g^{-1}$ for rGOCaf and ResFArGO, respectively) compared to the commercial carbon KJ600 (1383 $m^2 g^{-1}$). This higher specific surface area is instrumental for the accommodation of sulfur within the carbon matrix. The PSD analysis inferred that KJ600 presents an uneven pore size distribution, comprising both micropores (approximately 1 nm) and mesopores (around 5 nm). In contrast, graphene-based materials demonstrate a narrower distribution of micropore size. It is worth noting that the micropores in rGOCaf are wider than those in ResFArGO, as suggested by the isotherm shape. Therefore, the synthesized carbons present a higher specific surface area and narrower distribution of smaller pores compared to the reference KJ600, which are desired properties for Li-S application [43,44].

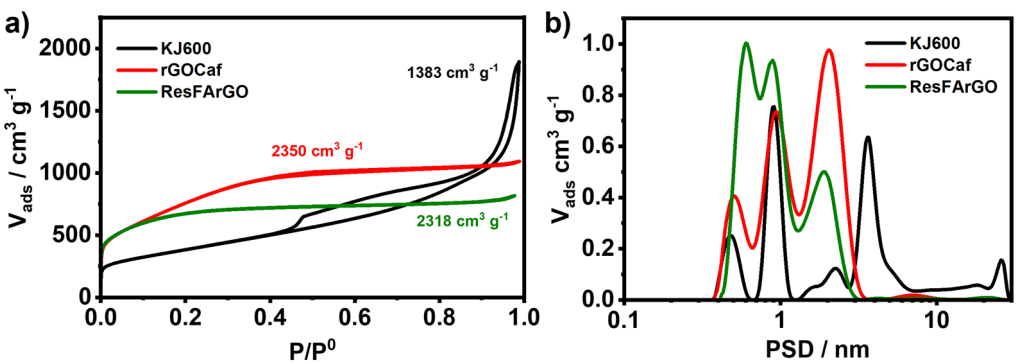

Figure 2.2. a) N_2 adsorption-desorption isotherms and **b)** calculated pore size distributions of KJ600, rGOCaf, and ResFArGO carbon materials.

In conjunction with the investigation of textural properties of carbonaceous materials, a detailed examination of their surface chemistry is essential for thorough characterization. While physical anchoring initially proves effective, it may not completely mitigate the shuttle effect due to the weak interaction with LiPS [45,46]. Hence, the presence of compatible surface chemistry can synergistically complement LiPS anchoring, thereby addressing the shuttle effect [47,48].

To evaluate the surface chemistry of the synthesized carbonaceous materials, X-ray photoelectron spectroscopy (XPS) analysis was conducted. **Figure 2.3** displays the O 1s spectra of KJ600 and ResFArGO carbonaceous materials. In the O 1s spectrum of KJ600, a bimodal distribution is evident, featuring two distinct peaks centered at

534 and 532 eV, corresponding to the C−O and C=O groups. In contrast, the peak distribution for ResFArGO diverges significantly. Here, an additional peak emerges at 530 eV, alongside the predominant C=O peak at 532 eV and a lowered C−O peak centered at 534 eV. This newly observed peak is assigned to carboxylic acids or esters (O−C=O group), sourced from the remaining original functional groups of GO. Compared to KJ600, the emergence of this new peak, superseding the C−O group, confers a polar characteristic to the ResFArGO surface. As extensively documented in the literature, the presence of this polar surface represents a key feature for enhancing the affinity with polar LiPS compounds [35,49–51].

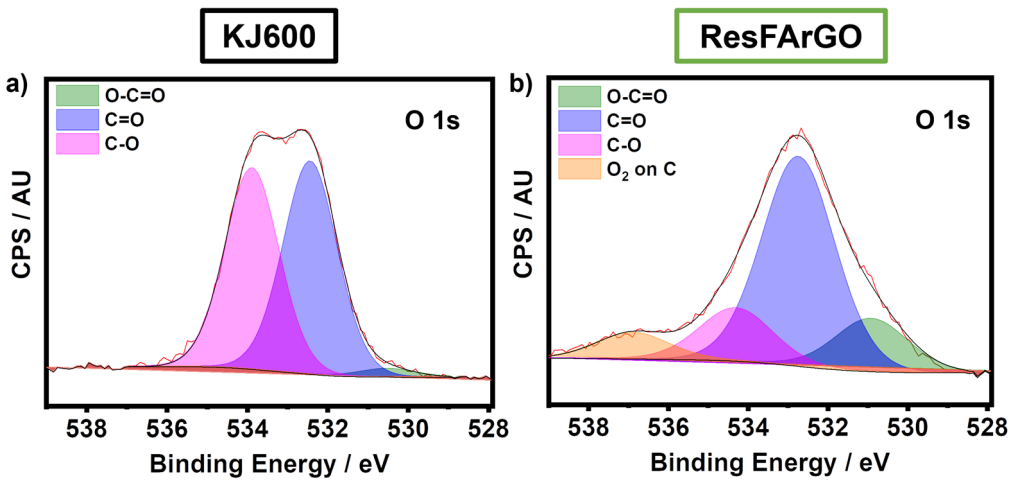

Figure 2.3. O 1s regions corresponding to XPS spectra of **a)** KJ600 and **b)** ResFArGO carbonaceous materials.

The effective entrapment of LiPS by carbon sulfur host is crucial for mitigating the shortcomings associated with the shuttle effect. In this sense, common carbon materials generally possess non-polar characteristics, leading to limited interaction with polar LiPS compounds. This weak affinity results in compromised long-term LSB cycling, due to the unmitigated shuttle effect [52–54]. Hence, to evaluate the LiPS trapping ability of the studied carbons, a visual test based on the color change associated with Li_2S_6 adsorption capacity was conducted. **Figure 2.4a** vividly illustrates the substantial differences in Li_2S_6 anchoring among the studied carbon materials. KJ600 exhibits the lowest LiPS adsorption capacity, evident by the darker coloration of the solution, while the two in-house synthesized materials show a more pronounced reduction in the solution coloration. As illustrated schematically in

Figures 2.4b and **c**, the difference in LiPS trapping is attributed to the synergistic combination of favorable structural and surface chemistry properties exhibited by the synthesized graphene-based ACs, as observed previously. Specifically, in contrast to KJ600, the higher specific surface area and narrower smaller PSD, coupled with the presence of polar-based functional groups presented by both rGOCaf and, particularly, ResFArGO materials, contributes to an enhanced affinity with LiPS. This fundamental feature holds the potential for an improved LSB performance.

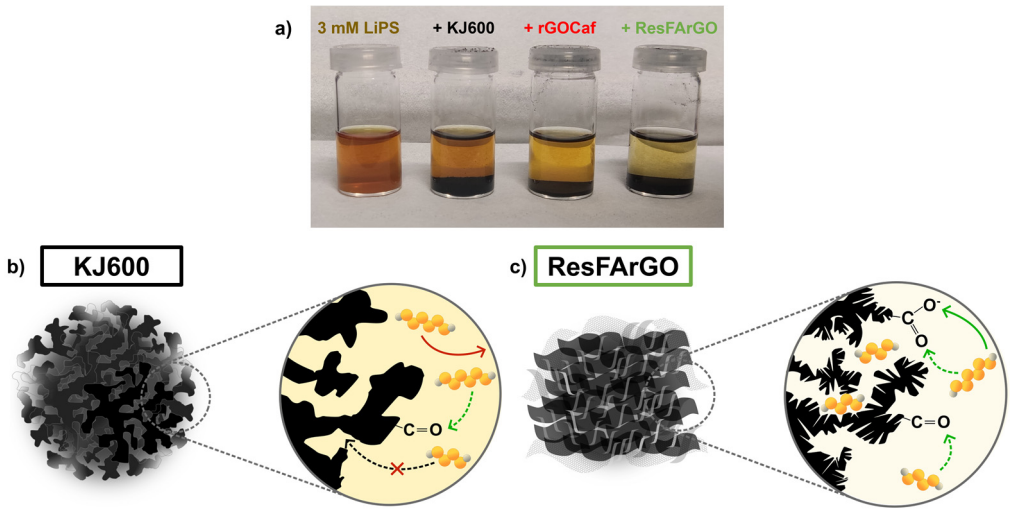

Figure 2.4. a) LiPS anchoring test of the studied carbon materials. Schematic illustration of the LiPS retention capability of **b)** KJ600, and **c)** graphene-based ACs.

2.2.3. Sulfur@carbon composite preparation and characterization

After synthesizing the two porous carbons, the sulfur@carbon composites, designated as S@KJ600, S@rGOCaf, and S@ResFArGO, were prepared with a sulfur-carbon material mass ratio of 71:29. The incorporation of sulfur into the carbon structures was accomplished using the melt diffusion process. This process entailed exposing the carbon materials to sulfur at a temperature of 155 °C for 12 hours under the Ar atmosphere. This temperature is selected especially because sulfur becomes molten and achieves its lowest viscosity point, thereby facilitating the infiltration process in the minute pores of the carbon materials without agglomerations to ensure optimal distribution and integration of the active material within the porous carbon matrix. By way of comparison, the widely known KJ600 commercial porous carbon was selected and studied to evaluate the potential of the in-house synthesized ACs.

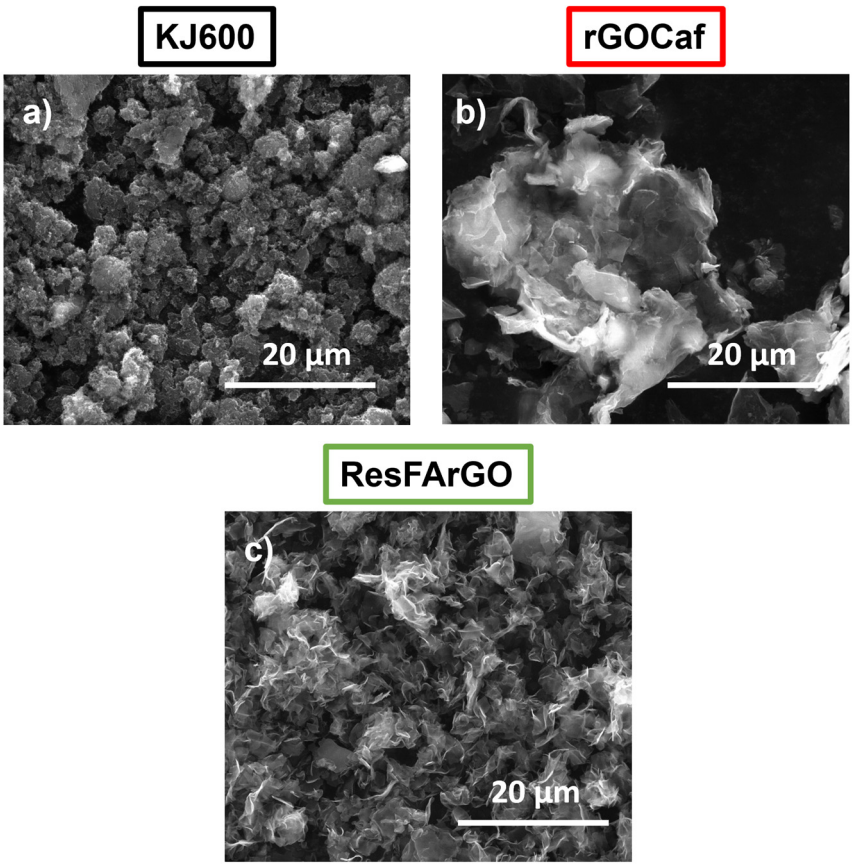

Figure 2.5. SEM images of the different S@carbon composite.

SEM images in **Figures 2.5a**, **b**, and **c** showcase the different S@C composites. Upon examining the SEM image of the S@KJ600 composite (**Figure 2.5a**), an increase in the particle size compared to that of the pristine KJ600 raw material (**Figure 2.1a**) is apparent. The size enlargement can be attributed to the aggregation of the carbon particles resulting from the incorporation of sulfur in the composite. Conversely, the SEM images of the graphene-based composites (**Figures 2.5b** and **c**) show no significant structural changes when compared to sulfur-free ACs (**Figures 2.2b** and **c**). Moreover, it is noteworthy that no active material agglomeration is observed in these images, indicating a homogeneous distribution of sulfur across the surface of the ACs.

The successful integration of sulfur in the carbon structure is further confirmed by the X-ray diffraction (XRD) patterns presented in **Figure 2.6a**. In the XRD

patterns of pristine S_8 (JCPDS No. 08-0247), well-defined and highly intense diffraction peaks are observed, indicating the crystalline nature of orthorhombic sulfur. However, upon infiltration of sulfur into the different carbonaceous materials, these peaks are noticeably diminished. This reduction in peak intensity can be correlated to the exceptional sulfur storage properties of the proposed carbons and the complete dispersion of sulfur within the activated carbon pores, resulting in the reduction of the diffraction peaks [55,56]. Further characterization of the S@C composite was conducted using the Raman analysis (**Figure 2.6b**).

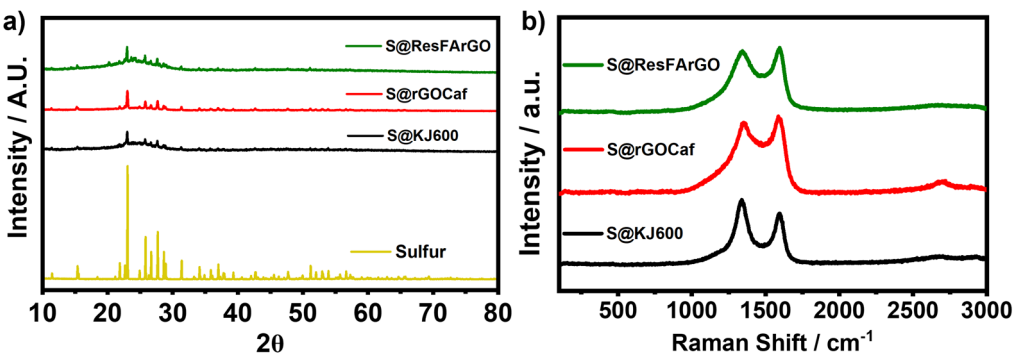

Figure 2.6. a) XRD patterns of sulfur (JCPDS No. 08-0247) and the three sulfur@carbon composites. **b)** Raman spectra of the noted samples.

The Raman spectra exhibited two broad peaks at approximately 1330 and 1600 cm^{-1}, assigned to the G and D bands of graphite, respectively. The G-band corresponds to sp2 carbon vibrations, while the D-band is associated with defect-induced vibrations resulting from the disordered structure of the graphene sheets. The ratio between the integrated areas of the D-band and G-band was found to be 1.89, 1.52, and 1.52 for S@KJ600, S@rGOCaf, and S@ResFArGO, respectively. This indicates a lower concentration of defects and a higher graphitization degree in the samples containing graphene. Importantly, no sulfur peaks were observed in the Raman spectra, further confirming that crystalline sulfur clusters are uniformly dispersed along the graphene surface [57].

2.2.4. Sulfur cathode preparation and characterization

To prepare the sulfur electrodes, S@ACs and S@KJ600 composites were combined with carboxymethyl cellulose (CMC) and styrene butadiene rubber (SBR) as cathode binders in deionized water, maintaining a mass ratio of 90:5:5, resulting in a

final sulfur content of 64 wt.%. Subsequently, these slurries were deposited on a carbon-coated aluminum current collector using a doctor blade technique, with the sulfur loading being controlled by adjusting the wet thickness of the slurry deposition. Two different loading values were fixed depending on the final application: i) medium loading of 2.5-3 mg_S cm^{-2} for the cycling rate evaluation, referred to as power cells, and ii) high loading of 4 mg_S cm^{-2} to evaluate high-capacity cells under mid rates, denoted as energy cells. In all cases, the laminates were thoroughly dried at room temperature to avoid crack formation followed by a drying process at 50 °C under vacuum overnight to ensure complete removal of any residual solvent.

After conducting a comprehensive analysis of the individual properties of the three carbon materials and the S@C composites, the study progressed to examine their behavior for sulfur cathode development, particularly at high sulfur loading targets (4 mg_S cm^{-2}, in this case). Alongside technological challenges, achieving high sulfur loading while maintaining suitable mechanical integrity in terms of packing and homogeneity presents a significant challenge in LSBs. Hence, the morphological evaluation of the high sulfur loading (4 mg_S cm^{-2}) was evaluated.

The optical image in **Figure 2.7a** reveals a notable issue observed in S@KJ600 electrodes, characterized by poor material adhesion and the development of large cracks on the electrode surface. This issue is attributed to the significant shrinkage during the slurry drying process in KJ600-based cathodes, primarily caused by the high amount of solvent retained within this carbon material during the electrode slurry preparation [58].

Furthermore, capillary stresses associated with the drying of aqueous slurries, due to the higher surface tension of water, lead to more aggressive cracking [59,60]. In contrast, **Figures 2.7b** and **c** demonstrate the superior ability of both ACs to enhance electrode component cohesion, attachment, and distribution, resulting in a high packing quality. The SEM image further validates these findings by depicting the presence of micro-sized cracks in KJ600 sulfur electrodes (**Figures 2.7d** and **g**), while the electrodes composed of graphene-based ACs (**Figures 2.7e-i**) exhibit a distinct absence of such defects. Additionally, the ACs-based electrodes demonstrate an exceptional particle distribution with no signal of sulfur particle agglomeration. These observations highlight the favorable mechanical properties, packing characteristics, and active material distribution of the synthesized graphene-based activated carbons,

which are key properties for the successful development of optimal high sulfur loading cathodes.

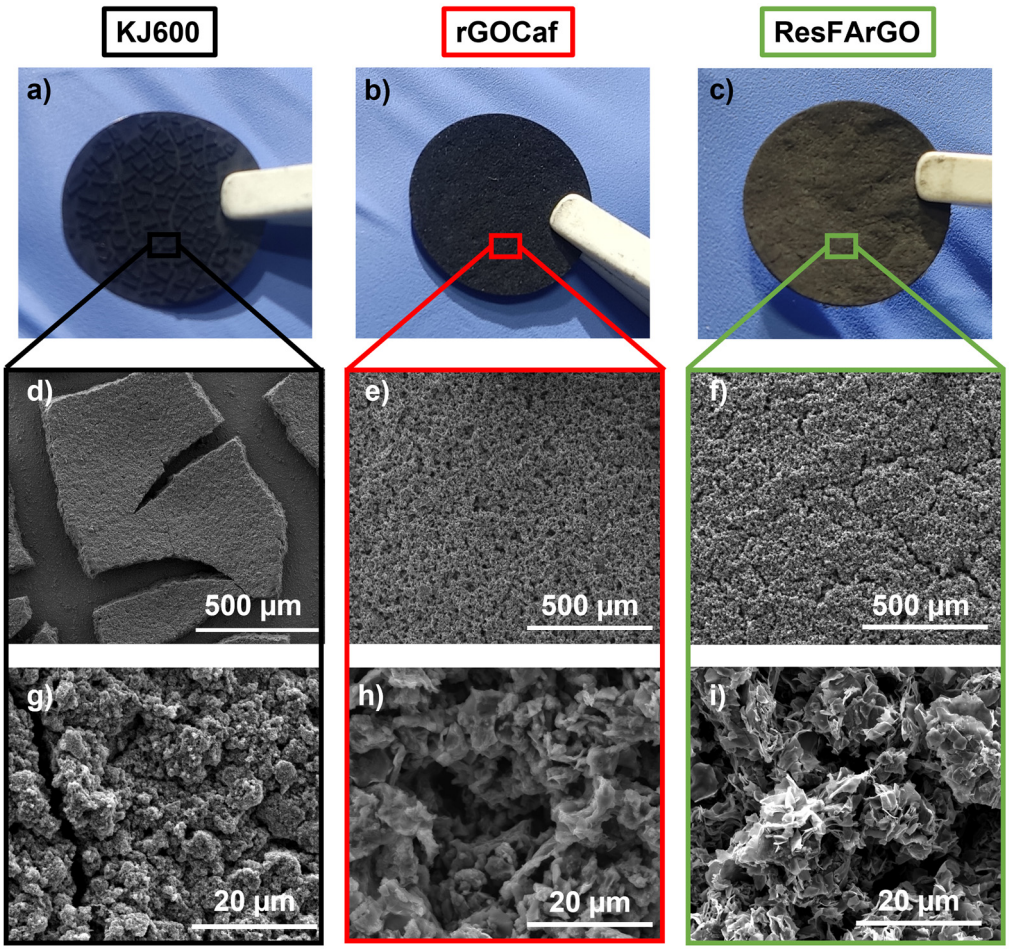

Figure 2.7. a-c) Optical and SEM images at **d-f)** low and **g-i)** high magnifications of the prepared high sulfur loading electrodes with the three different carbon materials.

In summary, the obtained results demonstrate that both ACs exhibit superior individual as well as sulfur electrode properties compared to the KJ600 reference material.

2.2.5. Electrochemical performance of the prepared sulfur cathodes

To assess the impact of these favorable properties on the performance of Li-S cells, a comprehensive electrochemical analysis was conducted through the galvanostatic cycling of the three sulfur electrodes developed in the current chapter. This analysis encompassed two different cell studies. Firstly, a C-rate test was employed to analyze the power capabilities of the newly synthesized carbons in the power cells, as described earlier. Secondly, long-term cycling was undertaken to evaluate the cycling stability of the different electrodes prepared in the energy cells.

For these cell studies, the conventional Li-S technology electrolyte was employed, consisting of a solution of 0.5 M lithium bis(trifluoromethanesulfonyl)imide (LiTFSI) and 0.5 M lithium nitrate ($LiNO_3$) dissolved in a 1:1 vol. mixture of DME/DOL Concerning the electrolyte amount, it is common in the existing literature to encounter studies reporting coin cell performance under flooded electrolyte conditions. However, this practice can lead to misinterpretation and may mask potential operational issues during battery cycling. Furthermore, it is important to note that these cycling conditions significantly diverge from practical application, making their transition to real cells challenging. Consequently, taking these factors into account, a reduced amount of electrolyte 7 µL mg_S^{-1} was employed in all the coin cell cycling tests performed throughout the thesis. This ratio was consistently adjusted to establish lean electrolyte conditions for this battery configuration, to facilitate its future scale-up.

2.2.5.1. Rate capability evaluation

For the C-rate test, moderate sulfur loadings were employed to mitigate possible operating challenges that the lithium anode may suffer under these harsh operating conditions. To this end, the power cells underwent galvanostatic cycling at different C-rates, including C/20, C/10, C/5, and C/2.

Henceforth, in all representations of battery electrochemical performance within this thesis, the dot representation will be linked to the CE on the right vertical axis, while the dash-dot representation will correspond to discharge capacity on the left vertical axis.

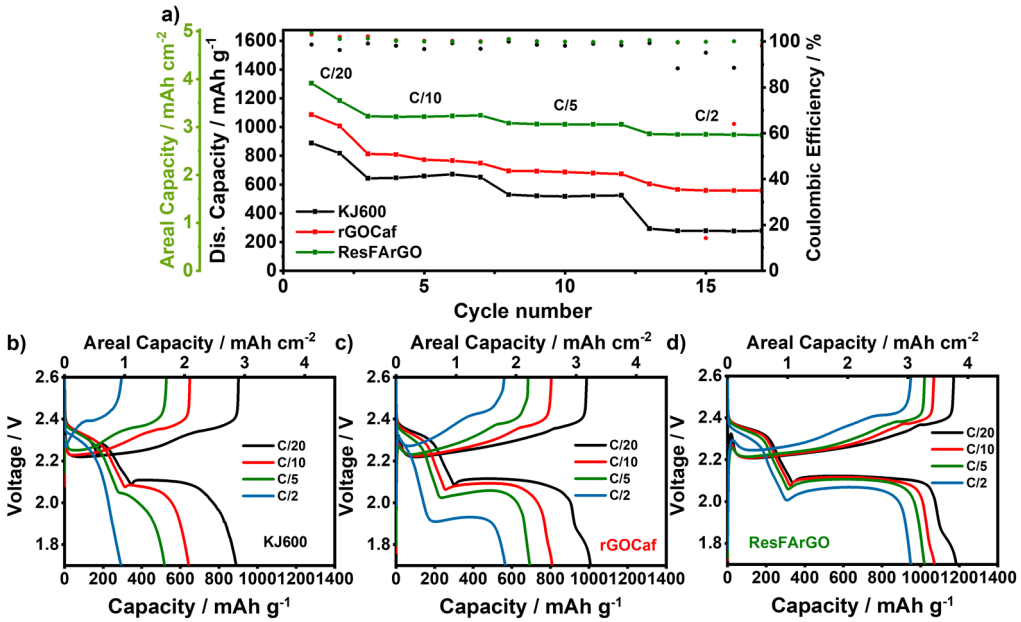

Figure 2.8. a) Rate capabilities of Li-S power cells using the studied carbon materials at different C-rates, along with the discharge/charge voltage profiles of **b)** S@KJ600, **c)** S@rGOCaf, and **d)** S@ResFArGO cells.

Figure 2.8a presents the gravimetric and areal capacity plots of the power cells. Notably, both rGOCaf and ResFArGO cells exhibit significantly higher specific and areal capacities across the entire range of the analyzed C-rates compared to the cells using commercial KJ600 as the sulfur host material. Additionally, the graphene-based cathodes demonstrate remarkable capacity retention as the C-rate increases from C/10 to C/2, with rGOCaf retaining 73% of the initial capacity and ResFArGO retaining an impressive 89%. This outstanding behavior can be attributed to the exceptional characteristics of the in-house ACs, which offer a combination of high specific surface area and highly accessible narrower pore size distribution for effective sulfur conversion and LiPS retention. These suitable properties, along with the excellent electronic conductivity provided by the rGO sheets, contribute to their robust response under fast cycling conditions, which is of particular importance for practical application.

It is worth highlighting the performance of the S@ResFArGO cathode, exhibiting the best rate capability among all the analyzed systems. At a high C-rate of C/2, it delivers stable discharge capacities of 950 mAh g^{-1} (around 2.5 mAh cm^{-2}) with

minimal polarization, defined as the voltage difference between charge and discharge profiles, at high current densities, as evidenced by the charge/discharge profiles shown in **Figure 2.8d**. Furthermore, the stability offered by the ResFArGO-based cell is highly commendable, achieving impressively high coulombic efficiencies exceeding 99.8% in all tested cycling rates. Compared to rGOCaf, this remarkable performance can be attributed to the narrower and smaller pore sizes and the material homogeneity of ResFArGO. Unlike coffee waste, which can present inherent material properties that are challenging to control, the quality of the resin produced by the polycondensation reaction showcases a higher quality as a carbon source. Therefore, the S@ResFArGO system is positioned as a promising candidate for high-rate Li-S cell application. For comparative analysis, charge/discharge profiles of the S@KJ600 and S@rGOCaf cells are included in **Figures 2.8b** and **c**. These profiles reveal a moderate polarization of the rGOCaf cell, while the reference KJ600-based system exhibits a significantly higher polarization, resulting in observable voltage shifts at C/10 and higher C-rates.

2.2.5.2 High sulfur loading LSB performance

After characterizing the behavior of the power cells, it is also crucial to analyze the performance of the energy cells under a constant cycling rate of C/10, preceded by 5 formation cycles at C/20 (**Figure 2.9a**). In this evaluation, both graphene-based electrodes feature a significantly improved capacity compared to the reference KJ600 cell. S@rGOCaf demonstrates a capacity of 780 mAh g^{-1} (3.12 mAh cm^{-2}), while S@ResFArGO showcases an even higher capacity of 1100 mAh g^{-1} (4.4 mAh cm^{-2}) compared to the lower capacity of 520 mAh g^{-1} (2.08 mAh cm^{-2}) delivered by the reference S@KJ600. The S@ResFArGO cell stands out for achieving the highest capacity and demonstrating remarkable cell stability.

Additionally, the S@ResFArGO cell presents an outstanding capacity retention of > 99.7% from the first to the last cycle at C/10, with charge/discharge profiles remaining unchanged over 50 cycles (**Figure 2.9d**). This exceptional capacity retention can be attributed to the carbon material's ability to effectively retain the first plateau related to the conversion of high-order LiPS. The combination of its strong LiPS trapping capability and excellent electronic conductivity allows for the fast and efficient conversion of the high-order LiPS, contributing to its impressive performance. For comparison, the charge/discharge profiles of S@KJ600 and

S@rGOCaf can be found in **Figures 2.9b** and **c**. It is worth noting that the S@rGOCaf cell displays some erratic charging behavior before cycle 40, which can be ascribed to the lithium instability and potentially mild LiPS attack at the anode. This phenomenon is less pronounced in the S@KJ600 cell due to its lower cell capacity, resulting in gentler lithium anode cycling stress and reduced LiPS generation. Considering these observations, S@ResFArGO demonstrates exceptional sulfur utilization, rate capability, capacity retention, and long cycle life. Therefore, this carbon material can be considered a highly promising candidate for sulfur cathode development in practical Li-S cells.

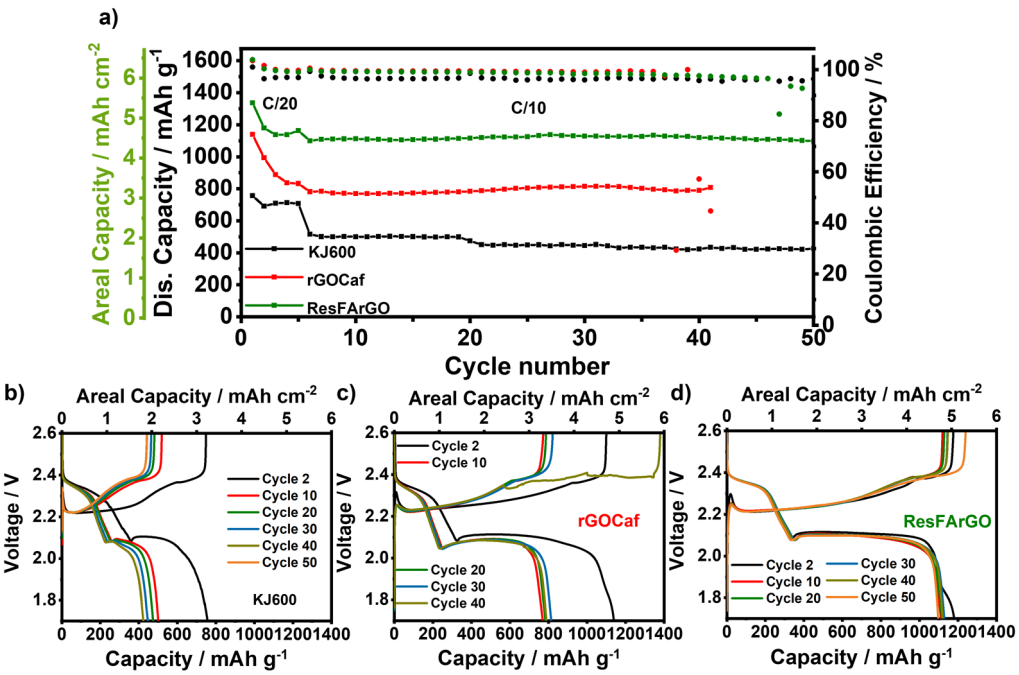

Figure 2.9. a) Long-term cycling performances of Li-S energy cells using the different carbon materials. Discharge and charge profiles of the **b)** S@KJ600, **c)** S@rGOCaf, and **d)** S@ResFArGO-based energy cells.

2.2.6 Post-mortem analysis and cell failure mechanism

Despite the enhanced performance demonstrated by the in-house synthesized graphene-based Acs both for power cells and energy cells presented in this chapter, particularly by the ResFArGO material, it is important to highlight that the Li-S cells present a relatively limited lifespan of approximately 50 cycles, which

hinders their potential practical application. Consequently, to understand the underlying cause of failure, a thorough post-mortem analysis of the high sulfur loading cells was conducted.

Figures 2.10 and **2.11** display optical images of the individual cell components after the energy cell cycling test, while SEM imaging was used to examine the recovered and washed cathodes and anodes.

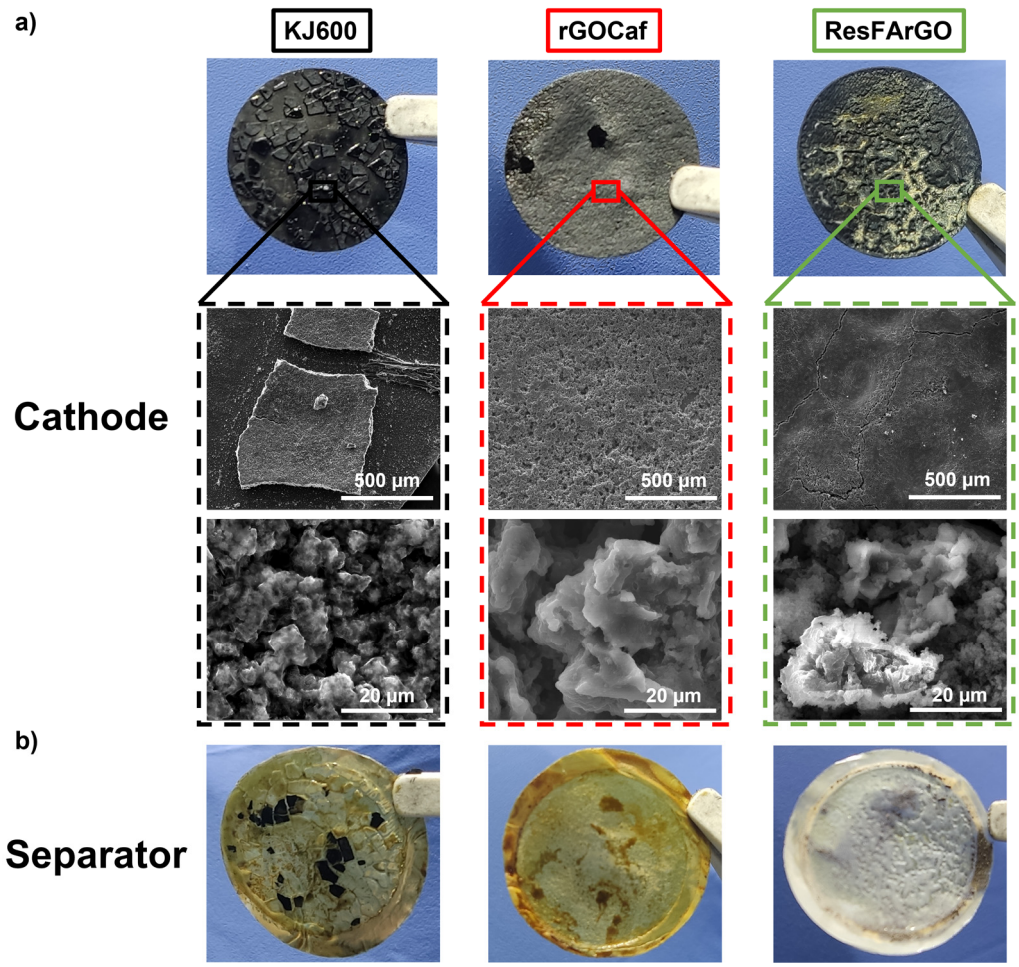

Figure 2.10. Post-mortem analysis of the different energy cells after cycling. Optical images of **a)** the cathode and **b)** the separator of high-loading cells at the end of their cycling life for the three carbon composites.

The optical image of the S@KJ600 cell's cathode reveals a fractured electrode with the active material detached from the current collector (**Figure 2.10a**). Fragments of the active material are observed adhering to the separator, which displays noticeable coloration due to the presence of dissolved LiPS in the electrolyte. This cathode disintegration, coupled with the prevalence of the soluble LiPS, explains the reduced capacity observed in this particular cell configuration.

In contrast, both S@rGOCaf and S@ResFArGO cycled cathodes remarkably maintain their structural integrity even after 40-50 cycles, as confirmed by SEM images. However, a discernible difference arises between these two AC systems. The S@rGOCaf cell exhibits a clear yellowish-orange color, typically associated with the dissolved LiPS (**Figure 2.10b**). Strikingly, despite achieving the highest sulfur utilization among the cells, the S@ResFArGO system preserves an unaltered appearance with no coloration on the Celgard® separator after 50 cycles, as shown in **Figure 2.10b**. Furthermore, distinct sulfur deposition is visible on the surface of the ResFArGO cathode, facilitating its subsequent utilization and enabling improved sulfur utilization and capacity retention.

Conversely, optical and SEM images reveal a noticeable degradation of the LMA in all systems (see **Figure 2.11**). On one hand, the irregular deposition of lithium on the anode surface indicates inadequate long-term compatibility between the employed conventional electrolyte and the lithium anode. The existing bibliography suggests that the consumption of $LiNO_3$ salt during cell cycling is responsible for this compatibility issue [61,62]. On the other hand, the conventional DME/DOL-based electrolyte is not designed to effectively suppress LiPS dissolution. Consequently, the presence of LiPS in the rGOCaf cell further accelerates the consumption of $LiNO_3$, which is the main responsible for maintaining cell stability. Therefore, the limited cycle life of the S@ResFArGO system can be primarily attributed to the stability problems induced by the LMA degradation during the employed challenging battery cycling, particularly under high areal capacities. A similar failure mechanism is presumed in the case of the S@rGOCaf cell, albeit accelerated by the presence of partially dissolved LiPS.

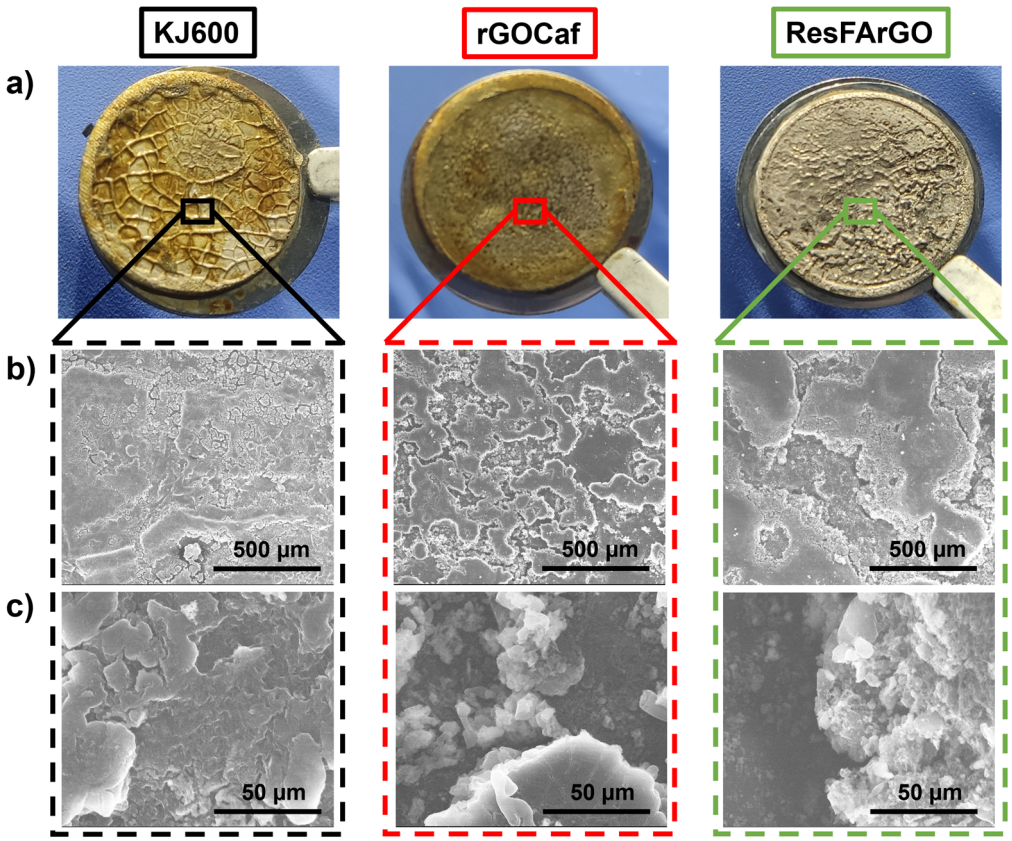

Figure 2.11. a) Optical and SEM images at **b)** low and **c)** high magnifications of the metallic lithium anodes of the noted energy cells after galvanostatic cycling.

2.3. Summary and conclusions

In conclusion, this chapter showcases the potential of employing carbonaceous materials, originally designed for electrochemical capacitors, to address various inherent challenges associated with Li-S battery technology, given the similar material requirements of both technologies. The combination of activated carbons and graphene oxide for the carbon material synthesis has been analyzed for the first time in the context of Li-S batteries, resulting in two new carbonaceous materials, rGOCaf and ResFArGO. The former is derived from coffee waste as an eco-friendly and sustainable precursor, while the latter is produced using high-purity and highly tunable polymer resins. Both materials exhibit favorable properties, including high surface area and optimized hierarchical pore size, making them highly compatible with sulfur and LiPS. As a result, the sulfur electrodes incorporating these materials

exhibit exceptional electrochemical performance. The presence of graphene and small micropores in these materials synergistically contributes to high electronic conductivity and efficient trapping of LiPS, resulting in beneficial effects for Li-S cells. Notably, the incorporation of ResFArGO material enables outstanding sulfur utilization, exceeding 1100 mAh g^{-1} (66% of sulfur utilization) at high sulfur loadings of 4 mg cm^{-2}, and exhibits remarkable rate capability. These findings suggest that the scalability study of ResFArGO holds great promise for the development of high-performance Li-S prototype cells, which will be further investigated in the subsequent chapters of this thesis. However, it is important to consider the degradation of the lithium anode under the employed realistic operation conditions and seek solutions, as these factors significantly affect the overall performance and cycle life of Li-S batteries.

2.4. Bibliography

[1] Y.T. Liu, S. Liu, G.R. Li, X.P. Gao, Strategy of enhancing the volumetric energy density for lithium–sulfur batteries, Adv. Mater. 2021, 33, 2003955. https://doi.org/10.1002/adma.202003955.

[2] H.J. Peng, J.Q. Huang, X.B. Cheng, Q. Zhang, Review on high-loading and high-energy lithium–sulfur batteries, Adv. Energy Mater. 2017, 7, 1700260. https://doi.org/10.1002/aenm.201700260.

[3] L. Huang, J. Li, B. Liu, Y. Li, S. Shen, S. Deng, C. Lu, W. Zhang, Y. Xia, G. Pan, X. Wang, Q. Xiong, X. Xia, J. Tu, Electrode design for lithium–sulfur batteries: Problems and solutions, Adv. Funct. Mater. 2020, 30, 1910375. https://doi.org/10.1002/adfm.201910375.

[4] R. Guo, Y. Yang, X.L. Huang, C. Zhao, B. Hu, F. Huo, H.K. Liu, B. Sun, Z. Sun, S.X. Dou, Recent Advances in Multifunctional Binders for High Sulfur Loading Lithium-Sulfur Batteries, Adv. Funct. Mater. 2023, 34, 2307108. https://doi.org/10.1002/adfm.202307108.

[5] E. Cha, M. Patel, S. Bhoyate, V. Prasad, W. Choi, Nanoengineering to achieve high efficiency practical lithium-sulfur batteries, Nanoscale Horizons. 2020, 5, 808–831. https://doi.org/10.1039/c9nh00730j.

[6] S. Li, B. Jin, X. Zhai, H. Li, Q. Jiang, Review of carbon materials for lithium-sulfur batteries, ChemistrySelect. 2018, 3, 2245–2260. https://doi.org/10.1002/slct.201703112.

[7] M.S. Md Zaini, N.F. Anuar, S.A.M. Al-Junid, S.S.A. Syed-Hassan, Agricultural biomass-based carbon cathode materials for lithium-sulfur batteries: A systematic review, Mater. Sci. Energy Technol. 2023, 6, 205–225. https://doi.org/10.1016/j.mset.2022.12.009.

[8] M. Wang, X. Xia, Y. Zhong, J. Wu, R. Xu, Z. Yao, D. Wang, W. Tang, X. Wang, J. Tu, Porous carbon hosts for lithium–sulfur batteries, Chem. - A Eur. J. 2019, 25, 3710–3725. https://doi.org/10.1002/chem.201803153.

[9] F. Schmidt, M. Fiedler, T. Arlt, A. De, F. Hoffmann, F. Wilde, S. Dörfler, B. Schumm, T. Abendroth, H. Althues, S. Kaskel, Impact of the carbon matrix composition on the S/C cathode porosity and performance in prototype Li–S cells, Energy Technol.

2023, 11, 2300518. https://doi.org/10.1002/ente.202300518.

[10] H.M. Bilal, K. Yuksel, D. Eroglu, Influence of sulfur loading on lithium-sulfur battery performance for different cathode carbon types, ChemistrySelect. 2023, 8, 202203944. https://doi.org/10.1002/slct.202203944.

[11] H. Fazal, D. Eroglu, A. Kilic, B. Dong, N. Ali, J. Zai, X. Qian, Atomic V- and Co-modified ketjen black-sulfur composite for high-performance lithium-sulfur batteries, ACS Appl. Energy Mater. 2023, 6, 6721–6731. https://doi.org/10.1021/acsaem.3c00889.

[12] T. Liu, H. Hu, X. Ding, H. Yuan, C. Jin, J. Nai, Y. Liu, Y. Wang, Y. Wan, X. Tao, 12 years roadmap of the sulfur cathode for lithium sulfur batteries (2009–2020), Energy Storage Mater. 2020, 30, 346–366. https://doi.org/10.1016/j.ensm.2020.05.023.

[13] C. Kensy, D. Leistenschneider, S. Wang, H. Tanaka, S. Dörfler, K. Kaneko, S. Kaskel, The role of carbon electrodes pore size distribution on the formation of the cathode–electrolyte interphase in lithium–sulfur batteries, Batter. Supercaps 2021, 4, 612–622. https://doi.org/10.1002/batt.202000195.

[14] Z. Gao, Y. Zhang, N. Song, X. Li, Biomass-derived renewable carbon materials for electrochemical energy storage, Mater. Res. Lett. 2017, 5, 69–88. https://doi.org/10.1080/21663831.2016.1250834.

[15] K. Chen, D. Xue, Multiple Functional Biomass-Derived activated carbon materials for aqueous supercapacitors, lithium-ion capacitors and lithium-sulfur batteries, Chinese J. Chem. 2017, 35, 861–866. https://doi.org/10.1002/cjoc.201600785.

[16] Z. Zhai, L. Zhang, T. Du, B. Ren, Y. Xu, S. Wang, J. Miao, Z. Liu, A review of carbon materials for supercapacitors, Mater. Des. 2022, 221, 111017. https://doi.org/10.1016/j.matdes.2022.111017.

[17] Z. Supiyeva, X. Pan, Q. Abbas, The critical role of nanostructured carbon pores in supercapacitors, Curr. Opin. Electrochem. 2023, 39, 101249. https://doi.org/10.1016/j.coelec.2023.101249.

[18] H. Xu, C. Wu, X. Wei, S. Gao, Hierarchically porous carbon materials with controllable proportion of micropore area by dual-activator synthesis for high-performance supercapacitors, J. Mater. Chem. A 2018, 6, 15340–15347. https://doi.org/10.1039/c8ta04777d.

[19] C.F. Liu, Y.C. Liu, T.Y. Yi, C.C. Hu, Carbon materials for high-voltage supercapacitors, Carbon N. Y. 2019, 145, 529–548. https://doi.org/10.1016/j.carbon.2018.12.009.

[20] L. Borchardt, D. Leistenschneider, J. Haase, M. Dvoyashkin, Revising the

concept of pore hierarchy for ionic transport in carbon materials for supercapacitors, Adv. Energy Mater. 2018, 8, 1800892. https://doi.org/10.1002/aenm.201800892.

[21] M.M. Sk, P. Pradhan, B.K. Patra, A.K. Guria, Green biomass derived porous carbon materials for electrical double-layer capacitors (EDLCs), Mater. Today Chem. 2023, 30, 101582. https://doi.org/10.1016/j.mtchem.2023.101582.

[22] Y. Xiang, L. Lu, A.G.P. Kottapalli, Y. Pei, Status and perspectives of hierarchical porous carbon materials in terms of high-performance lithium–sulfur batteries, Carbon Energy 2022, 4, 346-398. https://doi.org/10.1002/cey2.185.

[23] S.D. Magar, C. Leibing, J.L. Gómez-Urbano, R. Cid, D. Carriazo, A. Balducci, Brewery waste derived activated carbon for high performance electrochemical capacitors and lithium-ion capacitors, Electrochim. Acta 2023, 446, 142104. https://doi.org/10.1016/j.electacta.2023.142104.

[24] A. Benítez, J. Amaro-Gahete, Y.C. Chien, Á. Caballero, J. Morales, D. Brandell, Recent advances in lithium-sulfur batteries using biomass-derived carbons as sulfur host, Renew. Sustain. Energy Rev. 2022, 154, 111783. https://doi.org/10.1016/j.rser.2021.111783.

[25] S. Ghosh, R. Santhosh, S. Jeniffer, V. Raghavan, G. Jacob, K. Nanaji, P. Kollu, S.K. Jeong, A.N. Grace, Natural biomass derived hard carbon and activated carbons as electrochemical supercapacitor electrodes, Sci. Rep. 2019, 9, 16315. https://doi.org/10.1038/s41598-019-52006-x.

[26] P. Dubey, V. Shrivastav, P.H. Maheshwari, S. Sundriyal, Recent advances in biomass derived activated carbon electrodes for hybrid electrochemical capacitor applications: Challenges and opportunities, Carbon 2020, 170, 1–29. https://doi.org/10.1016/j.carbon.2020.07.056.

[27] X. Luo, S. Chen, T. Hu, Y. Chen, F. Li, Renewable biomass-derived carbons for electrochemical capacitor applications, SusMat. 2021, 1, 211–240. https://doi.org/10.1002/sus2.8.

[28] T. Tonoya, H. Ando, N. Takeichi, H. Senoh, T. Kojima, H. Hinago, Y. Matsui, M. Ishikawa, Capacity decay mechanism of lithium-sulfur batteries using a microporous activated carbon-sulfur composite as the cathode material, J. Phys. Chem. C. 2023, 127, 10038–10044. https://doi.org/10.1021/acs.jpcc.3c01961.

[29] G. Moreno-Fernández, J.L. Gómez-Urbano, M. Enterría, T. Rojo, D. Carriazo, Flat-shaped carbon-graphene microcomposites as electrodes for high energy supercapacitors, J. Mater. Chem. A. 2019, 7, 14646–14655. https://doi.org/10.1039/c9ta03295a.

[30] S.H. Jung, Y. Myung, B.N. Kim, I.G. Kim, I.K. You, T.Y. Kim, Activated biomass-

derived graphene-based carbons for supercapacitors with high energy and power density, Sci. Rep. 2018, 8, 1915. https://doi.org/10.1038/s41598-018-20096-8.

[31] G. Moreno-Fernández, J.L. Gómez-Urbano, M. Enterría, R. Cid, J.M. López del Amo, R. Mysyk, D. Carriazo, Understanding enhanced charge storage of phosphorus-functionalized graphene in aqueous acidic electrolytes, Electrochim. Acta 2020, 361, 136985. https://doi.org/10.1016/j.electacta.2020.136985.

[32] Y. Chen, S. Lu, J. Zhou, X. Wu, W. Qin, O. Ogoke, G. Wu, 3D graphene framework supported Li2S coated with ultra-thin Al2O3 films: binder-free cathodes for high-performance lithium sulfur batteries, J. Mater. Chem. A 2017, 5, 102–112. https://doi.org/10.1039/c6ta08039a.

[33] L. Zhang, Y. Wang, Z. Niu, J. Chen, Advanced nanostructured carbon-based materials for rechargeable lithium-sulfur batteries, Carbon. 2019, 141, 400–416. https://doi.org/10.1016/j.carbon.2018.09.067.

[34] A.I. Kamisan, T.I. Tunku Kudin, A.S. Kamisan, A.F. Che Omar, M.F. Mohamad Taib, O.H. Hassan, A.M.M. Ali, M.Z.A. Yahya, Recent advances on graphene-based materials as cathode materials in lithium-sulfur batteries, Int. J. Hydrogen Energy 2022, 47, 8630–8657. https://doi.org/10.1016/j.ijhydene.2021.12.166.

[35] P. Vélez, M. del C. Rojas, J. Velasco, M.L. Para, D. Barraco, E.P.M. Leiva, G.L. Luque, On the role of oxidized graphene interfaces in lithium sulfur batteries: Thermodynamic and kinetic aspects using density functional theory, Appl. Surf. Sci. 2021, 550, 149358. https://doi.org/10.1016/j.apsusc.2021.149358.

[36] K. Shen, H. Mei, B. Li, J. Ding, S. Yang, 3D printing sulfur copolymer-graphene architectures for Li-S batteries, Adv. Energy Mater. 2018, 8, 1701527. https://doi.org/10.1002/aenm.201701527.

[37] Y. Dou, Q. Bai, K. Yang, W. Guo, H. Wang, S. Chen, The effect of surface functional groups on the wettability of graphene oxide coated alumina substrate: Molecular dynamics simulations, J. Mol. Liq. 2022, 366, 120268. https://doi.org/10.1016/j.molliq.2022.120268.

[38] J.L. Gómez-Urbano, G. Moreno-Fernández, M. Arnaiz, J. Ajuria, T. Rojo, D. Carriazo, Graphene-coffee waste derived carbon composites as electrodes for optimized lithium ion capacitors, Carbon N. Y. 2020, 162, 273–282. https://doi.org/10.1016/j.carbon.2020.02.052.

[39] M. Thommes, K. Kaneko, A. V. Neimark, J.P. Olivier, F. Rodriguez-Reinoso, J. Rouquerol, K.S.W. Sing, Physisorption of gases, with special reference to the evaluation of surface area and pore size distribution (IUPAC Technical Report), Pure Appl. Chem. 2015, 87, 1051–1069. https://doi.org/10.1515/pac-2014-1117.

[40] L. Xu, J. Zhang, J. Ding, T. Liu, G. Shi, X. Li, W. Dang, Y. Cheng, R. Guo, Pore structure and fractal characteristics of different shale lithofacies in the dalong formation in the western area of the lower yangtze platform, Minerals 2020, 10, 72. https://doi.org/10.3390/min10010072.

[41] C.V. Neves, A.N. Módenes, F.B. Scheufele, R.P. Rocha, M.F.R. Pereira, J.L. Figueiredo, C.E. Borba, Dibenzothiophene adsorption onto carbon-based adsorbent produced from the coconut shell: Effect of the functional groups density and textural properties on kinetics and equilibrium, Fuel 2021, 292, 120354. https://doi.org/10.1016/j.fuel.2021.120354.

[42] R. Melouki, A. Ouadah, P.L. Llewellyn, The CO2 adsorption behavior study on activated carbon synthesized from olive waste, J. CO2 Util. 2020, 42, 101292. https://doi.org/10.1016/j.jcou.2020.101292.

[43] H.J. Kang, G.A.K.M. Rafiqul Bari, T.G. Lee, T.T. Khan, J.W. Park, H.J. Hwang, S.Y. Cho, Y.S. Jun, Microporous carbon nanoparticles for lithium-sulfur batteries, Nanomaterials 2020, 10, 2012. https://doi.org/10.3390/nano10102012.

[44] F. Wang, Y. Han, X. Feng, R. Xu, A. Li, T. Wang, M. Deng, C. Tong, J. Li, Z. Wei, Mesoporous carbon-based materials for enhancing the performance of lithium-sulfur batteries, Int. J. Mol. Sci. 2023, 24, 7291. https://doi.org/10.3390/ijms24087291.

[45] J. Li, L. Gao, F. Pan, C. Gong, L. Sun, H. Gao, J. Zhang, Y. Zhao, G. Wang, H. Liu, Engineering strategies for suppressing the shuttle effect in lithium–sulfur batteries, Nano-Micro Lett. 2024, 16, 12. https://doi.org/10.1007/s40820-023-01223-1.

[46] Y. Huang, L. Lin, C. Zhang, L. Liu, Y. Li, Z. Qiao, J. Lin, Q. Wei, L. Wang, Q. Xie, D.L. Peng, Recent advances and strategies toward polysulfides shuttle inhibition for high-performance Li–S batteries, Adv. Sci. 2022, 9, 2106004. https://doi.org/10.1002/advs.202106004.

[47] L. Zhou, D.L. Danilov, R.A. Eichel, P.H.L. Notten, Host materials anchoring polysulfides in Li–S batteries reviewed, Adv. Energy Mater. 2021, 11, 2001304. https://doi.org/10.1002/aenm.202001304.

[48] X. Xu, J. Xie, W. Ju, X. Xu, H. Duan, Y. Pan, Y. Zou, Z. Ma, W. Lei, Incomplete TiO2 coating assisted hosts to achieve multifunctional S-cathodes for lithium-sulfur battery, Electrochim. Acta 2023, 450, 142211. https://doi.org/10.1016/j.electacta.2023.142211.

[49] M. Zhang, S. Geng, G. Yan, J. Dong, H. Ji, Y. Feng, X. Hu, B. Liu, X. Zhang, Nucleophilic ring-opening of thiocyclic carbonates: A scheme to prepare sulfhydryl-rich binders for high-performance lithium-sulfur batteries, J. Colloid Interface Sci. 2023, 633, 1–10. https://doi.org/10.1016/j.jcis.2022.11.046.

[50] Y. Zhao, S. Geng, G. Yan, X. Qu, H. Ji, Y. Feng, X. Zhang, Design and synthesis of multi-functional polymeric binders for high-performance lithium-sulfur batteries based on ring opening polymerization of thiolactone, Chinese J. Chem. 2023, 41, 2619–2627. https://doi.org/10.1002/cjoc.202300159.

[51] Z. Li, Z. Wu, M. Bi, H. Yu, C. Ma, J. Xiang, S. Yao, A simple approach to fabricate self-supporting graphene oxide/carbon nanotubes hybrid membrane as efficient polysulfides trapping in lithium/sulfur batteries, J. Mater. Sci. Mater. Electron. 2022, 33, 12871–12883. https://doi.org/10.1007/s10854-022-08231-8.

[52] B.J. Lee, T.H. Kang, H.Y. Lee, J.S. Samdani, Y. Jung, C. Zhang, Z. Yu, G.L. Xu, L. Cheng, S. Byun, Y.M. Lee, K. Amine, J.S. Yu, Revisiting the Role of Conductivity and Polarity of Host Materials for Long-Life Lithium–Sulfur Battery, Adv. Energy Mater. 2020, 10, 1903934. https://doi.org/10.1002/aenm.201903934.

[53] S. Ruan, Z. Huang, W. Cai, C. Ma, X. Liu, J. Wang, W. Qiao, L. Ling, Enabling rapid polysulfide conversion kinetics by using functionalized carbon nanosheets as metal-free electrocatalysts in durable lithium-sulfur batteries, Chem. Eng. J. 2020, 385, 123840. https://doi.org/10.1016/j.cej.2019.123840.

[54] L. Zhou, H. Li, X. Wu, Y. Zhang, D.L. Danilov, R.A. Eichel, P.H.L. Notten, Double-Shelled Co3O4/C nanocages enabling polysulfides adsorption for high-performance lithium-sulfur batteries, ACS Appl. Energy Mater. 2019, 2, 8153–8162. https://doi.org/10.1021/acsaem.9b01621.

[55] J. Laverde, N.C. Rosero-Navarro, A. Miura, R. Buitrago-Sierra, K. Tadanaga, D. López, Impact of sulfur infiltration time and its content in an N-doped mesoporous carbon for application in Li-S batteries, Batteries 2022, 8, 58. https://doi.org/10.3390/batteries8060058.

[56] M. Xue, C. Chen, Y. Tan, Z. Ren, B. Li, C. Zhang, Mangosteen peel-derived porous carbon: synthesis and its application in the sulfur cathode for lithium sulfur battery, J. Mater. Sci. 2018, 53, 11062–11077. https://doi.org/10.1007/s10853-018-2370-9.

[57] E. Umeshbabu, B. Zheng, J. Zhu, H. Wang, Y. Li, Y. Yang, Stable Cycling lithium-sulfur solid batteries with enhanced Li/Li10GeP2S12 solid electrolyte interface stability, ACS Appl. Mater. Interfaces 2019, 11, 18436–18447. https://doi.org/10.1021/acsami.9b03726.

[58] K. Sun, C.A. Cama, J. Huang, Q. Zhang, S. Hwang, D. Su, A.C. Marschilok, K.J. Takeuchi, E.S. Takeuchi, H. Gan, Effect of carbon and binder on high sulfur loading electrode for Li-S battery technology, Electrochim. Acta 2017, 235, 399–408. https://doi.org/10.1016/j.electacta.2017.03.023.

[59] K. Rollag, D. Juarez-Robles, Z. Du, D.L. Wood, P.P. Mukherjee, Drying temperature and capillarity-driven crack formation in aqueous processing of Li-ion battery electrodes, ACS Appl. Energy Mater. 2019, 2, 4464–4476. https://doi.org/10.1021/acsaem.9b00704.

[60] W.B. Hawley, H.M. Meyer, J. Li, Enabling aqueous processing for LiNi0.80Co0.15Al0.05O2 (NCA)-based lithium-ion battery cathodes using polyacrylic acid, Electrochim. Acta 2021, 380, 138203. https://doi.org/10.1016/j.electacta.2021.138203.

[61] Y. Ye, M.K. Song, Y. Xu, K. Nie, Y. sheng Liu, J. Feng, X. Sun, E.J. Cairns, Y. Zhang, J. Guo, Lithium nitrate: A double-edged sword in the rechargeable lithium-sulfur cell, Energy Storage Mater. 2019, 16, 498–504. https://doi.org/10.1016/j.ensm.2018.09.022.

[62] D.W. Kang, J. Moon, H.Y. Choi, H.C. Shin, B.G. Kim, Stable cycling and uniform lithium deposition in anode-free lithium-metal batteries enabled by a high-concentration dual-salt electrolyte with high LiNO3 content, J. Power Sources 2021, 490, 229504. https://doi.org/10.1016/j.jpowsour.2021.229504.

Chapter III

Bringing ResFArGO Graphene-Based Activated Carbon toward Practical Lithium-Sulfur Application

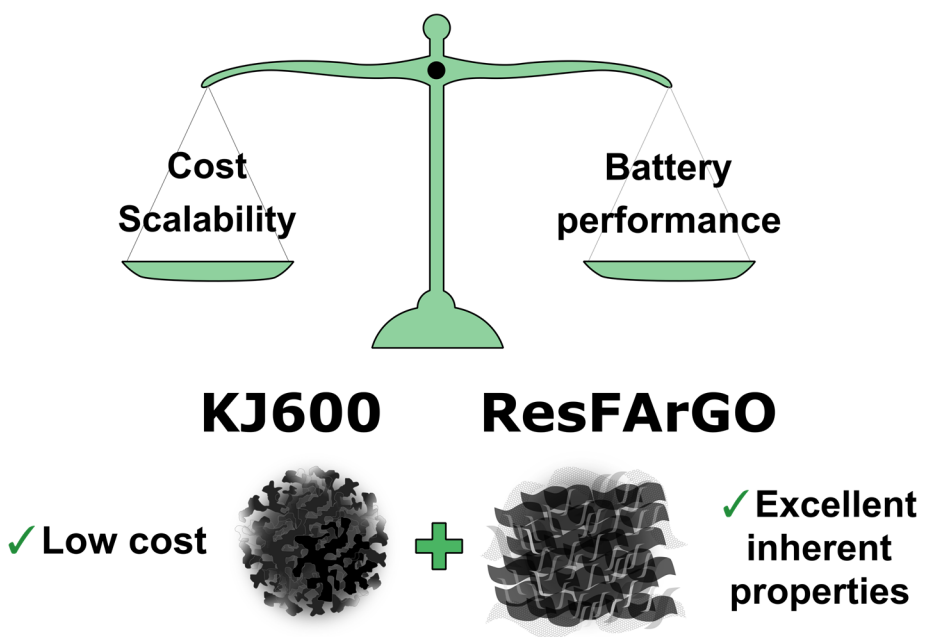

3.1. Introduction

In the preceding chapter, significant progress was made in overcoming most of the inherent challenges associated with the Li-S battery technology, including poor sulfur utilization and the shuttle effect. These improvements were directly attributed to the incorporation of well-suited graphene-based activated carbon as sulfur host, particularly by ResFArGO composite carbonaceous material. The exceptional textural properties, suitable LiPS compatibility, and remarkable cell performance exhibited by this material position it as a promising alternative for developing high-performing sulfur cathodes.

However, the development of practical LSBs is more than just about maximizing their performance. While guaranteeing its exceptional energy density is crucial, achieving cost-effectiveness is equally pivotal to positioning Li-S technology competitively against conventional Li-ion battery technologies [1–4]. Conventional LIBs, which rely on expensive metals as active materials like cobalt or nickel, result in average costs of around $100 per kilowatt-hour (KWh) [5,6]. In contrast, the use of sulfur as active material significantly contributes to the cost-effectiveness of LSBs due to its abundance and low cost, priced at approximately 0.05 $ kg^{-1} [7–9]. Consequently, researchers envision that optimized LSBs have the potential to achieve highly competitive costs, potentially falling below $50 per kWh [10–13]. In this sense, achieving these cost targets entails implementing economic cell optimization strategies, including selecting cost-effective sulfur host materials [14,15].

In the realm of Li-S technology, it is common to encounter studies detailing the development of advanced sulfur cathodes that exhibit exceptional battery performance at the laboratory scale [16,17]. However, these advancements frequently involve high costs and complex synthetic processes, posing challenges in their scalability for industrial applications [18–21]. This discrepancy between lab-scale and industrial performances underscores the need to develop solutions that not only address the technological challenges but also promote the applicability and cost-effectiveness of the LSBs.

The ResFArGO material presents promising properties as a potential sulfur host. However, its current synthesis process requires optimization to facilitate large-scale production. The primary challenge lies in the chemical activation step, where the textural properties of the carbon material are adjusted. This process, conducted under

the employed operating conditions, results in high energy consumption, leads to impurity formation, and generates waste streams, requiring extensive purification steps [1,22,23]. To address this bottleneck, a potential approach could involve the replacement of chemical activation with physical activation methods using agents like steam or carbon dioxide [24–26]. This modification enables streamlining of the production process, reduces associated costs, and facilitates the transition to industrial-scale manufacturing. However, the investigation of this process modification is beyond the scope of the current doctoral thesis but holds promise for future research work.

Motivated by this consideration, this chapter primarily focuses on addressing the cost challenges associated with the ResFArGO material without modifying its production process. To this end, a straightforward, scalable, and cost-effective strategy is proposed, involving the improvement of low-cost commercial carbon material-based sulfur cathode through the incorporation of tailored carbonaceous materials, such as ResFArGO, as additives. To comprehensively assess the effectiveness of this strategy, it will be compared not only to the reference KJ600 carbon material but also with an alternative additive approach composed of a mixture of various carbonaceous materials commonly documented in the literature, referred to as commercial additives (CAs). Initially, a thorough physicochemical characterization of the different sulfur electrodes prepared will be conducted to evaluate their textural properties and chemical surface characteristics. Subsequently, a comprehensive evaluation of the sulfur redox kinetics of these sulfur cathodes will be deeply studied. Finally, the potential applicability of the proposed strategy will be assessed by testing the studied sulfur cathodes in power and energy Li-S cells.

3.2. Bringing ResFArGO-based sulfur cathodes closer to practical application

3.2.1. Physicochemical characterization of carbonaceous mixtures

The commercial KJ600 carbon material presented in the previous chapter was selected as the main carbon component due to its low cost and high specific surface area, which are necessary attributes to accommodate large amounts of sulfur-active material. Two different types of carbon additives were incorporated at an initial amount of 10 wt.% of the total electrode composition. To prepare the first carbon mixture, referred to as KJ600 + ResFArGO$_{10}$, the KJ600 was gently mixed with the synthesized ResFArGO material, which was obtained following the previously

described synthesis process outlined in **Chapter II**. For the second carbon mixture, referred to as KJ600 + CAs, the additive consisted of a combination of commercially available carbonaceous materials, namely carbon black (C-65), multiwalled carbon nanotubes (MWCNTs), and graphene nanoplatelets (GNPs). These carbon materials were selected due to their high electronic conductivity and their ability to enhance the performance of the sulfur electrode, as widely reported in the literature.

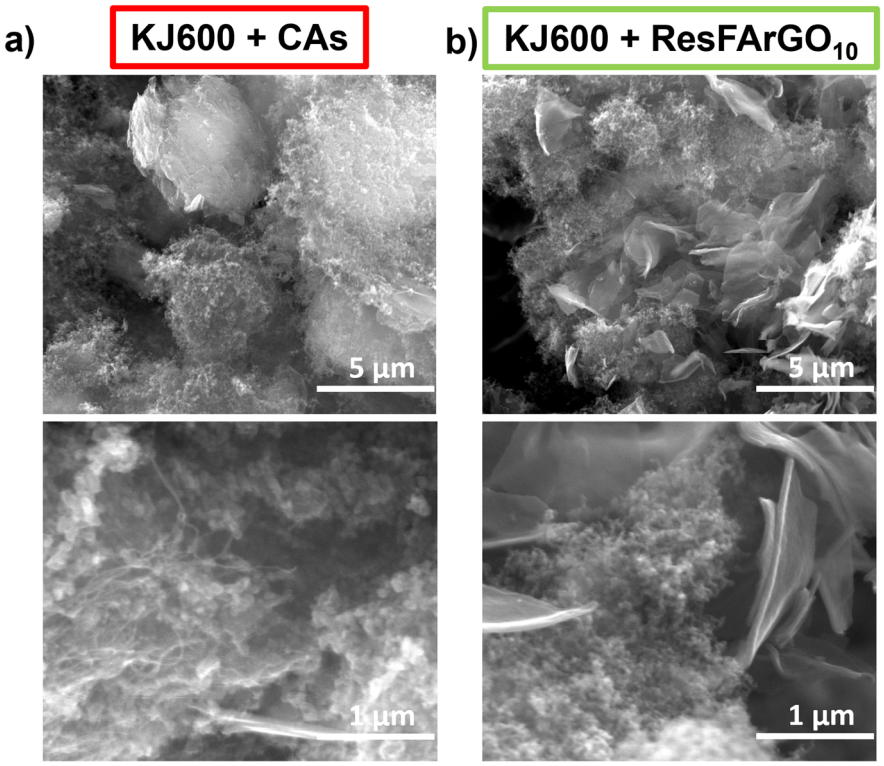

Figure 3.1. SEM images of the different carbon mixtures **a)** KJ600 + CAs and **b)** KJ600 + $ResFArGO_{10}$ under low (× 15000) and high (× 60000) magnifications.

The compatibility and mixability of the proposed additives with KJ600 were the first key parameters addressed in this study. To this end, the carbon mixtures were characterized using scanning electron microscopy, as shown in **Figure 3.1**. Both carbon mixtures exhibited a homogeneous distribution of all the components, indicating good compatibility and high affinity between the proposed materials. In the case of KJ600 + CAs (**Figure 3.1a**), the SEM images disclose two significant details to be highlighted. Firstly, the GNPs present a well-integrated structure within the carbon matrix, conferring their high electronic conductivities to the composite. Secondly, the

MWCNTs acted as interconnectors, establishing enhanced electronic pathways between the different particles. In the SEM images of the ResFArGO-based mixture (**Figure 3.1b**), a uniformly dispersed, flat-shaped structure of the ResFArGO material is observed, demonstrating effective coating and integration with KJ600 particle agglomerates. The resulting structure is not only anticipated to enhance the electronic conductivity of the composite but also ensure smooth lithium-ion diffusion along the surface of the carbonaceous composite.

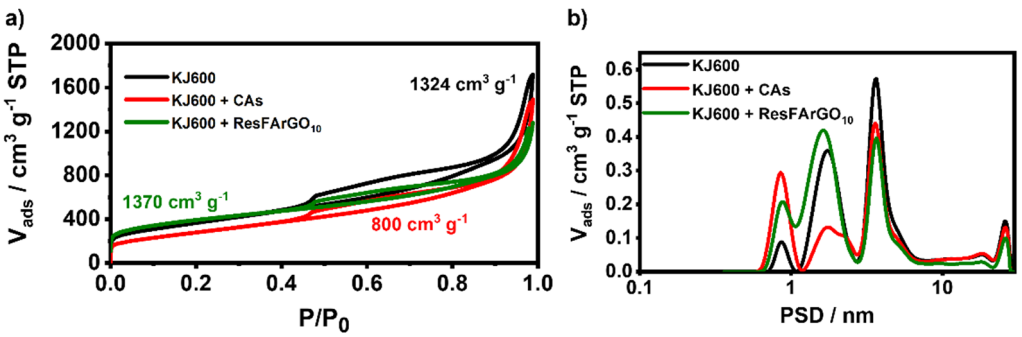

Figure 3.2. a) N_2 adsorption/desorption isotherms, **b)** Pore size distribution (PSD) of the studied carbon mixtures, K600, KJ600 + CAs, and KJ600 + ResFArGO$_{10}$.

Moreover, an in-depth study of the textural properties of the as-prepared carbon mixtures was performed through N_2 adsorption/desorption isotherm measurements at −196 °C. As presented in **Figure 3.2a**, all the carbonaceous mixtures exhibit a type IV isotherm, indicating a mesoporous nature according to the IUPAC classification [27,28]. This nature can be attributed to the inherent mesoporous structure of KJ600 material predominant in all the blends. Additionally, the obtained specific surface areas for the KJ600, CAs mixture, and ResFArGO mixture were calculated to be 1324, 800, and 1370 $m^2 g^{-1}$, respectively. The decrease in the specific surface area observed in the CAs blend compared to pristine KJ600 is attributed to the incorporation of non-porous materials (GNPs, C-65, and MWCNTs) in its composition. On the other hand, the ResFArGO mixture displays a slight increase in the specific surface compared to using KJ600 as the main carbon, ascribed to the incorporation of the highly porous ResFArGO material, as shown in the previous chapter. Furthermore, the pore size distribution shown in **Figure 3.2b** exhibits a heterogeneous distribution of pores ranging from 0.6 to 20 nm for all the carbonaceous materials, mainly influenced by the porosity characteristics of KJ600. However, in the case of the ResFArGO-containing blend, a larger portion of micropores is observed, primarily

derived from the higher microporosity provided by the graphene-based material, as evidenced in **Chapter II**.

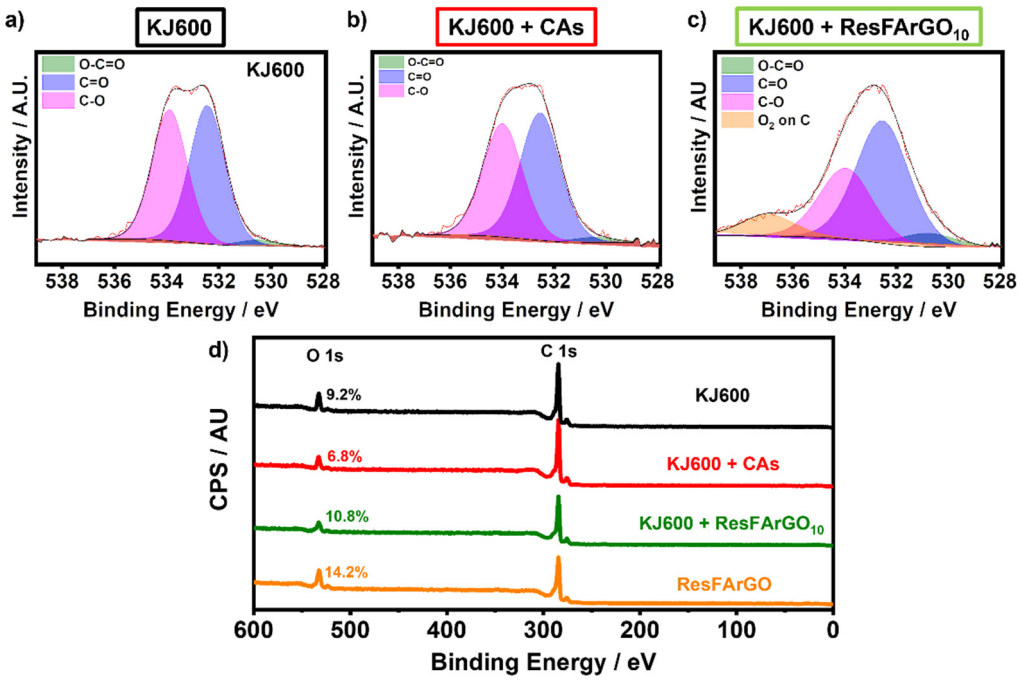

Figure 3.3. O 1s regions corresponding to XPS spectra of the studied carbon mixtures**, a)** KJ600, **b)** KJ600 + CAs, and **c)** KJ600 + ResFArGO$_{10}$. **d)** Full survey scan of XPS spectra of the different carbons and carbonaceous mixtures.

As previously highlighted, achieving optimal LSB performance requires special consideration of both the textural properties and surface chemistry of the carbon sulfur host. Therefore, an in-depth characterization of the surface chemistry of the carbon mixtures was conducted using XPS. **Figures 3.3a-c** present the O 1s spectra of KJ600, KJ600 + CAs, and KJ600 + ResFArGO, respectively. In **Chapter II** (**Figure 2.3**), significant differences in surface chemistry emerged when comparing the reference KJ600 with the graphene-based ACs, attributed to the presence of remaining functional groups originating from GO. In this case, the blend incorporating ResFArGO as additive exhibits a similar surface chemistry trend, characterized by the presence of oxygen-based polar functional groups. This observation aligns with the surface chemistry observed when ResFArGO is employed as the sole carbonaceous material. The resulting polar functional groups are assigned to carboxylic acids or ester compounds, as disclosed in **Chapter II**. Conversely, the blend based on CAs displays

similar characteristics to those obtained with KJ600 as the only carbonaceous material. This consistent trend is further reflected in the oxygen content, as illustrated in **Figure 3.3d**, where it becomes apparent that the presence of ResFArGO increases the oxygen content in the mixture compared to KJ600. In summary, the comprehensive characterization of the inherent physicochemical properties of the mixtures reveals that even in small quantities, the incorporation of ResFArGO confers advantageous properties to the final mixture. These advantages include an increase in the total specific surface area, enhanced microporosity, and a higher amount of oxygen and polar compounds on the mixture's surface, which are crucial to mitigating the shuttle effect.

Efficient trapping of LiPS during the Li-S cell operation is a key attribute for an ideal carbon sulfur host, which decisively impacts the final performance of the cell [29–31]. Hence, an investigation was carried out to determine if the different carbon blends formulated in this chapter demonstrated this crucial characteristic. For this evaluation, the polysulfide retention test, based on the visual determination of coloration change associated with Li_2S_6, was executed, as illustrated in **Figure 3.4a.** The figure reveals notable differences in the LiPS trapping ability among the investigated carbon mixtures. The ResFArGO-based mixture stands out with a significant reduction in dissolution coloration, underscoring its effectiveness in LiPS trapping even when incorporated as an additive. The other samples, albeit to a lesser extent, present a slight reduction in the coloration, suggesting that the commercial KJ600 possesses the ability to trap a certain amount of LiPS.

To quantitatively corroborate these visual observations, ultraviolet−visual spectroscopy (UV−vis) tests were carried out (**Figure 3.4b**). The UV-vis spectra provide further evidence that the incorporation of ResFArGO increases the polysulfide retention capacity, owing to its higher specific surface area and a heightened presence of polar oxygenated groups [29,32,33]. In contrast, the CAs-based mixture presents lower LiPS retention compared to the reference KJ600 material. This reduction in LiPS trapping capacity can be attributed to the decrease in the total specific surface area of the mixture due to the introduction of non-porous carbons as additives, and the non-polar surface of carbon blends.

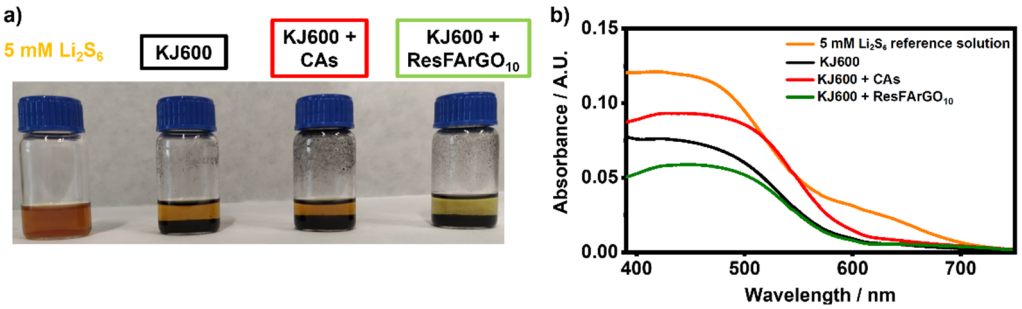

Figure 3.4. a) Li_2S_6 adsorption visual test of the analyzed carbon mixtures and their corresponding **b)** UV−vis spectra of the remaining Li_2S_6 solutions after the adsorption test.

Therefore, these findings, exemplified by the KJ600 + ResFArGO mixture, once again highlight the importance of the optimal physicochemical properties of the carbonaceous materials for being used in Li-S technology. These optimized properties directly lead to improved compatibility and retention of LiPS, a key feature for an optimal LSB operation by being able to reduce the shuttle effect.

3.2.2. Physicochemical characterization of additive-based sulfur electrodes

Once the individual properties of the carbonaceous mixtures were thoroughly analyzed and understood, the corresponding sulfur cathodes were prepared following the same procedure described in **Chapter II**. However, for the CAs-based sulfur cathode preparation, the melt diffusion process was executed solely with the KJ600, after which the carbon additives were mixed and incorporated by a dry mixing process. This modification was adopted to ensure efficient sulfur infiltration, due to the non-porous structure of the carbon materials constituting the CAs. To evaluate the impact of the studied additives on the LSB performance, both power cells (2.5-3 mg_S cm^{-2}) and energy cells (4 mg_S cm^{-2}) were developed.

Given the challenges associated with achieving high sulfur loading cathodes that maintain good structural integrity, the packing properties of the three different carbon composite cathodes with a loading of 4 mg_S cm^{-2} were evaluated using the SEM, as shown in **Figure 3.5**. Notably, even at low magnifications (**Figure 3.5a**), large cracks were observed in the reference KJ600-based cathode. This phenomenon, as previously discussed in **Chapter II**, results from shrinkage that occurred during the drying process of the electrode, attributed to the substantial amount of solvent retention by the KJ600 carbon material during the electrode slurry preparation and the difficulty of packing the agglomerated particles characteristic of this carbonaceous

material (observed in **Figure 2.1**). In contrast, the CAs-based sulfur electrode exhibited a significant reduction in electrode cracks, likely due to the lower amount of KJ600 in the formulation and the consequent decrease in the specific surface area after the incorporation of the non-porous conductive additives. Furthermore, both GNPs and MWCNTs have the potential to act as bridging agents of the KJ600 particle agglomerates, enhancing the compaction and reducing electrode cracks. Remarkably, the electrode containing ResFArGO as additive presents significantly improved homogeneity, compaction, and adhesion to the current collector, despite its high sulfur loading (4 mg_S cm^{-2}). These favorable processability characteristics can be attributed to the amphophilic nature of ResFArGO, stemming from the presence of functional groups on its surface, as previously demonstrated in the XPS data. These functional groups enhance its dispersibility in water, thereby reducing agglomerate formation. Notably, even in smaller quantities, the presence of ResFArGO as an additive results in cathodes with similarly exceptional properties as when used as main carbon.

Under higher magnification (**Figure 3.5b** and **Figure A.3.1**), the KJ600 reference electrode displays highly agglomerated particles. In contrast, the CAs electrode (**Figure 3.5b** and **Figure A.3.2)**, albeit still exhibiting some agglomerates, demonstrates a well-packed and interconnected structure. In this sense, the observation made in the SEM images of the carbon mixture related to the distribution of the CAs mixture suggests that MWCNTs may act as electron conductive bridges between the agglomerates, establishing the desired electron pathway through the electrode. Additionally, in the case of graphene-based activated carbon cathodes, the uniform and 2D flat-shaped structures inherent to ResFArGO material closely interact with KJ600 particles, facilitating high electrical conductivity across the entire electrode, as evidenced in **Figure 3.5b** and **Figure A.3.3**. These SEM images effectively showcase the packing properties of the selected additives, with the ResFArGO-containing composition demonstrating packing properties similar to those observed in cathodes composed solely of ResFArGO, as observed in **Chapter II**. Finally, the energy dispersive spectrometry (EDS) of the elemental mapping of sulfur in all the prepared electrodes confirms the excellent distribution of the active material within the entire cathode, without the presence of any sulfur clusters (**Figure 3.5c**). This observation once again highlights the effectiveness of the melt diffusion sulfur infiltration technique in achieving a homogeneous active material distribution within the cathode structure.

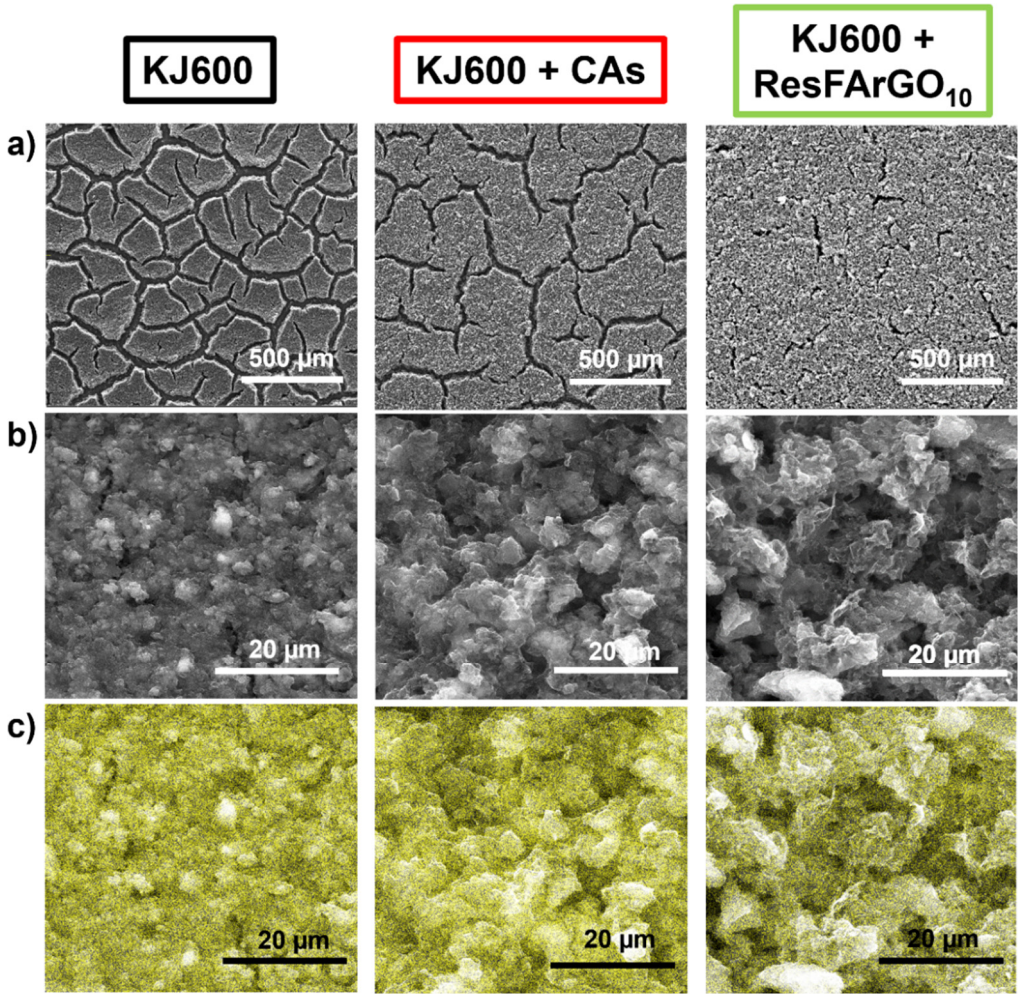

Figure 3.5. SEM images of the studied high sulfur loading cathodes under **a)** low and **b)** high magnifications, and **c)** EDS sulfur mapping.

3.2.3. Redox kinetics and electrochemical behavior of the additive-based cathodes

In contrast to conventional LIBs based on intercalation and deintercalation processes, the performance of the Li-S technology is governed by multiple redox reactions that take place during battery operation. Therefore, the analysis of the electrochemical behavior of the proposed sulfur cathodes is fundamental for gaining insights into their overall LSB performance.

Consequently, a comprehensive range of electroanalytical measurements was conducted to thoroughly evaluate the effect of incorporating the proposed carbonaceous additives on the electrochemical performance of the sulfur cathodes. Initially, to assess the influence of the additives on the redox kinetics, cyclic voltammetry (CV) at a scan rate of 0.2 mV s^{-1} of the as-prepared sulfur cathodes was carried out. **Figure 3.6a** presents the sulfur reduction-oxidation reaction curves of the studied systems. In all cases, the typical two distinct cathodic peaks are envisaged. The first peak, observed around 2.5−2.3 V, corresponds to the reduction of solid S_8 to soluble long-chain LiPS (Li_2S_n; where $4 \leq n \leq 8$). The second peak, situated around 2.1−2.0 V, is attributed to the successive conversion to insoluble short-chain LiPS (Li_2S2/ Li_2S) [34,35]. Additionally, in the anodic region, both ResFArGO and CAs-containing cells displayed the typical two peaks associated with the multistage oxidation from insoluble short-chain LiPS to S_8, with the intermediate formation of the soluble species [36,37]. However, this characteristic anodic profile is not observed for the reference KJ600-based system. In this system, the anodic region is characterized by a more flattened and irregular profile with multiple small peaks and a broader range of voltage. This different profile shape can be attributed to the sluggish redox kinetics of the KJ600 reference cell.

Notably, the CV curves reveal the positive impact resulting from the incorporation of ResFArGO or CAs as additives in the sulfur cathode composition. The KJ600 cathode presents broader and less intense peaks. Conversely, both additives lead to sharper and more pronounced cathodic and anodic peaks, while simultaneously reducing polarization, the voltage difference between the main reduction and oxidation peaks, when compared to the reference KJ600 cathode. In particular, the ResFArGO-containing sulfur cathode stands out by exhibiting the sharpest peaks in both cathodic and anodic regions. This distinctive CV profile underscores a significant enhancement in reaction kinetics, attributable to the enhanced electronic conductivity and improved contact with the active material at the cathode, as a consequence of the inclusion of ResFArGO [38–40].

This finding aligns with the results obtained in the Tafel plots of the main reduction and oxidation peaks (**Figures 3.6b** and **c**, respectively), derived from the CV curves (**Figure 3.6a**). Both ResFArGO and CAs exhibit significantly lower Tafel slopes (34.6 and 30.35 mV dec^{-1} for ResFArGO, 39.7 and 34.1 mV dec^{-1} for CAs) compared to the reference cathode (57.8 and 55.7 mV dec^{-1}). These reduced slopes indicate

improved Li–S redox reaction kinetics, ascribed to the enhanced electronic conductive network provided by the additives [41,42]. Significantly, the ResFArGO-containing cathode presents superior electrocatalytic behavior, which can be linked to the combined effect of enhanced electronic conductivity and the LiPS anchoring capability introduced by this additive.

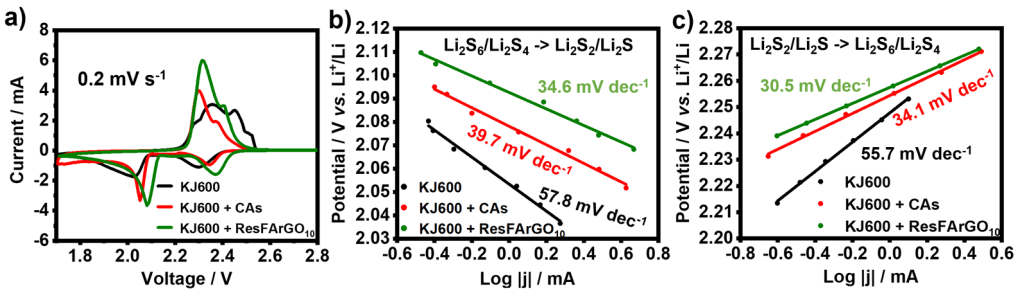

Figure 3.6. Sulfur redox kinetic study of the KJ600 reference, KJ600 + CAs, and KJ600+ ResFArGO$_{10}$ electrode-based cells: **a)** CV in a potential window from 1.7 to 2.8 V at a scan rate of 0.2 mV s^{-1}. Tafel plots for the **b)** cathodic and **c)** anodic conversion reactions, respectively.

Complementary to the Taffel plot, the Li^+ diffusivity is another important parameter for assessing redox kinetics within the sulfur cathode [43–45]. To evaluate this parameter, CV measurements were conducted at different scan rates, ranging from 0.1 to 0.4 mV s^{-1}. As displayed in **Figures 3.7a-c**, the CV curves present the three characteristic peaks associated with the sulfur redox reactions occurring during the LSB cycling, featuring two reduction peaks (labeled as peaks I and II) and a main oxidation peak (denoted as peak III). Notably, as the scan rate increases, there is a corresponding rise in the intensity of these redox peaks, coupled with a shift in the voltage at which these peaks occur. The fitting of each peak of the CV curves, displayed in **Figures 3.7d-f**, unveils a clear linear correlation with the square root of the scanning rates for all the electrodes, suggesting that the system is governed by a diffusion process [46,47]. According to the classical Randles-Sevcik equation, the Li^+ diffusivity is directly associated with the slope of the curves represented in **Figures 3.7d-f**. Notably, the additive-containing cathodes present steeper slopes compared to the reference KJ600 cathode, indicating an enhanced lithium-ion diffusion [48,49]. Among these cathodes, the ResFArGO-based cathode once again demonstrates the most substantial improvements, underscoring its potential for improving the reaction kinetics even in small quantities.

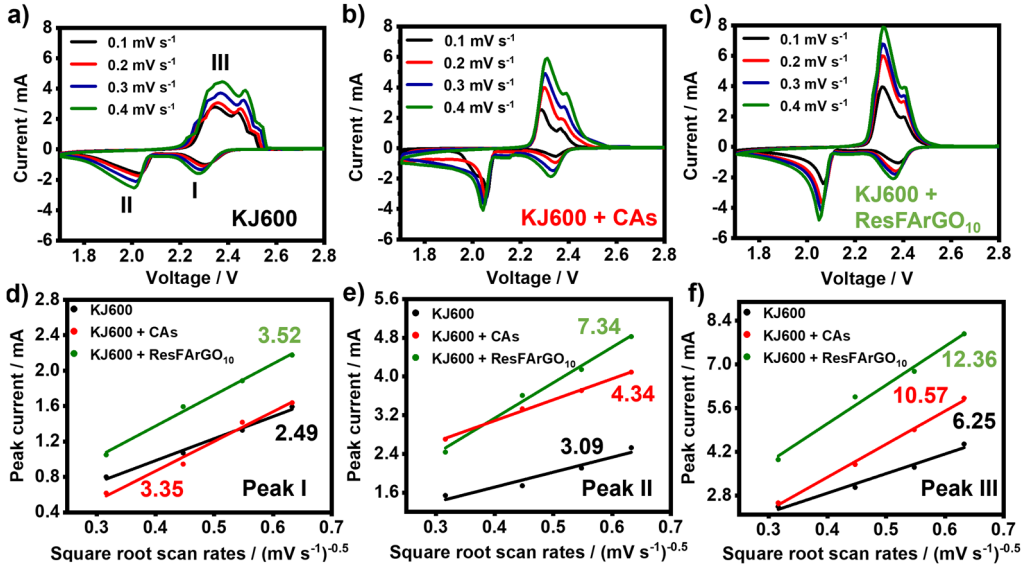

Figure 3.7. Li^+ diffusion coefficient analysis of the studied carbon mixtures: **a-c)** CV curves at different scan rates from 0.1 to 0.4 mV s^{-1}. **d–f)** Li^+ diffusion behavior analysis.

The deposition and nucleation processes of the Li_2S compound from Li_2S_4 play a crucial role during LSB operation, contributing up to 75% of its theoretical capacity [50]. To gain deeper insights into the catalytic activities provided by the different carbon mixtures, a detailed study into the nucleation and dissolution processes of Li_2S was conducted. The Li_2S precipitation plot, as illustrated in **Figures 3.8a–c**, reveals an initial monotonically decreasing current, which is correlated to the reduction process from the remaining higher-order LiPSs to Li_2S_4. Subsequently, a sharp and well-defined current peak is observed corresponding to the nucleation and growth of the solid Li_2S [51,52]. From these plots, two valuable conclusions can be drawn. Firstly, the ResFArGO-based system exhibits shaper current peaks, appearing in a shorter time than the other cathodes. This observation indicates a faster Li_2S nucleation process in the presence of the ResFArGO additive. Secondly, according to Faraday's law, the Li_2S nucleation capacity values of KJ600 (132 mAh g^{-1}), KJ600 + CAs (128 mAh g^{-1}), and KJ600 + $ResFArGO_{10}$ (142 mAh g^{-1}) cathodes were calculated, with the ResFArGO additive standing out by delivering the highest Li_2S nucleation capacity.

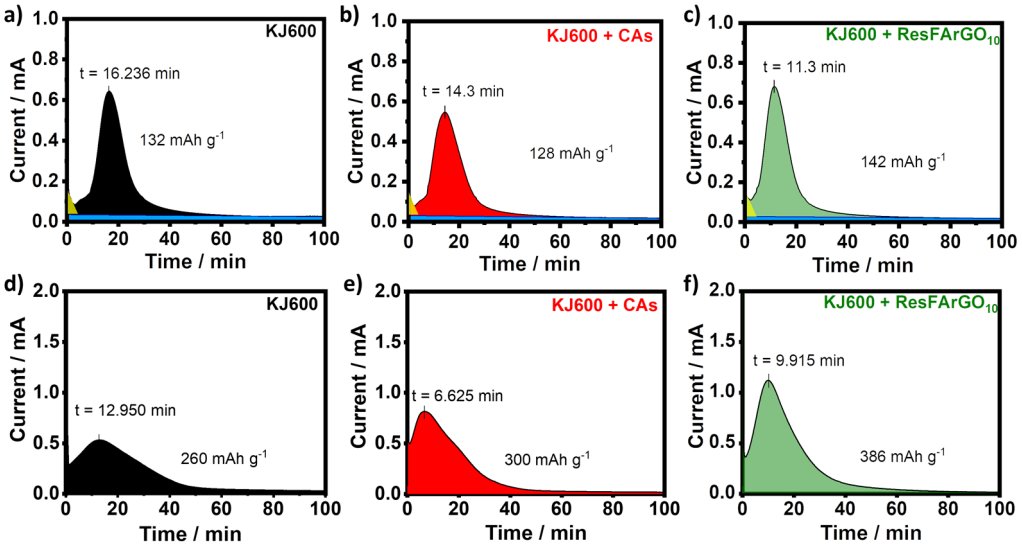

Figure 3.8. Potentiostatic charge curves of the Li_2S_8 solution to evaluate **a–c)** precipitation and **d–f)** dissolution kinetics of Li_2S for the three different carbon mixtures.

The Li_2S dissolution processes in the studied systems were performed by potentiostatic charging at 2.4 V (shown in **Figures 3.8d-f**). The Li_2S oxidation capacities of additive-based cathodes exhibited significantly higher values, appearing at earlier dissolution times compared to the reference cathode, validating the enhanced dissolution process of solid Li_2S [53,54]. Notably, despite the Li_2S dissolution peak of the KJ600 + CAs system appearing at shorter times compared to the ResFArGO-based cell, both samples present the onset of dissolution at the same point in time. However, the delay in achieving the peak aligns with the higher dissolution performance of the cathode incorporating KJ600 + $ResFArGO_{10}$ compared to KJ600 + CAs. This is evidenced by the respective capacities of 386 mAh g^{-1} and 300 mAh g^{-1}, as observed in **Figure 3.8e** and **f**.

In summary, the extensive electrochemical kinetic study conducted during this work, as depicted in **Figures 3.6, 3.7, and 3.8**, unequivocally demonstrates the advantages of incorporating conductive additives into the sulfur cathode formulation to enhance the kinetics of conversion reactions. Among the two developed strategies, the incorporation of ResFArGO in the sulfur cathode as additive stands out as it serves as a catalyst, significantly accelerating the conversion reactions and enhancing both the nucleation and dissolution processes of Li_2S. This favorable performance can be

solely attributed to the previously analyzed suitable physicochemical properties of the carbon mixture incorporating the ResFArGO material.

3.2.4. Li-S battery performance of additive-based sulfur cathodes

3.2.4.1. Rate capability of additive-based sulfur cathodes

The favorable theoretical properties demonstrated by the proposed approach must be validated in the cell performance to establish their significance. To this end, the effectiveness of the ResFArGO additive in sulfur cathodes was assessed in Li-S technology through power cells subjected to a C-rate test (**Figure 3.9a**). It is worth noting that, in Li-S literature, C-rate capability tests are often conducted employing low sulfur loadings, typically below 2 mg cm^{-2} (equivalent to theoretical capacities lower than 3.3 mAh cm^{-2}), to evaluate the response of the proposed strategy. However, these conditions are far from practical application scenarios and can lead to misleading expectations [55–58]. Therefore, to obtain meaningful and realistic conclusions, sulfur loading of 3 mg cm^{-2} (equivalent to a theoretical capacity of approximately 5 mAh cm^{-2}) has been employed in this study to conduct the C-rate characterization of the power cells closer to practical applications.

The electrochemical performance of the power cells confirms the kinetics results previously reported. Both additive-containing sulfur cathodes delivered higher specific and areal capacities across the entire range of C-rates compared to reference KJ600 cells (**Figure 3.9a**). Moreover, remarkable capacity retention was observed when increasing the cycling rate from C/10 to C/2 after additive incorporation, with ResFArGO exhibiting 80% capacity retention and CAs 75%. This reduced capacity difference between mild and high cycling rates (i.e., C/10 and C/2) further reinforced the enhanced reaction kinetics provided by the well-selected additives, with the ResFArGO proving particularly effective in this regard. Notably, even at the challenging rate of 1C, the cells demonstrated outstanding high capacities, delivering 800 and 740 mAh g^{-1} for ResFArGO and CAs, respectively. These values correspond to areal capacities close to 2 mAh cm^{-2}, four times higher compared to the reference cell.

Figure 3.9b displays the galvanostatic charge/discharge profiles of the different power cell configurations, showing the two characteristic discharge plateaus corresponding to the multi-step sulfur reaction mechanism. Remarkably, both additive formulations contribute to the reduction in cell overpotential (139 mV and

180 mV for ResFArGO and CAs additives, respectively) compared to the reference KJ600 cathode (310 mV), with ResFArGO exhibiting the lowest cell polarization. This enhanced behavior provided by ResFArGO material can be attributed to its effective LiPS trapping ability and enhanced catalytic properties, aligning well with the previous results obtained during the electroanalytical measurements.

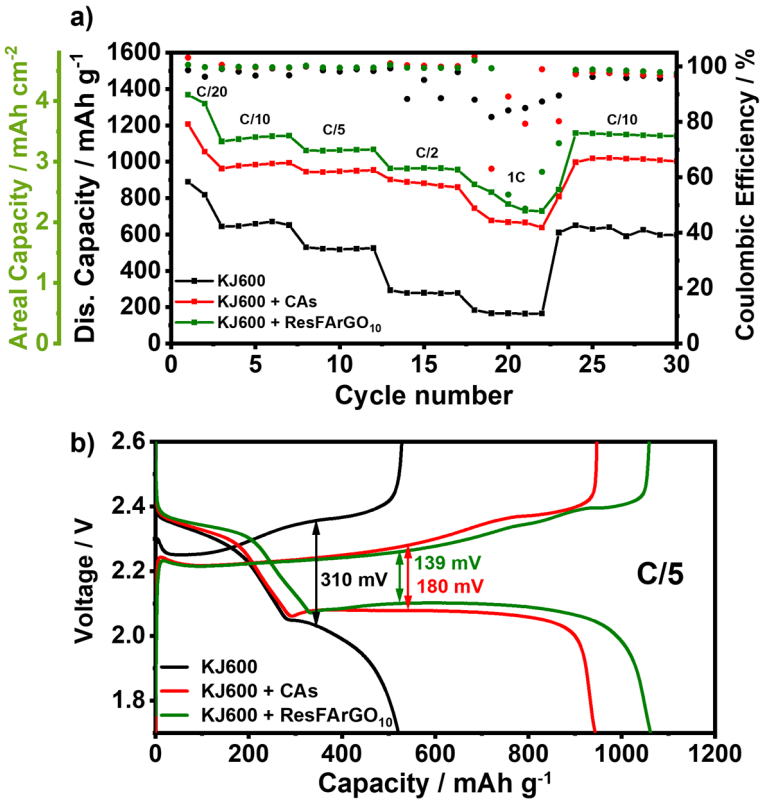

Figure 3.9. a) Rate capabilities of Li–S cells using KJ600 as the reference and CAs and ResFArGO additive-based cathode formulations. **b)** Galvanostatic discharge/charge profiles of the studied electrodes at C/5.

Nevertheless, despite achieving high capacity values at 1C, **Figure 3.9a** reveals that the CE obtained at this high C-rate presents irregular behavior. These irregular CE values can be attributed to instability issues on the lithium anode side, particularly during the charging process when Li deposition on the lithium metal anode occurs. It is important to highlight that, at a cycling rate of 1C, a current density of 5 mA cm^{-2} is applied to the cell with a sulfur loading of 3 mg_S cm^{-2}. Under these demanding and harsh cycling conditions, the lithium metal anode faces significant challenges in

maintaining stable cycling. To verify this hypothesis, a Li stripping and plating test was performed on Li/Li symmetric cells at different current densities. As shown in **Figure 3.10a**, the results confirm that while lithium deposition occurs uniformly at low current densities, when it exceeds 0.5 mA cm^{-2}, the deposition behavior starts to exhibit a non-uniform deposition profile. This behavior is associated with the development of inhomogeneous plating, which is exacerbated at 4 mA cm^{-2}.

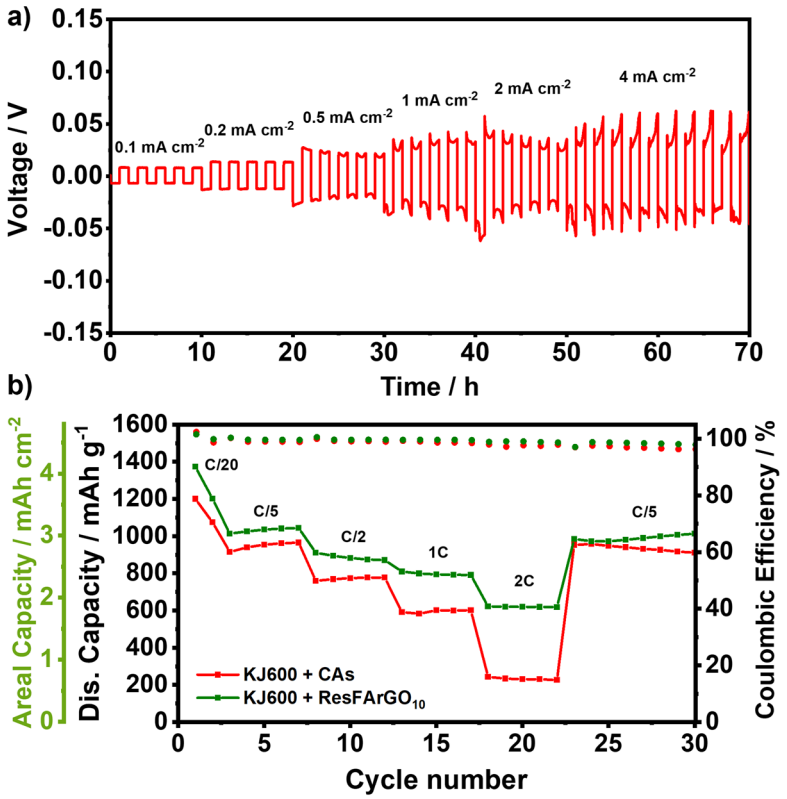

Figure 3.10. a) Galvanostatic cycling at different current densities of the employ. **b)** C-rate response of the three systems containing additives using a constant charge rate of C/2.

To address the cycling stability issues associated with high charge currents, an alternative C-rate cycling test was conducted maintaining a constant charge rate of C/2 (equivalent to a current density of 2.5 mA cm^{-2}), aiming to ensure a smoother Li deposition process. The results obtained with this approach, as displayed in **Figure 3.10b**, showed a significant improvement in the stability of the power cells, resulting in a high average CE of 99.2% and enabling battery operation at a high discharge rate of 2C. Under these conditions, a remarkable capacity of 620 mAh g^{-1}

(equivalent to 1.8 mAh cm^{-2}) was achieved with the ResFArGO-containing cathode. These results are in alignment with those obtained in the kinetic study, highlighting the favorable properties of ResFArGO as a promoter of the sulfur redox conversion reaction, even when used in small quantities. However, in the case of CAs, due to their lower catalytic properties (as demonstrated in **Figures 3.6, 3.7, and 3.8**), the performance improvement is insufficient to sustain cycling at 2C with competitive discharge capacities (200 mAh g^{-1} / 1 mAh cm^{-2}).

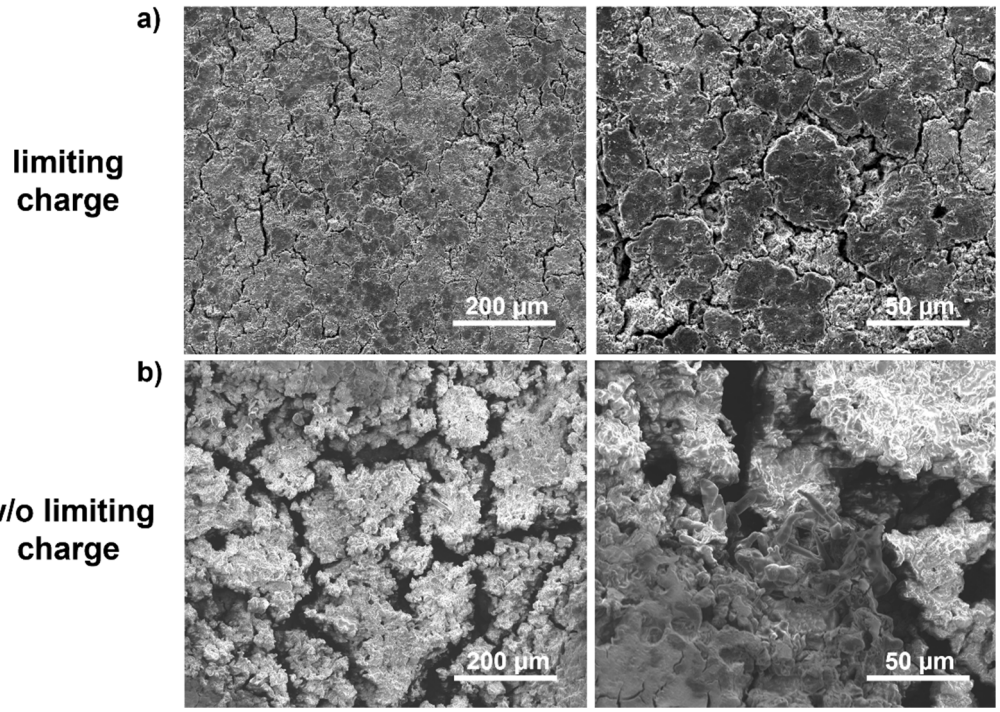

Figure 3.11. SEM images of the post-mortem analysis of the lithium anode after cycling by **a)** limiting the charge to C/2 and **b)** without limiting the charge at low and high magnifications.

To gain deeper insights into the stability issues identified during the C-rate tests at high charging currents and to confirm their connection with the lithium metal anode, a postmortem study was conducted. The anode surfaces were analyzed through SEM after completing the C-rate at 1C or C/2 charging. **Figure 3.11a** reveals that the lithium surface after charging at C/2 presents a flat and dense surface appearance without the presence of fibrillar structures, suggesting a more uniform and dense lithium deposition on the anode. In contrast, as depicted in **Figure 3.11b**, after charging at 1C, the anode surface appears more porous, with the proliferation

of whisker-like fibrillar structures. This finding proves the hypothesis that the irregular CE values observed during the C-rate are directly associated with the lithium metal anode. Therefore, to achieve the highly desired fast charging operation in this system under realistic conditions, future studies should prioritize stabilizing the lithium metal anode. This can be achieved either by electrolyte engineering to facilitate the formation of a suitable and protective solid electrolyte interface, by implementing ex-situ protection strategies, or by the combination of these approaches.

3.2.4.2. Long-term cycling of additive-based high sulfur loading cathodes

Once the feasibility of achieving high-power batteries through this development approach was determined, the long cycling test of the energy cells was tested. For this analysis, high sulfur loading cathodes were used to assemble the Li-S cells, and they were cycled at a constant rate of C/10 (as depicted in **Figure 3.12a**).

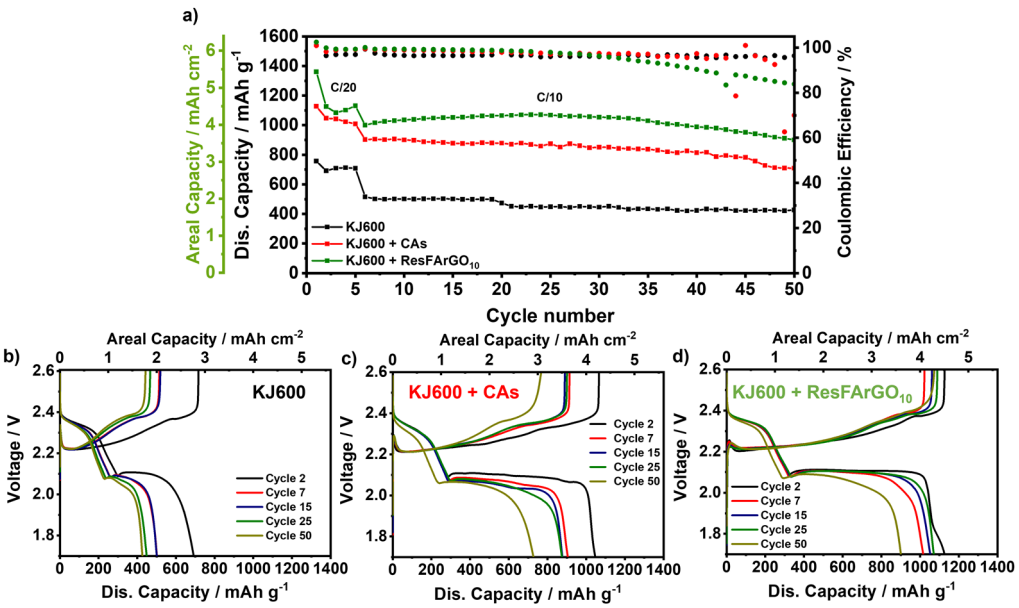

Figure 3.12. a) Battery performance of the three studied carbon mixtures and the reference KJ600 in the long cycling test, and **b-d)** the corresponding charge-discharge profiles corresponding to the studied carbon mixtures.

Consistent with previous results, the additive-containing cathodes exhibited significantly improved cell performance, particularly in terms of sulfur utilization, when compared to the reference KJ600-based cathode. Notably, the

incorporation of ResFArGO additive in the sulfur cathode enabled the achievement of superior utilization, resulting in high discharge capacities of 1070 mAh g^{-1} (corresponding to 4.3 mAh cm^{-2}). This achievement is of pivotal importance as it brings Li-S technology closer to reaching the areal capacity targets required to compete with conventional LIBs [57,59,60]. Conversely, although to a lesser extent than in the case of ResFArGO, the inclusion of CAs yielded a substantial and stable capacity of 850 mAh g^{-1} (around 3.6 mAh cm^{-2}). This capacity nearly doubles that of the reference cell relying solely on KJ600, which delivers a lower capacity of 480 mAh g^{-1} (around 1.9 mAh cm^{-2}).

These results confirm the conclusions drawn throughout this chapter of the thesis. The reference cathode lacks the essential porosity, electronic conductivity, and surface polarity required to activate sulfur active material and/or retain the LiPS close to the reaction places. As depicted in the charge and discharge profiles (**Figure 3.12b**), this deficiency leads to a short second conversion plateau that decreases with cycling. Additionally, the overvoltage in the reference system is notably high, which can be ascribed to the significant presence of LiPS in the electrolyte, as the carbon is unable to effectively trap them, thus reducing the electrolyte conductivity. On the other hand, in the case of the CAs system, benefiting from the improved electronic conductivity through the incorporation of additives into the slurry recipe results in an increased sulfur utilization. This, in turn, enhances the second discharge plateau as observed in **Figure 3.12c**. However, the limited presence of polar superficial groups, coupled with the lower specific surface area of the carbon mixture, leads to insufficient retention of LiPS on the cathode surface, as previously discussed. This behavior is evidenced in the voltage profiles, manifesting a progressive reduction of the second plateau and an increase in the overpotential of the system. Finally, the use of ResFArGO as carbon additive in the cathode results in a dual and positive impact on battery performance. It enhances the electronic conductivity within the sulfur cathode, leading to high discharge capacities that are directly linked with the extended second plateau. Additionally, it demonstrates the ability to effectively trap LiPS. Thanks to this dual effect, the overpotential of the system is lower compared to the rest of the systems and remains constant during cycling until the depletion of $LiNO_3$ (**Figure 3.12d)**

These results evidence the effectiveness and applicability of the proposed additive strategy for optimizing sulfur cathode composition to enhance the overall performance of the LSBs. Additionally, it emphasized the importance of careful

selection of additives for cathode integration. In this case, ResFArGO material has proven to be an effective and potential candidate for this strategy due to its combination of tailored particle morphology, favorable textural properties, and polar surface chemistry that synergistically enhance its ability LiPS trapping while offering improved electrocatalytic characteristics.

3.2.5. Increasing active material content for more practical LSBs

Inspired by the considerable potential demonstrated by the proposed strategy of incorporating ResFArGO as an additive, it was decided to go a step further in the exploitation of this approach. In the context of Li-ion batteries, active material contents exceeding 90 wt.% are commonly employed, primarily due to their non-insulating nature. This inherent feature not only simplifies the attainment of higher active material loadings but also facilitates achieving increased areal capacities. Nevertheless, the insulating properties of sulfur demand the incorporation of higher amounts of porous carbon materials to enhance the electronic conductivity within the positive electrode. Consequently, this leads to an increased cathode porosity, an unfavorable feature that strongly penalizes the volumetric energy density, becoming a notable Achilles' heel of Li-S technology [61,62]. Additionally, the presence of larger amounts of electrochemically inactive materials poses challenges in achieving high sulfur loading values, thereby impacting the gravimetric energy density.

Therefore, to make LSBs more industrially attractive, it is necessary to overcome this limitation [63,64]. In this context, a systematic approach that entails the increase in the amount of active material while reducing the content of carbonaceous materials was pursued, aiming to obtain higher sulfur loading cathodes with lower electrode porosity (reduced sulfur cathode thickness). However, while this strategy may initially appear rational and straightforward, it often results in unsuitable LSB performance due to the low active material utilization caused by the loss of electronic conductivity within the cathode. Motivated by this challenge and encouraged by the outstanding performance achieved by ResFArGO as an additive, the strategy of maximizing the sulfur content within the cathode was studied. For this purpose, sulfur cathodes with a high sulfur content of 70 wt.%, a reduced amount of 5 wt.% of ResFArGO, and a final amount of 20 wt.% of carbon materials were fabricated, using the same preparation process described earlier.

3.2.5.1. Mechanical integrity and structural properties of the high sulfur content cathode

Firstly, it is essential to highlight that the new cathode formulation, comprising 70 wt.% of sulfur, requires a lower wet thickness during the electrode slurry casting process to achieve the target high sulfur loading of 4 mg_S cm^{-2} compared to the previous composition. This observation indicates the increased compactness of the newly prepared cathode, aligning with one of the primary objectives of this strategy. Subsequently, a comprehensive analysis of the mechanical and structural properties of the new cathode was conducted.

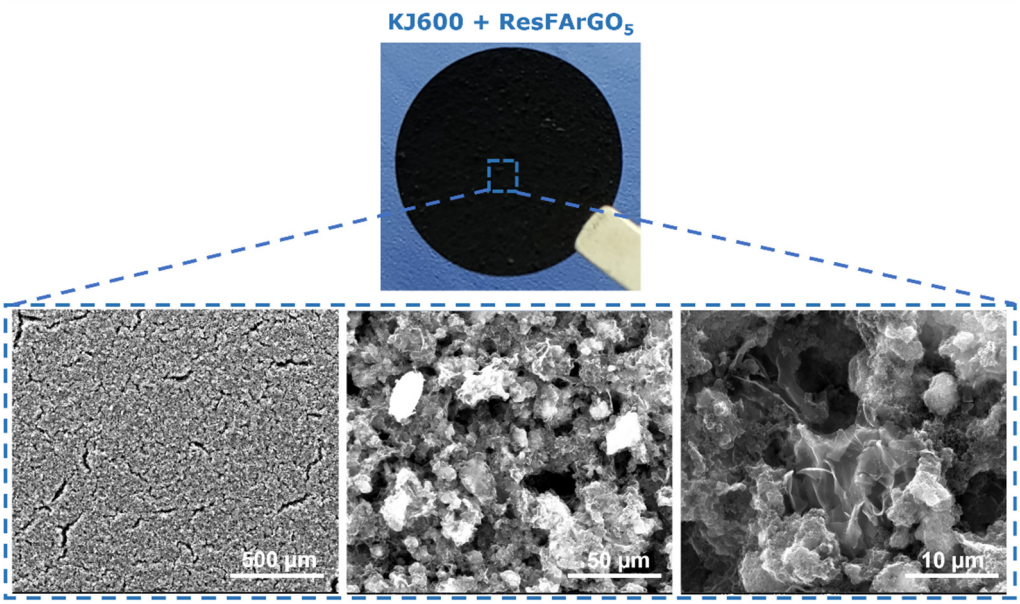

Figure 3.13. The mechanical integrity of the 5 wt.% ResFArGO-based high sulfur loading cathode by visual and SEM images.

The optical image of the sulfur cathode (**Figure 3.13**) demonstrates that despite the significantly low amount of ResFArGO material, its incorporation maintains the compactness and mechanical integrity of the cathode, without the presence of visual surface cracks. This observation is further confirmed by the SEM images at low magnifications (**Figure 3.13**), which reveal the excellent homogeneity prevailing on the cathode surface, with only minimal superficial cracks discernible. Moreover, higher magnification SEM images validate the good affinity between KJ600 and ResFArGO after the cathode preparation, a highly desirable behavior for boosting

the beneficial properties provided by both materials. Consequently, even present in very small quantities, ResFArGO plays a crucial role in achieving homogeneous and compact high sulfur loading cathodes with minimal crack formation in the electrode.

3.2.5.2. Li-S battery performance of the high sulfur content cathode

After confirming the structural integrity of the high sulfur content cathode, even with the incorporation of a minimal amount of ResFArGO, a comprehensive electrochemical performance analysis of the cells was conducted to evaluate the impact of this approach on cell behavior.

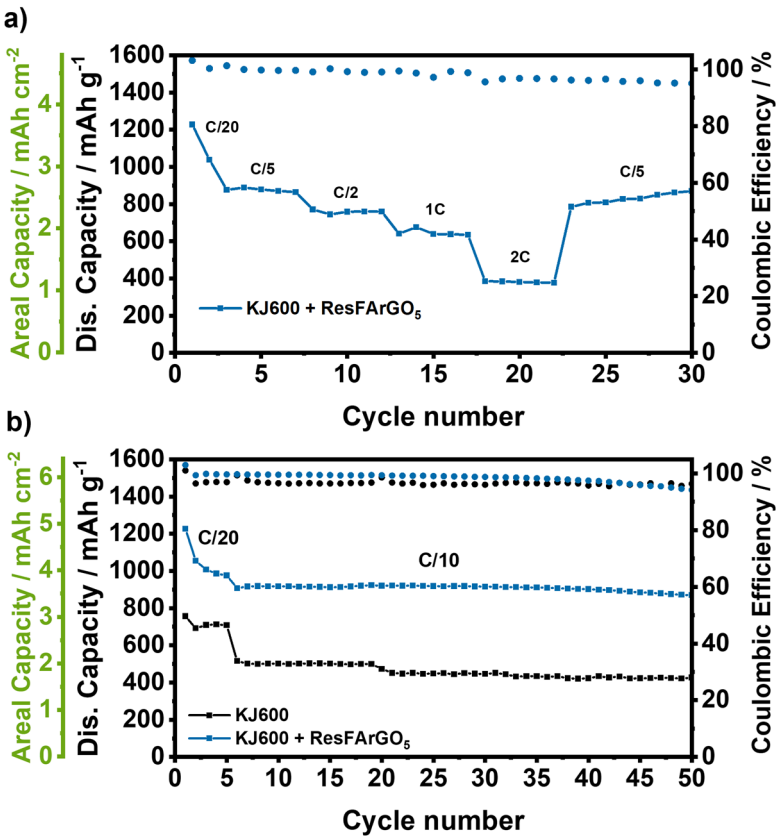

Figure 3.14. a) Rate capability test of the 5 wt.% ResFArGO containing power cell and **b)** long-term cyclability test of the energy cell compared to the reference KJ600 cell.

Firstly, the rate capability of the power cells was assessed through a galvanostatic cycling test at different cycling rates (**Figure 3.14a and Figure A.3.4a**). In

this case, the limitation of the charge rate to C/2 was directly employed for the C-rate test evaluation to ensure system stability at high C-rates. Outstandingly, the cell with high sulfur content and only 5 wt.% ResFArGO demonstrated remarkable performance, delivering discharge capacities comparable to those achieved by the CAs-based cathode but employing half the amount of additive and higher sulfur content. Notably, the cell with just 5 wt.% ResFArGO exhibited suitable electrochemical performance at different cycling rates, demonstrating a commendable capacity of 700 mAh g^{-1} (2.2 mAh cm^{-2}) at high 1C rates. As expected, the high sulfur content cell exhibits slightly lower performance compared to the 10 wt.% ResFArGO system. However, these differences become more pronounced at high discharge rates, particularly at 2C. This behavior can be attributed to the reduction in electronic conductivity and catalytic capacity due to the lower additive content and higher amount of the insulator active material. Nevertheless, the results obtained are highly promising, highlighting the potential of ResFArGO as an effective additive for enhancing the performance of the power cells even when employed in minimal quantities.

To further explore the proposed approach, the long-term cycling of the cathode was evaluated in energy cells under a cycling rate of C/10. As displayed in **Figure 3.14b** and **Figure A.3.4b**, the cell with 5 wt.% ResFArGO exhibited impressive performance, maintaining relatively high discharge capacity values of 900 mAh g^{-1} (equivalent to 3.6 mAh cm^{-2}) during the 50 analyzed cycles. While it may not deliver the same capacity levels as the cell with higher ResFArGO content, these results are highly encouraging and demonstrate the effectiveness of ResFArGO as a suitable material for the additive approach even in small quantities to meet the target values for commercialization under more practical conditions.

3.3. Summary and conclusions

The promising results achieved with the ResFArGO graphene-based material as the main carbon prompted a step further toward practical application. This chapter is centered on improving the reference cathode based on the low-cost KJ600 material to ensure economic feasibility and streamline the manufacturing process of the sulfur cathodes. To this end, two different carbonaceous materials selected for their unique properties have been integrated into the reference cathode composition. By including ResFArGO as an additive in a 10 wt.%, the carbon blend retained the inherent properties of ResFArGO, such as high specific surface area, enhanced microporosity,

and the presence of polar functional groups in the surface, which led to enhanced interaction and trapping ability of LiPS. Consequently, compared to the CAs-based approach, ResFArGO significantly improved both the electronic conductivity and catalytic activity within the sulfur cathode. As a result, the ResFArGO-containing cathode exhibited excellent power capability, delivering discharge capacities of 800 mAh g^{-1} and 620 mAh g^{-1} at high discharge rates of 1C and 2C, respectively. Furthermore, its performance in high sulfur loading cells was outstanding, delivering a remarkable discharge capacity of 1070 mAh g^{-1} (equivalent to 4.3 mAh cm^{-2}), demonstrating superior sulfur utilization compared to CAs. These results were comparable to those achieved previously with ResFArGO as the main carbon, further supporting the effectiveness of the proposed strategy. Encouraged by these exceptional results, the practical application of this approach was further optimized by tuning the composition of the sulfur cathode. The content of inactive materials was reduced by decreasing the ResFArGO content to only 5 wt.% and the total carbon content to 20 wt.% in the cathode formulation, aiming to maximize the active material content. Under these realistic and challenging working conditions, the sulfur cathode with the proposed new composition demonstrated favorable rate capability, even at high cycling rates, and exhibited excellent performance in high sulfur loading cells, meeting the targets set for LSBs to compete with Li-ion batteries. Therefore, the approach of incorporating ResFArGO as an additive proved to be a successful and effective strategy for developing high-performing and cost-effective sulfur cathodes. However, as corroborated in **Chapter II** and this chapter, the utilization of the conventional Li-S electrolyte based on DME/DOL falls short of guaranteeing long-term cycling. Therefore, addressing the challenge associated with electrolyte optimization emerges as a fundamental requirement for the practical feasibility and commercial viability of the LSBs based on the current cathode development.

3.4. Brief outlook and perspective

Chapter II and **Chapter III** have focused on optimizing the sulfur cathode to mitigate the inherent challenges associated with the Li-S technology. This purpose has been accomplished by a systematic evaluation of the carbonaceous material, either employed individually or as a mixture of different compounds, serving as a sulfur host within the cathode composition. **Figure 3.14** provides a schematic summary of the performances offered by each developed formulation, with the KJ600-based system serving as a reference:

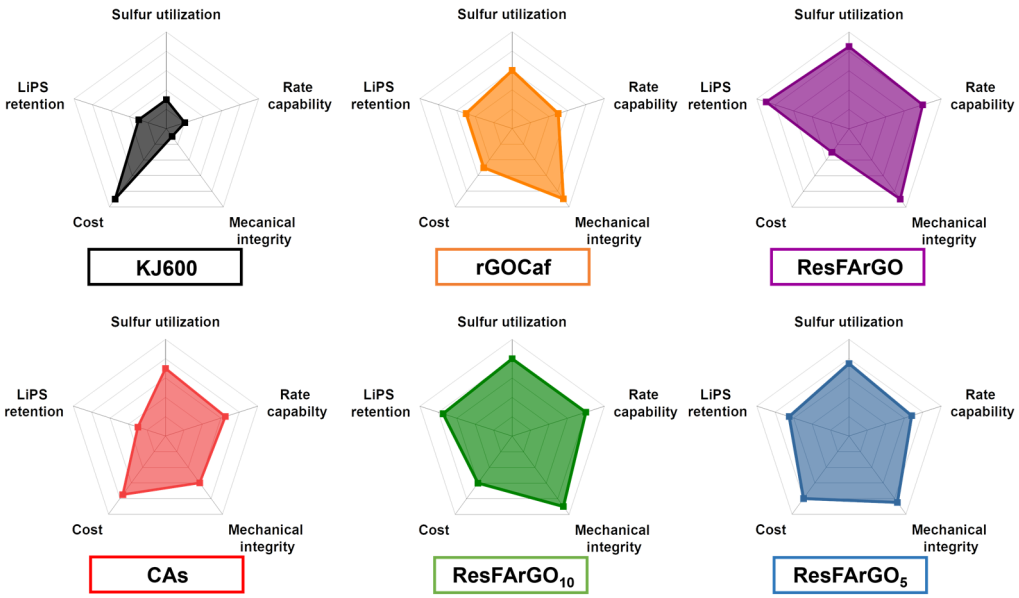

Figure 3.15. Radar chart of the different sulfur cathode formulations developed in **Chapter II** and **Chapter III** reflecting their cathode and battery features.

The ResFArGO and rGOCaf materials, synthesized in **Chapter II** for their use as sulfur carbon host, have demonstrated significantly improved textural properties and mechanical integrity of the electrodes compared to the reference material KJ600. The major difference shown between the two synthesized carbons is the improved affinity for LiPS exhibited by ResFArGO. This characteristic proves to be of great importance for cell performance. Benefiting from the high electronic conductivity derived from the presence of rGO, coupled with the excellent affinity shown with LiPS, the ResFArGO-based cell displayed exceptional rate capability and remarkable sulfur utilization. These features allow it to meet the set cell targets to be competitive with conventional LIBs. However, the current synthesis process of ResFArGO is expensive and requires further optimization, thereby contributing to an increase in the final cost of the battery that incorporates it. To overcome the cost challenges posed by this synthesis process, **Chapter III** has introduced an improved iteration of the system, from the applicability point of view. The incorporation of tailored conductive additives, particularly ResFArGO material, was successful in preserving the mechanical integrity of the electrodes. Furthermore, it reaffirmed the key role of combining suitable textural properties and a good affinity with LiPS in determining the final performance of the batteries. In the case of the CAs system, a substantial

improvement in the LSB performance was observed compared to the KJ600 reference, motivated by the improvement in their electronic conductivity. Nevertheless, the lack of affinity of CAs with LiPS emphasizes the advantage of incorporating a tailored additive material like ResFArGO. Notably, the $ResFArGO_{10}$ system presented comparable cell performances to those achieved by the ResFArGO employed as main carbon, with the added benefit of cost reduction and enhanced practical viability for the system. This approach of incorporating ResFArGO in small quantities was strategically exploited to maximize the sulfur content of the cathodes, resulting in the development of the $ResFArGO_5$ system. This system not only enables satisfactory cell yields but also enhances the practical feasibility of the overall setup. However, the toll for higher sulfur content together with a very small amount of ResFArGO resulted in performance levels that were not up to ResFArGO as main carbon or $ResFArGO_{10}$ systems. Therefore, in pursuit of a balance between performance and practical feasibility, the cathode composition based on $ResFArGO_{10}$ has been selected for further optimizations in subsequent chapters.

On the other hand, in **Chapters II** and **III**, a significant challenge of Li-S technology has become apparent, which is the issue of short cell cycle life. Despite optimizing the performance of sulfur cathodes through the introduced advancements, high-loading energy cells could only undergo approximately 50 cycles before reaching the end of their operating life. This limited cycle life is attributed to the lack of long-term affinity between the conventional Li-S electrolyte used for cell testing and the Li metal anode. Consequently, the imperative task of developing new electrolytes to improve the long-term cycling of LSBs will be addressed in subsequent chapters.

3.5. Bibliography

[1] M. Zhong, J. Guan, J. Sun, X. Shu, H. Ding, L. Chen, N. Zhou, Z. Xiao, A cost- and energy density-competitive lithium-sulfur battery, Energy Storage Mater. 2021, 41, 588–598. https://doi.org/10.1016/j.ensm.2021.06.037.

[2] Y. Gong, J. Li, K. Yang, S. Li, M. Xu, G. Zhang, Y. Shi, Q. Cai, H. Li, Y. Zhao, Towards practical application of Li–S battery with high sulfur loading and lean electrolyte: Will carbon-based hosts win this race?, Nano-Micro Lett. 2023, 15, 150. https://doi.org/10.1007/s40820-023-01120-7.

[3] S. Zhou, J. Shi, S. Liu, G. Li, F. Pei, Y. Chen, J. Deng, Q. Zheng, J. Li, C. Zhao, I. Hwang, C.J. Sun, Y. Liu, Y. Deng, L. Huang, Y. Qiao, G.L. Xu, J.F. Chen, K. Amine, S.G. Sun, H.G. Liao, Visualizing interfacial collective reaction behaviour of Li–S batteries, Nature. 2023, 621, 75–81. https://doi.org/10.1038/s41586-023-06326-8.

[4] A. Benítez, D. Brandell, A renaissance for lithium-sulfur batteries through low-cost, efficient, and sustainable biomass cathodes, One Earth 2022, 5, 224–226. https://doi.org/10.1016/j.oneear.2022.02.009.

[5] S. Lee, A. Manthiram, Can cobalt be eliminated from lithium-ion batteries?, ACS Energy Lett. 2022, 7, 3058–3063. https://doi.org/10.1021/acsenergylett.2c01553.

[6] C. Yang, P. Li, J. Yu, L. Da Zhao, L. Kong, Approaching energy-dense and cost-effective lithium–sulfur batteries: From materials chemistry and price considerations, Energy 2020, 201, 117718. https://doi.org/10.1016/j.energy.2020.117718.

[7] Z. Wang, M. Feng, H. Sun, G. Li, Q. Fu, H. Li, J. Liu, L. Sun, A. Mauger, C.M. Julien, H. Xie, Z. Chen, Constructing metal-free and cost-effective multifunctional separator for high-performance lithium-sulfur batteries, Nano Energy. 2019, 59, 390–398. https://doi.org/10.1016/j.nanoen.2019.02.029.

[8] D. McNamara, M. Shaibani, M. Majumder, M.R. Hill, A nanoporous permselective polymer coating for practical low N/P ratio lithium metal batteries, Adv. Sustain. Syst. 2023, 7, 2300231. https://doi.org/10.1002/adsu.202300231.

[9] Y. Li, S. Guo, Material design and structure optimization for rechargeable lithium-sulfur batteries, Matter. 2021, 4, 1142–1188. https://doi.org/10.1016/j.matt.2021.01.012.

[10] L. Mauler, F. Duffner, W.G. Zeier, J. Leker, Battery cost forecasting: A review of methods and results with an outlook to 2050, Energy Environ. Sci. 2021, 14, 4712–4739. https://doi.org/10.1039/d1ee01530c.

[11] G. Benveniste, H. Rallo, L. Canals Casals, A. Merino, B. Amante, Comparison of the state of lithium-sulphur and lithium-ion batteries applied to electromobility, J. Environ. Manage. 2018, 226, 1–12. https://doi.org/10.1016/j.jenvman.2018.08.008.

[12] E.J. Berg, S. Trabesinger, Viability of Polysulfide-retaining barriers in Li–S battery, J. Electrochem. Soc. 2018, 165, A5001–A5005. https://doi.org/10.1149/2.0021801jes.

[13] A. Fotouhi, D.J. Auger, L. O'Neill, T. Cleaver, S. Walus, Lithium-sulfur battery technology readiness and applications - A review, Energies 2017, 10, 1937. https://doi.org/10.3390/en10121937.

[14] J. He, A. Bhargav, A. Manthiram, High-energy-density, long-life lithium-sulfur batteries with practically necessary parameters enabled by low-cost fe-ni nanoalloy catalysts, ACS Nano 2021, 15, 8583–8591. https://doi.org/10.1021/acsnano.1c00446.

[15] X. Chen, G. Du, M. Zhang, A. Kalam, Q. Su, S. Ding, B. Xu, Nitrogen-doped hierarchical porous carbon derived from low-cost biomass pomegranate residues for high performance lithium-sulfur batteries, J. Electroanal. Chem. 2019, 848, 113316. https://doi.org/10.1016/j.jelechem.2019.113316.

[16] Y. Chen, T. Wang, H. Tian, D. Su, Q. Zhang, G. Wang, Advances in lithium–sulfur batteries: From academic research to commercial viability, Adv. Mater. 2021, 33 2003666. https://doi.org/10.1002/adma.202003666.

[17] T. Liu, H. Hu, X. Ding, H. Yuan, C. Jin, J. Nai, Y. Liu, Y. Wang, Y. Wan, X. Tao, 12 Years Roadmap of the Sulfur Cathode for Lithium Sulfur Batteries (2009–2020), Energy Storage Mater. 2020, 30, 346–366. https://doi.org/10.1016/j.ensm.2020.05.023.

[18] H. Li, Y. Li, L. Zhang, Designing principles of advanced sulfur cathodes toward practical lithium-sulfur batteries, SusMat 2022, 2, 34–64. https://doi.org/10.1002/sus2.42.

[19] Y. He, S. Bi, C. Jiang, J. Song, Recent progress of sulfur cathodes and other components for flexible lithium–sulfur batteries, Mater. Today Sustain. 2022, 19,

100181. https://doi.org/10.1016/j.mtsust.2022.100181.

[20] Q. Du, M. Benedikter, K. Küster, T. Acartürk, U. Starke, J.L. Hoslauer, T. Schleid, M.R. Buchmeiser, Sulfurized polypropylene as low-cost cathode material for high-capacity lithium-sulfur batteries, Batter. Supercaps 2022, 5, 202200277. https://doi.org/10.1002/batt.202200277.

[21] M.S. Kim, M.S. Kim, V. Do, Y. Xia, W. Kim, W. Il Cho, Facile and scalable fabrication of high-energy-density sulfur cathodes for pragmatic lithium-sulfur batteries, J. Power Sources 2019, 422, 104–112. https://doi.org/10.1016/j.jpowsour.2019.02.093.

[22] J. Pallarés, A. González-Cencerrado, I. Arauzo, Production and characterization of activated carbon from barley straw by physical activation with carbon dioxide and steam, Biomass and Bioenergy 2018, 115, 64–73. https://doi.org/10.1016/j.biombioe.2018.04.015.

[23] H. Yi, K. Nakabayashi, S.H. Yoon, J. Miyawaki, Pressurized physical activation: A simple production method for activated carbon with a highly developed pore structure, Carbon 2021, 183, 735–742. https://doi.org/10.1016/j.carbon.2021.07.061.

[24] J. Saleem, U. Bin Shahid, M. Hijab, H. Mackey, G. McKay, Production and applications of activated carbons as adsorbents from olive stones, Biomass Convers. Biorefinery 2019, 9, 775–802. https://doi.org/10.1007/s13399-019-00473-7.

[25] N.Z. Mohd Azmi, A. Buthiyappan, A.A. Abdul Raman, M.F. Abdul Patah, S. Sufian, Recent advances in biomass based activated carbon for carbon dioxide capture – A review, J. Ind. Eng. Chem. 2022, 116, 1–20. https://doi.org/10.1016/j.jiec.2022.08.021.

[26] A.R. Tobi, J.O. Dennis, H.M. Zaid, A.A. Adekoya, A. Yar, U. Fahad, Comparative analysis of physiochemical properties of physically activated carbon from palm bio-waste, J. Mater. Res. Technol. 2019, 8, 3688–3695. https://doi.org/10.1016/j.jmrt.2019.06.015.

[27] V.G. Baldovino-Medrano, V. Niño-Celis, R. Isaacs Giraldo, Systematic analysis of the nitrogen adsorption-desorption isotherms recorded for a series of materials

based on microporous-mesoporous amorphous aluminosilicates using classical methods, J. Chem. Eng. Data. 2023, 68, 2512–2528. https://doi.org/10.1021/acs.jced.3c00257.

[28] L. Wang, J. Sun, H. Zhang, L. Xu, G. Liu, Preparation of benzoxazine-based N-doped mesoporous carbon material and its electrochemical behaviour as supercapacitor, J. Electroanal. Chem. 2020, 868, 114196. https://doi.org/10.1016/j.jelechem.2020.114196.

[29] H. Shi, W. Lv, C. Zhang, D.W. Wang, G. Ling, Y. He, F. Kang, Q.H. Yang, Functional carbons remedy the shuttling of polysulfides in lithium–sulfur batteries: confining, trapping, blocking, and breaking up, Adv. Funct. Mater. 2018, 28, 1800508. https://doi.org/10.1002/adfm.201800508.

[30] Y.C. Huang, H.I. Hsiang, S.H. Chung, Investigation and design of high-loading sulfur cathodes with a high-performance polysulfide adsorbent for electrochemically stable lithium-sulfur batteries, ACS Sustain. Chem. Eng. 2022, 10, 9254–9264. https://doi.org/10.1021/acssuschemeng.2c02332.

[31] Y. Yang, G. Meng, H. Wang, W. Wang, J. Zhang, Efficient polysulfides trapping and redox enabled by Co/N-carbon implanted Li+-montmorillonite for advanced lithium-sulfur batteries, Chem. Eng. J. 2023, 451, 138914. https://doi.org/10.1016/j.cej.2022.138914.

[32] L. Huang, W. Zhou, S. Cheng, H. Yao, W. Dong, L. Li, X. Ji, Preparation of functional groups-rich graphene oxide for high-performance lithium–sulfur batteries, Mater. Today Sustain. 2023, 21, 100300. https://doi.org/10.1016/j.mtsust.2022.100300.

[33] S. Karuppiah, B. Kalimuthu, M.A. Nazrulla, S. Krishnamurty, K. Nallathamby, An effective polysulfide trapping polar interlayer for high rate Li-S batteries, J. Mater. Chem. A. 2019, 7, 10067–10076. https://doi.org/10.1039/c9ta00233b.

[34] C.Y. Zhang, C. Zhang, J.L. Pan, G.W. Sun, Z. Shi, C. Li, X. Chang, G.Z. Sun, J.Y. Zhou, A. Cabot, Surface strain-enhanced MoS2 as a high-performance cathode catalyst for lithium–sulfur batteries, EScience. 2022, 2, 405–415. https://doi.org/10.1016/j.esci.2022.07.001.

[35] H. Zhang, H. Cui, J. Li, Y. Liu, Y. Yang, M. Wang, Frogspawn inspired hollow Fe3C@N-C as an efficient sulfur host for high-rate lithium-sulfur batteries, Nanoscale 2019, 11, 21532–21541. https://doi.org/10.1039/c9nr07388d.

[36] T. Sun, X. Zhao, B. Li, H. Shu, L. Luo, W. Xia, M. Chen, P. Zeng, X. Yang, P. Gao, Y. Pei, X. Wang, NiMoO4 nanosheets anchored on N-S doped carbon clothes with hierarchical structure as a bidirectional catalyst toward accelerating polysulfides conversion for Li-S battery, Adv. Funct. Mater. 2021, 31, 2101285. https://doi.org/10.1002/adfm.202101285.

[37] P. Wang, B. Xi, M. Huang, W. Chen, J. Feng, S. Xiong, Emerging catalysts to promote kinetics of lithium–sulfur batteries, Adv. Energy Mater. 2021, 11, 2002893. https://doi.org/10.1002/aenm.202002893.

[38] C. Zhao, B. Jiang, Y. Huang, X. Sun, M. Wang, Y. Zhang, N. Zhang, Highly active and stable oxygen vacancies via sulfur modification for efficient catalysis in lithium-sulfur batteries, Energy Environ. Sci. 2023, 16, 5490–5499. https://doi.org/10.1039/d3ee01774e.

[39] T. Feng, T. Zhao, N. Zhang, Y. Duan, L. Li, F. Wu, R. Chen, 2D amorphous mo-doped CoB for bidirectional sulfur catalysis in lithium sulfur batteries, Adv. Funct. Mater. 2022, 32, 2202766. https://doi.org/10.1002/adfm.202202766.

[40] X.X. Yang, W.Z. Du, X.T. Li, Y. Zhang, Z. Qian, M.J. Biggs, C. Hu, Cobalt(II) tetraaminophthalocyanine-modified multiwall carbon nanotubes as an efficient sulfur redox catalyst for lithium–sulfur batteries, ChemSusChem 2020, 13, 3034–3044. https://doi.org/10.1002/cssc.202000648.

[41] J. Cho, S. Ryu, Y.J. Gong, S. Pyo, H. Yun, H. Kim, J. Lee, J. Yoo, Y.S. Kim, Nitrogen-doped MoS2 as a catalytic sulfur host for lithium-sulfur batteries, Chem. Eng. J. 2022, 439, 135568. https://doi.org/10.1016/j.cej.2022.135568.

[42] W. Qu, Z. Lu, C. Geng, L. Wang, Y. Guo, Y. Zhang, W. Wang, W. Lv, Q.H. Yang, Targeted catalysis of the sulfur evolution reaction for high-performance lithium-sulfur batteries, Adv. Energy Mater. 2022, 12, 2202232. https://doi.org/10.1002/aenm.202202232.

[43] G. Liu, Q. Zeng, Z. Fan, S. Tian, X. Li, X. Lv, W. Zhang, K. Tao, E. Xie, Z. Zhang,

Boosting sulfur catalytic kinetics by defect engineering of vanadium disulfide for high-performance lithium-sulfur batteries, Chem. Eng. J. 2022, 448, 137683. https://doi.org/10.1016/j.cej.2022.137683.

[44] M. Zhao, X. Chen, X.Y. Li, B.Q. Li, J.Q. Huang, An Organodiselenide Comediator to Facilitate Sulfur Redox Kinetics in Lithium–Sulfur Batteries, Adv. Mater. 2021, 33, 2007298. https://doi.org/10.1002/adma.202007298.

[45] Y.T. Liu, L. Wang, S. Liu, G.R. Li, X.P. Gao, Constructing high gravimetric and volumetric capacity sulfur cathode with LiCoO2 nanofibers as carbon-free sulfur host for lithium-sulfur battery, Sci. China Mater. 2021, 64, 1343–1354. https://doi.org/10.1007/s40843-020-1552-7.

[46] X. Gao, D. Zhou, Y. Chen, W. Wu, D. Su, B. Li, G. Wang, Strong charge polarization effect enabled by surface oxidized titanium nitride for lithium-sulfur batteries, Commun. Chem. 2019, 2, 66. https://doi.org/10.1038/s42004-019-0166-8.

[47] F. Hu, H. Peng, T. Zhang, W. Shao, S. Liu, J. Wang, C. Wang, X. Jian, A lightweight nitrogen/oxygen dual-doping carbon nanofiber interlayer with meso-/micropores for high-performance lithium-sulfur batteries, J. Energy Chem. 2021, 58, 115–123. https://doi.org/10.1016/j.jechem.2020.09.032.

[48] G.H. Kim, Y.J. Lee, J.W. Park, A. Raza, M.B. Raza, D. Kim, M. Park, H. Choi, Enhanced performance of lithium-sulfur battery cathode via composition optimization using modified MWCNTs as a conductive material and poly (acrylic acid) as a binder, Int. J. Electrochem. Sci. 2023, 18, 100217. https://doi.org/10.1016/J.IJOES.2023.100217.

[49] Z. Shi, J. Wei, H. Xu, L. Wang, H. Yue, Z. Cao, H. Dong, Y. Yin, S. Yang, A faster lithium ion diffusion pathway constructed by uniform distribution of sulfur using simple one step spray drying method, Chem. Eng. J. 2020, 379, 122353. https://doi.org/10.1016/j.cej.2019.122353.

[50] L. Tian, Z. Zhang, S. Liu, G. Li, X. Gao, High-entropy spinel oxide nanofibers as catalytic sulfur hosts promise the high gravimetric and volumetric capacities for lithium–sulfur batteries, Energy Environ. Mater. 2022, 5, 645–654. https://doi.org/10.1002/eem2.12215.

[51] Y. Yang, X. Li, R. Luo, X. Zhang, J. Fu, Y. Zheng, K. Huo, T. Zhou, A topochemically constructed flexible heterogeneous vanadium-based electrocatalyst for boosted conversion kinetics of polysulfides in Li-S batteries, Mater. Chem. Front. 2021, 5, 3830–3840. https://doi.org/10.1039/d0qm01142h.

[52] Z. Ye, Y. Jiang, L. Li, F. Wu, R. Chen, A High-Efficiency CoSe Electrocatalyst with Hierarchical Porous Polyhedron Nanoarchitecture for Accelerating Polysulfides Conversion in Li–S Batteries, Adv. Mater. 2020, 32, 2002168. https://doi.org/10.1002/adma.202002168.

[53] Y. Boyjoo, H. Shi, E. Olsson, Q. Cai, Z.S. Wu, J. Liu, G.Q. Lu, Molecular-Level Design of Pyrrhotite Electrocatalyst Decorated Hierarchical Porous Carbon Spheres as Nanoreactors for Lithium–Sulfur Batteries, Adv. Energy Mater. 2020, 10, 2000651. https://doi.org/10.1002/aenm.202000651.

[54] M. Zheng, C. Guo, Z. Luo, J. Wu, X. Tang, L. Li, Q. Sun, Q. Ouyang, B. Shi, H. Nie, J.J. Shao, G. Zhou, Molybdenum disulfide (MoS2)/porous silica nanosheet composite barrier for polysulfide shuttling inhibition in lithium-sulfur batteries, Compos. Part B Eng. 2023, 264, 110898. https://doi.org/10.1016/j.compositesb.2023.110898.

[55] S. Dasarathan, J. Sung, Y.J. Lee, H.Y. Choi, J.W. Park, D. Kim, Lithium phosphate incorporated carbon nanotube interlayer as an efficient polysulfide immobilizer for high performance lithium sulfur batteries, Electrochem. Commun. 2023, 155, 107584. https://doi.org/10.1016/j.elecom.2023.107584.

[56] R. Paste, S. Li, J.H. Fu, Y.H. Chiang, A.I. Inamdar, M.H. Chiang, V. Tung, H.C. Lin, C.W. Chu, Capillary-induced self-crumpled and sulfur-deficient MoS2 nanosheets inhibit polysulfide cycling in lithium-sulfur batteries, J. Mater. Chem. A 2023, 11, 8265–8276. https://doi.org/10.1039/d3ta00411b.

[57] M. Zhao, B.Q. Li, X.Q. Zhang, J.Q. Huang, Q. Zhang, A perspective toward practical lithium-sulfur batteries, ACS Cent. Sci. 2020, 6, 1095–1104. https://doi.org/10.1021/acscentsci.0c00449.

[58] F. Shi, L. Zhai, Q. Liu, J. Yu, S.P. Lau, B.Y. Xia, Z.L. Xu, Emerging catalytic materials for practical lithium-sulfur batteries, J. Energy Chem. 2023, 76, 127–145. https://doi.org/10.1016/j.jechem.2022.08.027.

[59] H.J. Peng, J.Q. Huang, X.B. Cheng, Q. Zhang, Review on High-Loading and High-Energy Lithium–Sulfur Batteries, Adv. Energy Mater. 2017, 7, 1700260. https://doi.org/10.1002/aenm.201700260.

[60] G. Zhou, H. Chen, Y. Cui, Formulating energy density for designing practical lithium–sulfur batteries, Nat. Energy 2022, 7, 312–319. https://doi.org/10.1038/s41560-022-01001-0.

[61] A. Bhargav, J. He, A. Gupta, A. Manthiram, Lithium-Sulfur Batteries: Attaining the Critical Metrics, Joule 2020, 4, 285–291. https://doi.org/10.1016/j.joule.2020.01.001.

[62] C. Luo, E. Hu, K.J. Gaskell, X. Fan, T. Gao, C. Cui, S. Ghose, X.Q. Yang, C. Wang, A chemically stabilized sulfur cathode for lean electrolyte lithium sulfur batteries, Proc. Natl. Acad. Sci. 2020, 117, 14712–14720. https://doi.org/10.1073/pnas.2006301117.

[63] Y.T. Liu, S. Liu, G.R. Li, X.P. Gao, Strategy of enhancing the volumetric energy density for lithium–sulfur batteries, Adv. Mater. 2021, 33, 2003955. https://doi.org/10.1002/adma.202003955.

[64] S.H. Chung, C.H. Chang, A. Manthiram, Progress on the critical parameters for lithium–sulfur batteries to be practically viable, Adv. Funct. Mater. 2018, 28, 1801188. https://doi.org/10.1002/adfm.201801188.

Chapter IV

Gel Polymer Electrolytes for Safe and High-Performing Room-Temperature Li-S Batteries

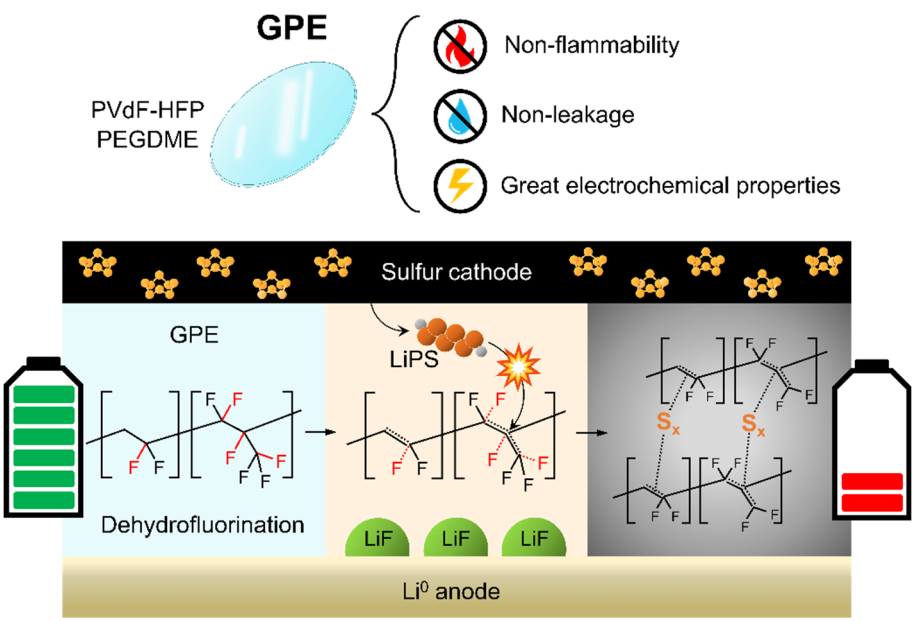

4.1. Introduction

The research conducted in the preceding two chapters has resulted in the development of a high-performing sulfur cathode by the integration of synthesized graphene-based activated carbon with tailored properties into the electrode formulation. However, concurrent research has revealed the challenge associated with ensuring an extended operational lifespan when employing the conventional electrolyte under realistic and demanding operating conditions. Consequently, there is an imperative need to explore innovative electrolyte solutions explicitly tailored for efficient LSBs. These advanced electrolytes should not only ensure superior sulfur utilization but also guarantee the long-term cyclability of the batteries, thereby aligning with the industry-established requirements for practical applications.

In the context of LSBs, the conventional approach has involved the use of liquid electrolytes composed of organic solvents. These solvents predominantly belong to the ether-type compound family, giving rise to the well-established liquid electrolyte that comprises LiTFSI dissolved in the solvent combination of DOL/DME, with $LiNO_3$ acting as the additive [1–4]. This electrolyte, employed in **Chapters II** and **III** for cathode performance evaluation, has become the preferential electrolyte choice due to its remarkable characteristics, particularly its high ionic conductivity, ensuring efficient charge and discharge processes. As a result, it guarantees high sulfur utilization values and, consequently, notable battery capacity values, even under practical operating conditions [5,6]. Nonetheless, this electrolyte suffers from a severe shuttle effect due to significant LiPS dissolution in the organic solvents (up to 6 M of Li_2S_6) [7,8]. Additionally, its inherent stability with the LMA is compromised due to the continuous consumption of the $LiNO_3$ additive during cycling, significantly limiting the cyclability of LSBs, especially under practical operating conditions [9,10]. Furthermore, using this type of liquid electrolyte introduces a range of safety challenges attributed to the highly flammable nature of the solvents employed for its formulation. These challenges encompass the risk of leakage, combustion, or explosion [11,12]. These safety concerns are further exacerbated when combined with LMA due to its intrinsic reactivity. Therefore, the imperative shift away from conventional organic electrolytes towards safer and more stable alternatives has become crucial to ensure the safety and long-term cycling performance of the battery system [13–15].

In response to these pressing concerns, all solid-state electrolytes have garnered significant attention due to their potential to mitigate the safety issues associated with liquid electrolytes [16–18]. These solid-state electrolytes, typically constructed from polymer or ceramic materials, offer several advantages, including reduced flammability risks, improved resistance to dendrite growth, and prevention of LiPS dissolution and migration [19,20]. Despite the noteworthy benefits achieved through extensive research efforts in recent years, solid electrolytes present several challenges that need to be faced for their industrial implementation. These challenges include i) poor interfacial contact, ii) low ionic conductivity at RT, and iii) difficulties in scaling up manufacturing processes [21–23]. While there is optimism about overcoming these challenges through future advances in the coming years, practical implementation is not foreseen until the next decade. Hence, it is imperative to explore new alternatives to bridge the gap in the short term and address the pressing needs of the industry.

Within this context, gel polymer electrolytes (GPEs), also known as semi-solid or quasi-solid electrolytes, emerge as a promising alternative to guide the transition from liquid electrolytes to all solid-state counterparts [24–27]. These innovative electrolytes seek to amalgamate the advantageous safety properties inherent in solid electrolytes with the enhanced performance characteristics typically associated with liquid electrolytes [28–30]. For this purpose, GPEs are designed with a solid polymeric matrix that incorporates a liquid component, comprising a plasticizer and a lithium salt.

Among the different polymer matrices under investigation, poly(vinylidene fluoride) (PVdF)-based polymers stand out as one of the most widely used materials. This prominence is attributed to their outstanding mechanical, chemical, and electrochemical properties [31–33]. Particularly, the utilization of PVdF copolymers, such as poly(vinylidene fluoride-co-hexafluoropropylene) (PVdF-HFP), presents a highly promising alternative. This is primarily due to their ability to incorporate a larger proportion of liquid inside the polymer matrix, which is achieved through the introduction of amorphous nature copolymers, such as the HFP component [34–36]. In the context of plasticizers, conventional liquid electrolytes have commonly been employed to enhance ionic conductivity values, closely approaching those of their liquid counterparts. Regrettably, this practice comes at the expense of compromising the safety of the GPEs, resulting in an increased risk of

flammability. Therefore, in the search for new cost-effective, chemically stable, and safe plasticizers, the glyme solvent family emerges as a potential alternative, thanks to its favorable electrochemical and safety properties [37,38].

With the primary objective of improving the cyclability and safety of Li-S cells, this chapter of the thesis focuses on the development of a GPE based on a PVdF-HFP polymer matrix, plasticized with poly(ethylene glycol dimethyl ether) (PEGDME), utilizing a straightforward and scalable one-pot manufacturing process. The selection of PEGDME as the plasticizer is driven by its commendable safety properties, which include a high boiling point (> 250 °C) and low vapor pressure (< 0.01 hPa at 20 °C), along with its excellent electrochemical properties, such as high ionic conductivity and lithium compatibility [39,40]. In this sense, the prepared GPEs will undergo comprehensive characterization, encompassing both physicochemical and electrochemical properties. Furthermore, an evaluation of the safety properties of the GPE will be conducted, comparing them with the conventional DME/DOL-based electrolyte. Finally, the suitability of these GPEs will be assessed by testing both their compatibility with the LMA and their performance in LSBs.

4.2. GPE development for safe and high-performance LSBs

4.2.1. GPE preparation and composition screening

As previously mentioned, a straightforward and easily scalable one-pot solvent-casting manufacturing method was employed for the preparation of the GPEs, as schematically illustrated in **Figure 4.1a**. This method involves the combination of all the components, dissolving them in acetone, and finally forming the GPE through a drying process (see the Experimental Section for more details).

A systematic screening of GPE composition was carried out to identify the optimal ratio that balances mechanical integrity, thermal resistance, and ionic conductivity. This screening involved varying the ratio between the solid polymer matrix and liquid electrolyte from 50-50 wt.% to 10-90 wt.%. The resulting GPEs were labeled based on the percentage of the polymer host, including GPE_50, GPE_40, GPE_30, GPE_20, and GPE_10. GPEs containing up to 20 wt.% PVdF-HFP content were successfully developed, resulting in solid-like self-standing, transparent, and flexible membranes. These membranes exhibited remarkable structural integrity, displaying no signs of liquid leakage. These favorable structural properties serve as the initial

indication of the suitability of the selected preparation method. Nevertheless, GPEs with a polymer matrix content below 20 wt.% (e.g., 10 wt.%) were excluded from subsequent analyses due to their inadequate mechanical integrity and inability to form a firm structure, rendering them challenging their processability.

In the pursuit of identifying the optimal GPE composition, beyond the mechanical integrity previously reported, two fundamental factors were considered: thermal stability (to guarantee the safety of the battery system) and ionic conductivity at RT. To evaluate the thermal properties, thermogravimetric analysis (TGA) was conducted. For reference purposes, pure compounds of PVDF-HFP as the polymer matrix and PEGDME as the plasticizer were included in the study. As displayed in **Figure 4.1b** all the analyzed GPE compositions exhibited excellent thermal stability, with decomposition temperatures exceeding 250 °C. This temperature threshold is considerably higher than the typical operating temperatures of battery systems. Furthermore, the developed GPEs demonstrated intermediate thermal properties when compared to the PVdF-HFP and PEGDME references. This outcome underscores the effectiveness of the polymer matrix in retaining the plasticizer, effectively serving as a barrier to reduce its volatility. Interestingly, the effect of the liquid content in the GPE composition on the thermal stability of the developed GPE was found to be negligible. No significant differences in the thermal stability were discernible across the analyzed GPE compositions, further highlighting the robustness of the developed GPEs.

In the evaluation of individual electrochemical properties, **Figure 4.1c** provides an overview of the ionic conductivities exhibited by the prepared GPEs in comparison to the PEGDME liquid electrolyte used as a reference. All GPEs present lower ionic conductivities than the reference PEGDME liquid electrolyte. Notably, an increase in ionic conductivity was evidenced with a higher proportion of the liquid component. Additionally, it is important to highlight that only GPE compositions with a PVdF-HFP content of less than 40 wt.% were able to surpass the targeted conductivity threshold necessary for effective battery electrolyte operation at RT, set at 1.0×10^{-4} S cm^{-1} [41]. Among the different GPEs prepared, GPE_20 stood out presenting notably high ionic conductivity at RT (3.4×10^{-4} S cm^{-1}). This, combined with its favorable thermal and mechanical properties, positioned GPE_20 as the most promising alternative, prompting its selection for further evaluation and analysis.

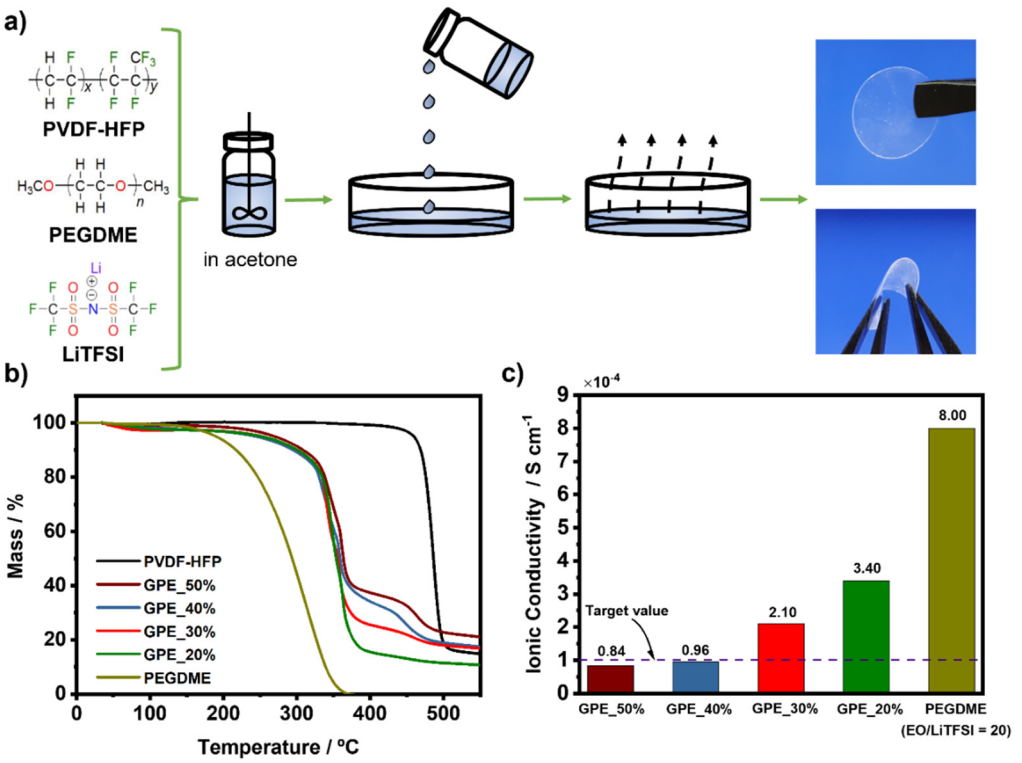

Figure 4.1. a) Schematic illustration of the solvent casting preparation process, **b)** TGA results, and **c)** ionic conductivities at RT of the different GPEs analyzed.

4.2.2. In-depth characterization of GPE_20

4.2.2.1. Electrochemical properties of GPE_20

After selecting the optimal GPE composition, further evaluation of GPE_20 was conducted. The electrolyte characterizations began with the ionic conductivity analysis of the GPE_20 under different operating temperatures, ranging from 20 to 80 °C. The results, displayed in **Figure 4.2a**, reveal a non-linear relationship, diverging from the typical Arrhenius plot and aligning more closely with Vogel-Tamman-Fulcher behavior [42,43]. This deviation from linearity suggests that the ionic conductivity is influenced by a combination of migration through the redistribution of free volume and polymer segmental motion [44]. Furthermore, it indicates that the movement of Li^+ primarily occurs with the amorphous phase of the PVDF-HFP matrix, where plasticizer-rich zones are located.

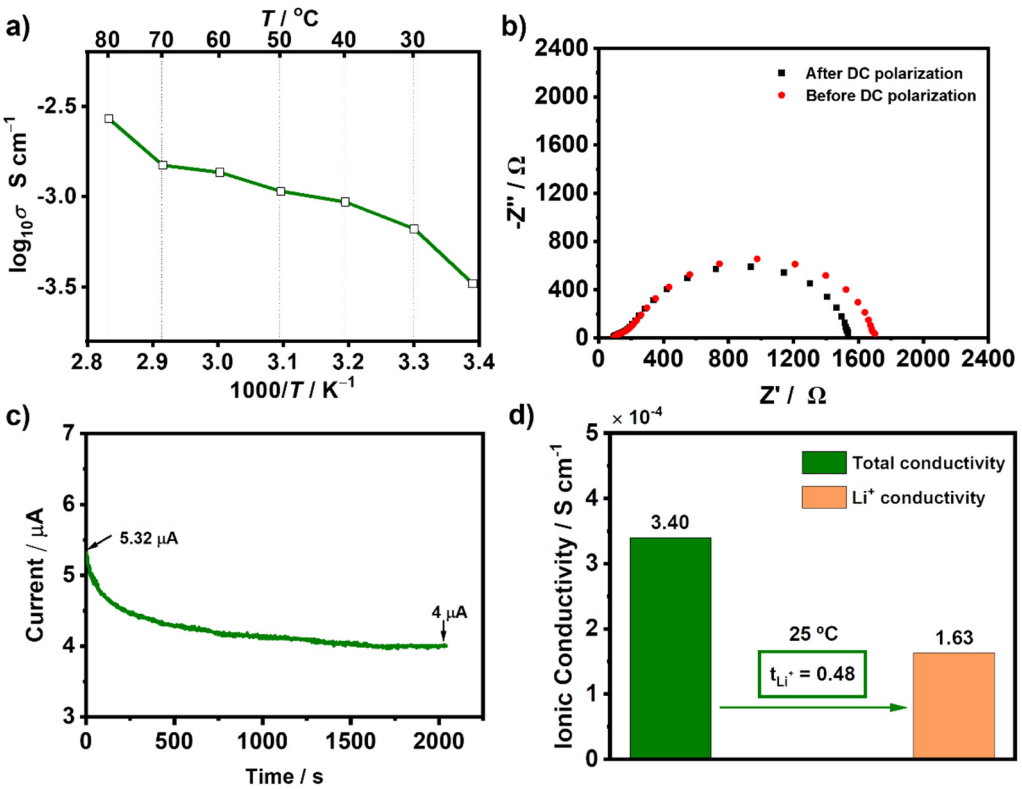

Figure 4.2 a) Temperature dependence of ionic conductivity of the GPE_20 electrolyte. **b)** Impedance spectra and **c)** time-dependence response of current to 10 mV polarization for GPE_20 electrolyte at RT. **d)** Total and lithium ionic conductivity values at RT.

Furthermore, the lithium-ion transference number (t_{Li+}) was assessed using the Bruce-Vincent method, as described in the experimental section. This parameter plays a crucial role in the electrolyte characterization as it quantifies the fraction of ionic conductivity attributed to the lithium ions compared to their counterions. As calculated by the parameters obtained from the alternating current (AC) impedance and direct current (DC) polarization measurements (**Figures 4.2b** and **c**, respectively), GPE_20 exhibited a t_{Li+} value of 0.48, whereas the reference PEGDME liquid electrolyte presented a value of 0.45. This slight difference can be attributed to the highly polarized C-F bonds within the PVdF-HFP structure, which may facilitate the role of the lithium salt as a cross-linker between the polymer matrix and the salt anion, as exemplified by the interactions: C−F (from PVDF-HFP)−Li^+−O=S (from TFSI anion), C−F (from PVDF-HFP)−Li^+−F−C (from TFSI anion)) [45]. This interaction leads to the

retention of the salt anion within the polymer matrix while allowing the Li ions to move freely through the plasticizer. This notable t_{Li+} value indicates a high contribution of Li^+ to the overall ionic conductivity of GPE_20 and a reduced susceptibility of the system to polarization due to salt concentration gradients [46,47]. This behavior further contributes to the improved charge-discharge performance of a battery system. Consequently, the combination of the obtained ionic conductivity and t_{Li+} values results in a notably high Li-ion conductivity for the GPE_20, particularly 1.6×10^{-4} S cm^{-1} (**Figure 4.2d**).

4.2.2.2. Safety properties of GPE_20

To evaluate the safety properties of GPE_20, a flammability test was conducted, yielding interesting insights as depicted in **Figure 4.3**. In addition to the developed electrolyte GPE_20, two reference cases were included for comparative analysis: the conventional liquid electrolyte based on the DME/DOL mixture and the GPE plasticized with this electrolyte. The conventional liquid electrolyte exhibited a concerning propensity for combustion, igniting instantaneously and sustaining the flame for more than 10 seconds until its complete combustion. This observation aligns with the well-documented safety concerns associated with the use of volatile organic solvent-based electrolytes. In contrast, the GPE incorporating DME/DOL showcased a completely different behavior. Although it initially ignited, the duration of the combustion was notably brief (less than 5 seconds), presenting a comparatively smaller flame. This finding underscored two key observations. Firstly, it underscores the remarkable ability of the polymer matrix to confine the liquid electrolyte, consequently enhancing the safety of the system and demonstrating the effectiveness of the proposed one-pot manufacturing approach. Secondly, it emphasizes the persistent safety concerns associated with the utilization of such highly flammable electrolytes. Regarding the proposed GPE_20 electrolyte, it exhibited exceptional resistance to flammability, without any sign of ignition (**Figure 4.3b)**. This behavior can be attributed to the inherently low vapor pressure of the PEGDME plasticizer, in combination with the additional protection afforded by the polymeric matrix. As a result, GPE_20 demonstrates an exceptional safety profile. The insights derived from the flammability and thermal stability characterization evidence that PEGDME emerges as an exemplary plasticizer for the GPE composition, significantly enhancing its safety attributes. Additionally, this also highlights the effectiveness of the selected

GPE preparation method in bolstering safety standards, a paramount requirement for LMB applications.

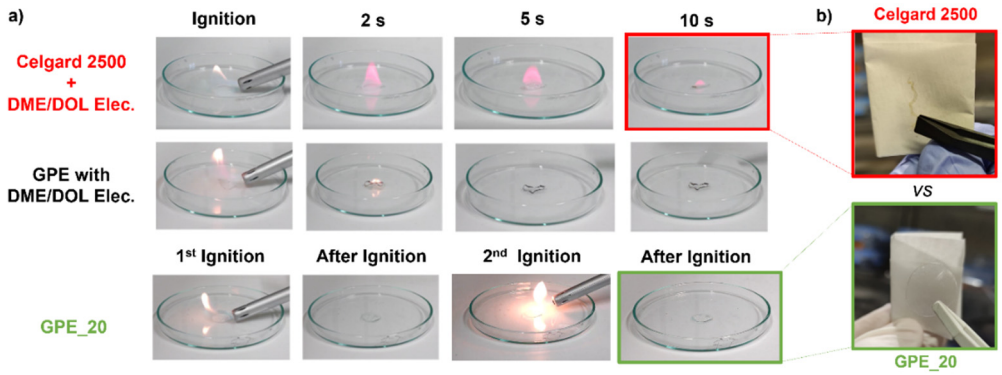

Figure 4.3. **a)** Flammability test of reference DME/DOL liquid electrolyte, the DME/DOL-based GPE, and GPE_20. **b)** Optical images of the Celgard® 2500 separator and GPE_20 after the flammability test.

4.2.3. Compatibility of the GPE_20 against LMA

The electrochemical compatibility between the LMA and the GPE is of paramount importance for ensuring optimal performance and long-term cyclability in LMBs. To rigorously evaluate this compatibility, different galvanostatic cycling tests were carried out on Li metal symmetric cells at RT. In the initial experiment, a current test was performed on GPE_20 at different current densities, ranging from 0.05 mA cm^{-2} to 0.5 mA cm^{-2}, as shown in **Figure 4.4a**. Notably, GPE_20 exhibited low overpotential and smooth performance when subjected to low current densities. However, as the current density reaches the threshold of 0.5 mA cm^{-2}, the cycling behavior becomes unstable, hindering long-term cyclability. Therefore, it becomes evident that the maximum applicable current density for this electrolyte to ensure stable long-term cycling in the Li metal symmetric cells should not exceed 0.33-0.5 mA cm^{-2}.

Consequently, to evaluate the performance within this established limit and to analyze the long-term compatibility with the Li metal, constant galvanostatic cycling was conducted at a current density of 0.1 mA cm^{-2} (**Figure 4.4b**). Under these conditions, the GPE_20 exhibits smooth and extended cycle profiles, with a remarkable endurance surpassing 600 hours with a low overpotential of 70 mV.

Furthermore, no signs of dendrite-induced short circuits or erratic cycling behavior were observed. In contrast, for comparative purposes, **Figure A.4.1** shows that the PEGDME-based liquid electrolyte system presents a remarkably unstable, noisy, and erratic cycling profile. This instability is likely attributed to the formation of an unstable organic-based SEI over the Li metal surface, leading to continuous electrolyte consumption and reduced stability. This performance contrast underscores the ability of the polymer matrix to prevent unfavorable interactions between the PEGDME liquid electrolyte and the LMA, thereby enhancing the overall stability of the system.

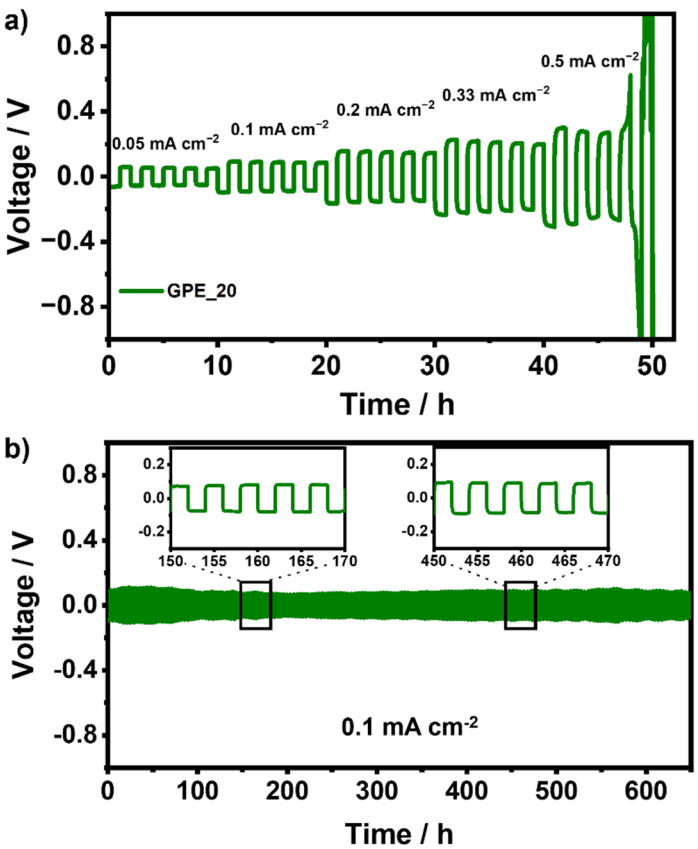

Figure 4.4. a) Current test under different current densities and **b)** long-term galvanostatic cycling at a current density of 0.1 mA cm^{-2} of the GPE_20.

The favorable galvanostatic cycling performance observed in the Li metal symmetric cell with the GPE_20 can be directly attributed to the suitable morphology and quality of the SEI formed between the GPE electrolyte and the Li metal. To explore

the interfacial properties, SEM and XPS measurements of the deposited Li metal were conducted, as depicted in **Figures 4.5a** and **4.5b**, respectively. To this end, a galvanostatic deposition of lithium metal onto a copper current collector was performed under a constant current of 0.1 mA cm^{-2} for 20 h. SEM images reveal a homogeneous lithium metal deposition on the Cu substrate, without evident dendritic structures. However, it is important to note that the deposited layer falls short of optimal density, exhibiting a porous nature. This characteristic may explain the suboptimal performance observed at high current densities in **Figure 4.4a**. Furthermore, the F 1s spectrum in **Figure 4.5b** underscores the presence of the LiF compound in the composition of the SEI layer, a key component for ensuring the SEI's robust mechanical properties [48,49]. The presence of LiF can be associated with the reduction of both LiTFSI salt and PVDF-HFP polymer matrix, contributing to the stability of the SEI layer.

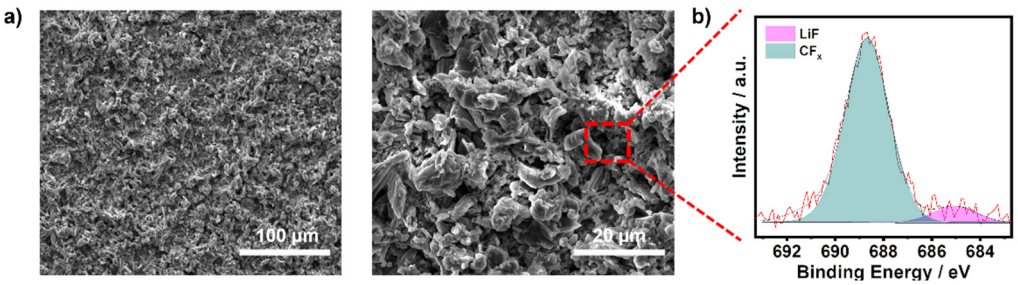

Figure 4.5. a) Li metal deposition on the Cu substrate and **b)** the corresponding F 1s region XPS spectra in the presence of GPE_20.

4.2.4. LSB performance of the GPE_20 at RT

Until now, GPE_20 has demonstrated exceptional intrinsic physicochemical, safety, and electrochemical properties, positioning it as a promising electrolyte candidate for LSBs at RT. To analyze the viability of GPE_20 in the Li-S technology, a battery cycling test at RT was performed. In this test, the cathode developed in the previous chapter, incorporating 10 wt.% of ResFArGO as additive in the formulation, with a sulfur loading of 2-2.5 mg_S cm^{-2} was employed. The battery cycling protocol comprised 5 preconditioning cycles at C/20, followed by subsequent cycling at C/10, as shown in **Figure 4.6a**.

Despite the promising initial discharge capacity, where GPE_20 exhibits an impressive value of 1061 mAh g^{-1}, the system shows a poor cycling performance characterized by an abrupt and constant capacity decay throughout cycling. Within just 20 cycles, GPE_20's capacity sharply declines to a mere 250 mAh g^{-1}, representing a significant reduction of nearly 80% from its initial capacity. Intriguingly, during the initial cycles, the CE exceeded 100%, an unexpected phenomenon that suggests the occurrence of undesirable and irreversible reactions during the LSB cycling process. This unsatisfactory performance of GPE_20 in Li-S technology was further supported by the evolution of the charge and discharge profiles, depicted in **Figure 4.6b**. These profiles represent the charge/discharge profiles at the C/20 and C/10 cycling rates of the cell. Initially, the charge/discharge profiles of the GPE_20 cell displayed the two distinctive plateaus associated with sulfur redox reactions characteristic of Li-S technology, following the dissolution-precipitation operating mechanism. However, as cycling progresses, these profiles change, and the first plateau nearly disappears during cycling at C/10. Furthermore, there is a notable increase in the cell overpotential, which becomes significantly higher with the increase in the cycling rate. These findings evidence the poor LSB performance of the GPE_20, falling short in ensuring both cyclability (unable to exceed 20 cycles with acceptable capacity values) and sulfur utilization (offering a meager 15% sulfur utilization).

At this point, it is pertinent to pose the question of whether, despite the exceptional individual properties shown by GPE_20, the main cause of the observed suboptimal LSB performance can be solely attributable to the electrolyte or if it is a consequence of the intricate operating conditions of the technology.

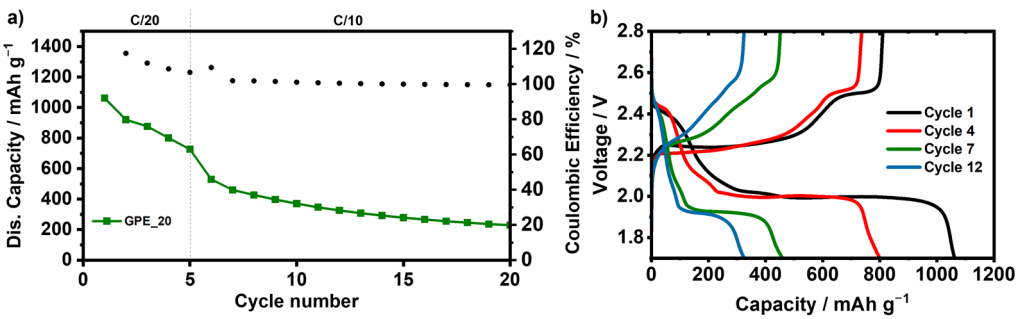

Figure 4.6. a) LSB performance of the developed GPE_20 and **b)** its corresponding charge/discharge profiles.

4.3. The performance of the GPE_20 in LFP-based Lithium-Metal Batteries

However, despite the less-than-encouraging results observed in Li-S technology, further battery cycling studies were conducted. This decision stemmed from the excellent individual properties exhibited by GPE_20 during its characterization. The main objective of this study was to determine whether the poor performance of the GPE_20 in LSBs was intrinsic to the electrolyte itself or potentially influenced by other factors associated with the challenging operating conditions of the Li-S technology. Consequently, to reassess the applicability of GPE_20 in LMBs, a new battery cycling was performed, involving the replacement of the sulfur cathode with a well-established LFP cathode chemistry. This active material shares certain attributes with sulfur, such as cost-effectiveness and environmental sustainability, albeit it offers lower energy densities [50,51].

Given the exclusive focus of this thesis on the development of Li-S technology, the findings concerning the performance of GPE_20 in LFP-based LMBs are comprehensively detailed in **Appendix 4**. In the initial results obtained at the coin cell level with high LFP loading (7 mg cm^{-2}, around 1.2 mAh cm^{-2}), GPE_20 exhibited exceptional performance (**Figure A.4.2**). Notably, it demonstrated outstanding rate capability, displaying a low capacity drop from high (C/20) to low (C/5) rates. Moreover, it displayed remarkable capacity recovery upon reverting to the C/10 rate. The cell also presented excellent stability, retaining up to 98% of its capacity after 60 cycles and maintaining an impressive CE of 99.2%.

Encouraged by the promising results achieved with the GPE_20 electrolyte at the coin cell level, a comprehensive evaluation of its scalability at the prototype level was performed by assembling a 20 cm^2 pouch cell (**Figure A.4.3**). The potential feasibility, flexibility, and safety of the GPE_20-based LFP pouch were successfully demonstrated by powering a bank of 20 commercial light-emitting diode (LED) lamps under different conditions. In addition, the developed pouch cell exhibited outstanding performance, mirroring the rate capability observed in the coin cell and delivering substantial capacity values. While the promising results achieved thus far were indeed encouraging, the effort to scale up this system was advanced through the integration of a thinner LMA of 50 µm thickness (**Figure A.4.4**). The significant reduction in the thickness of the LMA resulted in a proportional decrease in the N/P ratio, from 85 (using 500 µm) to 8.5 (using 50 µm). This modification was aimed at

aligning the system even more closely with practical operating conditions, representing a significant milestone in the ongoing exploration and development of the system. The prototype cell demonstrated successful cycling for up to 30 cycles, consistently delivering remarkable capacity values. Moreover, the cell exhibited relatively stable capacity values during its cycling at a C-rate of C/10, highlighting the exceptional compatibility of the system even with this thinner anode configuration.

As a result, this investigation, involving the substitution of the battery's active material, unequivocally evidenced that the observed poor performance of the GPE_20 electrolyte in Li-S cells was attributed to factors beyond the characteristics of the electrolyte. This underscores the imperative need for a detailed analysis of the underlying causes behind the performance observed in the Li-S system.

4.4. Deeper analysis of the poor LSB performance causes

As demonstrated in the previous section, the developed GPE confirmed its good properties by achieving stable cycling under practical conditions using LFP as cathode active material, even at the prototype level. Given this successful performance and the poor results obtained in the Li-S technology, as reported in **Section 4.2.4**, an in-depth study of the Li-S system was required to ascertain the cause behind this behavior.

4.4.1. Evaluation of GPE_20 compatibility with LMA

Fluorinated polymers are generally recognized for their notable resistance to electrochemical degradation. However, it is noteworthy that certain studies have indicated compromised stability of these polymers in alkaline environments, raising concerns about potential reactivity with the LMA [33,52,53]. Unfortunately, there has been limited investigation of this issue in the literature. To ascertain the chemical compatibility of GPE_20 with the LMA, different Li metal symmetric cells with this electrolyte were assembled and subjected to extended storage periods for subsequent post-mortem analysis.

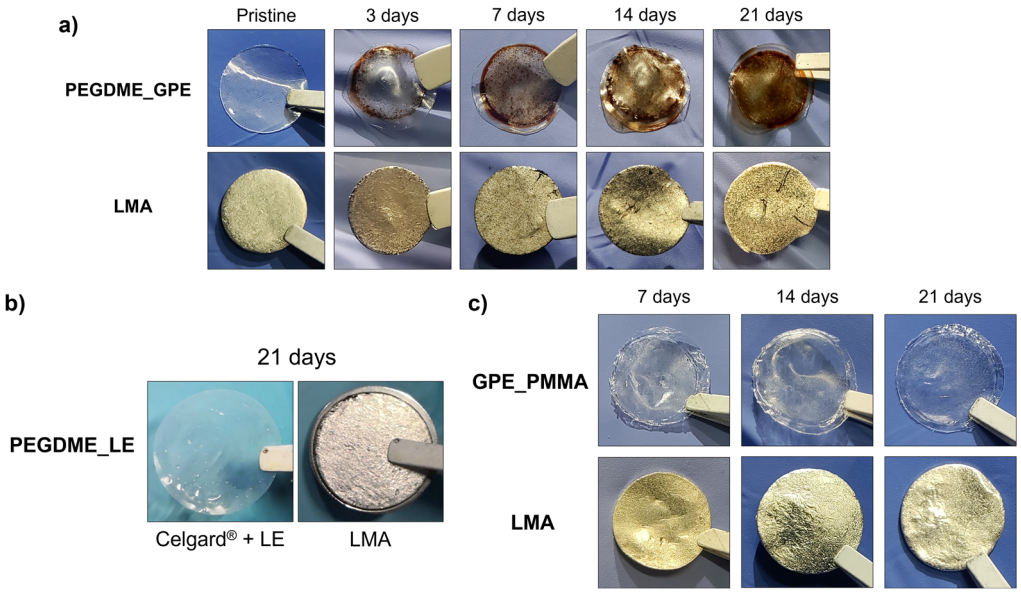

Figure 4.7. Li metal stability test of **a)** GPE_20, **b)** PEGDME_LE soaked in Celgard® separator, and **c)** PMMA-based GPE_20.

Figure 4.7a provides a graphical representation illustrating the compatibility of the developed GPE with the lithium metal over the exposure time, unmistakably revealing the degradation of the GPE_20 electrolyte. This observation is corroborated by the discernible changes in coloration and the emergence of brownish regions over exposure time. Significantly, the increasing extent of these colored regions over time unequivocally suggested an ongoing chemical interaction between the LMA and the GPE_20. With the confirmation of this chemical interaction, further experiments were conducted to identify the origin of this phenomenon, whether it originated from the liquid or the polymeric component of GPE_20. To this end, an identical stability study was performed using a Celgard® 2500 separator impregnated with PEGDME-based liquid electrolyte (PEGDME_LE). The results, depicted in **Figure 4.7b**, showcase the unaltered conditions of both the LMA and the separator, conclusively demonstrating the stability of the liquid component within the GPE_20. To further clarify the root cause of the degradation, a parallel stability investigation was carried out by preparing the GPE_20 electrolyte but replacing the PVdF-HFP polymer matrix with poly(methyl methacrylate) (PMMA) polymer material. As illustrated in **Figure 4.7c**, in this case, no discernible chemical reaction emerges, preserving the inherent transparency of the

GPE throughout the test duration. These additional experiments decisively implicate PVdF-HFP as the component responsible for the observed interaction with the LMA.

4.4.2. Chemical evaluation of the degradation reaction process

Subsequently, to gain further insights into the demonstrated degradation process, comprehensive attenuated total reflectance-Fourier transform infrared (ATR-FTIR) and XPS measurements of the degraded GPE_20 were carried out.

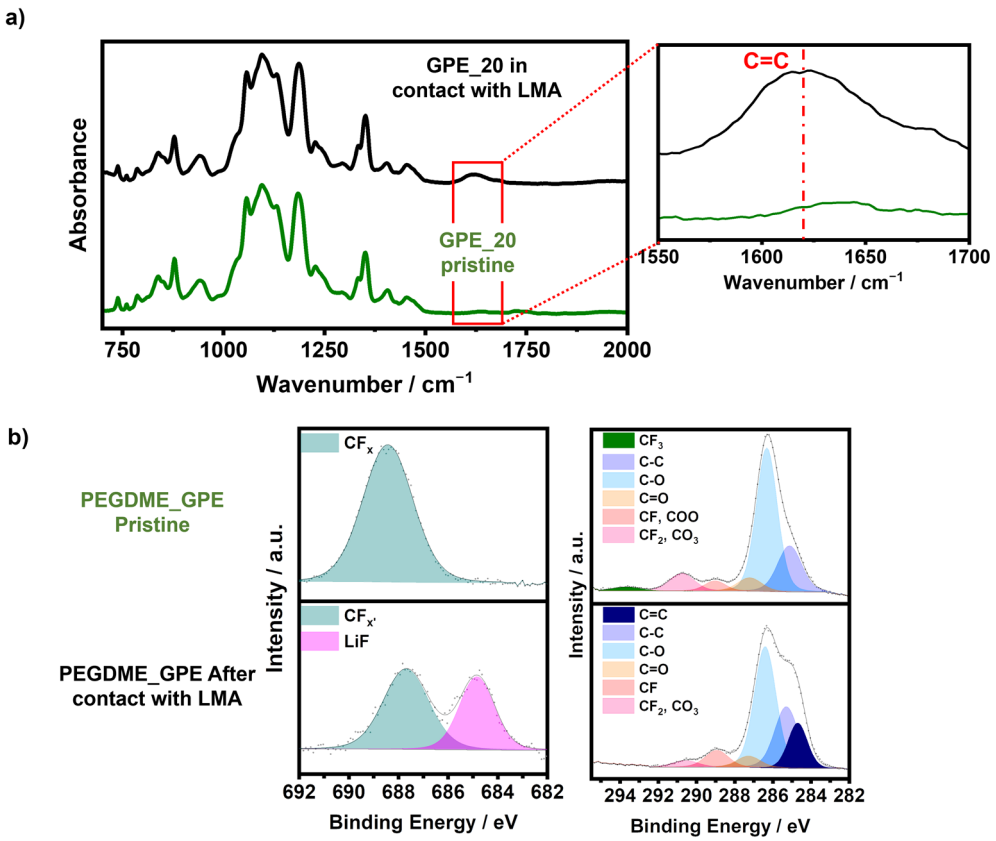

Figure 4.8. a) ATR-FTIR spectra of GPE_20 before and after being in contact with the Li anode and **b)** F 1s and C 1s regions corresponding XPS spectra of the pristine and degraded GPE_20.

For the ATR-FTIR analysis (**Figure 4.8a**), the pristine GPE_20 was used as the reference and compared with its counterpart after seven days of exposure to Li metal. The ATR-FTIR results indicate that, while there are no substantial changes in the spectra, a distinct peak emerges at 1600 cm^{-1}. This signal is assigned to the appearance

of the C=C double bond, a group formed by exposure of the polymer to Li metal by the release of HF from the polymer structure. This finding provides evidence of the reactivity between these two components.

To further corroborate this affirmation, an XPS analysis was conducted. **Figure 4.8b** illustrates the XPS spectra of both the pristine GPE and the GPE after seven days of contact with the Li metal. In the F 1s spectrum of the pristine GPE_20, a broad peak centered at 688.4 eV is evident, indicative of the CF_x units. This broad peak encompassed the CF_3, CF_2, and CF chemical environments of PVdF-HFP, as there is a minimal chemical shift between these environments in the F 1s core level. However, in the C 1s spectrum, a pronounced chemical shift between the various CF_x environments is evidenced, with distinct peaks at 293.7 eV, 290.8 eV, and 289.0 eV for CF_3, CF_2, and CF units, respectively. This shift resulted from the reduction in the electron density of carbon atoms as the number of highly electronegative fluorine neighbors increased. Upon exposure to Li metal, notable changes in these spectra became evident. The peak at 293.7 eV (CF_3) vanished, and the one at 290.8 eV (CF_2) diminished, while the signal at 289.0 eV (CF) significantly increased.

These observations unequivocally pointed to the defluorination process of the GPE_20 electrolyte when in contact with the Li metal. This is further supported by the shift and narrowing of the CF_x component in the F 1s spectrum, now centered at 687.7 eV. Moreover, a portion of the fluorine atoms of the GPE reacts with the Li metal, leading to the formation of the LiF compound at the electrolyte interface, as evidenced by the peak at 684.8 eV. Additionally, in the low binding energy region of the C 1s spectrum, an increase in the signal is observed, and an additional component at 284.5 eV is required for a proper fit. This finding further reinforced the formation of the C=C bonds due to the defluorination process of the GPE, consistent with the earlier suggestion from the ATR-FTIR analysis.

Hence, the findings presented in **Figure 4.8** offer substantial confirmation that the chemical instability experienced by the GPE_20 upon exposure to Li metal is unequivocally linked to the defluorination reaction occurring within the PVdF-HFP polymer matrix. This reaction resulted in the release of HF and the consequent formation of C=C double bonds within the GPE. Importantly, this chemical transformation is commonly facilitated by alkaline environments. In this case, this

alkaline environment can be generated by the native SEI layer of Li metal, which is highly rich in alkaline nature carbonate compounds.

4.4.3. Interfacial behavior analysis of the Li metal/GPE_20 system

To gain a better understanding of how this interfacial interaction influenced cell performance, an electrochemical impedance spectroscopy (EIS) analysis on the lithium symmetric cells was conducted. These analyses were performed during constant galvanostatic cycling at a current density of 0.3 mA cm^{-2}, which is representative of the current applied during LSB cycling at C/10.

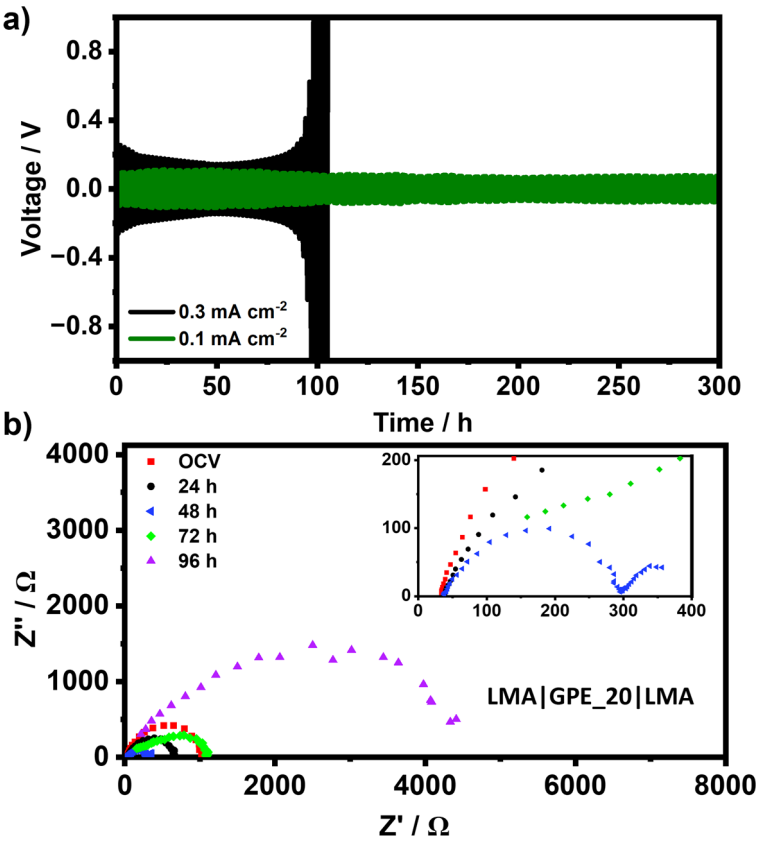

Figure 4.9. a) Li metal symmetric cell cycling comparison of the GPE_20 at different current densities and **b)** electrochemical impedance spectroscopy analyses during Li metal cycling at 0.3 mA cm^{-2}.

As displayed in **Figure 4.9a**, the GPE_20 system exhibits stable cycling with a 200 mV overvoltage for over 90 hours. However, beyond this cycling time, its overpotential fluctuates and gradually increases, ultimately leading to cell failure. By comparing these results with those obtained at a current density of 0.1 mA cm^{-2}, a noticeable difference in cell stability becomes evident with increasing current density.

The results from the EIS analysis conducted during Li metal symmetric cell cycling, as displayed in **Figure 4.9b**, offer valuable insights into the behavior of the high current cell. Remarkably, the bulk resistance of GPE_20 exhibited exceptional stability throughout the experiment, aligning with the impedance results observed in the LFP pouch cell during cycling. This observation confirms the preservation of an effective Li^+ transport process of the GPE_20, despite the ongoing chemical interaction with the LMA.

Shifting the focus to interfacial behavior, a significant evolution was observed. Initially, it exhibits a steady decrease for up to 50 hours of cycling, consistent with the reduction in the overvoltage shown in **Figure A.4.4b**. This phenomenon can be attributed to the formation of a stable LiF passivating layer over the Li metal electrode, a compound recognized for enhancing the cycling performance in LMBs. This decrease in overpotential can be concurrently associated with the improved initial kinetics of interfacial Li^+ transport. However, after the initial 72 hours of cycling, there is a sudden increase in the interfacial resistance. This notable rise may primarily stem from the dehydrofluorination degradation of the GPE, resulting in the formation of an excessively thick and rough layer on the LMA surface. Interestingly, these impedance results were consistent with the abrupt increase in cell overpotential observed at approximately 100 hours of cycling, as displayed in **Figure 4.9a**, thereby explaining the root causes of the cell failure. Therefore, the performance differences compared to low current densities can be attributed to the accelerated degradation process due to the increase in the current densities. This phenomenon leads to a more rapid formation of a thick layer on the LMA, consequently translating into a substantial increase in the interfacial resistance.

Following the EIS analysis, a post-mortem study of the cell components was conducted. As depicted in **Figure 4.10a**, GPE_20 undergoes a transition from its initial transparency to a brownish color, accompanied by the formation of a dark layer on the surface of the LMA. This observation is in line with the results presented in

Figure 4.7, where this behavior was evident only by exposing the electrolyte to fresh lithium. Additionally, the XPS data of the LMA (**Figure 4.10b**) unequivocally confirmed the occurrence of dehydrofluorination reaction within the polymer matrix. This process leads to the generation of a LiF-rich SEI layer on the surface of the LMA. As previously highlighted, the presence of this layer is of paramount importance, as it contributes to a more uniform distribution of ions and stabilizes the Li deposition, ultimately enhancing the stability of the LMA. However, it is noteworthy that the LiF compound presents extremely low ionic conductivity, measured at 10^{-13} to 10^{-14} S cm^{-1} in the anode surface [54,55]. Hence, an excessively thick LiF-rich layer may hinder efficient Li^+ transport, leading to an increase in interfacial resistivity. With this in mind, the formation of an excessively thick LiF-rich insulating layer due to the continuous reaction between GPE and LMA is corroborated as the main factor of the sudden overpotential increase observed in the symmetric cell cycling and its remarkable increase in the interfacial resistance (**Figures 4.9a** and **b**, respectively).

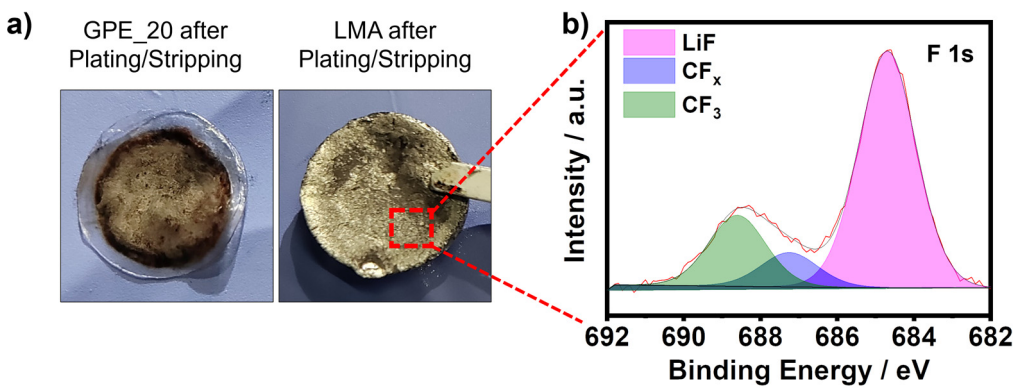

Figure 4.10. a) Post-mortem images of GPE_20 and LMA after the 0.3 mA cm^{-2} cycling test and **b)** the corresponding F 1s region of the XPS spectra of the Li metal surface.

The PVdF-based GPE displays evident reactivity with the LMA, noticeable not only upon contact but also significantly accentuated after galvanostatic cycling. However, the evaluation of the LFP-based LMB cycling results reveals a remarkable performance demonstrated by GPE_20. This observation is noteworthy, given that GPE_20 shows a similar reactivity process with the LMA as in the case of Li-S cells. Consequently, the dehydrofluorination reaction alone cannot be solely attributed as the exclusive cause of the poor performance of GPE_20 in Li-S technology.

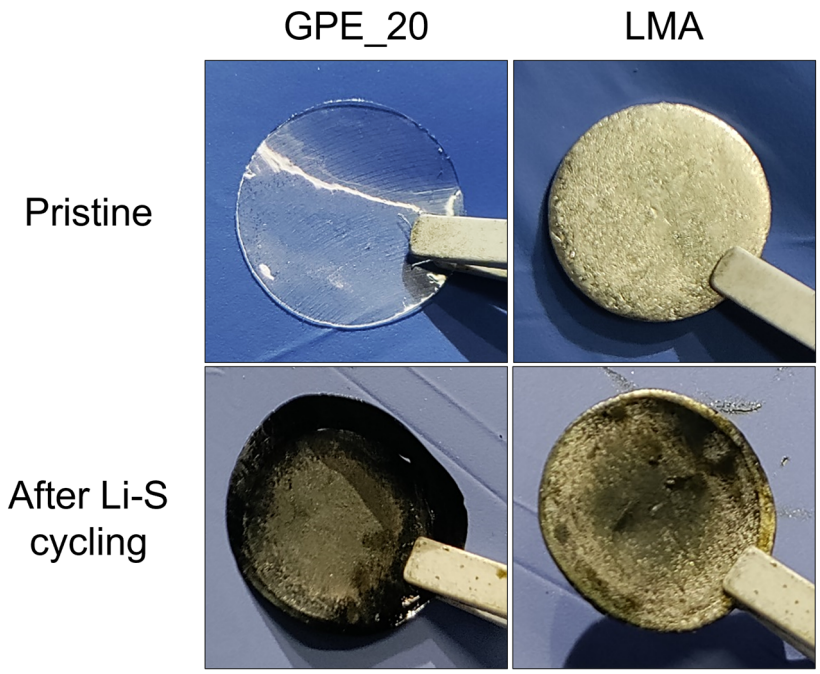

Figure 4.11. Optical images comparison of GPE_20 and LMA before and after Li-S cycling.

Consequently, to thoroughly explore the underlying factors, a post-mortem analysis of the Li-S cell after cycling was performed. As displayed in **Figure 4.11**, no additional degradation was observed in the LMA when compared to its state after the galvanostatic cycling. This observation suggested that the capacity drop was not attributable to any additional anode-related issues. Conversely, the GPE_20 membrane presented a darker color, which was more intense than that observed in the case of Li metal symmetric cells. The heightened level of degradation in the Li-S cells raises questions regarding the stability of the GPE_20 in the presence of LiPS.

4.4.4. GPE_20 degradation mechanism in Li-S technology

In response to the emerging question, a complementary study was completed to assess the compatibility of GPE_20 when exposed to the different elements of the Li-S cell.

As depicted in **Figure 4.12a**, upon the introduction of LiPS dissolution, GPE_20 undergoes a change in coloration to a reddish hue, primarily due to the presence of these compounds. Remarkably, there was no observable degradation within the

electrolyte. Unfortunately, this experiment underscores that developed GPE does not serve as an impermeable barrier to LiPS. Lastly, the interaction between the partially dehydrofluorinated matrix and the LiPS solution was evaluated. Under these conditions, GPE_20 experiences complete degradation, resulting in a dark blackish coloration consistent with the observations in the post-mortem analysis. This outcome strongly suggested a potential interaction between the dehydrofluorinated GPE_20 and the LiPS compounds present during battery cycling.

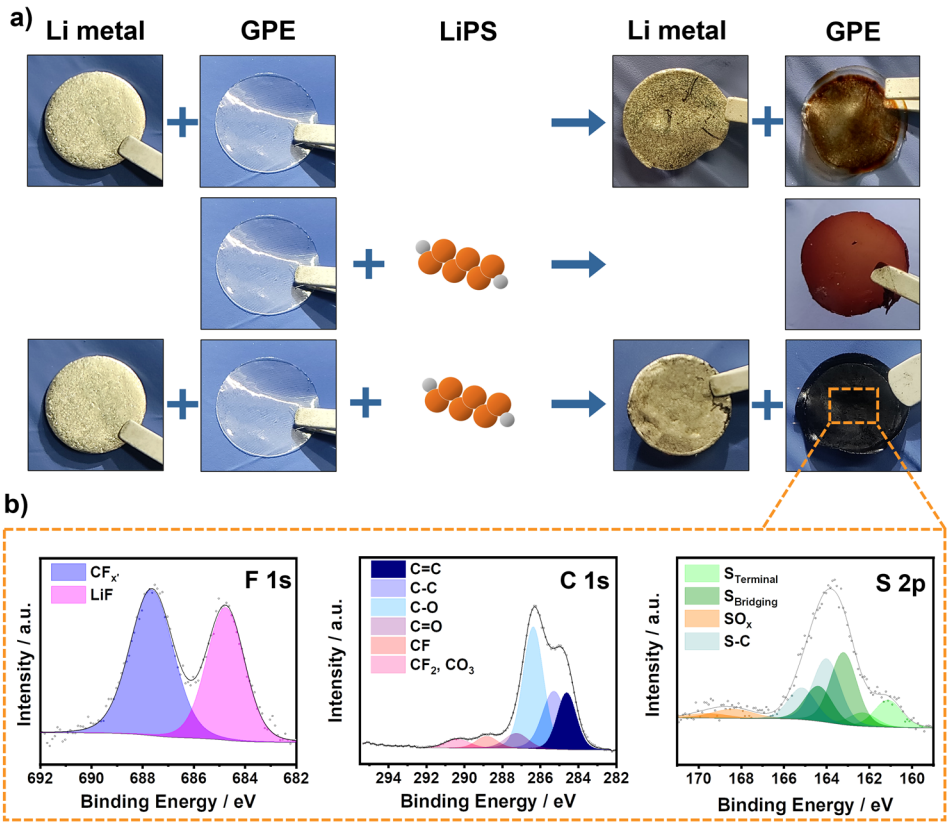

Figure 4.12. a) Schematic illustration of the behavior of the membrane towards the different cell compounds. **b)** XPS of F 1s, C 1s, and S 2p of the GPE after the combination of the dehydrofluorination process of the GPE and the presence of LIPS.

The XPS analysis of the sample (**Figure 4.12b**) subsequently confirmed the covalent nature of the interaction between LiPS and the dehydrofluorinated polymeric matrix, resulting in the formation of C–S bonds. This phenomenon was evident from the emergence of the light blue S 2p doublet, essential for accurate

spectrum fitting, along with the two green doublets representing the bridging and terminal sulfurs within the LiPS chains.

Consequently, the poor performance of the GPE_20 in Li-S cells stemmed from the undesirable interaction between the LiPS dissolved in the liquid component of the GPE and the C=C bonds generated by the dehydrofluorination reaction of the PVdF-HFP polymer matrix with the LMA. This interaction leads to the formation of C-S bonds, resulting in the irreversible loss of active material. Notably, this reaction exhibited similarities to the vulcanization process, where sulfur groups react with the C=C carbon double bonds in the system. This provides a highly plausible explanation for the observed capacity drop in the Li-S cells. Additionally, this hypothesis would also explain the favorable performance of GPE_20 in LFP-based LMBs. In this case, the absence of LiPS during its cycling, coupled with the suitable individual properties of GPE_20, allows exceptional cycling in this technology.

4.4.5. Strategy for improving the performance of GPE_20 in LSBs

Upon the comprehensive analysis and profound understanding of the root causes contributing to the poor performance of the GPE_20 in Li-S technology, an effective approach was developed to improve the obtained cell performance. In response to this challenge, the incorporation of $LiNO_3$ as electrolyte additive emerged as a potential solution. The selection of $LiNO_3$ was motivated due to its potential to address the underlying issues. Firstly, $LiNO_3$ is renowned for its ability to form a nitrogen-rich protective layer over the LMA, thus mitigating the issues associated with the dehydrofluorination of the polymer matrix [56–58]. Secondly, it is documented that $LiNO_3$ serves as an oxidative catalyst for LiPS, effectively binding them and facilitating their redox reactions [59]. This property would alleviate the dissolution of LiPS within the liquid component, thereby preventing the undesired vulcanization process.

As a result of these considerations, 2 wt.% of $LiNO_3$ was introduced into the GPE_20 formulation. As depicted in **Figure 4.13a**, a comparative analysis of the LSB performance was conducted between two systems: one incorporating the $LiNO_3$ additive and one without it. The obtained performance results reveal a clear improvement in cell performance after the addition of $LiNO_3$. The initial capacity in the $LiNO_3$-containing cell was slightly lower, potentially attributed to the additional resistance introduced by the protective layer formed upon the reduction of the

additive on the LMA surface. However, a significant performance enhancement was evidenced in terms of mitigating the persistent capacity drop observed in the absence of $LiNO_3$. Instead, the $LiNO_3$-incorporated system exhibits stable cycling behavior, with an acceptable discharge capacity of 760 mAh g^{-1} after 15 cycles. This result underscores a significant enhancement of the LSB performance, validating the effectiveness of the proposed approach.

Nevertheless, it is important to note that the improvement observed upon the addition of $LiNO_3$ was sustained for a limited lifespan of 15 cycles, beyond which a constant capacity decay became apparent. This decline in cell performance can be ascribed to the complete consumption of the $LiNO_3$ additive, surfacing again the previously known issues **(Figure 4.13b**). This outcome highlights the critical importance and necessity of protecting the LMA to overcome the challenges encountered in PVdF-based GPEs within the context of Li-S technology. Such protection can be realized through the introduction of additives as an in-situ approach (as demonstrated in this case with $LiNO_3$ additive), by implementing ex-situ pretreatment of the LMA before cell assembly, or by employing a combination of both strategies. Furthermore, it emphasizes the significance of retaining LiPS at the cathode side to prevent their solubility into the electrolyte, thereby avoiding undesired reactions of C=C bonds presented in the polymer host after the dehydrofluorination. This holistic understanding of the interactions within the cell is essential for achieving improved performance in LSBs.

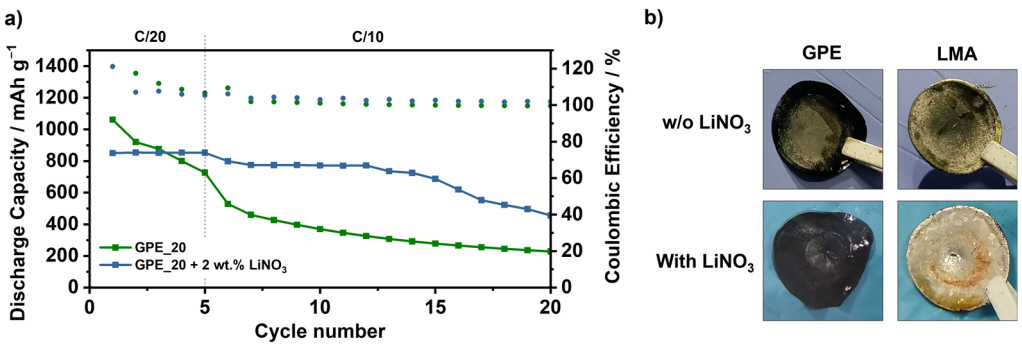

Figure 4.13. a) Comparison of the battery performance of GPE_20 with and without $LiNO_3$ additive and **b)** their corresponding optical post-mortem analysis of the membranes and LMA.

4.5. Summary and conclusions

In this chapter, the performance of gel polymer electrolytes in the context of LSBs has been explored. To this end, a PVDF-HFP-based GPE incorporating PEGDME as a plasticizer has been successfully prepared using a straightforward and readily scalable one-pot solvent-casting production method. This GPE exhibited outstanding individual properties, including notable mechanical properties, suitable RT ionic conductivity of 3.4×10^{-4} S cm^{-1}, excellent thermal stability up to 250 °C, and, crucially, non-flammable nature. Regarding the compatibility with the LMA, a notable interaction between the PVdF-HFP polymeric matrix with the negative electrode was observed, initiating the dehydrofluorination process of the GPE and the formation of a robust LiF-containing SEI layer on the surface of the LMA. This interaction proved highly favorable for the LFP-based LMB, yielding excellent performances at the coin cell level, even with a high LFP content (6-7 mg cm^{-2}). Furthermore, due to the substantial potential demonstrated by this system, the developed GPE was successfully scaled up for prototype cells under practical operating conditions, setting a significant milestone for such electrolytes in LMBs. However, despite the excellent results obtained in LFP batteries, the interaction between the polymer matrix and the LMA introduced an additional challenge in LSBs, resulting in poor performance for this technology. As elucidated throughout the chapter, this underperformance stemmed from the irreversible reaction between the LiPS dissolved during battery cycling in the liquid component of the GPE and the C=C double bonds formed in the polymer matrix due to the dehydrofluorination process. This reaction induced the irreversible loss of active material, resulting in a continuous decrease in capacity. This problem was partially mitigated by the incorporation of $LiNO_3$ salt as an additive in the GPE formulation. $LiNO_3$ effectively addressed the root causes of the irreversible reaction and temporally mitigated the capacity drop of the cell. Therefore, this chapter evidences the critical necessity for the development of meticulously engineered electrolytes that simultaneously prevent the LiPS dissolution in the media and effectively enhance the compatibility with the LMA to ensure a favorable operation of LSBs.

4.6. Bibliography

[1] Y. Liu, Y. Elias, J. Meng, D. Aurbach, R. Zou, D. Xia, Q. Pang, Electrolyte solutions design for lithium-sulfur batteries, Joule. 2021, 5, 2323–2364. https://doi.org/10.1016/j.joule.2021.06.009.

[2] Q. Zou, Y. Lu, Liquid electrolyte design for metal-sulfur batteries : Mechanistic understanding and perspective, 2021, 3, 12115. https://doi.org/10.1002/eom2.12115.

[3] N. Angulakshmi, R.B. Dhanalakshmi, S. Sathya, J. Ahn, A.M. Stephan, Understanding the electrolytes of lithium-sulfur batteries, Batteries Supercaps 2021, 4, 1064–1095. https://doi.org/10.1002/batt.202000273.

[4] F. Wu, F. Chu, G.A. Ferrero, M. Sevilla, A.B. Fuertes, O. Borodin, Y. Yu, G. Yushin, Boosting high-performance in lithium-sulfur batteries via dilute electrolyte, Nano Lett. 2020, 20, 5391–5399. https://doi.org/10.1021/acs.nanolett.0c01778.

[5] Y. Lin, S. Huang, L. Zhong, S. Wang, D. Han, S. Ren, M. Xiao, Y. Meng, Organic liquid electrolytes in Li-S batteries: actualities and perspectives, Energy Storage Mater. 2021, 34, 128–147. https://doi.org/10.1016/j.ensm.2020.09.009.

[6] S. Ponnada, M.S. Kiai, D.B. Gorle, A. Nowduri, History and recent developments in divergent electrolytes towards high-efficiency lithium-sulfur batteries-a review, Mater. Adv. 2021, 2, 4115–4139. https://doi.org/10.1039/d1ma00332a.

[7] X. Kong, Y. Kong, Y. Zheng, L. He, D. Wang, Y. Zhao, Hydrofluoroether diluted dual-salts-based electrolytes for lithium-sulfur batteries with enhanced lithium anode protection, Small 2022, 18, 2205017. https://doi.org/10.1002/smll.202205017.

[8] A. Gupta, A. Bhargav, A. Manthiram, Highly solvating electrolytes for lithium–sulfur batteries, Adv. Energy Mater. 2019, 9, 1803096. https://doi.org/10.1002/aenm.201803096.

[9] J. Sun, K. Zhang, Y. Fu, W. Guo, Benzoselenol as an organic electrolyte additive in Li-S battery, Nano Res. 2023, 16, 3814–3822. https://doi.org/10.1007/s12274-022-4361-z.

[10] Q. Jin, K.X. Zhao, L.L. Wu, L. Li, L. Kong, X.T. Zhang, Enhancing Li cycling coulombic efficiency while mitigating “shuttle effect” of Li-S battery through sustained release of LiNO3, J. Energy Chem. 2023, 84, 22–29. https://doi.org/10.1016/j.jechem.2023.05.020.

[11] H. Yang, C. Guo, J. Chen, A. Naveed, J. Yang, Y. Nuli, J. Wang, An intrinsic flame-retardant organic electrolyte for safe lithium-sulfur batteries, Angew. Chemie 2019, 58, 791–795. https://doi.org/10.1002/anie.201811291.

[12] M. He, X. Li, N.G. Holmes, R. Li, J. Wang, G. Yin, P. Zuo, X. Sun, Flame-retardant and polysulfide-suppressed ether-based electrolytes for high-temperature Li-SbBatteries, ACS Appl. Mater. Interfaces 2021, 13, 38296–38304. https://doi.org/10.1021/acsami.1c09492.

[13] P. Jaumaux, J. Wu, D. Shanmukaraj, Y. Wang, D. Zhou, B. Sun, F. Kang, B. Li, M. Armand, G. Wang, Non-flammable liquid and quasi-solid electrolytes toward highly-safe alkali metal-based batteries, Adv. Funct. Mater. 2021, 31, 2008644. https://doi.org/10.1002/adfm.202008644.

[14] J. Chen, A. Naveed, Y. Nuli, J. Yang, J. Wang, Designing an intrinsically safe organic electrolyte for rechargeable batteries, Energy Storage Mater. 2020, 31, 382–400. https://doi.org/10.1016/j.ensm.2020.06.027.

[15] Z. Ye, J. Li, Z. Li, Recent progress in nonflammable electrolytes and cell design for safe Li-ion batteries, J. Mater. Chem. A 2023, 11, 15576–15599. https://doi.org/10.1039/d3ta01951a.

[16] L. Meabe, I. Aldalur, S. Lindberg, M. Arrese-Igor, M. Armand, M. Martinez-Ibañez, H. Zhang, Solid-state electrolytes for safe rechargeable lithium metal batteries: a strategic view, Mater. Futur. 2023, 2, 033501. https://doi.org/10.1088/2752-5724/accdf3.

[17] H. Pan, Z. Cheng, P. He, H. Zhou, A review of solid-state lithium-sulfur battery: ion transport and polysulfide chemistry, Energy and Fuels 2020, 34, 11942–11961. https://doi.org/10.1021/acs.energyfuels.0c02647.

[18] Q. Zhu, C. Ye, D. Mao, Solid-state electrolytes for lithium – sulfur batteries: challenges , progress , and strategies, Nanomaterials, 2022, 12, 3612. https://doi.org/10.3390**/**nano12203612.

[19] X. Liang, L. Wang, X. Wu, X. Feng, Q. Wu, Y. Sun, H. Xiang, J. Wang, Solid-state electrolytes for solid-state lithium-sulfur batteries: Comparisons, advances and prospects, J. Energy Chem. 2022, 73, 370–386. https://doi.org/10.1016/j.jechem.2022.06.035.

[20] S. Yang, Z. Zhang, J. Lin, L. Zhang, L. Wang, S. Chen, C. Zhang, X. Liu, Recent Progress in quasi/all-solid-state electrolytes for lithium–sulfur batteries, Front. Energy Res. 2022, 10, 945003. https://doi.org/10.3389/fenrg.2022.945003.

[21] J. Janek, W.G. Zeier, Challenges in speeding up solid-state battery development, Nat. Energy 2023, 8, 230–240. https://doi.org/10.1038/s41560-

023-01208-9.

[22] S. Dong, L. Sheng, L. Wang, J. Liang, H. Zhang, Z. Chen, H. Xu, X. He, Challenges and prospects of all-solid-state electrodes for solid-state lithium Batteries, Adv. Funct. Mater. 2023, 33, 2304371. https://doi.org/10.1002/adfm.202304371.

[23] Y.Y. Sun, Q. Zhang, L. Yan, T.B. Wang, P.Y. Hou, A review of interfaces within solid-state electrolytes: fundamentals, issues and advancements, Chem. Eng. J. 2022, 437, 135179. https://doi.org/10.1016/j.cej.2022.135179.

[24] Z. Zhou, X. Pei, T. Zhang, L. Wang, J. Hong, Y. Lu, G. He, A gel polymer electrolyte with 2D filler-reinforced for dendrite suppression Li-Ion batteries, Electroanalysis 2023, 35, 02200306. https://doi.org/10.1002/elan.202200306.

[25] C. Ma, W. Cui, X. Liu, Y. Ding, Y. Wang, In situ preparation of gel polymer electrolyte for lithium batteries: Progress and perspectives, InfoMat 2022, 4, 12232. https://doi.org/10.1002/inf2.12232.

[26] J. Zhou, H. Ji, J. Liu, T. Qian, C. Yan, A new high ionic conductive gel polymer electrolyte enables highly stable quasi-solid-state lithium sulfur battery, Energy Storage Mater. 2019, 22, 256–264. https://doi.org/10.1016/j.ensm.2019.01.024.

[27] G. Jiang, C. Qu, F. Xu, E. Zhang, Q. Lu, X. Cai, S. Hausdorf, H. Wang, S. Kaskel, Glassy metal–organic-framework-based quasi-solid-state electrolyte for high-performance lithium-metal batteries, Adv. Funct. Mater. 2021, 31, 12232. https://doi.org/10.1002/adfm.202104300.

[28] H. Yong, H. Park, C. Jung, Quasi-solid-state gel polymer electrolyte for a wide temperature range application of acetonitrile-based supercapacitors, J. Power Sources 2020, 447, 227390. https://doi.org/10.1016/j.jpowsour.2019.227390.

[29] Y.G. Cho, C. Hwang, D.S. Cheong, Y.S. Kim, H.K. Song, Gel/solid polymer electrolytes characterized by in situ gelation or polymerization for electrochemical energy systems, Adv. Mater. 2019, 31, 1804909. https://doi.org/10.1002/adma.201804909.

[30] J. Zheng, W. Li, X. Liu, J. Zhang, X. Feng, W. Chen, Progress in gel polymer electrolytes for sodium-ion batteries, Energy Environ. Mater. 2023, 6, 12422. https://doi.org/10.1002/eem2.12422.

[31] G. Hernández, T.K. Lee, M. Erdélyi, D. Brandell, J. Mindemark, Do non-coordinating polymers function as host materials for solid polymer electrolytes? The case of PVdF-HFP, J. Mater. Chem. A 2023, 11, 15329–15335. https://doi.org/10.1039/d3ta01853a.

[32] S. Chen, K. Wen, J. Fan, Y. Bando, D. Golberg, Progress and future prospects of high-voltage and high-safety electrolytes in advanced lithium batteries: From liquid to solid electrolytes, J. Mater. Chem. A 2018, 6, 11631–11663. https://doi.org/10.1039/c8ta03358g.

[33] J. Qian, B. Jin, Y. Li, X. Zhan, Y. Hou, Q. Zhang, Research progress on gel polymer electrolytes for lithium-sulfur batteries, J. Energy Chem. 2021, 56, 420–437. https://doi.org/10.1016/j.jechem.2020.08.026.

[34] Y. Wu, Y. Li, Y. Wang, Q. Liu, Q. Chen, M. Chen, Advances and prospects of PVDF based polymer electrolytes, J. Energy Chem. 2022, 64, 62–84. https://doi.org/10.1016/j.jechem.2021.04.007.

[35] D. Mouraliraman, N. Shaji, S. Praveen, M. Nanthagopal, C.W. Ho, M.V. Karthik, T. Kim, C.W. Lee, Thermally stable PVDF-HFP-based gel polymer electrolytes for high-performance lithium-ion batteries, Nanomaterials 2022, 12, 1056. https://doi.org/10.3390/nano12071056.

[36] M. Celik, A. Kızılaslan, M. Can, T. Cetinkaya, H. Akbulut, Electrochemical investigation of PVDF: HFP gel polymer electrolytes for quasi-solid-state Li-O2 batteries: effect of lithium salt type and concentration, Electrochim. Acta 2021, 371 137824. https://doi.org/10.1016/j.electacta.2021.137824.

[37] J. Castillo, A. Santiago, X. Judez, I. Garbayo, J.A. Coca Clemente, M.C. Morant-Miñana, A. Villaverde, J.A. González-Marcos, H. Zhang, M. Armand, C. Li, Safe, flexible, and high-performing gel-polymer electrolyte for rechargeable lithium metal batteries, Chem. Mater. 2021, 33, 8812–8821. https://doi.org/10.1021/acs.chemmater.1c02952.

[38] V. Madhani, D. Kumar, D.K. Kanchan, M. Singh Rathore, Recent advances and prospects of K-ion conducting polymer electrolytes, J. Electroanal. Chem. 2023, 935, 117334. https://doi.org/10.1016/j.jelechem.2023.117334.

[39] C.H. Tsao, C.Y. Wang, E. Trevisanello, F.H. Richter, D. Kuo, J. Janek, C.H. Chang, H. Teng, P.L. Kuo, Polyethylene glycol dimethyl ether-plasticized poly(vinylidene difluoride)-based polymer electrolytes inhibit dendrite growth and enable stable cycling for lithium-metal batteries, ACS Appl. Energy Mater. 2023, 6, 5662–5670. https://doi.org/10.1021/acsaem.2c03892.

[40] Z. Fang, Y. Luo, H. Liu, Z. Hong, H. Wu, F. Zhao, P. Liu, Q. Li, S. Fan, W. Duan, J. Wang, Boosting the oxidative potential of polyethylene glycol-based polymer electrolyte to 4.36 V by spatially restricting hydroxyl groups for high-voltage flexible lithium-ion battery applications, Adv. Sci. 2021, 8, 2100736. https://doi.org/10.1002/advs.202100736.

[41] L. Porcarelli, C. Gerbaldi, F. Bella, J.R. Nair, Super soft all-ethylene oxide

polymer electrolyte for safe all- solid lithium batteries, Sci Rep. 2016, 6, 19892. https://doi.org/10.1038/srep19892.

[42] Q. Sun, S. Wang, Y. Ma, D. Song, H. Zhang, X. Shi, N. Zhang, L. Zhang, Li-ion transfer mechanism of gel polymer electrolyte with sole fluoroethylene carbonate solvent, Adv. Mater. 2023, 35, 2300998. https://doi.org/10.1002/adma.202300998.

[43] S. Zhang, Z. Liu, R. Liu, L. Du, L. Zheng, Z. Liu, K. Li, M.C. Lin, Y. Bian, M. Cai, H. Du, A facile in-situ polymerization of cross-linked Poly(ethyl acrylate)-Based gel polymer electrolytes for rechargeable aluminum batteries, J. Power Sources 2023, 575, 233110. https://doi.org/10.1016/j.jpowsour.2023.233110.

[44] H. Zhang, M. Armand, History of Solid Polymer Electrolyte-Based Solid-State Lithium Metal Batteries: A Personal Account, Isr. J. Chem. 61 (2021) 94–100. https://doi.org/10.1002/ijch.202000066.

[45] J. Zhang, B. Sun, X. Xie, K. Kretschmer, G. Wang, Enhancement of stability for lithium oxygen batteries by employing electrolytes gelled by poly(vinylidene fluoride-co-hexafluoropropylene) and tetraethylene glycol dimethyl ether, Electrochim. Acta 2015, 183, 56–62. https://doi.org/10.1016/j.electacta.2015.03.103.

[46] J. Wang, C. Wang, W. Wang, W. Li, J. Lou, Carboxymethylated nanocellulose-based gel polymer electrolyte with a high lithium ion transfer number for flexible lithium-ion batteries application, Chem. Eng. J. 2022, 428, 132604. https://doi.org/10.1016/j.cej.2021.132604.

[47] Y. Wang, K. Huang, P. Zhang, H. Li, H. Mi, PVDF-HFP based polymer electrolytes with high Li+ transference number enhancing the cycling performance and rate capability of lithium metal batteries, Appl. Surf. Sci. 2022, 574, 151593. https://doi.org/10.1016/j.apsusc.2021.151593.

[48] T. Chen, J. You, R. Li, H. Li, Y. Wang, C. Wu, Y. Sun, L. Yang, Z. Ye, B. Zhong, Z. Wu, X. Guo, Ultra-low concentration electrolyte enabling LiF-rich SEI and dense plating/stripping processes for lithium metal batteries, Adv. Sci. 2022, 9, 2203216. https://doi.org/10.1002/advs.202203216.

[49] K. Huang, S. Song, Z. Xue, X. Niu, X. Peng, Y. Xiang, In-situ formation of LiF-rich solid-electrolyte interphases on 3D lithiophilic skeleton for stable lithium metal anode, Energy Storage Mater. 2023, 55, 301–311. https://doi.org/10.1016/j.ensm.2022.12.003.

[50] S. Suttison, K. Pengpat, U. Intatha, J. Fan, W. Zhang, S. Eitssayeam, Preparation of LFP-based cathode materials for lithium-ion battery applications, Mater. Today Proc. 2022, 65, 2347–2350.

https://doi.org/10.1016/j.matpr.2022.05.302.

[51] J. Kumar, R.R. Neiber, J. Park, R. Ali Soomro, G.W. Greene, S. Ali Mazari, H. Young Seo, J. Hong Lee, M. Shon, D. Wook Chang, K. Yong Cho, Recent progress in sustainable recycling of LiFePO4-type lithium-ion batteries: Strategies for highly selective lithium recovery, Chem. Eng. J. 2022, 431 133993. https://doi.org/10.1016/j.cej.2021.133993.

[52] C. Xue, S. Guan, B. Hu, X. Wang, C. Xin, S. Liu, J. Yu, K. Wen, L. Li, C.W. Nan, Significantly improved interface between PVDF-based polymer electrolyte and lithium metal via thermal - electrochemical treatment, Energy Storage Mater. 2022, 46, 452–460. https://doi.org/10.1016/j.ensm.2022.01.034.

[53] T. Liu, Z. Chang, Y. Yin, K. Chen, Y. Zhang, X. Zhang, The PVDF-HFP gel polymer electrolyte for Li-O2 battery, Solid State Ionics 2018, 318, 88–94. https://doi.org/10.1016/j.ssi.2017.08.001.

[54] M. He, R. Guo, G.M. Hobold, H. Gao, B.M. Gallant, The intrinsic behavior of lithium fluoride in solid electrolyte interphases on lithium, Proc. Natl. Acad. Sci. 2020, 117, 73–79. https://doi.org/10.1073/pnas.1911017116.

[55] S. Park, S. Kim, J.A. Lee, M. Ue, N.S. Choi, Liquid electrolyte chemistries for solid electrolyte interphase construction on silicon and lithium-metal anodes, Chem. Sci. 2023, 14, 9996–10024. https://doi.org/10.1039/d3sc03514j.

[56] E. Winter, M. Briccola, T.J. Schmidt, S. Trabesinger, Enabling LiNO 3 in carbonate electrolytes by flame-retardant electrolyte additive as a cosolvent for enhanced performance of lithium metal batteries , Appl. Res. 2022, 2022, 202200096. https://doi.org/10.1002/appl.202200096.

[57] Y. Liang, W. Wu, D. Li, H. Wu, C. Gao, Z. Chen, L. Ci, J. Zhang, Highly Stable Lithium Metal Batteries by Regulating the Lithium Nitrate Chemistry with a Modified Eutectic Electrolyte, Adv. Energy Mater. 2022, 12, 2202493. https://doi.org/10.1002/aenm.202202493.

[58] S. Stuckenberg, M.M. Bela, C.T. Lechtenfeld, M. Mense, V. Küpers, T.T.K. Ingber, M. Winter, M.C. Stan, Influence of LiNO3 on the Lithium Metal Deposition Behavior in Carbonate-Based Liquid Electrolytes and on the Electrochemical Performance in Zero-Excess Lithium Metal Batteries, Small 2305203. https://doi.org/10.1002/smll.202305203.

[59] N. Ding, L. Zhou, C. Zhou, D. Geng, J. Yang, S.W. Chien, Z. Liu, M.F. Ng, A. Yu, T.S.A. Hor, M.B. Sullivan, Y. Zong, Building better lithium-sulfur batteries: From LiNO3 to solid oxide catalyst, Sci. Rep. 2016, 6, 33154. https://doi.org/10.1038/srep33154.

Chapter V

Development of Sparingly Solvating Electrolytes for High-Performing, Safe, and Long-Cycle Life Li-S Batteries

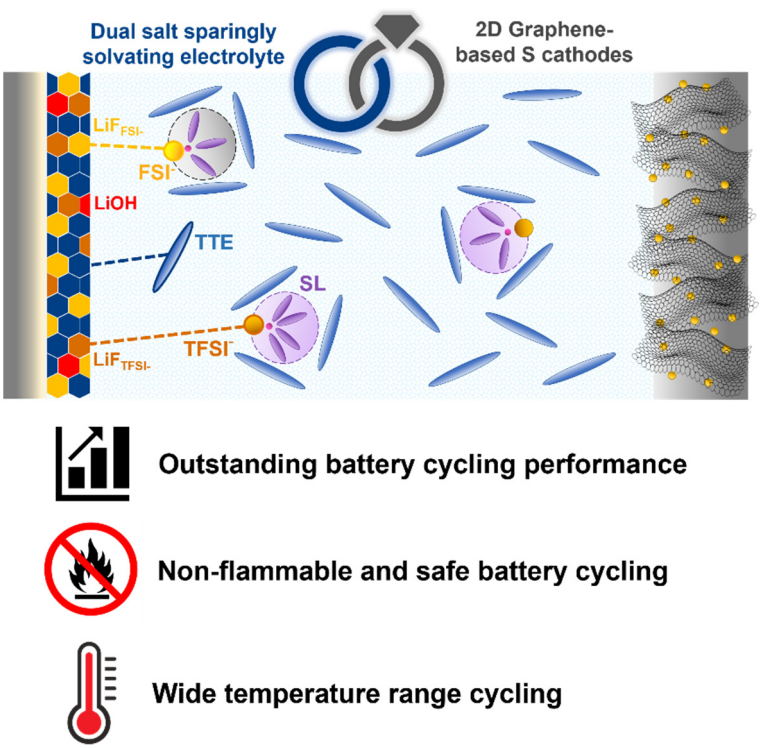

5.1. Introduction

The insights extracted from **Chapter IV** evidenced the challenges of developing an ideal electrolyte tailored for perfect integration in Li-S technology, given the complex operating nature of this battery technology. Consequently, the work to pursue an electrolyte capable of ensuring system safety and optimizing battery performance remains an ongoing task, the key to achieving the objectives outlined in this thesis.

The preceding chapters have brought to light the underlying factors contributing to the suboptimal performances observed in the employed electrolytes. Analogous to the conventional DME/DOL electrolyte, the PEGDME liquid electrolyte used for GPE formulation in **Chapter IV** displayed a pronounced dissolution of LiPS from the sulfur cathode. This phenomenon, coupled with the degradation of the PVdF-based polymer matrix with the LMA, initiates intricate parasitic reactions, thereby yielding suboptimal performance in LSB. Therefore, both DME/DOL and GPE_20 electrolytes exhibit LiPS dissolution as a shared feature, that directly influences the long-term cycling. Furthermore, the uneven deposition of lithium evidenced by the DME/DOL electrolyte, along with the undesired reactivity between the GPE and the LMA, highlights the imperative to protect the anode surface for stable cyclability. Hence, the limited solubility of LiPS and suitable compatibility with the LMA are established as the fundamental properties that an ideal electrolyte must possess.

To this end, different electrolyte alternatives have been explored as substitutes for conventional electrolytes to mitigate the challenge of LiPS dissolution. These alternatives encompass ionic liquids, solid-state electrolytes, highly concentrated electrolytes (HCEs), and localized high-concentration electrolytes (LHCEs) [1–4]. Among these options, the development of LHCEs, commonly referred to as sparingly solvating electrolytes (SSEs) in Li-S technology, has emerged as an appealing approach for their implementation in LSBs [5–7]. The functionality of SSEs lies in the formulation of an HCE, benefiting from the promising properties offered by their unique solvation structure [8,9]. However, the widespread commercial adoption of HCEs encounters several challenges, such as high viscosity, low ionic conductivity, and high cost [10–12]. As a solution for these limitations, inert solvents, primarily from the family of hydrofluoroethers (HFEs), have been incorporated as diluents to the HCE composition leading to the emergence of SSEs [13,14]. These co-solvents,

characterized by their low donor number and compatibility with the electrolyte solvents, do not dissolve lithium salt nor disrupt the solvation structure of HCEs [15,16].

The increase in the salt concentration of the electrolyte results in a reduction or suppression of LiPS solubility. This behavior arises from the decreased availability of free solvent molecules, thereby mitigating the operational issues associated with LiPS dissolution [17,18]. Additionally, a higher salt content in the electrolyte fosters stronger interaction between cations and anions. Consequently, the solvation structure predominantly comprises contact ion pairs (CIPs, where an anion is coordinated with a Li cation) and cation-anion aggregates (AGGs, where an anion is coordinated with two or more Li cations) [19–21]. This behavior leads to a notably increased migration rate of Li ions and exceptional compatibility with the LMA. This improved affinity with LMA is grounded in the formation of an inorganic-nature protective SEI layer that is primarily composed of the decomposition products of lithium salt anions rather than from the organic solvent molecules, as occurs in the conventional electrolyte [22,23]. Therefore, the adequate selection of the lithium salt anion employed for the SSE composition assumes paramount importance [24–26]. However, in the case of LSBs, the potential impact of the lithium salt anion on the SEI formation has not been fully exploited, being LiTFSI commonly employed as the sole lithium salt. While LiTFSI exhibits favorable properties in terms of thermal and chemical stability and high ionic conductivity, its highly stable anion molecule leads to the formation of a weak protective layer on the LMA, insufficient to ensure long cycle life [27].

Taking all these factors into consideration, the present study focuses on the development of a tailored SSE as an alternative approach to the conventional electrolyte for its application in Li-S technology. To this end, a thorough evaluation to discern the impact of lithium salt anion selection on the LSB performance was carried out. The investigation encompassed a comprehensive characterization of the intrinsic properties of the developed SSEs and an extensive analysis of their compatibility with the LMA as the cornerstone to evaluate its effectiveness, with the conventional electrolyte serving as the reference. Finally, the potential feasibility of the newly developed electrolytes was evaluated in Li-S cells, both using power and energy cells.

5.2. Tailored sparingly solvating electrolytes as Li-S electrolytes

5.2.1. SSE composition and preparation

SSEs consist of three primary components: an ion-conducting salt, a solvating solvent, and a non-solvating diluent. In this context, sulfolane was selected as the electrolyte solvent for its exceptional capacity to dissolve lithium salts, owing to its high dielectric constant, along with its low vapor pressure, which enhances the safety of the battery system [28]. On the other hand, 1,1,2,2-tetrafluoroethyl-2,2,3,3-tetrafluoropropylether (TTE) was the choice for the inert co-solvent based on its capacity to form a robust SEI on the LMA surface [29].

As described in the introduction section, the anion of the lithium salt employed for SSE formulation plays a determinant role in the formation of the SEI layer. However, this key aspect has received limited attention in the existing Li-S literature. Hence, a comprehensive study was conducted, focusing on two different SSE compositions to scrutinize the impact of the anion. The first electrolyte, referred to as SSE_REF, was formulated with LiTFSI as the unique lithium salt. Regarding the electrolyte preparation, after the dissolution of 2.5 M of LiTFSI in sulfolane, the TTE co-solvent was added in a 1:1.5 volume ratio. In contrast, the second electrolyte was developed through the combination of LiTFSI and lithium bis(fluoromethanesulfonyl)imide (LiFSI), resulting in SSE_LiFSI. This choice was motivated by the ability of LiFSI to act as a precursor for the formation of lithium fluoride (LiF)-rich protective SEI layer. The preparation of the SSE_LiFSI followed the same procedure as SSE_REF, except for incorporating LiFSI as an additive. In this case, 2 M LiTFSI and 0.5 M LiFSI were dissolved in sulfolane, followed by the introduction of TTE co-solvent in a 1:1.5 volume ratio.

5.2.2. Solvation structure analysis

As previously outlined, the distinctive feature of the SSEs falls in their solvation structure. Consequently, molecular dynamics (MD) simulations were performed to gain atomistic-level insights into the theoretical solvation structure of the prepared electrolytes and to assess the impact of the co-solvent incorporation on the microstructure of the Li salt/sulfolane mixtures.

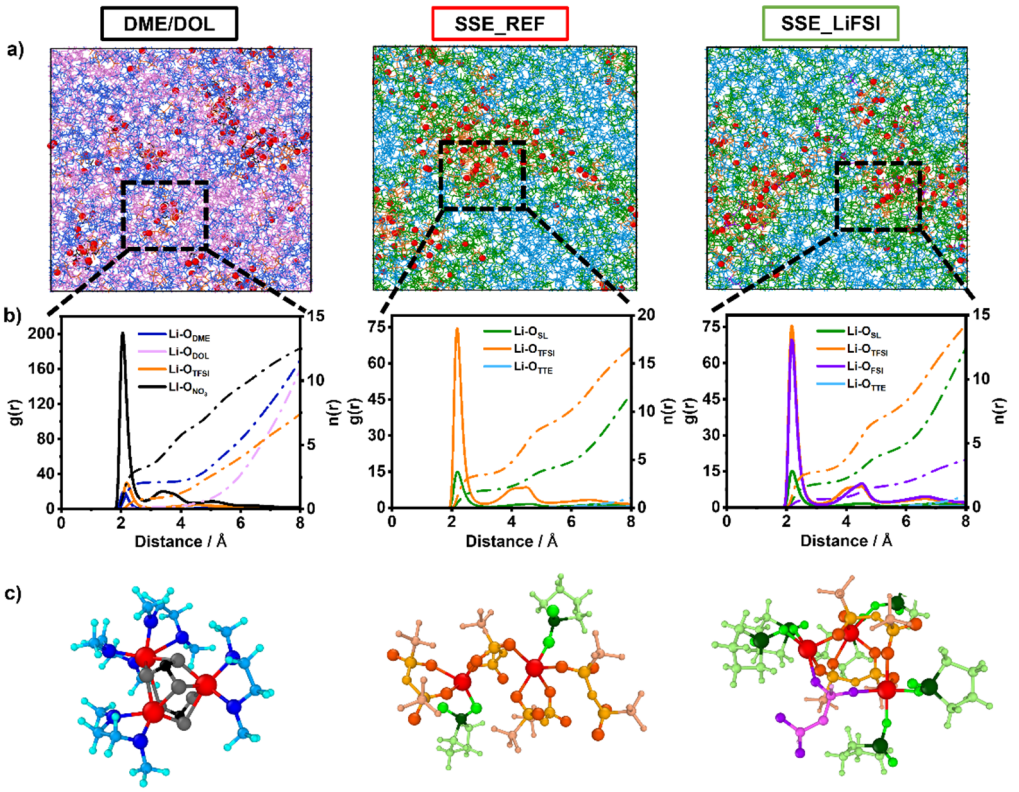

Figure 5.1. a) MD simulation snapshots, **b)** radial distribution function, and **c)** Illustrative examples of the Li^+ coordination environment of DME/DOL, SSE_REF, and SSE_LiFSI electrolytes.

Figure 5.1a depicts snapshots of the chemical structure of the different electrolytes after reaching thermodynamic equilibrium. For a comparative analysis of the solvation structures, radial distribution functions (g(r), represented by solid lines) and coordination numbers (n(r), denoted by dash-point lines) were computed, as illustrated in **Figure 5.1b**. The DME/DOL electrolyte primarily displayed a higher prevalence of solvent-separated ion pairs (SSIPs) structures, as evidenced by the low coordination number value of $Li\text{-}O_{TFSI}$, with Li^+ coordination mainly governed by DME and NO_3^-. In the radial distribution function, a sharp peak is observed for NO_3^- and a lower peak is associated with DME. The prominent peak of the NO_3^- can be attributed to its strong electrostatic interactions with Li^+ resulting from its small size and densely charged anion. **Figure 5.1c** offers a visual representation of the Li^+ coordination, emphasizing the role of NO_3^- as a bridge connecting various Li^+ ions, resulting in

aggregations. Meanwhile, in both SSEs, lithium salt anions are the predominant components within the first coordination shell of Li-ion as indicated by the acute Li-O_{TFSI} and Li-O_{FSI} (in the case of SSE_LiFSI) peaks at ≈ 2 Å, resulting in a key characteristic for the formation of anion-derived SEI [30,31]. As in the case of NO_3^- in the DME_DOL electrolyte, $TFSI^-$ and FSI^- play a similar role in connecting different Li^+, resulting in the formation of aggregates observed in **Figures 5.1c**. In contrast, the TTE molecules show negligible coordination with Li^+. These findings reveal that both prepared SSEs feature localized concentrations of Li salt/sulfolane pairs, enveloped by TTE co-solvent molecules primarily serving as diluents, without actively participating in the solvation structures of Li^+ [32,33].

The solvation structures of the formulated SSE electrolytes were further experimentally validated through Raman spectroscopy analysis. **Figure 5.2a** presents the Raman spectra illustrating the SO_2 scissoring vibration of sulfolane within the corresponding spectra range. In pure sulfolane, this peak occurs at 568 cm^{-1} and shifts towards a higher wavenumber upon complexation with Li^+, a phenomenon that becomes more pronounced with an increasing salt concentration in the electrolyte. This shift reflects the decrease in the amount of free sulfolane solvent molecules. Notably, this displacement remains consistent regardless of the lithium salt employed in the electrolyte formulation.

Furthermore, it is important to focus on the spectral region spanning 740 to 750 cm^{-1}, which corresponds to the CF_3 bending coupled with the S–N stretching vibration of the TFSI anions. In the same region, albeit with slightly lower Raman shifts (730-740 cm^{-1}), vibrations associated with the stretching of S-N moieties in the FSI anions are also observed. These specific vibrational modes are recognized for their sensitivity to variations in Li-ion coordination, as depicted in **Figure 5.2b**. When the compound remains uncoordinated, as in the case of low-concentration electrolytes, the Raman peak in this region exhibits a shift towards shorter wavelengths, especially around 740 cm^{-1}. However, upon closer examination of the spectra, it becomes apparent that an increase in the lithium salt concentration within the system leads to the formation of CIPs or AGGs. This phenomenon is characterized by the emergence of a new peak in the spectra, observed around 747 cm^{-1} (refer to the deconvoluted spectra of concentrated electrolytes in **Figure A.5.1**). Notably, this occurrence induces a shift in the spectral band toward longer wavelengths. For instance, this shift from 740 cm^{-1} to 742 cm^{-1} in the main peak of LiTFSI suggests the potential occurrence of

monodentate coordination between $TFSI^-$ and Li^+. In the case of electrolytes incorporating FSI anion in their composition, an additional peak appears at 734 cm^{-1} [34]. The shift observed in the Raman spectra strongly indicates that the SSEs developed in this study exhibit the formation of CIPs and AGGs involving the anions of the salts.

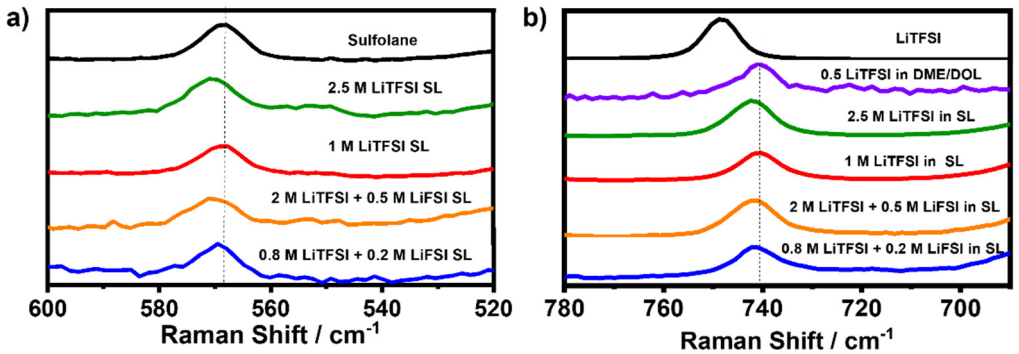

Figure 5.2. Raman spectra of different configurations of electrolytes for varied **a)** sulfolane and **b)** LiTFSI salt ranges.

5.2.3. Physicochemical properties of the electrolytes

Upon thorough examination and confirmation of the solvation structure of the different electrolytes, an evaluation of the physicochemical properties of the SSEs was conducted, using the conventional DME/DOL electrolyte as the reference. **Figure 5.3** presents the ionic conductivities of the examined electrolytes at RT (approximately 23 ± 2 °C). It can be observed that the conventional DME/DOL electrolyte exhibited the highest ionic conductivity, measuring 6.47 mS cm^{-1}, which is approximately three times higher than that of the developed SSEs. This difference can predominantly be attributed to the lower viscosity of the DME/DOL electrolyte and the reduced concentration of solvated salt by the solvent molecules. Nevertheless, it is important to emphasize that both SSEs demonstrated sufficiently high ionic conductivities for ensuring suitable RT battery operation, with SSE_REF registering a value of 1.21 mS cm^{-1}, while SSE_LiFSI achieved a higher value of 2.08 mS cm^{-1}. The slight ionic conductivity difference between SSE_LiFSI and SSE_REF can be attributed to the increased mobility of LiFSI molecules within the electrolyte.

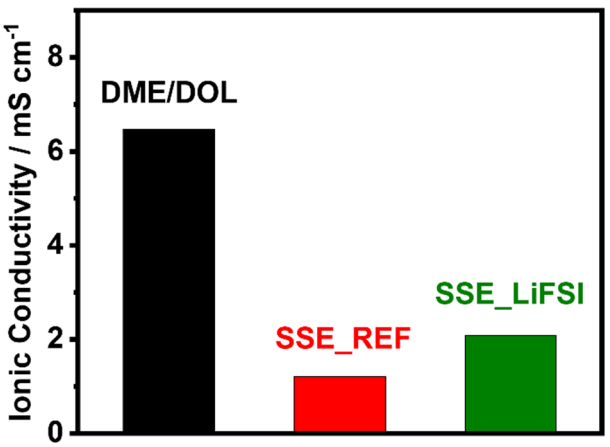

Figure 5.3. Ionic conductivity of the studied liquid electrolytes at RT (23 ± 2 °C).

To further corroborate the causes contributing to the diminished ionic conductivity of SSEs, a viscosity comparison between the DME/DOL and SSE_LiFSI electrolyte was carried out (**Figure 5.5a**). The results evidenced that the SSE possesses a viscosity approximately an order of magnitude higher than that of the conventional electrolyte. This increased viscosity can be ascribed to the inherently higher viscosity of the sulfolane solvent employed in their formulation, which is further saturated with a substantial amount of lithium salt [35]. Despite the inclusion of the diluent to mitigate this viscosity, it remains significantly higher compared to conventional electrolytes.

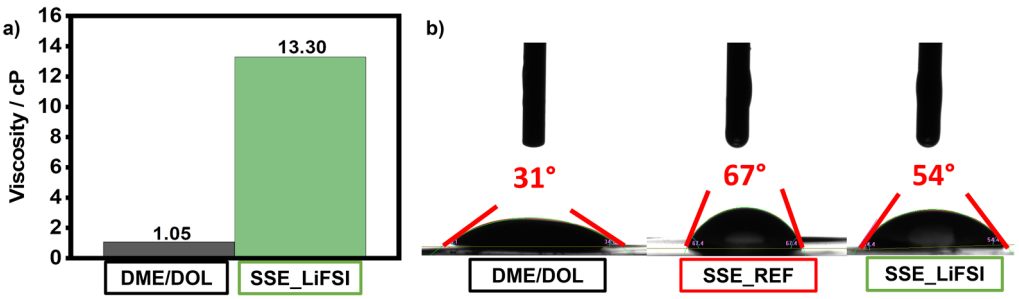

Figure 5.4. a) Viscosities of the DME/DOL and SSE_LiFSI electrolytes. **b)** Wettability test on Celgard® separator of DME/DOL, SSE_REF, and SSE_LiFSI electrolytes.

Considering the concerns of the increasing viscosity and its potential negative impact on the electrolyte's application, a wettability study was conducted. In addition,

the wettability study of the different electrolytes was performed on the Celgard® 2500 separator. The conventional electrolyte, composed of low viscosity and highly volatile solvents, demonstrates excellent wettability of the separator, as evidenced by a low contact angle of 31° (**Figure 5.4b**). In contrast, both SSEs exhibit reduced wetting characteristics, displaying contact angles of 67° and 54° for SSE_REF and SSE_LiFSI, respectively. Consequently, the higher viscosity exhibited by SSEs contributes to reduced ionic conductivity and poorer separator wettability when compared to the reference DME/DOL electrolyte.

5.2.4. Safety evaluation

The safety of the conventionally employed liquid electrolytes has been under intense examination, primarily stemming from their intrinsic high flammability, a characteristic linked to well-documented safety incidents [36,37]. Furthermore, when these liquid electrolytes are combined with the LMA, which is distinguished by its substantial energy density and heightened reactivity, safety concerns are amplified, posing the potential for more severe safety incidents than those reported previously [38]. Hence, ensuring the fire safety of the developed liquid electrolytes is of paramount importance in the implementation of safe battery systems. This imperative is intricately linked to the flammability characteristics and thermal stability of the employed electrolytes.

Consequently, to evaluate the safety properties, different flammability tests were conducted. **Figure 5.5** provides a visual record of the test, where the commercial Celgard® separator was immersed in the respective electrolytes. The conventional DME/DOL electrolyte exhibits highly flammable behavior, evident from its rapid ignition and violent combustion, resulting in complete combustion of the separator within a mere 1-second timeframe. Conversely, neither of the two SSEs displays any signs of ignition, underscoring their exceptional resistance to combustion. In this scenario, the separator experiences only minimal melting in specific areas, likely attributed to the elevated temperature of the lighter flame exceeding the melting point of the material. Additionally, as shown in **Figure A.5.2**, a complementary flammability test was carried out on the electrolytes individually to quantitatively assess their flame-retardant capabilities, characterized by the self-extinguishing time (SET) values. Once again, the conventional DME/DOL electrolyte's poor thermal stability and susceptibility to combustion are evident from the intense and long-

lasting flame, resulting in a SET value of 117 s g^{-1}. In contrast, both SSEs consistently exhibit their non-flammable nature, yielding negligible SET values. This substantial contrast highlights that replacing the conventional electrolyte with the developed SSEs will significantly enhance the fire safety attributes of the battery system.

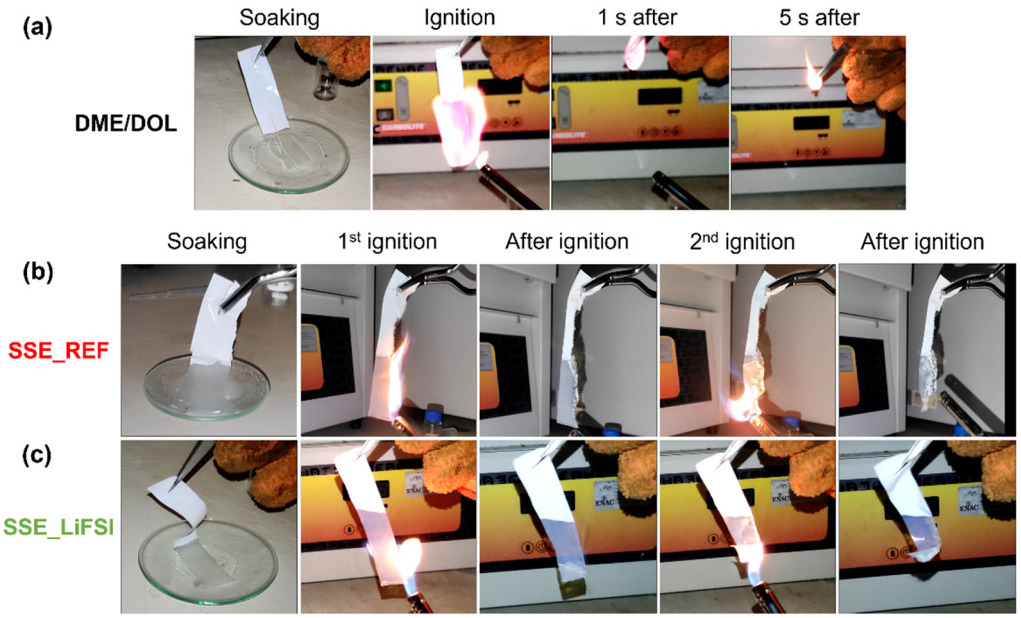

Figure 5.5. Flammability test of the Celgard® separator soaked in different electrolytes. The digital photos of the burning process of a) DME/DOL, b) SSE_REF, and c) SSE_LiFSI.

5.2.5. Compatibility with the lithium metal anode

In addition to the intrinsic properties, it is imperative to consider the electrolyte's compatibility with the LMA. As underscored in the preceding chapters, the correct interaction between the employed electrolyte and the LMA significantly influences the cycle life of the battery system. To this end, an exhaustive evaluation of the reversibility and stability of the Li metal during the plating and stripping process in the developed electrolytes was assessed using a series of Li||Cu and Li||Li cell tests, as illustrated in **Figure 5.6**, **Figure 5.9**, and **Figure 5.10**.

5.2.5.1. Li||Cu cell characterization

First, to assess the CE exhibited by the analyzed electrolytes, a Li plating and stripping cycling in Li||Cu cells at 0.5 mA cm^{-2} was performed (**Figure A.5.3**).

Figure 5.6a underscores the remarkable stability of the SSE_LiFSI electrolyte, as evidenced by an average CE value of 97% through the analyzed cycles. Significantly, this stands in stark contrast to the stability offered by SSE_REF, which yields an unsuitable CE value of < 80% due to the emergence of undesirable side reactions. Furthermore, as illustrated in **Figures A.5.4** and **A.5.5a**, SSE_LiFSI exhibits a substantially lower polarization voltage compared to SSE_REF, without manifesting any signs of cycling failure. Therefore, the incorporation of LiFSI salt in the SSE formulation demonstrates a significant enhancement in stability with the LMA. Conversely, the conventional DME/DOL electrolyte demonstrates high CE values during cycling and low polarization voltage (**Figure A.5.5b**). This behavior can be primarily attributed to the effective protection and denser Li deposition properties provided by the $LiNO_3$ additive.

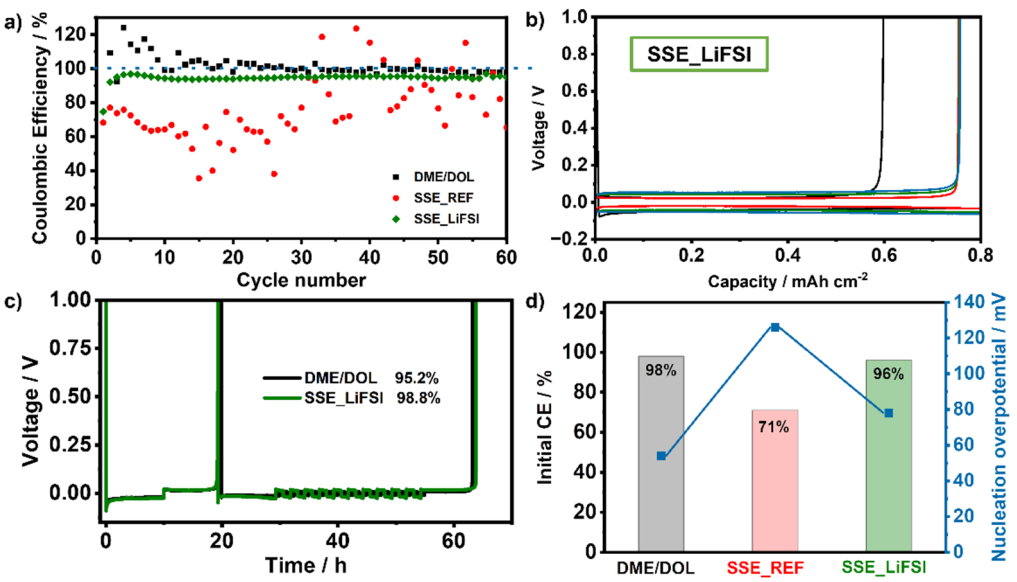

Figure 5.6. Electrochemical compatibility with Li^0 anode of the studied electrolytes. a) Coulombic efficiency of the cycling performance of Li||Cu cells employing different electrolytes. b) Polarization of SSE_LiFSI during the Li plating and stripping in Li||Cu cells. c) Li metal CE of the different electrolytes using the modified Aurbach method [39]. d) CE and nucleation overpotential of the first Li deposition.

As a complementary study for assessing the CE of Li metal in Li||Cu cells, the modified Aurbach method was employed [39]. Distinguishing from the previous approach, this method involves an initial preconditioning step of the Cu substrate (see

Experimental section). **Figure A.5.6** showcases the persistent incompatibility of SSE_REF with lithium, exhibiting a low CE value of 58.1%. This incompatibility is again successfully mitigated through the incorporation of LiFSI in the SSE composition. **Figure 5.6c** presents the results of the DME/DOL and SSE_LiFSI electrolytes, highlighting the commendable properties of LiFSI salt in establishing a robust SEI layer, resulting in an impressive CE of 98.8%. Notably, this CE value even surpasses that delivered by the conventional DME/DOL-based electrolyte, which achieves 95.2%. Regarding the plating/stripping profiles, it is worth noting that the conventional electrolyte, despite yielding a slightly lower CE, exhibits lower overpotential compared to SSE_LiFSI. This difference can be attributed to the higher ionic conductivity of the electrolyte and the formation of a conductive N-rich SEI protective layer facilitated by $LiNO_3$ in contrast to the insulator LiF-rich SEI layer formed in the SSE_LiFSI system [40–42]. The validity of this explanation is substantiated by **Figure 5.6d**, which reaffirms the robust compatibility of the SSE_LiFSI electrolyte with the Li metal. Remarkably, it is observed that despite the lower nucleation overpotential and higher initial CE displayed by the DME/DOL electrolyte, its compatibility with the LMA tends to slightly deteriorate after cycling. In contrast, the SSE_LiFSI maintains excellent compatibility with the LMA, even improving the initial CE value after the cycling test. Regardless, both electrolytes surpass the performance offered by the SSE_REF electrolyte.

In the ongoing examination of electrolyte compatibility with LMA, SEM analyses were conducted to investigate the surface and cross-sectional morphologies of the initial deposition on copper substrates (**Figure 5.7** and **Figure A.5.7**). This analysis was executed by depositing a Li reservoir of 4 mAh cm^{-2} under a constant current of 0.4 mA cm^{-2}. In **Figure A.5.7a** the Li metal deposition potential curves for examined electrolytes are presented. Notably, the conventional electrolyte exhibits the lowest nucleation overpotential, which can be attributable to the presence of $LiNO_3$. As reported in different studies, the inclusion of nitrogen compounds enhances the lithiophilicity of the Cu substrate and the charge transfer during the nucleation of Li embryos, resulting in an improved Li metal nucleation behavior [43,44]. For SSE_LiFSI, a higher nucleation overpotential is observed compared to DME/DOL, possibly stemming from the slightly higher charge transfer due to the formation of the inorganic anion-derived SEI. Nevertheless, SSE_LiFSI demonstrates an exceptional Li nucleation growth process, comparable to or slightly better than the DME/DOL electrolyte. This phenomenon underscores the formation of a highly ionically

conductive SEI film, contributing to the reduction of the mass transfer resistance [45,46]. Contrastingly, the SSE_REF electrolyte displays the poorest Li deposition behavior, manifesting the highest nucleation and growth overpotential.

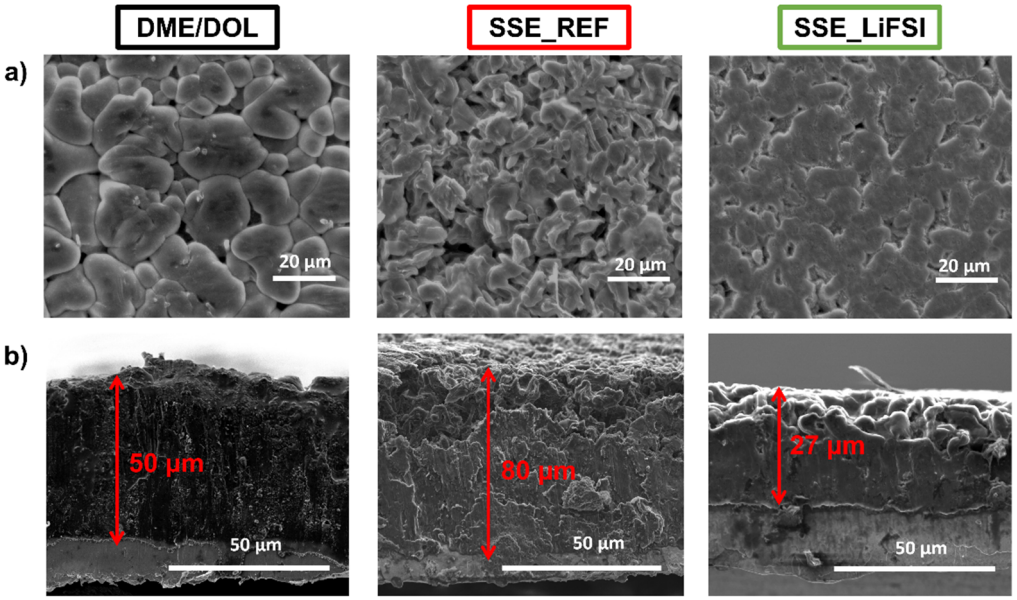

Figure 5.7. a) Surface and **b)** cross-section SEM images of the deposited Li on Cu substrate with the three different electrolytes: DME/DOL, SSE_REF, and SSE_LiFSI.

After analyzing the behavior of Li metal depositions, the subsequent necessary step involves investigating their impact on the morphology. The conventional DME/DOL electrolyte reveals a compact Li deposition film with a thickness of 50 µm, accompanied by the presence of sizable Li particles (**Figure 5.7a** and **b**). These observations evidence the good compatibility between lithium and the conventional electrolyte during the initial Li deposition. In contrast, concerning the SSE_REF electrolyte, the deposited Li film presents a porous and non-compact morphology, characterized by a loosely packed structure with an average thickness of approximately 80 µm (**Figure 5.7a** and **Figure 5.7b**). This non-compact morphology explains the unsuitable compatibility of this electrolyte with Li metal observed previously. Notably, SSE_LiFSI yields larger particle size, along with a tightly packed and smoother Li deposition, leading to a thin and compact film of about 27 µm (**Figure 5.7a** and **Figure 5.7b**). This compact Li deposition nature results in the reduction of the available Li surface for interaction with the electrolyte, leading to

higher CE values, as previously demonstrated [47,48]. These findings evidenced the substantial positive impact of the addition of LiFSI to the SSE formulation, highlighting the crucial importance of the lithium salt anion selection to enhance compatibility with LMA.

Additionally, to assess the robustness and durability of the deposition morphologies of the different electrolytes, a long-term cycling study was conducted (**Figure A.5.8a**). In both the conventional electrolyte and SSE_REF (**Figure A.5.8b** and **c**), there is a discernible emergence of porous, fibrillar, and whisker-like structures upon cycling, aligning with the observed behavior in **Figure 5.6c** and **d**. The pronounced deterioration in compatibility with the LMA of the DME/DOL during cycling can be attributed to the depletion of the $LiNO_3$ additive, which proves insufficient to ensure compact Li deposition over long-term cycling periods [42,49]. In contrast, it is noteworthy that even after 30 cycles, only a minor increase in surface porosity is observed in the SSE_LiFSI electrolyte, effectively maintaining large and densely packed Li deposition (**Figure A.5.8d**).

To gain further insights into the surface composition of the Lim deposition of the different electrolytes, XPS analyses were conducted. **Figure A.5.9** and **Table A.5.1** present the comprehensive XPS full spectra of the Li deposition surface on the Cu substrate with the different electrolytes, along with their respective atomic content of different elements.

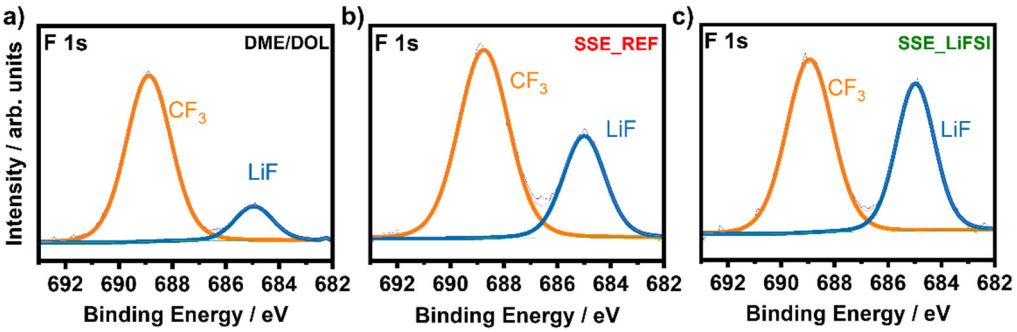

Figure 5.8. High-resolution XPS spectra of F 1s core level of the Li deposition on Cu substrate with **a)** DME/DOL, **b)** SSE_REF, and **c)** SSE_LiFSI electrolytes.

Interestingly, as evidenced in **Figure 5.8**, when SSE_LiFSI is employed, the surface of Li metal deposition exhibits a higher proportion of LiF compound compared

to SSE_REF and DME/DOL. This phenomenon can be ascribed to the enhanced interaction of LiFSI with Li metal, stemming from its weakened S-F bond (**Figure 5.8a**). The XPS results, in conjunction with the SEM images, provide compelling evidence that the incorporation of LiFSI not only promotes the formation of a more densely packed Li deposition but also leads to an interface rich in LiF (peak at 685 eV in F 1s core level). The presence of LiF, as explained in the previous chapter, is particularly desirable for ensuring the long-term stability of LMA.

Furthermore, there are qualitative and quantitative divergences in the O 1s spectra between SSE_REF and the other two electrolytes. Particularly, SSE_REF yields a SEI with lower O content, approximately 24%, in contrast to DME/DOL and SSE_LiFSI, which exhibit O contents of approximately 29% and 31%, respectively (as evidenced in **Table A.5.1)**. Moreover, additional O content presented by the DME/DOL and SSE_LiFSI electrolytes exhibits a distinct nature compared to SSE_REF, as indicated by their different O 1s spectra shapes (**Figure A.5.10a**). When DME/DOL and, especially, SSE_LiFSI electrolytes are used, a distinct peak at 528.6 eV emerges, suggesting the presence of Li_2O within the SEI composition. Additionally, in conjunction with the increase in Li_2O, the peak at around 531.5 eV, primarily consisting of carbonates and hydroxides, becomes the predominant constituent within the SEI.

An analysis of the Li 1s core level reveals a further qualitative difference between SSE_REF and the other two electrolytes. A detailed deconvolution of Li 1s (**Figure A.5.10b**) spectra highlights that the formation of LiOH, observed at 54.7 eV, contributes to the increase and shift of the peak at 531.5 eV when employing DME/DOL and SSE_LiFSI electrolytes. Consequently, the coexistence of Li_2O and LiOH seems to play a role in the formation of a more favorable and stable interface, as observed when employing SSE_LiFSI and DME/DOL electrolytes. Finally, the emergence of a distinct peak corresponding to metallic Li (discerned at 51.8 eV in Li 1s) when SSE_REF and DME/DOL electrolytes are used may suggest a non-compact, inhomogeneous, or exceptionally thin SEI. This SEI might be sporadically thin enough in certain regions to allow the collection of photoelectrons from the underlying Li metal plating. In contrast, the dense and compact Li deposits associated with SSE_LIFSI are covered by an equally compact and protective SEI layer, as revealed in the analysis. This compact and chemically more benign interface could provide a plausible explanation for the excellent compatibility demonstrated by SSE_LiFSI electrolyte with Li metal, as previously elucidated.

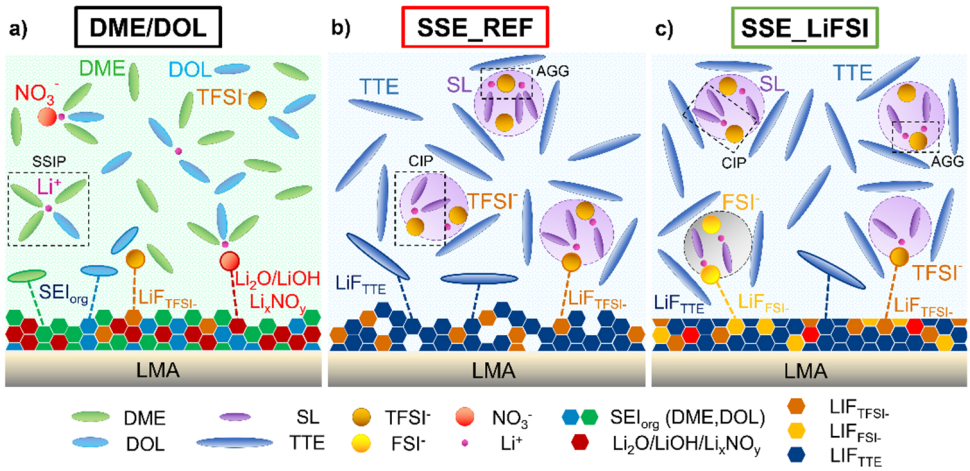

Figure 5.9. Schematic illustration of the electrolyte structure and the correspondingly formed SEI in **a)** DME/DOL, **b)** SSE_REF, and **c)** SSE_LiFSI electrolytes.

Based on the findings from SEM and XPS analysis, schematic representations illustrating the SEI layer formation for the different studied electrolytes are represented in **Figure 5.9**. For the conventional electrolyte, it is observed that formed SEI exhibits satisfactory quality, especially during the first Li deposition, primarily ascribed to the presence of the $LiNO_3$ additive. However, as discussed earlier, the ongoing consumption of $LiNO_3$ during cycling leads to a degradation in the quality of the SEI and compromises the morphology of Li deposition as cycling progresses. On the other hand, the addition of LiFSI as additive in the SSE formulation enhances the quality of the resultant SEI compared to the traditionally employed SSEs that solely rely on LiTFSI. As thoroughly demonstrated, this improvement is attributed to the increased decomposition of LiFSI, leading to a higher proportion of LiF within the SEI layer. Additionally, the presence of LiFSI in the SSE also exerts a positive influence on the morphology and compactness of the deposited Li.

5.2.5.2. Symmetric Li||Li cell plating and stripping characterization

To complete the electrochemical characterization of the different electrolytes, the plating and stripping performance of the symmetrical Li||Li was evaluated across a range of current densities, ranging from 0.1 mA cm^{-2} to 1 mA cm^{-2}.

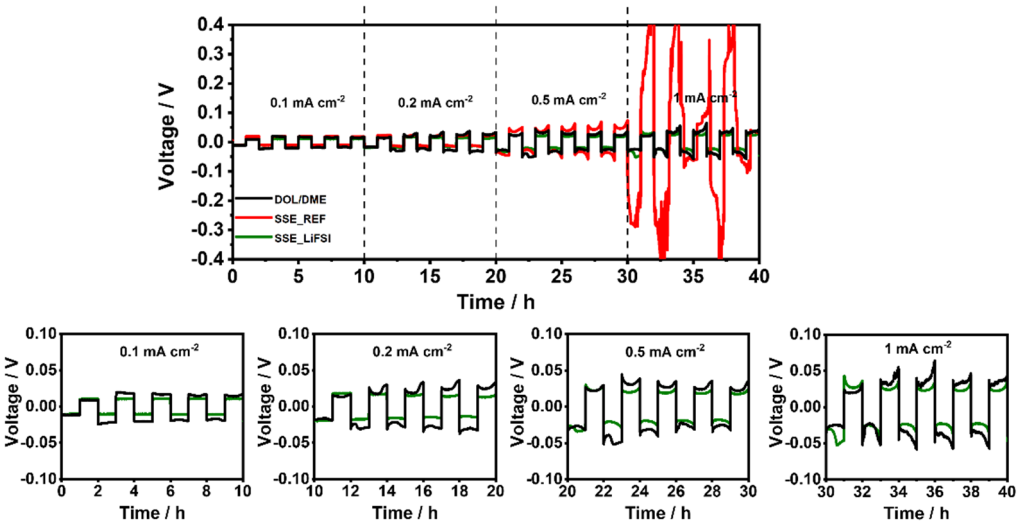

Figure 5.10. Electrochemical performance of different electrolytes in Li||Li cells. Current test of Li||Li cells using DME/DOL, SSE_REF, and SSE_LiFSI electrolytes at different current densities from 0.1 mA cm^{-2} to 1 mA cm^{-2} and the corresponding zoomed profiles of DME/DOL and SSE_LiFSI.

The results displayed in **Figure 5.10** align with previously observed results, demonstrating the instability of the SSE_REF electrolyte when paired with the LMA. This poor performance can be predominantly attributed to the irregular and fibrillar Li deposition induced by this electrolyte, coupled with the poor chemical quality of the formed SEI layer. In contrast, both the SSE_LiFSI and DME/DOL electrolytes demonstrate stable cycling with minimal polarization across the entire range of current densities. This further corroborates the favorable influence of the denser and more uniform Li deposition behavior evident in these two electrolytes. However, it is essential to note the presence of sporadic erratic cycles in the case of the DME/DOL electrolyte, especially at high current densities. This behavior can be attributed to the progressive deposition porosity exhibited by this electrolyte that becomes more evident over cycling due to the continuous consumption of $LiNO_3$. Significantly, upon closer examination of the voltage profiles, SSE_LiFSI consistently exhibits lower overpotential throughout all the analyzed current densities. This can be ascribed to its consistent capacity to perform more compact and thinner Li deposition film behavior, as previously evidenced.

5.2.5.3. Symmetric Li||Li cell critical current density characterization

In addition to the plating/stripping analysis, a complementary investigation encompassed the evaluation of the critical current density (CCD) for the given electrolytes. The CCD analysis provides valuable insights into the rate-limiting factors governing the kinetics of Li metal, which directly influences the power density of batteries [50]. Consequently, a thorough examination of the CCD is of paramount significance to assess the implementation of these electrolytes in LSBs, serving as a critical determinant of their suitability for high-power applications.

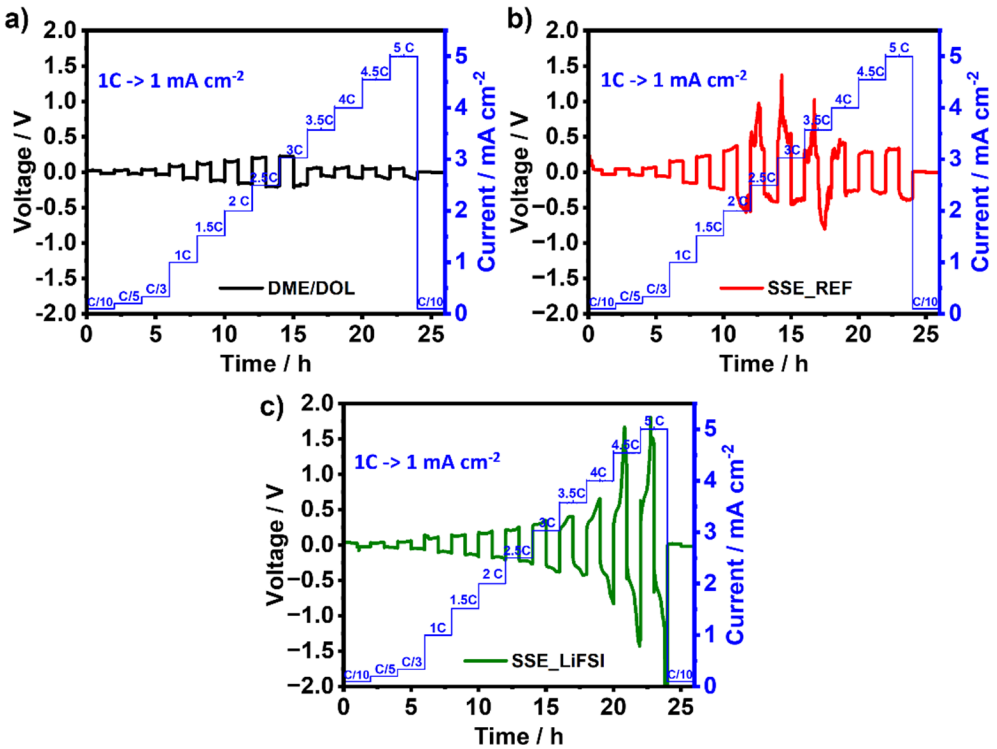

Figure 5.11. The critical current density of Li||Li cells using the different electrolytes: **a)** DME/DOL, **b)** SSE_REF, and **c)** SSE_LiFSI.

As depicted in **Figures 5.11a-c**, the previously observed trend remains consistent. The SSE_LiFSI electrolyte, characterized by its robust and compact Li deposition behavior, demonstrates a heightened resistance to current density, extending its superior performance even up to 4 mA cm^{-2}, surpassing all other analyzed electrolytes. However, beyond the current density of 4 mA cm^{-2}, some

instances of inhomogeneous Li deposition become apparent, resulting in irregularities in the current-voltage plateaus. Conversely, the DME/DOL electrolyte displays a comparatively lower stability, reaching a critical point with a short-circuit of the cell occurring at a current density of 3 mA cm^{-2}. Despite the initially uniform Li deposition observed during the early cycles, the DME/DOL electrolyte exhibits a progressive increase in deposition porosity, as previously corroborated. Furthermore, in contrast to the robust LiF-rich SEI layer in the SSE_LiFSI system, the SEI layer formed in the DME/DOL electrolyte experiences the depletion of $LiNO_3$ throughout cycling. This consumption of $LiNO_3$ is particularly pronounced at high current densities, resulting in a weaker SEI layer and eventual short-circuiting of the cell, attributed to the formation of Li dendrites. Finally, the SSE_REF electrolyte shows the poorest performance, consistent with earlier observations, exhibiting the lowest resistance to the current flow. This unsuitable performance is attributed to the porous and fibrillar nature of its Li depositions, which strongly impact its long-term compatibility with the LMA.

This comprehensive study of the electrolyte compatibility with the LMA has yielded fruitful insights. Firstly, the pivotal role of the anion associated with the lithium salt employed in SSE formulation has been underscored. The incorporation of LiFSI as additive has been proven to significantly enhance the compatibility of the electrolyte with the LMA. This enhancement is attributed to the compact and uniform Li depositions obtained with the SSE_LiFSI electrolyte. Secondly, when compared to the conventional electrolyte, SSE_LiFSI offers a similarly robust initial compatibility with the LMA. Nevertheless, the novel electrolyte developed in this work distinguishes itself by ensuring this exceptional affinity with the LMA over an extended cycling period, a weak point of the conventional electrolyte due to $LiNO_3$ depletion.

5.2.6. Li-S battery performance

Following the significant enhancement in the LMA affinity provided by the developed SSE_LiFSI electrolyte, its impact on the electrochemical performance in LSBs was further evaluated. This evaluation was conducted using the sulfur cathode developed in **Chapter III**, which incorporates ResFArGO 2D graphene-based activated carbon as an additive in a 10 wt.%.

5.2.6.1. Power capability of the SSE_LiFSI in LSBs

Consumers place significant importance on the battery's capacity for both charging and discharging across a wide range of rates, depending on the intended applications. Particularly, discharging at high C-rates reflects the battery's power capability, which is particularly valuable during initial startup procedures. Meanwhile, high C-rate charging represents a paramount factor in the evaluation of a battery's applicability, alongside its long-range cycling performance [51,52]. With these battery requirements in mind, additional electrochemical characterization was conducted to further study the potential applicability of the SSE_LiFSI electrolyte. This characterization involved the rate capability analysis of power cells, using medium sulfur loading cathodes of 3 mg_S cm^{-2}. Due to the differences in ionic conductivity observed at RT between the conventional electrolyte and SSE_LiFSI, the C-rate test was adjusted compared to those performed in previous chapters. In this case, the cycling protocol included 3 cycles of preconditioning at C/20, followed by 5 cycles at C/5, C4, C/3, and C/2, with a subsequent return to constant cycling at C/5.

As displayed in **Figure 5.12a**, both SSE_LiFSI and conventional electrolyte deliver comparable battery performance at low C-rates. However, at high C-rates, the SSE_LiFSI electrolyte exhibits superior sulfur utilization, achieving high discharge capacities of 829 mAh g^{-1} at C/2, surpassing the performance offered by the conventional electrolyte. It is noteworthy that the conventional electrolyte demonstrates a reduced C-rate capability compared to that exhibited in **Chapter III**. This discrepancy can be ascribed to differences in the cycling protocol and its connection to $LiNO_3$ consumption. In **Chapter III**, the cycling process was carried out at higher C-rates motivated by the favorable ionic conductivity of DME/DOL, resulting in faster cycling where the complete consumption of $LiNO_3$ was not evident. Conversely, the cycling process at lower C-rates in the present study entails a slower and extended period of cycling, leading to increased $LiNO_3$ consumption compared to the previous protocol.

The improved Li plating/stripping kinetics, suitable ionic conductivity, reduced LiPS solubility, and improved wettability by ResFArGO material can be envisaged as the multiple factors that explain this remarkable cycling rate performance under high C-rates. Furthermore, it is noteworthy that when SSE_LiFSI electrolyte is used, the cell's capacity is consistently recovered when returning to C/5, maintaining a stable

and high CE during the entire test (**Figure 5.12b**). In contrast, the DME/DOL electrolyte, while also able to recover capacity, presents a clear CE decay, probably due to the consumption of $LiNO_3$ during cycling, as explained earlier. These findings once again evidence the excellent affinity and the symbiotic effect exhibited by the combination of graphene-based sulfur cathodes and the SSE_LiFSI electrolyte.

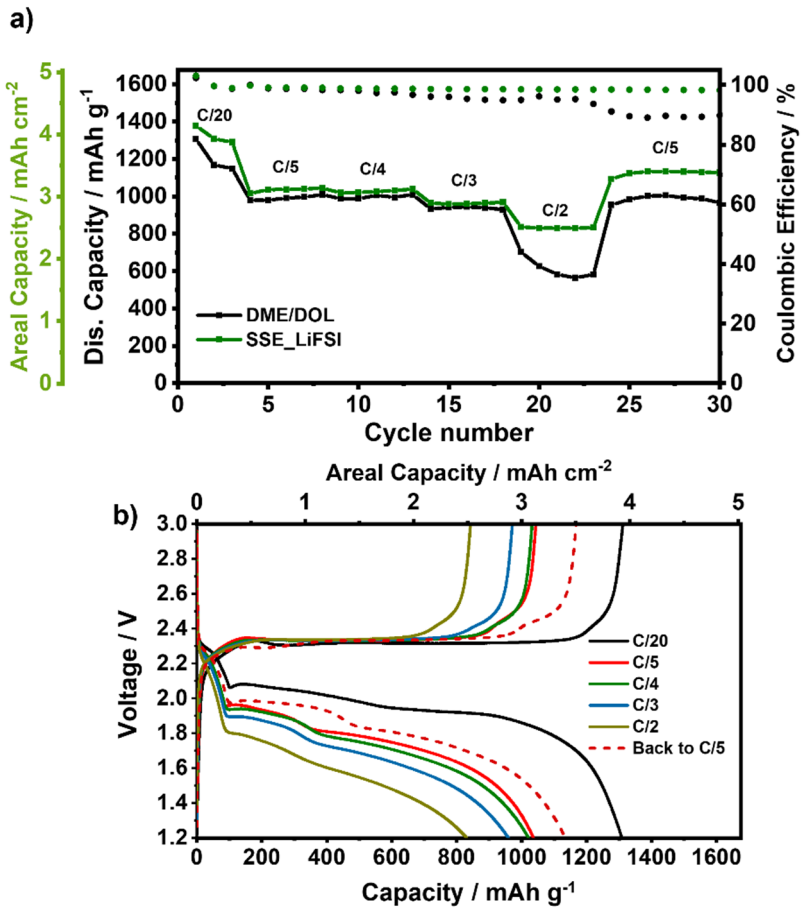

Figure 5.12. a) Rate capabilities comparison of Li-S cells using DME/DOL and SSE_LiFSI electrolytes. **b)** Voltage profiles of the LSB using SSE_LiFSI under different C-rates.

5.2.6.2. High sulfur loading LSB performance

The long-term cycling of the different electrolytes was evaluated using energy cells, characterized by a high-sulfur loading of 4 mg_S cm^{-2}. As described in previous

chapters, the cycling protocol consists of 5 preconditioning cycles at a low C-rate of C/20, followed by extended cycling at a moderate C-rate of C/10.

Figure 5.13 highlights that both SSE formulations exhibited remarkably high capacities, even though their lower conductivity and poorer separator wettability compared to the conventional electrolyte. Notably, the performance of the SSE_LiFSI stands out, offering initial capacity values that closely approach the theoretical ones and maintaining high capacity values throughout cycling. These exceptional results suggest a potential synergistic effect between this family of electrolytes and graphene-based cathodes. This effect can mainly be attributed to favorable compatibility induced by the ideal textural properties and surface chemistry of the ResFArGO material. Its textural properties are characterized by an open and 2D flat-shaped structure, which is reflected in the high-loading cathode depicted in **Figure A.5.11**. Additionally, the presence of O-rich polar functional groups on its surface, as shown in **Chapter III**, significantly enhances the wettability of the SSEs despite their higher viscosity (as shown in **Figure 5.3a**). All these characteristics contribute to maximizing sulfur utilization during cycling.

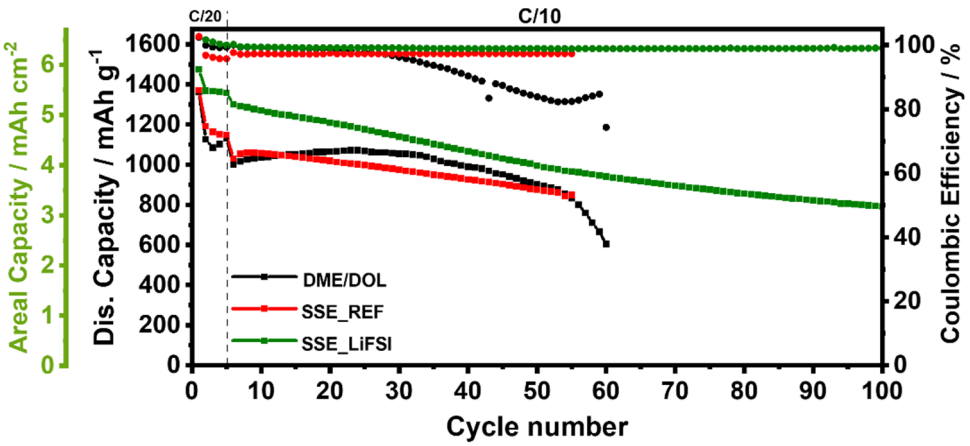

Figure 5.13. Long-term Cycling performance of ResFArGO-based high sulfur loading LSBs using different electrolytes.

The validation of this hypothesis was further substantiated through a parallel LSB cycling experiment conducted without the incorporation of the ResFArGO material, as illustrated in **Figure 5.14a**.

In this case, employing the CAs formulation high sulfur loading cathode (4 mg_S cm^{-2}) developed in **Chapter III**, the DME/DOL electrolyte, unaffected by wettability issues, demonstrated higher capacity values compared to SSE_LiFSI. Under these conditions, SSE_LiFSI, despite exhibiting exceptional battery stability capable of sustaining 150 cycles with remarkable capacity retention, falls short in promoting optimal sulfur utilization in the absence of the ResFArGO material.

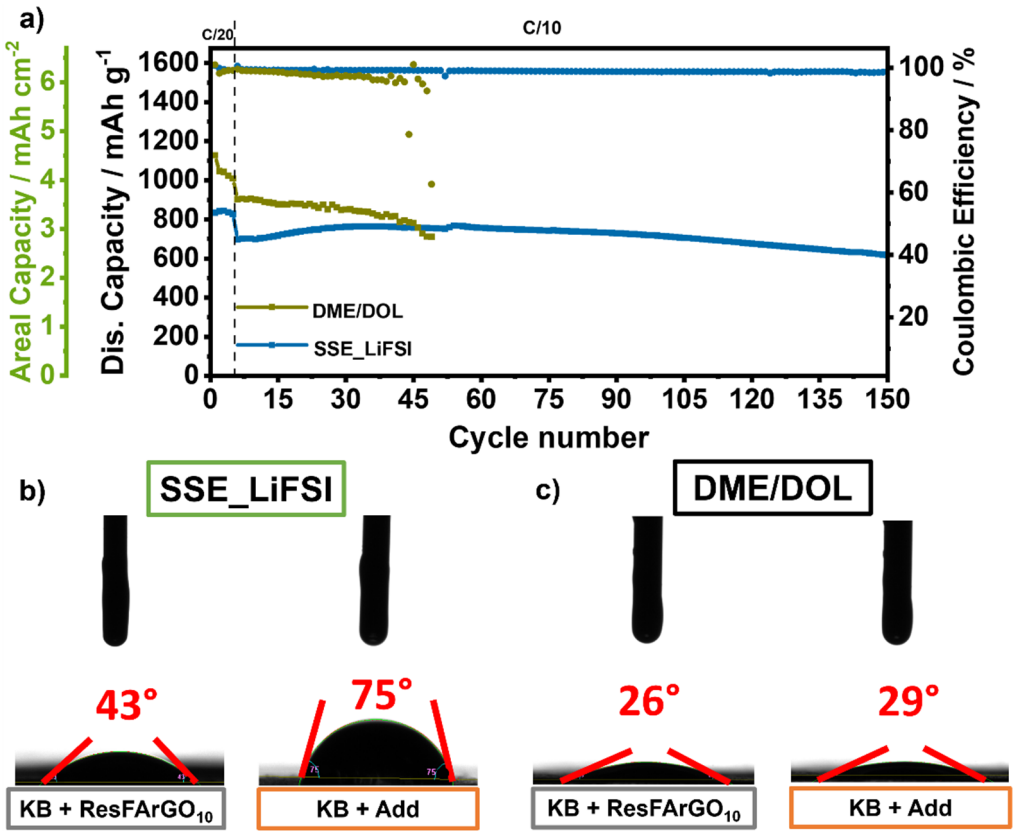

Figure 5.14. **a)** Long-term Cycling performance comparison of high sulfur loading LSBs employing KJ600 + Add cathode using DME/DOL and SSE_LiFSI electrolytes. **b)** Wettability study of the **b)** SSE_LiFSI and **c)** DME/DOL electrolytes over KJ600 + $ResFArGO_{10}$ and KJ600 + Add based sulfur cathodes.

To confirm the hypothesis regarding the capacity dependence on the improvement of system wettability due to the presence of ResFArGO, a wettability study was carried out, comparing it with the CAs cathode. It is worth recalling that, as outlined in **Chapter III**, this cathode featured a low presence of polar groups. As

displayed in **Figure 5.14b**, a clear decrease in the affinity of the SSE_LiFSI electrolyte with the CAs is evident when compared to the ResFArGO-based cathode. This reduction is directly associated with the weak polarity and unsuitable morphology of the carbon materials employed in the formulation of CAs. This poor electrolyte wettability of the cathode leads to diminished sulfur utilization, as evidenced in **Figure 5.14a**). In stark contrast, **Figure 5.14c** reveals that the wettability of the DME/DOL electrolyte remains consistent regardless of the type of cathode used, demonstrating excellent and comparable wettability properties in both cases. Consequently, owing to this favorable wettability, the DME/DOL electrolyte does not present sulfur utilization issues depending on the cathode employed. These findings highlight the significant impact of the sulfur cathode type on the effective performance promotion of SSEs.

On the other hand, cyclability represents another pivotal cell behavior that is strongly impacted by electrolyte selection. As presented in **Figure 5.13**, the SSE_LiFSI electrolyte demonstrates exceptional battery stability, maintaining an impressively high and consistent CE value of 99.2% throughout the analyzed cycles. This performance effectively addresses a well-known weakness of this Li-S technology. In contrast, the DME/DOL electrolyte showed a continuous decay in the CE from cycle 30, and the cell can only endure 60 cycles due to the depletion of the $LiNO_3$ additive. The effectiveness of the anion-selection strategy, exemplified by SSE_LiFSI, deserves special recognition for its remarkable improvement in both the capacity and, particularly, the stability of the Li-S cell. When compared to the SSE_REF electrolyte, SSE_LiFSI exhibits a significantly extended cycle life and superior CE values (96.7% vs. 99.2%, respectively) that are consistent with the results obtained during the compatibility studies with the LMA. Moreover, the excellent long-term compatibility of the SSE_LiFSI electrolyte is further substantiated by its ability to support high sulfur loading long-term cycling at C/5 (**Figure A.5.12**). This electrolyte not only yields an outstanding discharge capacity value of 1200 mAh g^{-1} but also maintains exceptional cell stability up to 60 cycles. These results underscore the considerable potential of the SSE_LiFSI electrolyte, emphasizing the advantages of incorporating LiFSI in the electrolyte formulation, while simultaneously discouraging the use of SSE_REF, based on LiTFSI as the unique salt, due to its poor performance in both Li symmetric and Li-S cells. Furthermore, the favorable properties of SSE_LiFSI, particularly the compatibility with LMA, persist irrespective of the sulfur cathode employed, ensuring long-term cycling in all cases.

5.2.6.3. Optimizing the SSE_LiFSI high sulfur loading LSB performance

Despite the promising results demonstrated by the SSE_LiFSI electrolyte in high sulfur loading LSBs, a gradual capacity decay process has been observed during the long cycling test. To address this challenge, the cut-off voltage impact on the cycling performance was thoroughly analyzed. To this end, three different voltage ranges were investigated: 1.2-3.0 V, 1.4-2.7 V, and 1.7-2.5 V.

Figure 5.15 reveals two divergent trends. On one hand, employing broader voltage ranges enhances sulfur utilization, translating into higher discharge capacity values. Particularly, the diminished sulfur activation observed during cycling at 1.7-2.5 V reveals that this narrower voltage range falls short of meeting the required discharge capacity values (**Figure A.5.13**). This limitation can be attributed to the transition from the dissolution-precipitation conversion process to a slower solid-to-solid pathway. On the other hand, it is evident that the wider the voltage range used, the more pronounced the capacity drop process becomes. The results reveal that a voltage range of 1.7-2.5 V presents the highest capacity retention, maintaining 80% of its initial capacity after 100 cycles. In comparison, the 1.4-2.7 V voltage range results in 69% retention, while 1.2-3 V shows 61% retention. Consequently, the range of 1.4-2.7 V has been selected as the optimal working voltage range for this system seeking a balance between sulfur utilization and capacity retention during battery cycling.

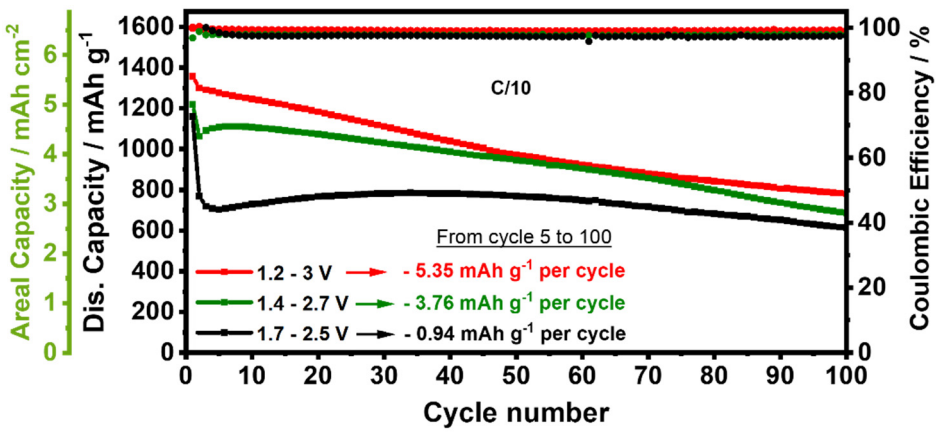

Figure 5.15. Cut-off voltage impact study on the cycling performance of high sulfur loading LSBs using SSE_LiFSI electrolyte.

5.2.6.4. High-temperature LSB performance of SSE_LiFSI

The operation temperature window represents a key parameter that strongly impacts battery health and its safe operation. Currently, to meet the requirement for most portable electronic devices, it is imperative to guarantee a wide temperature operating range [53]. To achieve this goal, the electrolyte, known as the "lifeblood" of the battery, plays an important role in enabling suitable battery performance under wide temperature conditions [15]. Encouraged by the excellent safety properties demonstrated by the SSE_LiFSI electrolyte, the assessment of the energy cell performance at high-temperature cycling conditions (60 °C) was carried out.

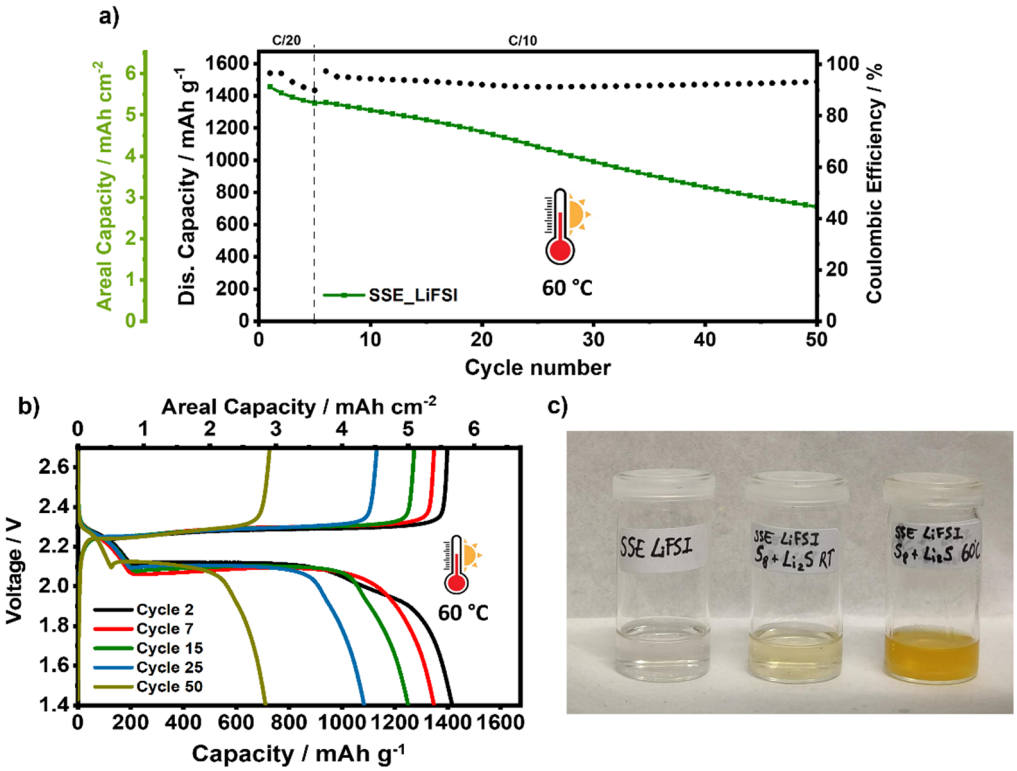

Figure 5.16. a) Cycling behavior of LSBs with SSE_LiFSI electrolyte at high temperature (60 °C). **b)** Discharge/charge profiles of the high sulfur loading LSB using SSE_LiFSI cycled at 60 °C. **c)** LiPS generation test in SSE_LiFSI electrolyte at different temperatures taking SSE_LiFSI as reference electrolyte.

Figure 5.16a evidences the exceptional cycling performance of the SSE_LiFSI electrolyte at high temperatures. The cell exhibits remarkably high sulfur utilization,

highlighting its capability to ensure safe battery cycling even under high-temperature operating conditions. However, at 60 °C, the capacity decay process becomes more exacerbated compared to RT cycling, resulting in a lower average CE. In **Figure 5.16b**, the charge and discharge profiles at 60 °C are presented. A comparison with the voltage profiles at RT reveals a distinct shift in the reaction mechanism towards the dissolution-precipitation process characteristic of low-concentration electrolytes. This behavior is manifested by the emergence of two clear plateaus in the voltage profile, akin to the behavior observed with the DME/DOL electrolyte. This voltage profile modification indicates the increased solubility of high-order LiPS in the electrolyte due to the raised temperature.

To validate this hypothesis, a polysulfide generation and dissolution test was performed in the SSE_LiFSI electrolyte. In this test, S_8 and Li_2S were stoichiometrically mixed in the electrolyte and stirred at the two studied cycling temperatures, particularly RT and 60 °C. As illustrated in **Figure 5.16c**, after several days of reaction, minimal coloration is observed at 25 °C. However, at 60 °C, a noticeable color change is evident, with the solution transitioning to an orange hue. These findings corroborate the hypothesis regarding the modification of the charge and discharge profiles, demonstrating that the increased temperature drives the solubility of LiPS in the electrolyte. The heightened solubility, in turn, induces a shift in the LSB conversion mechanism from quasi-solid at RT to precipitation-dissolution process at 60 °C and a decrease in CE, due to the shuttle effect.

In any case, SSE_LiFSI is considered a promising electrolyte alternative for ensuring safe cycling even at high temperatures. However, potential strategies such as adjusting the salt concentration within the electrolyte may be considered to address the emerging challenge.

5.2.6.5. Evaluation of the impact of other lithium salt anions in LSB performance

Encouraged by the positive results achieved through the suitable selection of the anion of the lithium salt incorporated in the formulation of the SSEs, the applicability of other potential anion alternatives was evaluated. To this end, $LiNO_3$ and lithium (difluoromethanesulfonyl)(trifluoromethanesulfonyl)imide (LiDFTFSI) lithium salts were selected as appealing alternatives. As disclosed previously, $LiNO_3$ is commonly used in low-concentration electrolytes due to its great ability to mitigate the shuttle effect. The high ionic conductivity of the N-rich SEI nature generated from

the reduction of this salt on the LMA makes it an attractive alternative. On the other hand, LiDFTFSI has previously demonstrated its applicability for Li-S technology, ensuring extended cyclability when used in the composition of PEO-based all solid-state polymer electrolytes [54,55]. The exceptional properties of the SEI formed by this salt, characterized by the presence of LiF and LiH compounds, serve as its selling point. For the formulation of SSEs, in the case of $LiNO_3$, owing to its limited solubility in the presence of fluorinated ethers, a reduced concentration of 0.05 M was employed in combination with 1 M LiTFSI (named SSE_$LiNO_3$). Conversely, for LiDFTFSI, the same composition employed in the SSE_LiFSI electrolyte was used, consisting of 0.8 M LiTFSI and 0.2 M LiDFTFSI (referred to as SSE_LiDFTFSI).

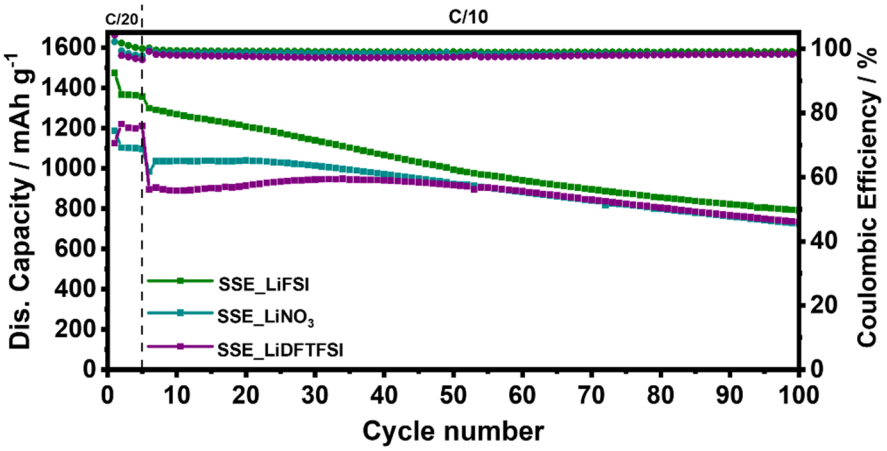

Figure 5.17. Long-term cycling performance comparison between LiFSI, $LiNO_3$, and LiDFTFSI additives in SSE formulation.

As observed in **Figure 5.17**, the incorporation of suitable SEI-forming additives allows again for substantially improved cyclability of high sulfur loading cells, effortlessly achieving 100 cycles without any signs of failure. In this way, these novel electrolytes surpass the performance offered by the conventional DME/DOL electrolyte and SSE_REF. It is noteworthy that, despite its reduced concentration in the electrolyte composition, SSE_$LiNO_3$ demonstrates superior cell performance compared to SSE_LiDFTFSI. Of particular importance are the exceptional cell stability and its affinity with the LMA, resulting in a high CE value of 98.5% (**Figure A.5.14)**. However, when compared to the SSE_LiFSI electrolyte, none of them manages to surpass its performance, neither in terms of sulfur utilization nor compatibility with the LMA. Nevertheless, the promising results offered by $LiNO_3$ as an additive in SSEs,

even at reduced concentration, open the door to further investigations aimed at optimizing this system after increasing its limited solubility in this system.

5.3. Summary and conclusions

This chapter underscores the potential applicability of engineered sparingly solvating electrolytes as promising alternatives for high-performing and safe RT LSBs. It has been demonstrated that the suitable selection of the anion of the lithium salt plays a key role in improving the LSB performance. In this sense, the transition from the conventionally employed low-concentrated electrolytes based on organic solvents to SSEs has greatly enhanced the safety of the system, primarily due to the non-flammable nature of the developed electrolyte. Furthermore, the incorporation of LiFSI in the SSE formulation, contrary to the widely employed SSE solely based on LiTFSI, has demonstrated exceptional LMA compatibility, even surpassing the performance offered by the DME/DOL electrolyte, particularly in long-term cyclability. In Li/Cu cells, the SSE_LiFSI electrolyte attains an impressive Coulombic efficiency of 98.8%, associated with compact, thin, and dense Li deposition promoted by this electrolyte. Regarding the LSB performance, the synergy between the graphene-based sulfur cathode, developed in previous chapters, and the SSE_LiFSI electrolyte has showcased an unprecedented symbiotic effect. This combination has led to substantial improvement in cell stability and sulfur utilization compared to the conventional electrolyte and SSE_REF. Significantly, this engineered SSE has successfully addressed one of the weaknesses commonly blamed on Li-S technology, which is long-term cyclability. Additionally, SSE_LiFSI electrolyte has demonstrated an exceptional rate capability delivering remarkable sulfur utilization even at high C-rate and outstanding capacity recovery. Furthermore, the excellent thermal properties shown by the SSE_LiFSI have enabled the successful cycling of over 50 cycles at a high temperature of 60 °C, delivering remarkable discharge capacity values. Finally, other potential lithium salts were studied as potential alternatives, showcasing improved cell stability but without managing to outperform the SSE_LiFSI results. Consequently, the implementation of a holistic LSB approach, with the combination of the strategies developed in different thesis chapters, has proved to be a successful strategy for improving the performance of this technology. This achievement paves the way for further studies into upscaling this system for prototype cells, bringing it closer to practical applications.

5.4. Brief outlook and perspective

Chapters II and **III**, despite the integration of effective advancements in sulfur cathodes, have provided detailed evidence of the conventional electrolyte's incapacity to ensure stable LSB cycling. This problem arises from its limited long-term compatibility with the LMA, thereby jeopardizing the primary objective of upscaling exploration established for this thesis. In light of this challenge, **Chapters IV** and **V** have undertaken the pivotal task of formulating new electrolyte alternatives to replace the conventional DME/DOL electrolyte and foster long-term cycling in LSBs. To achieve this objective, two different strategies have been implemented.

In **Chapter IV**, the viability of integrating GPEs into Li-S technology has been explored. Through the implementation of a readily scalable and effective one-pot manufacturing process, the GPE_20 electrolyte was developed. Notably, this electrolyte showcased exceptional individual properties, manifesting an outstanding balance among structural integrity, electrochemical properties, thermal stability, and safety characteristics. Nonetheless, the unmitigated dissolution of LiPS coupled with the reactivity of the fluorinated polymer matrix with the LMA triggered a series of parasitic reactions, leading to unsatisfactory LSB performance. Despite initial concerns regarding GPE_20's performance, sustained focus on its applicability resulted in unexpectedly excellent cyclability when implemented in LFP-based LMBs. This successful application provided the opportunity to explore its scalability process under operating conditions more closely resembling practical scenarios, consistently yielding highly promising results. Therefore, despite exemplifying a failed strategy to enhance the performance of LSBs, this study has played a crucial role in highlighting the significance and establishing the mitigation of LiPS dissolution and ensuring compatibility with the LMA as indispensable characteristics for an electrolyte in Li-S technology to guarantee optimal performance.

In response to these requirements, a strategic decision was made to revisit the approach and focus on the development of liquid electrolytes with low or negligible solubility of LiPS. For this purpose, **Chapter V** delved into the formulation of a customized SSE as an appealing alternative for LSBs, resulting in the development of the SSE_LiFSI electrolyte. Distinguishing itself from previously reported SSEs in the literature, SSE_LiFSI has exploited the distinctive solvation structure of this electrolyte family through the incorporation of LiFSI salt as additive. This strategic integration

empowered SSE_LiFSI to exhibit excellent Li metal deposition and form an effective LiF-rich protective SEI layer. These pivotal attributes allowed for demonstrating its exceptional long-term compatibility with the LMA. Furthermore, the unique solvation structure of the SSEs, marked by a minimal presence of free solvent molecules, resulted in a diminished dissolution of LiPS. Finally, SSE_LiFSI not only fulfilled the criteria for an optimal LSB electrolyte but also established a synergistic relationship with the graphene-based sulfur cathode developed in **Chapter III**. This compendium of properties translated into remarkable LSB performance, featuring an excellent equilibrium between sulfur utilization and stable long-term cycling. Furthermore, the versatility of the system was underscored by the successful incorporation of new additives, paving the way for future works aimed at continued optimization.

These results substantiate the effectiveness of the proposed holistic approach, as demonstrated by the SSE_LiFSI system, for the development of high-performing, safe, and stable LSBs. Consequently, the encouraged results observed in this system form a compelling foundation for exploring its scalability in prototype cells closely aligned with practical applications.

5.5. Bibliography

[1] H. Asano, J. Liu, K. Ueno, K. Dokko, T. Kojima, N. Takeichi, T. Miyuki, Y. Yamakawa, M. Watanabe, Enhancing the reversibility of Li deposition/dissolution in sulfur batteries using high-concentration electrolytes to develop anode-less batteries with lithium sulfide cathode, J. Power Sources 2023, 554, 232323. https://doi.org/10.1016/j.jpowsour.2022.232323.

[2] G.X. Liu, J.X. Tian, J. Wan, Y. Li, Z.Z. Shen, W.P. Chen, Y. Zhao, F. Wang, B. Liu, S. Xin, Y.G. Guo, R. Wen, Revealing the high salt concentration manipulated evolution mechanism on the lithium anode in quasi-solid-state lithium-sulfur batteries, Angew. Chemie 2022, 61, 202212744. https://doi.org/10.1002/anie.202212744.

[3] J. Huang, T. Yan, M. Tao, W. Zhang, W. Li, G. Zheng, L. Du, Z. Cui, X. Wang, S. Liao, H. Song, Localized high-concentration carbonate electrolyte creating functional in situ interfaces: Side reaction inhibition for lithium sulfur batteries, J. Power Sources 2023, 563, 232783. https://doi.org/10.1016/j.jpowsour.2023.232783.

[4] X. Liu, A. Mariani, H. Adenusi, S. Passerini, Locally Concentrated Ionic Liquid Electrolytes for Lithium-Metal Batteries, Angew. Chemie 2023, 62, 202219318. https://doi.org/10.1002/anie.202219318.

[5] H. Ye, Y. Li, Towards practical lean-electrolyte Li–S batteries: Highly solvating electrolytes or sparingly solvating electrolytes?, Nano Res. Energy. 2022, 1, 9120012. https://doi.org/10.26599/nre.2022.9120012.

[6] A. Ghosh, J. Liu, S. Li, K. Ueno, K. Dokko, M. Watanabe, Lithium aluminate nanoflakes as an additive to sulfur cathodes for enhanced mass transport in high-energy-density lithium-sulfur pouch cells utilizing sparingly solvating electrolytes, ACS Appl. Mater. Interfaces 2023, 15, 23104–23114. https://doi.org/10.1021/acsami.3c01574.

[7] X.Q. Zhang, Q. Jin, Y.L. Nan, L.P. Hou, B.Q. Li, X. Chen, Z.H. Jin, X.T. Zhang, J.Q. Huang, Q. Zhang, Electrolyte structure of lithium polysulfides with anti-reductive solvent shells for practical lithium–sulfur batteries, Angew. Chemie 2021, 60, 15503–15509. https://doi.org/10.1002/anie.202103470.

[8] C. Zhu, C. Sun, R. Li, S. Weng, L. Fan, X. Wang, L. Chen, M. Noked, X. Fan, Anion-

diluent pairing for stable high-energy Li metal batteries, ACS Energy Lett. 2022, 7, 1338–1347. https://doi.org/10.1021/acsenergylett.2c00232.

[9] Z. Xu, K. Deng, S. Zhou, D. Mo, High-performance lithium metal batteries enabled by fluorinated aromatic diluent assisted nonflammable localized high-concentration electrolytes, J. Power Sources 2023, 559, 232631. https://doi.org/10.1016/j.jpowsour.2023.232631.

[10] C. Sauter, R. Zahn, V. Wood, Understanding electrolyte Infilling of Lithium Ion Batteries, J. Electrochem. Soc. 2020, 167, 100546. https://doi.org/10.1149/1945-7111/ab9bfd.

[11] X. Cao, H. Jia, W. Xu, J.-G. Zhang, Review—localized high-concentration electrolytes for lithium batteries, J. Electrochem. Soc. 2021, 168, 010522. https://doi.org/10.1149/1945-7111/abd60e.

[12] J. Wang, Y. Yamada, K. Sodeyama, C.H. Chiang, Y. Tateyama, A. Yamada, Superconcentrated electrolytes for a high-voltage lithium-ion battery, Nat. Commun. 2016, 7, 12032. https://doi.org/10.1038/ncomms12032.

[13] Y. Zhao, T. Zhou, T. Ashirov, M. El Kazzi, C. Cancellieri, L.P.H. Jeurgens, J.W. Choi, A. Coskun, Fluorinated ether electrolyte with controlled solvation structure for high voltage lithium metal batteries, Nat. Commun. 2022, 13, 2575. https://doi.org/10.1038/s41467-022-29199-3.

[14] Q. Liu, Y. Liu, Z. Chen, Q. Ma, Y. Hong, J. Wang, Y. Xu, W. Zhao, Z. Hu, X. Hong, J. Wang, X. Fan, H. Bin Wu, An inorganic-dominate molecular diluent enables safe localized high concentration electrolyte for high-voltage lithium-metal batteries, Adv. Funct. Mater. 2023, 33, 2209725. https://doi.org/10.1002/adfm.202209725.

[15] K. Park, Y. Jo, B. Koo, H. Lee, H. Lee, Wide temperature cycling of Li-metal batteries with hydrofluoroether dilution of high-concentration electrolyte, Chem. Eng. J. 2022, 427, 131889. https://doi.org/10.1016/j.cej.2021.131889.

[16] Q. Wu, Y. Qian, X. Tang, J. Teng, H. Ding, H. Zhao, J. Li, Stable cycling of lithium-metal batteries in hydrofluoroether-based localized high-concentration electrolytes with 2-fluoropyridine additive, ACS Appl. Energy Mater. 2022, 5, 5742–5749. https://doi.org/10.1021/acsaem.2c00037.

[17] C. Kensy, F. Schwotzer, S. Dörfler, H. Althues, S. Kaskel, Impact of carbon porosity on sulfur conversion in Li−S battery cathodes in a sparingly polysulfide solvating electrolyte, Batter. Supercaps 2021, 4, 823–833. https://doi.org/10.1002/batt.202000286.

[18] F. Yang, X. Qi, H. Du, R. Jiang, R. Zhao, Y. Pan, Q. Jin, X. Jin, L. Qie, Y. Huang, From sparingly solvating to weakly solvating: Fine electrolyte regulation for lean-electrolyte Li-SeS2 batteries, Energy Storage Mater. 2023, 55, 272–278. https://doi.org/10.1016/j.ensm.2022.11.051.

[19] J.X. Guo, W.B. Tang, X. Xiong, H. Liu, T. Wang, Y. Wu, X.B. Cheng, Localized high-concentration electrolytes for lithium metal batteries: progress and prospect, Front. Chem. Sci. Eng. 2023, 17, 1354–1371. https://doi.org/10.1007/s11705-022-2286-4.

[20] C.M. Efaw, Q. Wu, N. Gao, Y. Zhang, H. Zhu, K. Gering, M.F. Hurley, H. Xiong, E. Hu, X. Cao, W. Xu, J.G. Zhang, E.J. Dufek, J. Xiao, X.Q. Yang, J. Liu, Y. Qi, B. Li, Localized high-concentration electrolytes get more localized through micelle-like structures, Nat. Mater. 2023, 22, 1531–1539. https://doi.org/10.1038/s41563-023-01700-3.

[21] Y. Chen, M. Li, Y. Liu, Y. Jie, W. Li, F. Huang, X. Li, Z. He, X. Ren, Y. Chen, X. Meng, Origin of dendrite-free lithium deposition in concentrated electrolytes, Nat. Commun. 2023, 14, 2655. https://doi.org/10.1038/s41467-023-38387-8.

[22] R. May, J.C. Hestenes, N.A. Munich, L.E. Marbella, Fluorinated ether decomposition in localized high concentration electrolytes, J. Power Sources 2023, 553, 232299. https://doi.org/10.1016/j.jpowsour.2022.232299.

[23] Y. Zhang, L. Zeng, Z. Ding, W. Wu, L. Deng, L. Yao, Stable electrode/electrolyte interfaces regulated by dual-salt and localized high-concentration strategies for high-voltage lithium metal batteries, Chem. Commun. 2023, 59, 12593–12596. https://doi.org/10.1039/d3cc02705h.

[24] L. Wang, Z. Luo, H. Xu, N. Piao, Z. Chen, G. Tian, X. He, Anion effects on the solvation structure and properties of imide lithium salt-based electrolytes, RSC Adv. 2019, 9, 41837–41846. https://doi.org/10.1039/c9ra07824j.

[25] J. Fu, X. Ji, J. Chen, L. Chen, X. Fan, D. Mu, C. Wang, Lithium nitrate regulated

sulfone electrolytes for lithium metal batteries, Angew. Chemie. 2020, 132, 22378–22385. https://doi.org/10.1002/ange.202009575.

[26] J. Chen, H. Zhang, M. Fang, C. Ke, S. Liu, J. Wang, Design of localized high-concentration electrolytes via donor number, ACS Energy Lett. 2023, 8, 1723–1734. https://doi.org/10.1021/acsenergylett.3c00004.

[27] J. Xu, V. Koverga, A. Phan, A. min Li, N. Zhang, M. Baek, C. Jayawardana, B.L. Lucht, A.T. Ngo, C. Wang, Revealing the anion–solvent interaction for ultralow temperature lithium metal batteries, Adv. Mater. 2023, 2306462. https://doi.org/10.1002/adma.202306462.

[28] X. Ren, S. Chen, H. Lee, D. Mei, M.H. Engelhard, S.D. Burton, W. Zhao, J. Zheng, Q. Li, M.S. Ding, M. Schroeder, J. Alvarado, K. Xu, Y.S. Meng, J. Liu, J.G. Zhang, W. Xu, Localized high-concentration sulfone electrolytes for high-efficiency lithium-metal batteries, Chem. 2018, 4, 1877–1892. https://doi.org/10.1016/j.chempr.2018.05.002.

[29] L. Xia, S. Lee, Y. Jiang, S. Li, Z. Liu, L. Yu, D. Hu, S. Wang, Y. Liu, G.Z. Chen, Physicochemical and electrochemical properties of 1,1,2,2-tetrafluoroethyl-2,2,3,3-tetrafluoropropyl ether as a co-solvent for high-voltage lithium-ion electrolytes, ChemElectroChem 2019, 6, 3747–3755. https://doi.org/10.1002/celc.201900729.

[30] L. Su, F. Lu, X. Liu, C. Wang, Y. Gao, S. Passerini, L. Zheng, G. Xinpei, Molecular insight into nano-heterogeneity of localized high-concentration electrolyte: Correlation with lithium dynamics and solid-electrolyte interphase formation, J. Power Sources 2023, 557, 232545. https://doi.org/10.1016/j.jpowsour.2022.232545.

[31] Y. Xiao, X. Wang, K. Yang, J. Wu, Y. Chao, C. Xi, M. Li, Q. Zhang, Z. Liu, L. Li, Y. Yu, C. Yang, The anion-dominated dynamic coordination field in the electrolytes for high-performance lithium metal batteries, Energy Storage Mater. 2023, 55, 773–781. https://doi.org/10.1016/j.ensm.2022.12.038.

[32] S. Angarita-Gomez, P.B. Balbuena, Ion mobility and solvation complexes at liquid-solid interfaces in dilute, high concentration, and localized high concentration electrolytes, Mater. Adv. 2022, 3, 6352–6363. https://doi.org/10.1039/d2ma00541g.

[33] Y. Wu, A. Wang, Q. Hu, H. Liang, H. Xu, L. Wang, X. He, Significance of Antisolvents on Solvation Structures Enhancing Interfacial Chemistry in Localized

High-Concentration Electrolytes, ACS Cent. Sci. 2022, 8, 1290–1298. https://doi.org/10.1021/acscentsci.2c00791.

[34] M. Martinez-Ibañez, N. Boaretto, L. Meabe, X. Wang, H. Zhu, A. Santiago, O. Zugazua, M. Forsyth, M. Armand, H. Zhang, Revealing the anion chemistry effect on transport properties of ternary gel polymer electrolytes, Chem. Mater. 2022, 34, 7493–7502. https://doi.org/10.1021/acs.chemmater.2c00260.

[35] H. Jia, Y. Xu, L. Zou, P. Gao, X. Zhang, B. Taing, B.E. Matthews, M.H. Engelhard, S.D. Burton, K.S. Han, L. Zhong, C. Wang, W. Xu, Sulfone-based electrolytes for high energy density lithium-ion batteries, J. Power Sources 2022, 527, 231171. https://doi.org/10.1016/j.jpowsour.2022.231171.

[36] X. Wang, W. He, H. Xue, D. Zhang, J. Wang, L. Wang, J. Li, A nonflammable phosphate-based localized high-concentration electrolyte for safe and high-voltage lithium metal batteries, Sustain. Energy Fuels. 2022, 6, 1281–1288. https://doi.org/10.1039/d1se01919h.

[37] X. Chen, Y. Meng, D. Xiao, Y. Wu, L. Qin, Tunning solvation structure in non-flammable, localized high-concentration electrolytes with enhanced stability towards all aluminum substrate-based K batteries, Energy Storage Mater. 2023, 61, 102923. https://doi.org/10.1016/j.ensm.2023.102923.

[38] S. Yuan, K. Ding, X. Zeng, D. Bin, Y. Zhang, P. Dong, Y. Wang, Advanced nonflammable organic electrolyte promises safer Li-metal batteries: From solvation structure perspectives, Adv. Mater. 2023, 35, 2206228. https://doi.org/10.1002/adma.202206228.

[39] B.D. Adams, J. Zheng, X. Ren, W. Xu, J.G. Zhang, Accurate determination of coulombic efficiency for lithium metal anodes and lithium metal batteries, Adv. Energy Mater. 2018, 8, 1702097. https://doi.org/10.1002/aenm.201702097.

[40] F. Wang, Z. Wen, Z. Zheng, W. Fang, L. Chen, F. Chen, N. Zhang, X. Liu, R. Ma, G. Chen, Memory effect of MgAl layered double hydroxides promotes LiNO3 dissolution for stable lithium metal anode, Adv. Energy Mater. 2023, 13, 2203830. https://doi.org/10.1002/aenm.202203830.

[41] S. Kim, K.Y. Cho, J.H. Kwon, K. Sim, D. Seok, H. Tak, J. Jo, K.S. Eom, An inorganic-

rich SEI layer by the catalyzed reduction of LiNO3 enabled by surface-abundant hydrogen bonding for stable lithium metal batteries, Small. 2023, 19, 2207222. https://doi.org/10.1002/smll.202207222.

[42] S. Stuckenberg, M.M. Bela, C.T. Lechtenfeld, M. Mense, V. Küpers, T.T.K. Ingber, M. Winter, M.C. Stan, Influence of LiNO3 on the lithium metal deposition behavior in carbonate-based liquid electrolytes and on the electrochemical performance in zero-excess lithium metal batteries, Small. 2023, 2305203. https://doi.org/10.1002/smll.202305203.

[43] R. Zhang, X.R. Chen, X. Chen, X.B. Cheng, X.Q. Zhang, C. Yan, Q. Zhang, Lithiophilic sites in doped graphene guide uniform lithium nucleation for dendrite-free lithium metal anodes, Angew. Chemie 2017, 56, 7764–7768. https://doi.org/10.1002/anie.201702099.

[44] C. Liao, L. Han, W. Wang, W. Li, X. Mu, Y. Kan, J. Zhu, Z. Gui, X. He, L. Song, Y. Hu, Non-flammable electrolyte with lithium nitrate as the only lithium salt for boosting ultra-stable cycling and fire-safety lithium metal batteries, Adv. Funct. Mater. 2023, 33, 2212605. https://doi.org/10.1002/adfm.202212605.

[45] H. Cheng, H. Jin, H. Liu, N. Cai, C. Gao, P. Zhang, M. Wang, An interconnected silver coated carbon cloth framework as a host to reduce lithium nucleation over-potential for dendrite-free lithium metal anodes, J. Electroanal. Chem. 2020, 878, 114569. https://doi.org/10.1016/j.jelechem.2020.114569.

[46] R.M. Kasse, N.R. Geise, J.S. Ko, J. Nelson Weker, H.G. Steinrück, M.F. Toney, Understanding additive controlled lithium morphology in lithium metal batteries, J. Mater. Chem. A 2020, 8, 16960–16972. https://doi.org/10.1039/d0ta06020h.

[47] C. Chang, Y. Yao, R. Li, Z. Cong, L. Li, Z.H. Guo, W. Hu, X. Pu, Stable lithium metal batteries enabled by localized high-concentration electrolytes with sevoflurane as a diluent, J. Mater. Chem. A 2022, 10, 9001–9009. https://doi.org/10.1039/d1ta10618j.

[48] M. Jia, C. Zhang, Y. Guo, L. Peng, X. Zhang, W. Qian, L. Zhang, S. Zhang, Advanced nonflammable localized high-concentration electrolyte for high energy density lithium battery, Energy Environ. Mater. 2022, 5, 1294–1302. https://doi.org/10.1002/eem2.12246.

[49] L. Fu, X. Wang, L. Wang, M. Wan, Y. Li, Z. Cai, Y. Tan, G. Li, R. Zhan, Z.W. Seh, Y. Sun, A salt-in-metal anode: stabilizing the solid electrolyte interphase to enable prolonged battery cycling, Adv. Funct. Mater. 2021, 31, 2010602. https://doi.org/10.1002/adfm.202010602.

[50] Y. Lu, C.Z. Zhao, H. Yuan, X.B. Cheng, J.Q. Huang, Q. Zhang, Critical current density in solid-state lithium metal batteries: Mechanism, influences, and strategies, Adv. Funct. Mater. 2021, 31, 2009925. https://doi.org/10.1002/adfm.202009925.

[51] Y. Liu, Y. Zhu, Y. Cui, Challenges and opportunities towards fast-charging battery materials, Nat. Energy 2019, 4, 540–550. https://doi.org/10.1038/s41560-019-0405-3.

[52] B.S. Vishnugopi, E. Kazyak, J.A. Lewis, J. Nanda, M.T. McDowell, N.P. Dasgupta, P.P. Mukherjee, Challenges and Opportunities for Fast Charging of Solid-State Lithium Metal Batteries, ACS Energy Lett. 2021, 6, 3734–3749. https://doi.org/10.1021/acsenergylett.1c01352.

[53] X. Shangguan, G. Xu, Z. Cui, Q. Wang, X. Du, K. Chen, S. Huang, G. Jia, F. Li, X. Wang, D. Lu, S. Dong, G. Cui, Additive-assisted novel dual-salt electrolyte addresses wide temperature operation of lithium–metal batteries, Small 2019, 15, 1900269. https://doi.org/10.1002/smll.201900269.

[54] A. Santiago, J. Castillo, I. Garbayo, A. Saenz De Buruaga, J.A. Coca Clemente, L. Qiao, R. Cid Barreno, M. Martinez-Ibañez, M. Armand, H. Zhang, C. Li, Salt additives for improving cyclability of polymer-based all-solid-state lithium-sulfur batteries, ACS Appl. Energy Mater. 2021, 4, 4459–4464. https://doi.org/10.1021/acsaem.1c00091.

[55] H. Zhang, U. Oteo, X. Judez, G.G. Eshetu, M. Martinez-Ibañez, J. Carrasco, C. Li, M. Armand, Designer anion enabling solid-state lithium-sulfur batteries, Joule 2019, 3, 1689–1702. https://doi.org/10.1016/j.joule.2019.05.003.

Chapter VI

From Lab-Scale Coin Cell to Ah-Level Prototype Li-S Cell Performance

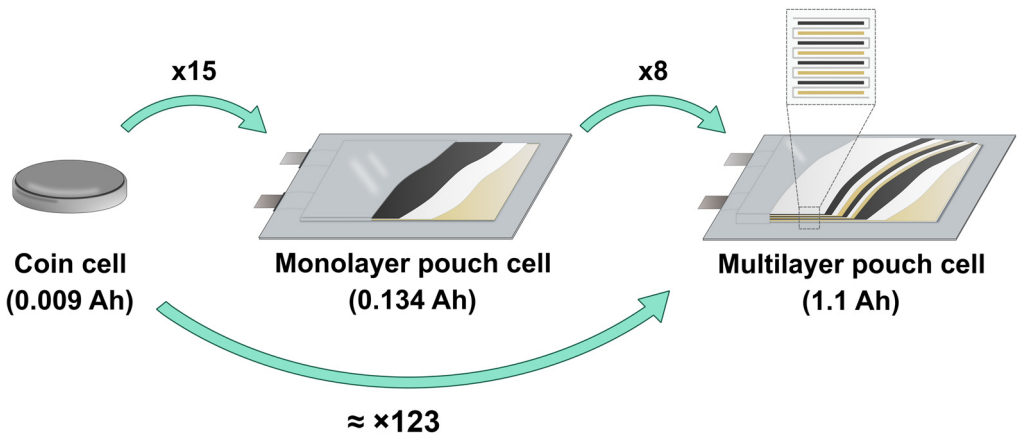

6.1. Introduction

In the preceding chapters, different approaches were designed to address the intricate technological challenges associated with Li-S technology. Among them, the holistic perspective adopted in **Chapter V,** combining an engineering electrolyte with a high-performing cathode, both developed under the current thesis, has stood out by demonstrating exceptional and auspicious results. The effectiveness of this approach lies in confronting the multidisciplinary challenges of the technology by implementing multiple strategies into a final device. However, it is crucial to emphasize that all the advancements thus far have been conducted on lab-scale coin cells, far from industrial needs. Therefore, these results serve as motivation to further optimize the system by evaluating its scalability process for eventual practical application.

To date, considerable research effort has been dedicated to solving the inherent challenges within Li-S technology to enhance its electrochemical performance. These efforts have yielded the development of innovative strategies focusing on each component of the cell, including using new sulfur hosts to mitigate LiPS dissolution, modifications of electrolytes and separators, and the design of artificial solid electrolyte interphase. Nevertheless, it is noteworthy that most of the reported studies use coin-cell configurations characterized by low sulfur mass loadings (≤ 2 mg_S cm^{-2}), excessive amounts of electrolyte (≥ 10 µL mg_S^{-1}), and high excess of LMA conditions (N/P ≥ 25) [1–3]. The improvements obtained under these operating conditions may potentially diverge the research direction and underestimate the challenges associated with the upscaling process under more realistic operating conditions. Additionally, utilizing these ideal operating conditions would yield very low and unfeasible cell energy densities, rendering their commercialization impossible.

In recent years, the awareness of the operating conditions issue has catalyzed a substantial paradigm shift in the Li-S research towards the incorporation of more realistic operating conditions during cell testing. This adjustment enables a more accurate selection of potential advancements. Despite the commendable performance observed in coin cells, a notable gap persists in the scientific literature concerning the evaluation of prototype pouch cell performance. Although there has been a recent uptick in publications reporting pouch cell performances, as evidenced

in **Figure 6.1a**, the overall contribution remains insufficient, representing a mere 4.4% of total publications in the field of LSBs in the last 10 years (**Figure 6.1b**). This disparity underscores the scarcity of insights into pouch cell behavior, raising questions regarding the transferability of improvements achieved with developed materials to practical Li-S cells, accentuating the gap between academic and industrial research [4–7].

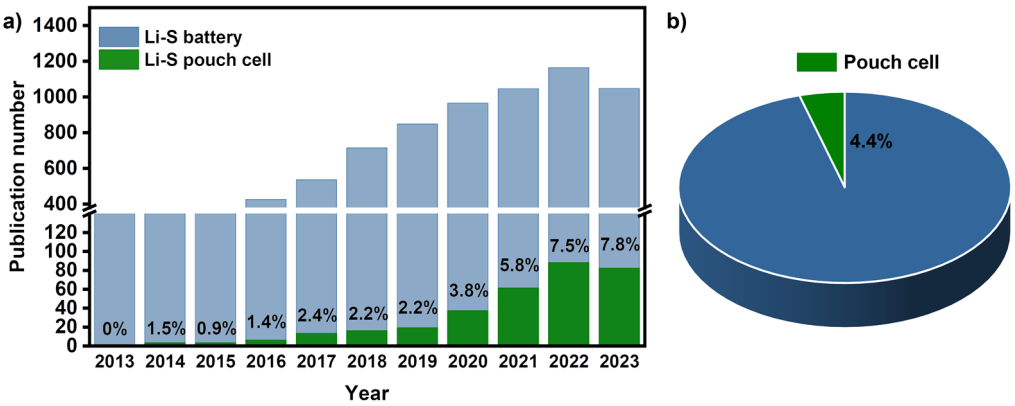

Figure 6.1. Literature analysis of the Li–S pouch cell area. **a)** Publication number per year of Li–S pouch cells and LSBs and **b)** the total percentage of Li–S pouch cell publications accounting in the LSB field from 2013 to 2023.

The lack of insights transferability between these two entities is evidenced by the considerable disparities in cell cyclability. While studies have asserted 1000 cycles at coin cell level, the cyclability reported for Ah-level pouch cells is only several tens of cycles [8–10]. This significant cyclability divergence is deeply rooted in the marked differences in operating conditions between coin and pouch cells, an aspect thoroughly detailed in **Chapter I**. Notably, the introduction of a substantial scalability factor during the transition from coin to practical cells, coupled with the adjusted operating conditions of prototype cells oriented towards high energy density values, give rise to extremely harsh cycling environment. Under these conditions, new operational challenges emerge compared to coin cells, particularly LMA degradation and electrolyte depletion [11–13]. These emerging challenges collectively contribute to rendering cyclability the Achilles heel of practical Li-S pouch cells. This unresolved issue hampers the widespread commercialization of LSBs, a milestone yet to be accomplished [14,15]. Therefore, validating the results obtained in coin cells for their

applicability to pouch cells is a fundamental step in evaluating the practical potential of the proposed advancements.

In the evaluation of prototype cells, the determination of cell energy density emerges as a pivotal metric for analyzing their prospective applicability [16,17]. This parameter is expressed either as gravimetric energy density, denoting energy storage per unit cell mass, or volumetric energy density, representing energy storage per cell volume. The significance of gravimetric energy density lies in its representation of the battery's capacity to store more energy within smaller device mass, rendering it particularly critical for weight-sensitive applications such as drones, buses, or trucks. Conversely, a higher volumetric energy density implies the storage of a greater amount of energy within a diminished volume, a factor of paramount importance in applications constrained by limited space, exemplified by electric cars. In this context, LSBs stand out due to their high energy density compared to commercial LIBs. This distinction would allow for a substantial reduction in the mass of current batteries, positioning LSBs as particularly well-suited for weight-critical applications, thereby constituting their main market niche [14,18–20].

This chapter presents a comprehensive study of the upscaling process of the different strategies proposed in this thesis, aiming to evaluate their practical applicability in cells closely aligned with industrial requirements. Firstly, given the remarkable differences in operating conditions between coin and pouch cells, and seeking to meet industrial requirements for its future commercialization, an in-depth analysis of the key parameters that significantly impact the energy density of prototype Li-S cells will be conducted. This analysis will be crucial to establishing the necessary operating conditions for the development of high-energy-density Li-S cells. Subsequently, as an intermediate step, the performance of each proposed strategy in this thesis will be assessed in monolayer pouch cell design. This study will be instrumental in evaluating the initial results in larger surface area pouch cells and allowing for a meaningful comparison with the performances achieved previously in small coin cells. Finally, an analysis of Ah-level pouch cells will be conducted to ascertain the applicability in cells closely aligned to real-world applications.

6.2. Formulating energy density model

6.2.1. Calculation of gravimetric energy density

As a key initial step, the transparent calculation of energy density at the cell level is essential for the accurate analysis of the cell upscaling process [6,17,21]. In this case, the evaluation of the gravimetric energy density is conducted, considering all the active and inactive components of the cell. In this case, the calculation will be centered at the cell level, thereby excluding cell packaging weight.

As outlined in **Chapter I**, the energy density of a Li-S cell (in Wh kg^{-1}) can be defined as:

$$E_G = \frac{C_S \times U_{nom}}{m_{cell}} \quad (6.1)$$

where C_S is the specific cell capacity (in Ah), U_{nom} is the nominal voltage of the (in V), and m_{cell} is the overall weight of the cell (in kg).

The total weight of the cell is calculated as the sum of the weight of every single component of the cell (in kg), including the mass of the Li anode (m_{Li}), cathode (m_{cath}), cathode current collector (m_{cc_cath}), separator (m_{sep}), and electrolyte (m_{LE}).

$$m_{cell} = m_{Li} + m_{cath} + m_{cc\_cath} + m_{sep} + m_{LE} \quad (6.2)$$

In some scenarios, the mass corresponding to the anode current collector, typically composed of copper, needs to be considered when calculating the total mass. However, in this particular case, Li metal was used both as the anode and the current collector, rendering the mass corresponding to the copper current collector exempt from consideration.

Concerning the LMA, its mass is calculated by considering the ratio between the anode capacity and the cathode capacity, denoted as the N/P ratio (r_{NP}). This parameter indicates the surplus of lithium present in the cell. In commercial LIBs, this excess typically falls within the range of 5-10% at most. However, in the case of LMBs, an additional excess is often introduced to mitigate potential parasitic reactions associated with the high reactivity of the LMA. Therefore, the Li mass is calculated as follows:

$$m_{Li} = r_{NP} \times L_S \times C_{S\_theo} \times \frac{A_{anode}}{C_{Li\_theo}} \quad (6.3)$$

where L_S is the sulfur loading of the cathode (in g_S cm^{-2}), C_{S_theo} is the theoretical capacity of sulfur (in Ah g^{-1}, being 1.675 Ah g^{-1}), A_{anode} is the geometric surface area of the anode (in cm^2, equal to $A_{cathode}$), and C_{Li_theo} is the theoretical capacity of lithium (in Ah g^{-1}, being 3.860 Ah g^{-1}).

The total weight of the cathode is calculated by:

$$m_{cath} = \frac{A_{cath} \times L_S}{\omega_s} \quad (6.4)$$

where $A_{cathode}$ is the total area of the sulfur cathode (in cm^2) and ω_S is the mass content of sulfur in the cathode composition.

Considering the possible scenario of a multilayer cell with the slurry coated on both sides of the current collector, the total area of the cathode is obtained by:

$$A_{cath} = 2 \times A_{1cath} \times n_{cath} \quad (6.5)$$

where A_{1cath} is the surface area of one side of an electrode and n_{cath} is the number of double-side coated cathodes in the cell.

The mass of the current collector of the cathode can be obtained from the following equation:

$$m_{cc\_cath} = A_{cc\_cath} \times n_{cath} \times \rho_{Al} \times t_{Al} \quad (6.6)$$

where A_{cc_cath} is the total area of the aluminum current collector, (in cm^2, being equal to $A_{cathode}$), ρ_{Al} is the density of aluminum (in g cm^{-3}), and t_{Al} is the thickness of the aluminum current collector.

In each multilayer cell, the double-side coated sulfur cathodes are separated from their respective LMAs by one sheet of separator. Thus, the total mass of the separator inside the cell can be obtained by:

$$m_{sep} = A_{sep} \times 2 \times n_{cath} \times L_{sep} \quad (6.7)$$

where A_{sep} represents the area of each separator piece (in cm^2) and L_{sep} is the areal density of the separator (in g cm^{-2}), which is inherent to the type of separator employed.

As the systems under study rely on liquid electrolytes, the energy density calculation is determined based on the widely used ratio of electrolyte volume to sulfur mass, E/S ratio. Therefore, the mass of the electrolyte is defined as:

$$m_{LE} = A_{cath} \times L_S \times r_{E/S} \times \rho_{LE} \quad (6.8)$$

where ρ_{LE} is the density of the employed electrolyte (in g cm^{-3})

Finally, the specific capacity of the cell can be described as a function of the sulfur utilization rate (μ_S) as follows:

$$C_S = C_{S,theo} \times \mu_S \times L_S \times A_{cath} \quad (6.9)$$

To perform energy density calculations, a set of necessary parameters related to the systems developed in this thesis have been extracted and compiled in **Table A.6.1**. Additionally, MATLAB codes can be found in the Appendix section of **Chapter VI**.

6.2.2. Evaluation of key design parameters to achieve high-energy-density LSBs

The detailed calculations outlined above have identified five parameters with the potential to impact the final energy density of Li-S cells. These parameters include the E/S ratio, N/P ratio, sulfur utilization rate, sulfur loading, sulfur weight content in the cathode formulation, and electrolyte density. Notably, particular attention was placed on the E/S ratio and N/P ratio among these parameters. This focus arises from the recognition that electrolyte and anode excess have been identified as primary contributors to misinterpretations of lab-scale cell results, masking the fundamental degradation mechanisms in LSBs.

At this point, building upon the results obtained in the preceding chapters, a reference cell has been defined with specific features: a sulfur utilization rate of 75%, sulfur content of 64 wt.%, sulfur loading of 4 mg_S cm^{-2}, an electrolyte density of 1.1 g cm^{-3}. Regarding the E/S ratio and N/P ratio parameters, aligned with the established guidelines from the Li-S literature for achieving high energy density cells,

they have been set at 3 µL mg_S^{-1} and 3, respectively. The correlations between the energy density and the five parameters are represented in **Figure 6.2, Figure 6.3, and Figure 6.4**. Each subfigure delineated the influence of two key parameters on energy density while maintaining the remaining parameters constant, employing the values disclosed above.

Sulfur utilization, indicative of the system's efficacy in promoting sulfur redox reactions and directly linked to the practical specific capacity of the cell, has long held a central focus in the Li-S research literature. As illustrated in **Figure 6.2a**, the energy density exhibits a linear increase with maximizing sulfur utilization until reaching a point where the improvement becomes less pronounced. These findings reveal that a sulfur utilization exceeding 0.6 is pivotal for achieving high energy density values surpassing 300 Wh kg^{-1}. However, it is worth noting that the positive impact of increased sulfur utilization on energy density can be significantly compromised when sulfur loadings below 2 mg_S cm^{-2} are used.

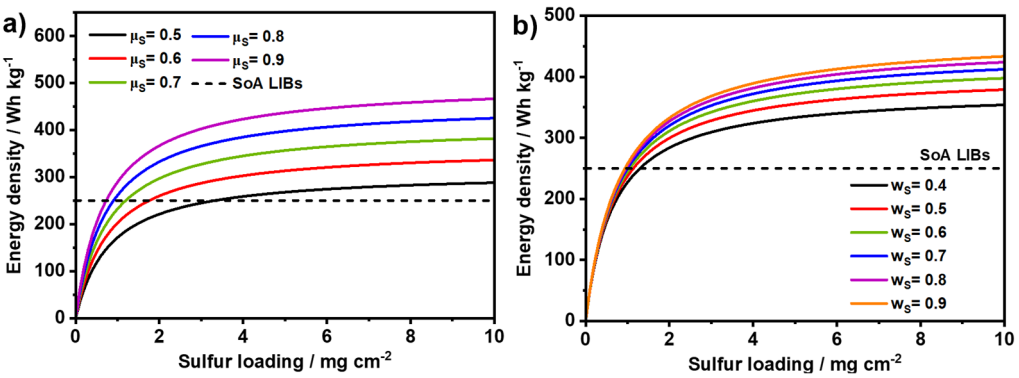

Figure 6.2. The projected gravimetric energy density of a multilayered Li-S pouch cell evaluating the impact of different operating parameters: **a)** sulfur utilization rate and **b)** sulfur content within the cathode composition by varying the sulfur loading.

As discussed in **Chapter III**, the sulfur content in the cathode formulation is another key parameter to consider. The motivation for increasing the sulfur content lies in minimizing the mass attributed to inactive materials within the sulfur cathode, such as carbonaceous materials and binders, which can negatively impact energy density. **Figure 6.2b** reveals that sulfur content does not appreciably influence the energy density of the cell until the sulfur loading exceeds 3 mg_S cm^{-2}. Below this threshold, the cathode's contribution to the overall cell mass is minimal, rendering

the effect of sulfur content practically negligible. Even at higher sulfur loadings, the impact of sulfur remains of low significance, except for the cases where sulfur content falls below 0.6. This phenomenon can be attributed to the minimal contribution of inactive components to the overall weight of the whole cell.

Another parameter to consider in the study of energy density is the sulfur loading of the cathode. This parameter is widely recognized in the literature as a pivotal parameter for achieving high energy density values in Li-S cells. As depicted in **Figures 6.2a** and **b**, there is a pronounced increase in energy density with a corresponding rise in sulfur loading. However, the advantage of increasing sulfur loading toward higher energy densities reaches a saturation point at 3.5-4 mg_S cm^{-2}, akin to the concept of diminishing marginal effect in the field of economics. This suggests that the energetic density of the cell is not favorably inclined to further increase by incorporating more sulfur into the system. The additional sulfur, coupled with the concomitant increase in anode and electrolyte amounts, would result in a higher cell mass without a proportionate increase in energy density. Nevertheless, achieving energy density values exceeding 300 Wh kg^{-1} requires the use of sulfur loading exceeding 3.5 mg_S cm^{-2}.

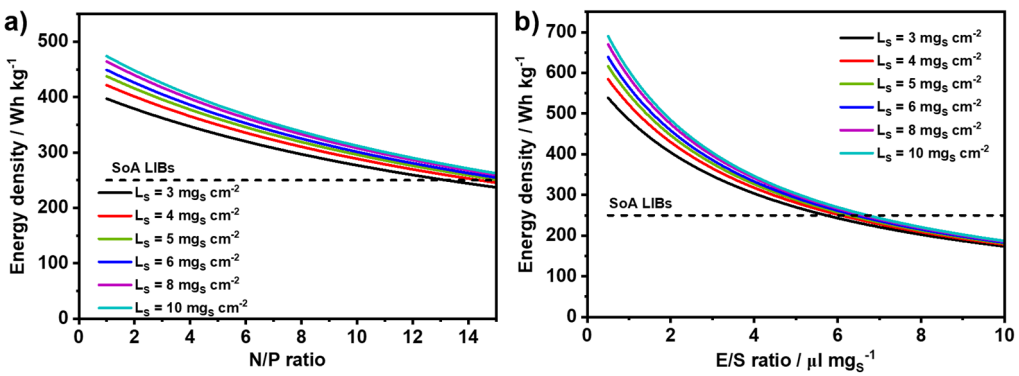

Figure 6.3. Impact of the **a)** N/P ratio and **b)** E/S ratio in the projected gravimetric energy density in Li-S cells.

Figures 6.3a and **b** illustrate the correlation between energy density and both the N/P ratio and the E/S ratio, respectively. In both cases, a reduction in the N/P ratio and the E/S ratio presents a favorable trend toward achieving higher energy densities. Remarkably, the influence of the N/P ratio is comparatively less pronounced, primarily due to the low mass density of lithium. In contrast, the E/S ratio demonstrates a

substantial influence on energy density, emerging as the most critical parameter for developing high energy density Li-S pouch cells. Therefore, these outcomes attest that maintaining E/S ratio values below 5 µL mg_S^{-1} is imperatively necessary to guarantee high energy density LSBs exceeding 300 Wh kg^{-1}. On the other hand, while its impact is relatively minor compared to the E/S ratio, it is crucial to keep N/P ratio values below 4. This threshold not only ensures high energy density values but also secures the cost-effectiveness of LSBs, given that lithium stands as its most expensive component.

Emphasizing the importance of the E/S ratio, it is noteworthy that in Li-S cells, due to the combination of sulfur's high inherent capacity as an active material and its low density, the mass of the electrolyte appears as a significant contributing factor, constituting approximately half of the total cell mass [22]. Even under strictly lean electrolyte conditions (E/S = 2 µL mg_S^{-1}), the mass fraction of the electrolyte is twice as high as that in conventional LIBs. Given the critical role of the electrolyte, the importance of considering the electrolyte density becomes necessary, a parameter often overlooked in the literature when assessing the energy density of LSBs [23,24].

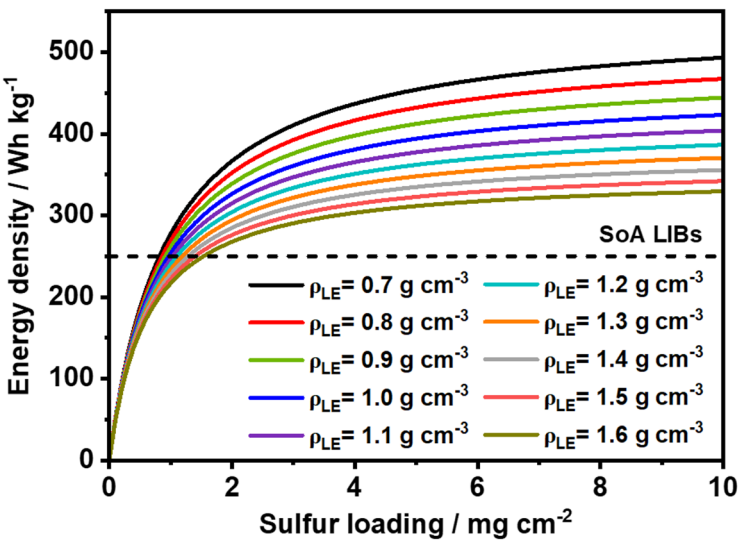

Figure 6.4. Relationship between the electrolyte mass density and the projected gravimetric energy density in Li–S cells.

Figure 6.4 shows the impact of the mass density of the electrolyte at different sulfur loadings on the energy density of the cell. These results evidence the negative

impact of the electrolyte density on energy density. Based on these findings, a comparative analysis between an electrolyte with a density of 1.0 g cm^{-3} and another of 1.4 g cm^{-3}, operating under identical cycling conditions (N/P = 3, E/S = 3 µL mg_S^{-1}, L_S = 4 mg_S cm^{-2}, and w_S = 64 wt.%) and exhibiting equivalent cell performance (μ_S = 0.75), reveals that the lower-density electrolyte achieves an energy density of 380 Wh kg^{-1}, whereas the higher-density electrolyte is compromised to an energy density of 325 Wh kg^{-1}. This comparison emphasizes that employing a low-density electrolyte can significantly reduce the electrolyte weight contribution at the same E/S ratio. Therefore, the adjustment of the electrolyte mass density is considered crucial in the pursuit of high energy density values in Li-S cells.

This comprehensive evaluation of specific parameters has revealed that the sulfur utilization rate, the N/P ratio, and the E/S ratio exert the most significant impact on the final energy density of LSBs. Particularly, the E/S ratio stands out prominently as the most influential parameter, underscoring the crucial importance of both decreasing the amount and mass density of the electrolyte due to its large contribution to the overall cell mass [6,7,17,25]. In general, based on the presented results, it can be concluded that achieving a sulfur utilization rate > 0.7, maintaining sulfur content in the cathode > 60%, ensuring sulfur loading > 3.5 mg_S cm^{-2}, adhering to an N/P ratio < 4, and keeping the E/S ratio < 5 µL mg_S^{-1} are essential conditions for the successful development of high energy density LSBs. These parameters would not only ensure to outperform commercial LIBs but also exceed the threshold of 300 Wh kg^{-1}.

6.2.3. Establishing the operating conditions for high-energy-density LSBs

The previous section provides a guideline for determining the necessary operating conditions to achieve the desired high energy density LSBs. However, in this specific context, certain parameters analyzed earlier are already constrained by the characteristics of the developed strategies throughout this thesis. It is established that the sulfur loading of the cathodes is 4 mg_S cm^{-2}, the sulfur content is 64 wt.%, and the sulfur utilization rate hovers around 0.75. Consequently, the N/P ratio and the E/S ratio remain the sole parameters requiring specification. To this end, an analysis of the impact of these two parameters within the developed system was conducted.

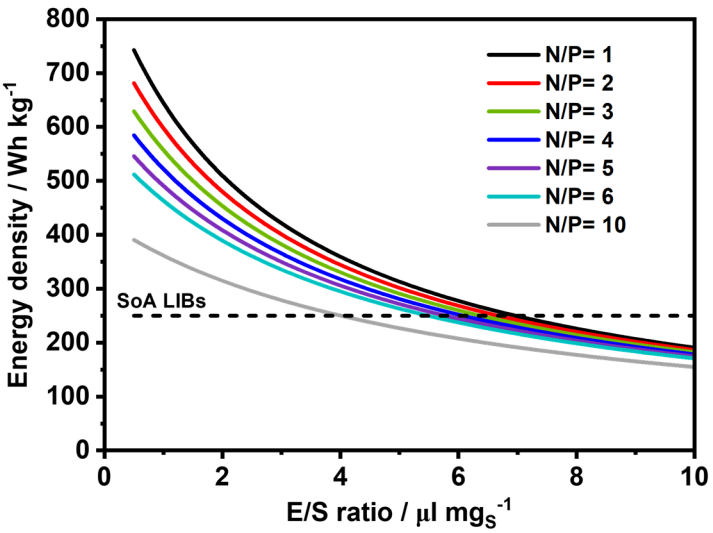

Figure 6.5. Influence of the N/P ratio and E/S ratio on the energy density of the Li-S prototype cell based on the already fixed operating parameters.

Figure 6.5 validates the consistent trend observed earlier, reaffirming that increasing both the N/P ratio and the E/S ratio leads to a significant penalty on the energy density of the proposed system. Therefore, it is evident that surpassing the energy density offered by commercial LIBs requires using an N/P ratio of less than 5 and an E/S ratio of less than 6 µL mg_S^{-1}.

However, given that the objective of LSBs is not only to match but to surpass the values exhibited by commercial LIBs, two different scenarios were outlined for the investigation of multilayer cells. The first scenario adopts an intermediate approach, reducing the E/S ratio to 4.5 µL mg_S^{-1}, yielding energy density values of 300 Wh kg^{-1}. The second scenario pursues a more ambitious path, adjusting the amount of electrolyte to a reduced E/S ratio of 3 µL mg_S^{-1}. This adjustment is projected to deliver remarkable energy density values of 370 Wh kg^{-1}, potentially exerting a high impact at the industrial level. Nevertheless, to realize these scenarios, these adjustments in the E/S ratio must be coupled with a tight N/P ratio value of 3. Despite the relatively minor influence of this parameter on energy density, this adjusted value was selected not only to facilitate the evaluation of more realistic and higher energy density prototype cells but also to control the cost associated with lithium, the most expensive component of LSBs.

6.3. Prototype Li-S cell performance evaluation

To evaluate the different strategies developed in the current thesis under operating conditions closely aligned with practical applications, a detailed evaluation of prototype cells was carried out.

6.3.1. Monolayer pouch cells performances evaluation

The results obtained at coin cell level provide the groundwork for evaluating the performance of the prototype cells. Nevertheless, it is crucial to consider that the upscaling process is not straightforward and demands optimization of the cell assembly system and the preparation of materials in larger quantities. To underscore the magnitude of the upscaling process challenge, **Figure 6.6** provides an optical image illustrating both the coin and the pouch cells, along with the different electrodes that constitute them, accompanied by a scale for size comparison. This image reveals that the upscaling process involves the preparation of electrodes with surface and sulfur amounts 15 times larger than those employed in the coin cells. Consequently, as an intermediate step towards multilayer cells, the performance of the previously developed strategies was first assessed in monolayer pouch cells.

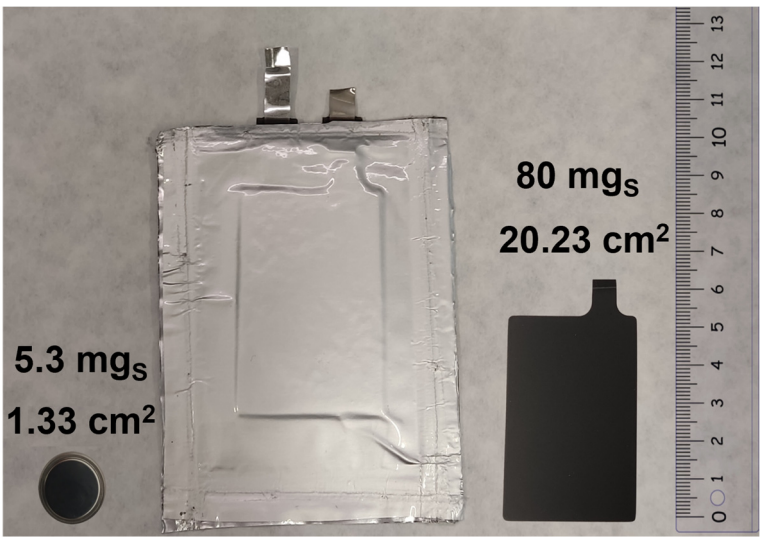

Figure 6.6. Optical images of the coin and pouch size sulfur cathodes, along with the corresponding pouch cell.

In contrast to multilayer design, assembling monolayer pouch cells is more straightforward, facilitating the initial exploration of prototype cells. However, due to the reduced number of layers inside the cell, the dead volume is significantly higher compared to the multilayer configuration, posing a challenge to achieving uniform adhesion between the separator and the two electrodes. Hence, establishing adjusted operating parameters to achieve high energy densities, as analyzed above, becomes a difficult task. Given these challenges, the evaluation of monolayer pouch cells maintained the same operating conditions established for the coin cells, with an electrolyte amount featuring an E/S ratio of 7 µL mg_S^{-1}. For the anode, a 500 µm thick Li foil was employed, representing an N/P ratio of 20. The use of this thick LMA, while deviating from real working conditions, serves to adjust the internal pressure of the cell, promoting improved contact between its components. To conduct the study of the monolayer pouch cells, a cycling protocol involving 5 cycles of preconditioning at a low C-rate of C/20, followed by long cycling at a moderate rate of C/10 was employed.

6.3.1.1. DME/DOL-based systems performance evaluation

Figure 6.7 and **Figure A.6.1** show the performance of the monolayer pouch cells corresponding to the different strategies developed in this thesis employing the conventional DME/DOL electrolyte, along with their corresponding charge and discharge profiles across different cycles. Notably, all strategies demonstrate successful scalability, enabling the cycling of prototype cells with high-capacity values closely resembling those obtained in lab-scale coin cells, despite the substantial scalability factor introduced. These findings highlight the practical effectiveness of the strategies developed in this thesis.

The results displayed in **Figure 6.7** reveal that the capacity trends observed in the coin cells are consistently maintained across the different cell configurations. Notably, the cell incorporating ResFArGO as the main carbon material stands out, yielding extraordinary capacity values at C/10 of 1230 mAh g^{-1} (equivalent to μ_S=0.75, 98.4 mAh, and 4.9 mAh cm^{-2}). Following closely are the cells comprising KJ600 + $ResFArGO_{10}$, exhibiting commendable capacity values at C/10 of 1089 mAh g^{-1} (equivalent to μ_S = 0.65, 87 mAh, and 4.4 mAh cm^{-2}). Therefore, even at the prototype scale, the highly favorable impact of incorporating ResFArGO as the component

responsible for achieving high sulfur utilization values is corroborated. This consolidates ResFArGO as a tangible and effective alternative as a sulfur carbon host.

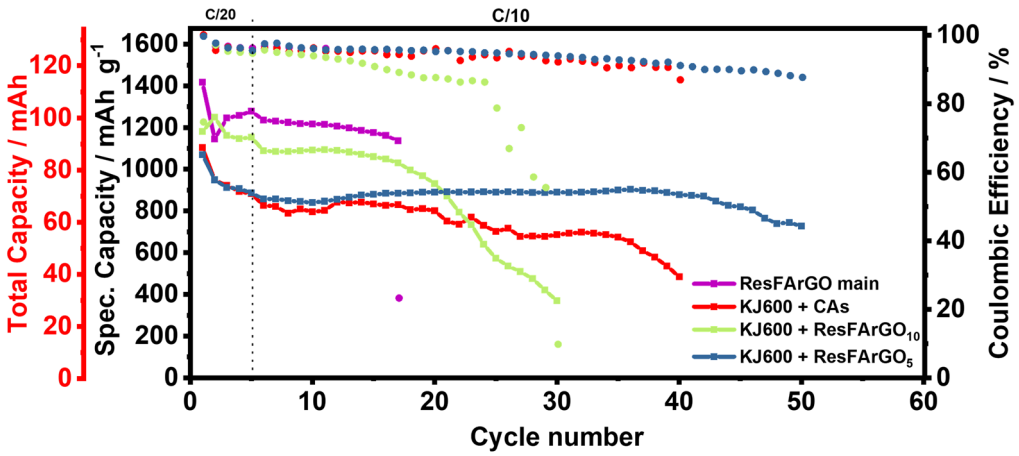

Figure 6.7. Long-term cycling performance of the monolayer pouch cells with the different strategies developed in this thesis employing the DME/DOL electrolyte.

Finally, the cells constructed from the cathodes composed of KJ600 + CAs and KJ600 + ResFArGO$_5$ deliver slightly lower but still acceptable sulfur utilization, achieving capacity values at C/10 of 842 mAh g^{-1} (equivalent to μ_S = 0.51, 67 mAh, and 3.4 mAh cm^{-2}) and 889 mAh g^{-1} (equivalent to μ_S = 0.53, 71 mAh, and 3.6 mAh cm^{-2}), respectively. In alignment with observations in coin cells, the KJ600 + ResFArGO$_5$ cell, with a higher proportion of insulating sulfur and a lower concentration of ResFArGO, delivers reduced capacity values compared to the cells with higher ResFArGO content. Nevertheless, considering the inherent challenges posed by this composition modification of the sulfur cathode, the results attained by the KJ600 + ResFArGO$_5$ cell are noteworthy. Additionally, they underscore the exceptional performance offered by ResFArGO, demonstrating its ability to outperform other additives, such as CAs, even when present in lower quantities.

Despite the consistent capacity trends observed between small coin cells and prototype monolayer pouch cells, there is a substantial divergence in the cyclability of the systems. All cells based on DME/DOL, except for the KJ600 + ResFArGO$_5$ cell, show a drastic reduction in cycling stability, not being able to reach 30 cycles. Furthermore, the CE obtained in all systems is lower than that achieved at the laboratory level, suggesting potential issues arising from the LMA. These results strongly underscore

the incapacity of the DME/DOL electrolyte in ensuring stable cycling in LSBs due to the limited long-term compatibility with the LMA, which is exacerbated at the prototype level. These results yield two valuable insights. Firstly, the substantial challenges associated with the upscaling process are evidenced, emphasizing that the results obtained at lab-scale coin cells are not easily extrapolated to larger prototype cells. Therefore, the practical evaluation of advances achieved in coin cells must be demonstrated in prototype cells. Second, **Figure 6.7** demonstrates the inability of the conventional DME/DOL electrolyte to guarantee the long-term cycling performances of LSBs, a limitation accentuated in the evaluation of the prototype cells with higher LMA surface area.

Within the DME/DOL-based systems, the performance of the KJ600 + ResFArGO$_5$ cell emerges as an exception to the stability issues. However, it is crucial to recognize that this cell exhibits lower capacity compared to the other systems, except for KJ600 + CAs, and this diminished capacity reduces the stress on the LMA, thereby potentially enhancing its stability. Additionally, despite the stable capacity delivered, the cell experiences a constant drop in CE from cycle 30 onwards. In this case, the excess of lithium present in the anode masks the issues related to the declining CE, enabling that the capacity of the cell is not adversely affected. However, these considerations do not diminish the excellent and promising results shown by this system despite its challenging cathode composition. The remarkable outcomes become evident when compared to the KJ600 + CAs system. Despite initially exhibiting comparable capacity values, the stability of the KJ600 + CAs cell is compromised by a constant capacity drop, potentially attributable to the high dissolution of LiPS due to the weak affinity of its cathode carbon materials. In contrast, the KJ600 + ResFArGO$_5$ benefits from the inherent properties of ResFArGO, extensively described in **Chapters II** and **III**, enabling stable cell capacities owing to its improved compatibility with LiPS, even in small quantities.

To ascertain the causes contributing to the poor cycle life observed in systems employing the conventional DME/DOL electrolyte, a post-mortem analysis was carried out. For this investigation, the system incorporating ResFArGO as the main carbon was selected due to its manifested poor cell cyclability.

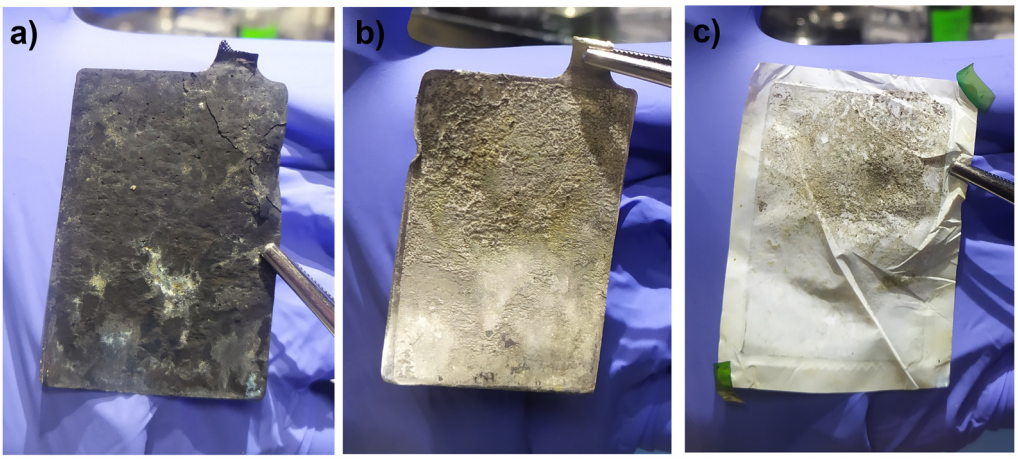

Figure 6.8. Post-mortem analysis images of the **a)** sulfur cathode, **b)** LMA, and **c)** separator after monolayer pouch cell cycling in the full ResFArGO-based system with DME/DOL electrolyte.

Figure 6.8 presents visual images of the sulfur cathode, LMA, and separator after prototype cell cycling. Notably, the sulfur cathode preserves its structural integrity after cycling, exhibiting only a slight yellow coloration on its surface, indicative of the presence of residual LiPS (**Figure 6.8a**). However, **Figure 6.8b** evidences a significant degradation of the LMA, emerging as the primary factor contributing to the cell failure. A porous and powdery layer is visibly formed on the surface of the LMA, mainly ascribed to the formation of mossy and dead lithium upon cycling. This observation aligns with existing research, attributing the degradation of the LMA to the higher current density applied in prototype cells compared to coin cells, stemming from the increased amount of active material [26–28]. This increased current density promotes the nucleation and growth of dendrites that subsequently lead to the formation of dead and/or mossy Li. Consequently, the presence of this porous layer amplifies the contact surface and reactivity between the Li metal and the organic electrolyte, intensifying electrolyte consumption [8]. This phenomenon is exacerbated by the poor long-term compatibility of the conventional electrolyte with the LMA. Furthermore, due to the poor adhesion of this layer, a large amount of dead Li is visible on the surface of the separator, as illustrated in **Figure 6.8c**.

6.3.1.2 SSE_LiFSI-based systems performance evaluation

As corroborated in **Chapter V**, a tailored SSE, as exemplified by the SSE_LiFSI electrolyte, allows to substantially improve the compatibility of the electrolyte with the LMA leading to a remarkable improvement in the cycling of the LSBs. Therefore, to see if this favorable performance can be sustained at prototype scale, the evaluation of the SSE_LiFSI electrolyte in monolayer pouch cells was carried out, employing the KJ600 + ResFArGO$_{10}$ as the sulfur cathode.

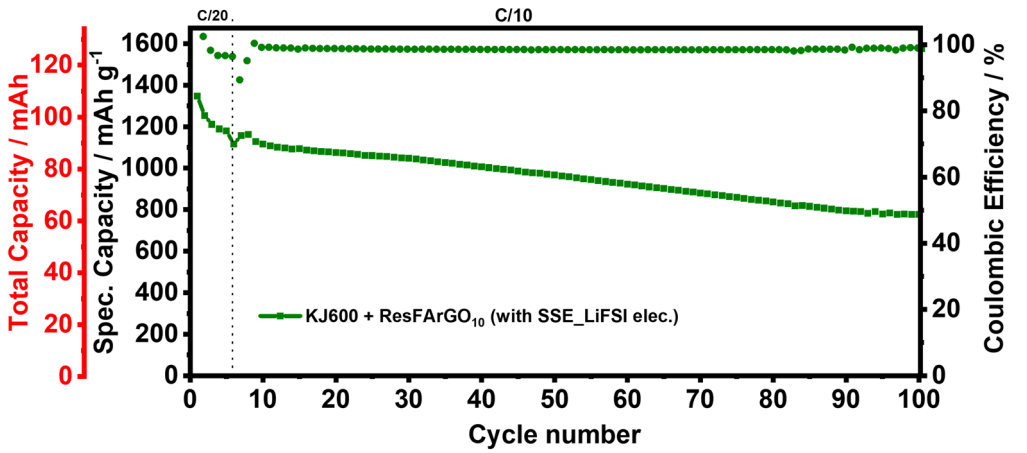

Figure 6.9. Long-term cycling performance of the monolayer pouch cells based on the combination of graphene-based sulfur cathode and the SSE_LiFSI electrolyte.

In **Figure 6.9** and **Figure A.6.2**, the SSE_LiFSI electrolyte demonstrates outstanding cell performance in terms of sulfur utilization, exhibiting highly comparable results to those obtained at coin cell level. Similar to the DME/DOL-based systems, these results reaffirm the success of upscaling the different proposed strategies. Particularly, the SSE_LiFSI cell showcases a discharge capacity of 1115 mAh g^{-1} (equivalent to μ_S=0.67, 89.2 mAh, and 4.5 mAh cm^{-2}) at a C-rate of C/10, with a remarkable capacity retention of 70% after 100 cycles.

Interestingly, in stark contrast to systems employing the DME/DOL electrolyte, the KJ600 + ResFArGO$_{10}$ cell coupled with the developed SSE_LiFSI electrolyte demonstrates comparable cell stability to that observed at lab-scale coin cells. This configuration enables stable cycling, showcasing an exceptionally high CE of 99% over the presented 100 cycles. These results serve to strengthen the effectiveness of the SSE_LiFSI electrolyte in ensuring long-term compatibility with the

LMA when compared to the conventional DME/DOL electrolyte. This is evidenced by the stabilization of the anode side and the reduction of dendrite or mossy lithium formation. Additionally, the notable synergy with graphene-based sulfur cathode is manifested, further emphasizing the robustness of this cell configuration.

For comparative purposes, a post-mortem analysis of the cell using the SSE_LiFSI electrolyte, capable of sustaining exceptional long-term cyclability even in prototype cells, was conducted.

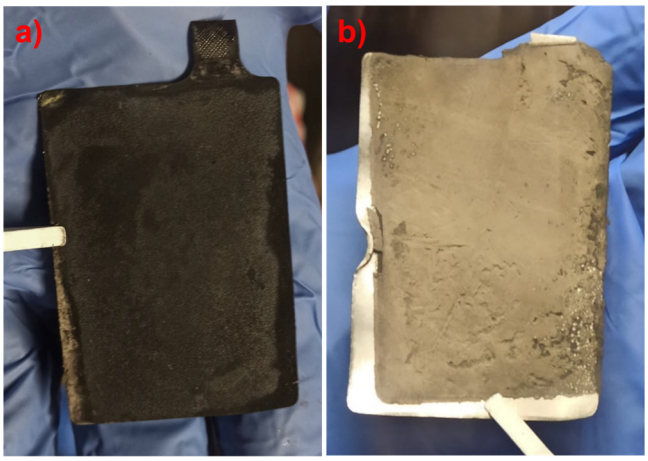

Figure 6.10. Post-mortem analysis images of the **a)** sulfur cathode and **b)** LMA after monolayer pouch cell cycling in KJ600 + ResFArGO$_{10}$-based system with the SSE_LiFSI electrolyte.

Similar to the DME/DOL-based system, **Figure 6.10a** corroborates that the sulfur cathode maintains its structural integrity after cycling, thereby validating the scalability of the different strategies developed for sulfur cathode optimization. Notably, the absence of yellow coloration on the surface of the sulfur cathode is noteworthy, indicating the inhibition of LiPS dissolution due to the developed SSE. Interestingly, the main divergence between the two electrolyte systems is observed in the behavior of the LMA, which, despite undergoing more than 100 cycles, remains in exceptionally good condition. As depicted in **Figure 6.10b**, the use of the SSE_LiFSI electrolyte results in the formation of a uniform and compact protective layer on the surface of the LMA. As extensively discussed in **Chapter V**, the inherent solvation structure of the developed SSE electrolyte leads to the formation of this uniform LiF-rich protective layer, proving to be crucial to guarantee stable cycling for at least 100 cycles. Consequently, this finding underscores the effectiveness of this well-tailored

SSE to stabilize the lithium anode interphase, thereby providing long-term cyclability in LSBs, even at the prototype level.

In summary, the performance evaluation of the monolayer pouch cells has yielded insightful and decisive conclusions. Firstly, all the strategies developed during the current thesis have demonstrated remarkable performance in terms of capacity values, mirroring those observed at the coin cell level. This underscores the successful scalability of the different advancements made in optimizing the sulfur cathode. Additionally, the inadequacy of the conventional DME/DOL electrolyte in ensuring long-term cycling is corroborated, being accentuated at prototype level. These results provide firsthand insights into the challenges associated with extrapolating results from small coin cells to larger prototype cells when the system is not thoroughly optimized. Lastly, it highlights the practical potential of the holistic system, combining graphene-based sulfur cathode with the SSE_LiFSI electrolyte, emerging as the sole configuration capable of transferring excellent results to prototype cells. These promising outcomes reinforce the practical effectiveness of this system, paving the way for further upscaling evaluation in industrially relevant Ah-level multilayer prototype cells.

6.3.2. Multilayer pouch cell performances evaluation

To ensure the industrial relevance of this study, 1.1 Ah multilayer pouch cells were assembled. At this point, it is crucial to emphasize the substantial leap in the scalability factor associated with the fabrication of this cell type. As previously highlighted, the transition from lab-scale coin cells to monolayer pouch cells entails a scalability factor exceeding 15. Notably, this subsequent progression to multilayer pouch cells represents a remarkable increase in the scalability factor, reaching 123 concerning coin cells and 8 about monolayer pouch cells, as schematically illustrated in **Figure 6.11**. This challenging transition process, in addition to employing a larger quantity of materials, requires a comprehensive optimization of both the preparation process of the different cell components and the final assembly (see the **Experimental Section** for further details).

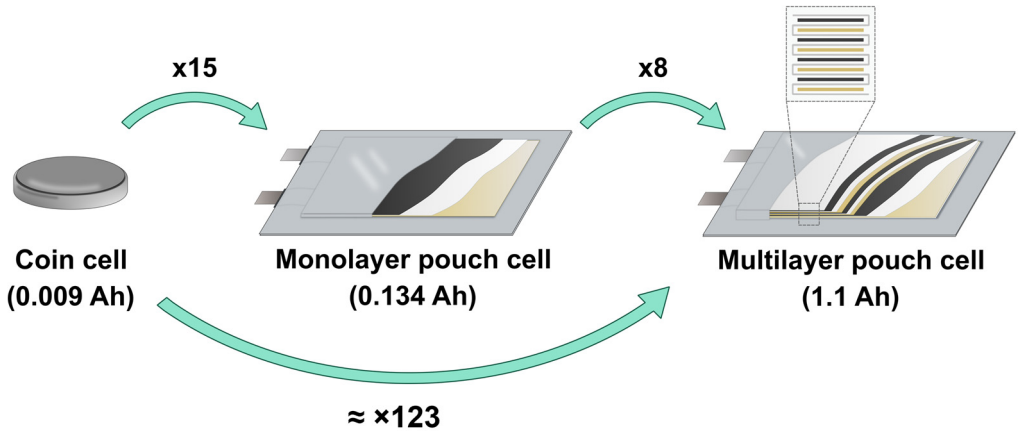

Figure 6.11. Schematic representation of the upscaling factor related to the transition from coin cell to monolayer pouch cells and, finally, to multilayer pouch cells.

As mentioned earlier, two different scenarios were planned to evaluate the performance of the multilayer pouch cells. Initially, the first scenario, which establishes an N/P ratio of 2.3 and an E/S ratio of 4.5 µL mg_S^{-1}, was carried out, meeting all the criteria for high energy density Li-S pouch cell. In this case, the multilayer pouch cell cycling protocol comprised constant cycling at a C-rate of C/20. Encouraged by the promising results observed in monolayer pouch cells, the performance of the SSE_LiFSI electrolyte was analyzed, with the conventional electrolyte serving as a reference.

Figure 6.12 illustrates the comparative performance of the two electrolytes under analysis within the Ah-level prototype cells. It is essential to highlight the commendable scalability process of the system, demonstrating its efficacy in operating within 1.1 Ah prototype cells. Delving into details of cell performance, the system based on the SSE_LiFSI electrolyte delivers a capacity value close to 0.4 Ah, equivalent to a relatively modest sulfur utilization rate of 36% (**Figure 6.12a**). This observed performance falls considerably short of the promising potential witnessed in the monolayer pouch cell. In sharp contrast, the system employing the DME/DOL electrolyte demonstrates outstanding cell performance, showcasing an impressive cell capacity value of 0.76 Ah, equivalent to a remarkable sulfur utilization rate of 70% (**Figure 6.12b**). Consequently, under the established operating conditions, this cell achieves a notably high energy density of 310 Wh kg^{-1}. Nevertheless, despite these commendable results, this cell encounters some charging problems before reaching

the 2.6 V cut-off. These issues can be attributed to the incompatibility between the conventional electrolyte and LMA, as discussed in previous chapters, leading to parasitic reactions between both components.

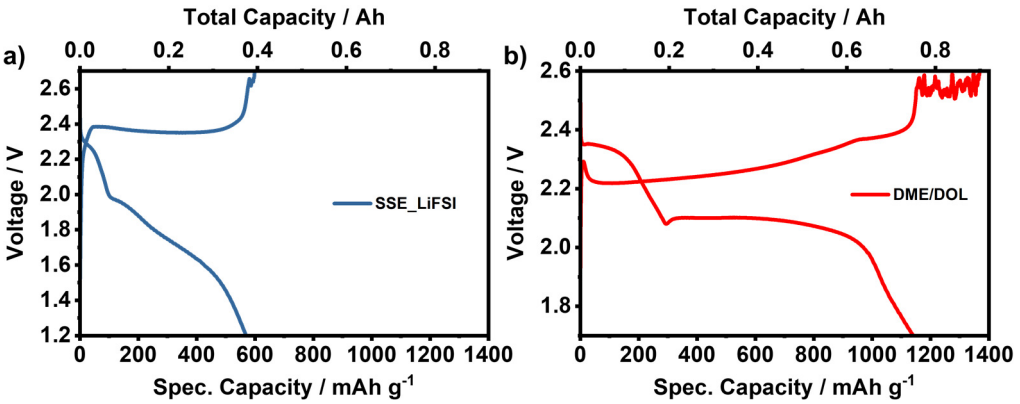

Figure 6.12. Ah-level prototype cell performances of **a)** SSE_LiFSI system and **b)** DME/DOL system.

The less favorable results observed with the SSE_LiFSI system can be attributed to wettability issues arising from the high viscosity exhibited by this electrolyte, as presented in **Chapter V**. The configuration of coin and monolayer pouch cells, assembled by the stacking of individual cell components, facilitates the uniform distribution of the electrolyte over the sulfur cathode surface. This feature enhances the wetting properties of the electrolyte, resulting in the noteworthy capacity values observed earlier. However, this does not apply to multilayer pouch cells, given their stack-on-stack design, particularly when dealing with highly viscous electrolytes. It is this viscosity contrast that enables the exceptional performance of the DME/DOL system under the same operating conditions.

The electrolyte wetting represents a pivotal step in the realm of the battery manufacturing process [29,30]. Achieving a uniform distribution of the electrolyte within the cell, along with its thorough infiltration into the cell components (particularly in the porous sulfur cathode in LSBs), is indispensable to ensure optimal cell performance and to prevent failures arising from the “unwetting” process. The efficacy of the electrolyte infiltration process is heavily dependent on the intrinsic characteristics of the electrolyte, including viscosity, density, polarity, and affinity with both the electrode and separator [31,32]. To enhance this challenging process,

different strategies are employed, such as applying vacuum and/or temperature during the electrolyte filling process. Therefore, considering the high viscosity exhibited by the SSE_LiFSI electrolyte at room temperature, the impact of temperature on this crucial parameter was investigated.

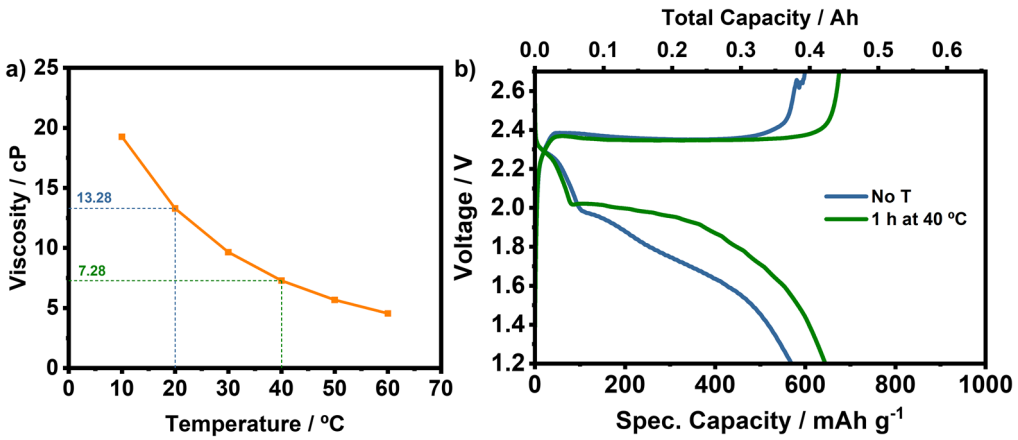

Figure 6.13. a) Temperature dependence of the SSE_LiFSI electrolyte's viscosity (showing the difference in viscosity from 20 to 40 °C) and **b)** performance comparison of the prototype cell after 1 h of temperature-assisted wetting process.

In **Figure 6.13a**, the temperature-dependent evolution of the viscosity of the SSE_LiFSI electrolyte is illustrated. A substantial decrease in viscosity is evident with rising the temperature. For instance, the viscosity of the electrolyte decreases from 13.28 cP at 20 °C to 7.28 cP at 40 °C, representing a 50% reduction in viscosity with just a 20 °C temperature increase. This substantial temperature sensitivity of the electrolyte's viscosity underlines the consideration of applying temperature during the cell resting process. This strategy aims to enhance the wettability characteristics of the system, thereby improving cell performance. Consequently, a temperature of 40 °C was selected for this study to strike a balance between viscosity reduction and safety, as high temperatures have the potential to induce gas formation in the cell and, consequently, introduce safety concerns.

Figure 6.13b shows the impact of applying a temperature of 40 °C for one hour during the cell resting process on the capacity of multilayer cells. Notably, this single-hour treatment at 40 °C enhances the capacity exhibited by the cell by almost 100 mAh g^{-1} (equivalent to 0.066 Ah), resulting in a non-negligible total cell capacity approaching 0.45 Ah.

Although the SSE_LiFSI-based system did not attain the capacity values exhibited by the DME/DOL-based system, the observed improvement motivated the exploration of the long-term cycling cell performances of both systems.

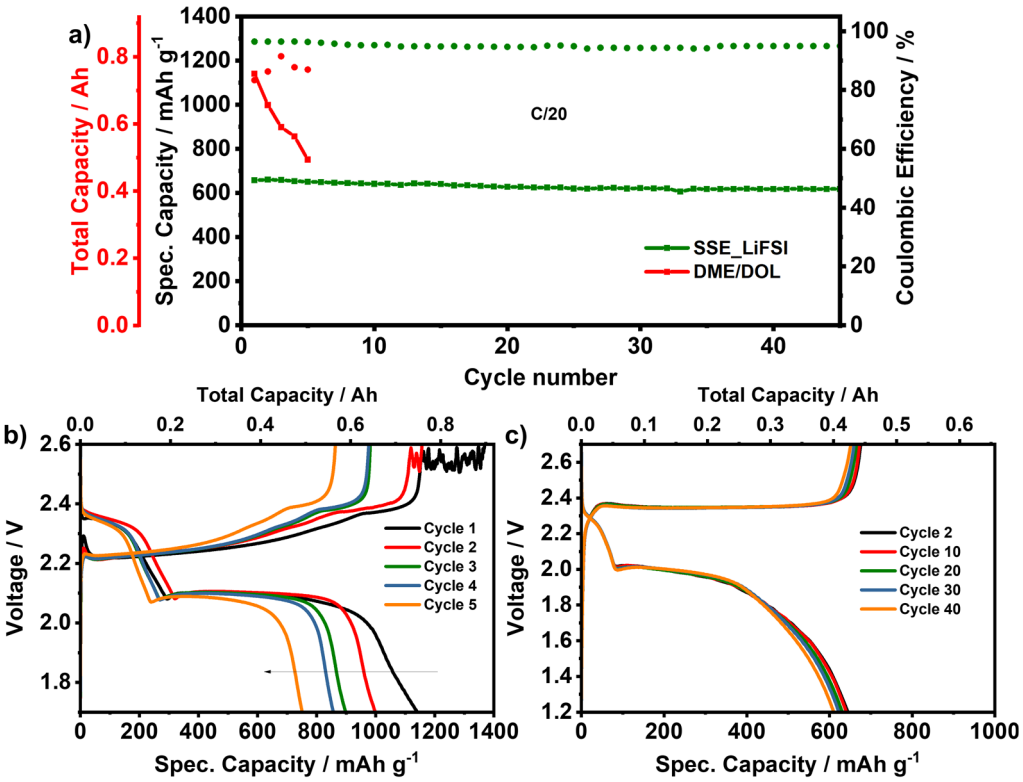

Figure 6.14. a) Long-term cycling performance of Ah-level prototype cells. The discharge/charge profiles **b)** DME/DOL-based and **c)** SSE_LiFSI-based systems.

The differences in cell cycling, as shown in **Figure 6.14a**, unveil compelling insights. Consistent with the results observed in **Figure 6.12**, the DME/DOL system exhibits superior cell capacity when compared to the SSE_LiFSI system. However, this higher capacity is only sustained for the initial 5 cycles, beyond which cell failure emerges. Additionally, despite the impressive capacity values delivered in the first two cycles, DME/DOL cell experiences a continuous drop in cell capacity and displays a relatively low CE (< 90%), failing short of guaranteeing long-term cell stability. In stark contrast, despite presenting a lower cell capacity, the SSE_LiFSI system demonstrates outstanding cell stability, sustaining a consistent capacity of 0.42 Ah for up to 45 cycles. Furthermore, this exceptional long-term cycling is coupled with a stable and

remarkably high CE of 95%. These findings reveal the potential of the SSE_LiFSI electrolyte to guarantee stable cycling even in Ah-level prototype cells. The charge and discharge profiles of both systems, as represented in Figures 6.16b and c, align with the previously detailed behavior. As cycling progresses, the DME/DOL system experiences a significant drop in capacity, as observed in Figure 6.16b. Conversely, the profiles corresponding to the SSE_LiFSI system remain practically unchanged, demonstrating its commendable cycling stability. Notably, the SSE_LiFSI system manifests a consistent absence of fluctuations during the charging process, in stark contrast to the observed behavior in the DME/DOL cell.

To shed light on the causes contributing to the divergent stabilities observed in cell cycling, a post-mortem analysis was performed. Initially, as evident in **Figure 6.15a**, the cell employing the DME/DOL electrolyte displays noticeable swelling. This swelling phenomenon is attributed to the generation of gases, such as C_2H_6 and CH_4 (among others), resulting from the high reactivity of the ether solvents with the LMA [33,34]. Remarkably, the SSE_LiFSI system exhibits an absence of the cell swelling process, thereby preserving the cell's uniformity and compact appearance (**Figure 6.15b**). This observation highlights the exceptional compatibility of the SSE_LiFSI electrolyte with the LMA, facilitating stable cell cycling without any gas generation [35]. Such a feature is highly desirable, as it has the potential to eliminate the necessity for formation and degassing steps in battery manufacturing. This would not only streamline the manufacturing process but also lead to substantial reductions in both time and cost.

Delving into the post-mortem analysis, **Figure 6.15a** and **Figure A.6.3** show the different components of the DME/DOL-based cell after cycling, providing intriguing insights. Primarily, it is essential to highlight the significant degradation of the LMA after cycling, evident in highly porous regions and an area where the anode appears to have undergone complete consumption due to its reaction with the electrolyte. Moreover, the presence of unreacted areas is apparent, possibly indicating areas where gas generated from the LMA-electrolyte reaction has been trapped. In addition, the separator, exhibiting a distinct yellowish-orange hue attributed to the presence and dissolution of LiPS in the electrolyte, displays certain areas where residual dead Li remains adhered. Consequently, electrolyte depletion, leading to gas formation, and pronounced LMA degradation are the primary contributors to the performance loss of DME/DOL-based pouch cells. On a positive

note, it is worth noting the exceptional structural integrity presented by the sulfur cathode.

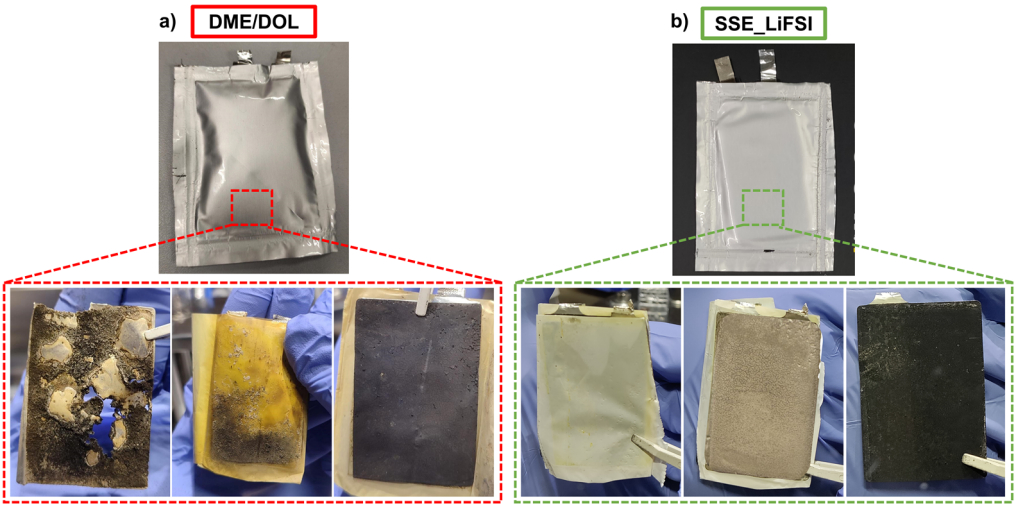

Figure 6.15. Post-mortem analysis of the prototype cells. Optical images of **a)** DME/DOL-based and **b)** SSE_LiFSI-based systems pouch cells and their corresponding cell components.

This behavior substantially contrasts with the observations in the SSE_LiFSI system. In this electrolyte configuration, the LMA exhibits a uniform and smooth surface, owing to the formation of a protective SEI layer, as evidenced in **Figure 6.15b**. Furthermore, the absence of any discernible unreacted zones attests to the lack of gas accumulation within the cell layers, providing further confirmation of SSE_LiFSI electrolyte's efficacy in suppressing gas formation during cell cycling (**Figure A.6.4)**. Therefore, the remarkable stability during the cycling of the prototype cell by this system is attributed to its excellent compatibility with the LMA and the effective suppression of gas generation. Another sign of this favorable compatibility is the absence of any dead Li on the surface of the separator. Additionally, the absence of observable coloration on the separator indicates the minimization or suppression of LiPS dissolution and migration by the SSE_LiFSI during cell cycling. This observation aligns with previous findings at the coin cell and monolayer scale. This finding likely played a role in enhancing the observed stability of the system. Finally, akin to the DME/DOL system, the outstanding structural integrity of the graphene-based sulfur cathode confirms its success in upscaling to prototype scale.

6.3.3. Multilayer pouch cell performance improvements

Considering the challenges encountered by both studied systems in their operation within the Ah-level prototype cell, the implementation of tailored strategies to enhance their respective performances was conducted.

6.3.3.1. Degassing strategy for DME/DOL system

As evidenced in **Figure 6.15**, the DME/DOL-based system underwent notable cell swelling during the 5 cycles that the battery endured operative. The primary factor contributing to this phenomenon is the generation of gas during the formation of the SEI layer on the LMA surface, exacerbated by the considerable reactivity presented by ether-based solvents with the anode. It is important to note that this gassing process is not uncommon and is a prevalent issue faced by commercial LIBs. To address the gas formation and its consequential adverse effects on both the performance and safety of the cell, a degassing process, widely employed in the battery manufacturing industry, was implemented [36–38].

To this end, a formation step was introduced in the cell cycling protocol. In this process, the cell was cycled at low rates (i.e., C/20) for 2 cycles to facilitate the formation of the SEI layer. Subsequently, the gas accumulated inside the cell was extracted. To achieve this, the pouch bag design was modified leaving an empty zone to collect the generated gas. After the formation step, this gas accumulation zone was punctured, and the gas was extracted. Finally, the emptied gas bag was removed, and the cell was sealed again on the open side.

As plotted in **Figure 6.16**, the Ah-pouch cell demonstrates a capacity of approximately 1200 mAh g^{-1} during the formation step at C/20, representing a high sulfur utilization rate of 70%. Consequently, this cell delivers an impressive energy density of 325 Wh kg^{-1} with a substantial cell capacity of 0.79 Ah. Additionally, the implementation of the formation step contributes to enhanced, enabling the cell to endure 15 cycles at C/10. Notably, while not achieving long-term cyclability, this behavior is consistent with the outstanding stability observed in monolayer pouch cell cycling. Furthermore, with the cycling rate increased to C/10, the cell continues to offer commendable capacity values, achieving an energy density of around 270 Wh kg^{-1} and a total cell capacity of 0.66 Ah. This improved and remarkably respectable cell performance underscores the success of the implemented degassing

strategy. The strategy not only improves the stability of the Ah-level but also yields energy density values that surpass or align with those of commercial LIBs. However, as evidenced throughout this thesis work, the DME/DOL-based electrolyte proves unable to guarantee the long-term cycling of LSBs, particularly in prototype cells.

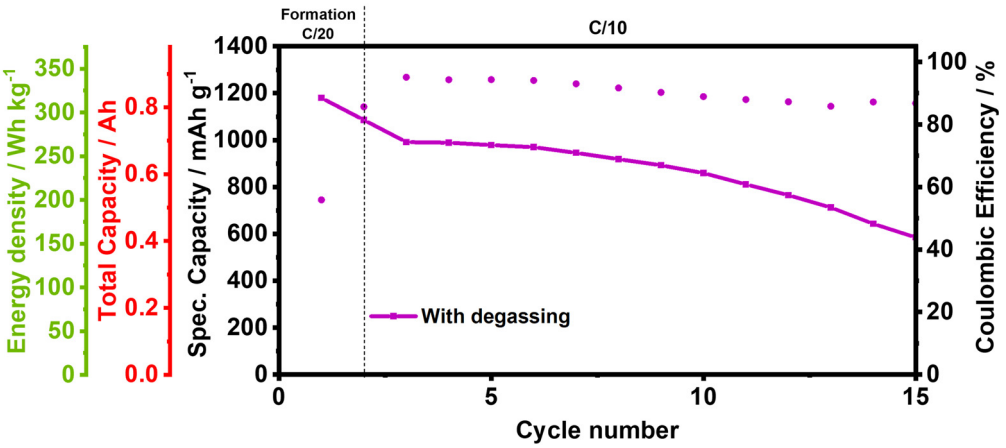

Figure 6.16. DME/DOL-based Ah-level prototype cell performance after implementing the degassing process.

6.3.3.2. Deepening in the temperature-assisted wetting for SSE_LiFSI system

Despite the promising cell stability shown by the SSE_LiFSI-based system in the Ah prototype cell, the provided capacity falls below the targets set to surpass the values offered by commercial LIBs. The root cause of this low capacity is attributed to wettability issues with the electrolyte within the cell components. The electrolyte exhibits high viscosity at RT, hindering its wetting in multilayer prototype cells, a design that is not conducive to facilitating this process. A previous attempt was made to address this issue by utilizing a temperature-assisted wetting process for 1 hour, yielding notable but still insufficient improvements in the delivered capacity. Therefore, to maximize the effectiveness of this strategy, an extended wetting process time was implemented.

Figure 6.17 shows the discharge /charge profiles of the first cycle at different temperature-assisted wetting times of the SSE_LiFSI-based system. Notably, an increase in the wetting time at 40 °C manifests a positive effect on the capacity offered by the cell. Particularly, a comparison between the values obtained without

temperature application and those following a 24 hour wetting duration reveals a substantial capacity increase of approximately 270 mAh g^{-1}, equivalent to 0.18 Ah. Although the implemented strategy results in a clear enhancement of the system, the obtained capacities remain below the expected values. Additionally, the obtained energy density values by the SSE_LiFSI system are substantially below those observed with the DME/DOL system.

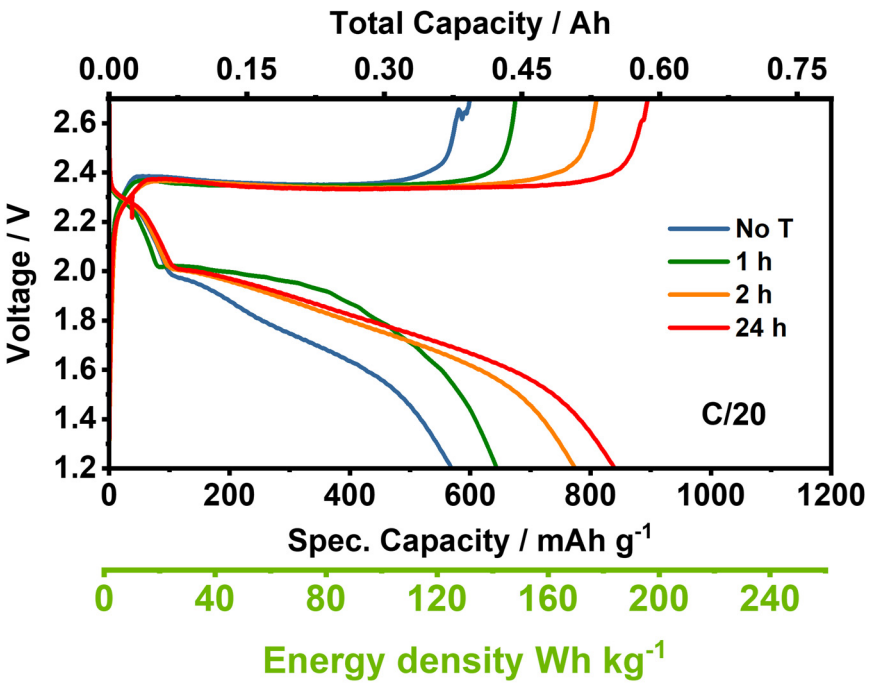

Figure 6.17. Discharge/charge profiles of the first cycle at different temperature-assisted wetting times in the SSE_LiFSI system.

It is essential to highlight that, beyond exhibiting a diminished capacity, the energy density achieved when aligning the capacity values is consistently lower for the SSE_LiFSI system. This divergence can be explained by the notable difference in electrolyte density between the two systems. As displayed in **Figure A.6.5**, the RT density of the DME/DOL electrolyte is 1.06 g cm^{-3}, while that of the SSE_LiFSI electrolyte is 1.48 g cm^{-3}. Therefore, as detailed in **Section 6.2.2.**, this substantial density difference, attributed to the presence of the highly fluorinated TTE co-solvent, significantly hampers the final energy density of the SSE_LiFSI-based system.

6.4. Summary and conclusions

This chapter provided a detailed evaluation of the upscaling process of LSBs, building upon the different strategies developed in preceding chapters. Initiating with the energy density modeling, the operational parameters exerting the most substantial influence on LSB energy density are elucidated. This investigation enables the establishment and adjustment of these parameters to attain high energy density values. Subsequently, as an intermediate step toward Ah-level cells, the performance evaluation of the monolayer pouch cells highlights the results of the SSE_LiFSI-based system, demonstrating a commendable compromise between high capacity and long-term cyclability. In addition, the observed performance differences between monolayer pouch cells and coin cells emphasize the challenge involved in transitioning from lab-scale to prototype cell configurations. More importantly, the successful upscaling to 1.1 Ah multilayer cells has been achieved for both the DME/DOL and SSE_LiFSI-based systems. The DME/DOL system demonstrates outstanding sulfur utilization, achieving a remarkable energy density of 320 Wh kg^{-1}. Moreover, the implementation of the degassing process contributes to a partial improvement of cell stability. However, it underscores once again the inability to ensure long-term cycling with the DME/DOL system. In contrast, the SSE_LiFSI system encounters wettability issues due to its elevated viscosity, resulting in diminished capacity values compared to monolayer pouch cell performance. However, the incorporation of the temperature-assisted wetting strategy proves partially effective, culminating in a remarkable total cell capacity of 0.5 Ah. Furthermore, the SSE_LiFSI system exhibits exceptional cell stability even at the multilayer scale, attributed to its remarkable excellent compatibility with LMA, underscoring its potential applicability. Consequently, these findings establish a critical groundwork for the upscaling process to prototype cells within this system, paving the way for future optimizations aimed at enhancing overall system performance.

6.5. Brief outlook and perspective

Chapter VI has exemplified the significant challenges associated with the upscaling process from lab-scale coin cells to prototype cells. As detailed in the introduction, this disparity primarily stems from the considerable reduction in stability observed in larger cells. The combination of a substantial scalability factor and the adjustment of operating parameters towards values closely aligned to practical applications emerges as the main factor exacerbating this difference. In this context, the stability of the LMA, evidently compromised by the described factors, stands out as the key element to ensure long-term cycling in prototype cells. Consequently, its effective protection, achieved through an ex-situ formation of an artificial protective SEI layer, paired with a tailored electrolyte, such as SSE_LiFSI, proves to be a promising strategy addressing anode-related concerns.

Furthermore, this chapter underscores the importance of other parameters in the cycling of prototype cells, such as viscosity, particularly evident in the case of the SSE_LiFSI. In this sense, aligning with the approach demonstrated by the SSE_LiFSI, the exploration of novel solvent alternatives to mitigate electrolyte viscosity issues becomes a key avenue to pursue. Addressing this wettability challenge holds the promise of enhancing sulfur utilization, thereby resulting in an increased capacity. Following this line, the detrimental impact of a high-density electrolyte on achieving high energy density values in LSBs has been illustrated. Therefore, the pursuit of new alternative co-solvents to alleviate the high density associated with highly fluorinated HFEs becomes pivotal for future improvements. This modification is anticipated to improve the energy density of the system for the same cell performance and will enable the implementation of the most ambitious scenario in terms of operating conditions (detailed in **Section 6.2.3**). Finally, after succinctly selecting appropriate materials to address the outlined challenges, a primary objective should be the reduction of electrolyte volume to enhance the energy density of the system owing to its strong influence. As evidenced in the sensitivity map displayed in **Figure 6.18**, the implementation of these adjustments on the base system developed in this thesis will exert a considerable increase in its energy density. Combined with the enhanced stability of the LMA, these improvements are anticipated to yield appealing LSBs suitable for industrial applications.

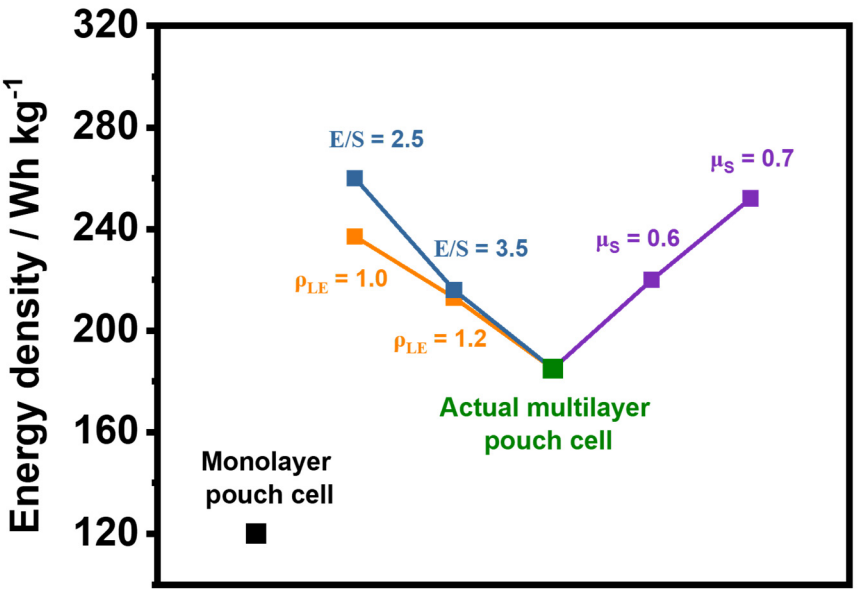

Figure 6.18. Sensitivity analysis map evidencing the impact of adjusting E/S ratio, sulfur utilization, and electrolyte density to improve the energy density of the actual multilayer pouch cell based on the SSE_LiFSI system.

6.6. Bibliography

[1] M. Zhao, B.Q. Li, X.Q. Zhang, J.Q. Huang, Q. Zhang, A perspective toward practical lithium-sulfur batteries, ACS Cent. Sci. 2020, 6, 1095–1104. https://doi.org/10.1021/acscentsci.0c00449.

[2] F. Shi, L. Zhai, Q. Liu, J. Yu, S.P. Lau, B.Y. Xia, Z.L. Xu, Emerging catalytic materials for practical lithium-sulfur batteries, J. Energy Chem. 2023, 76, 127–145. https://doi.org/10.1016/j.jechem.2022.08.027.

[3] M. Zhao, B.Q. Li, H.J. Peng, H. Yuan, J.Y. Wei, J.Q. Huang, Lithium–sulfur batteries under lean electrolyte conditions: challenges and opportunities, Angew. Chemie 2020, 59, 12636–12652. https://doi.org/10.1002/anie.201909339.

[4] L. Shi, S.M. Bak, Z. Shadike, C. Wang, C. Niu, P. Northrup, H. Lee, A.Y. Baranovskiy, C.S. Anderson, J. Qin, S. Feng, X. Ren, D. Liu, X.Q. Yang, F. Gao, D. Lu, J. Xiao, J. Liu, Reaction heterogeneity in practical high-energy lithium-sulfur pouch cells, Energy Environ. Sci. 2020, 13, 3620–3632. https://doi.org/10.1039/d0ee02088e.

[5] O. Leonet, Á. Doñoro, A. Fernández-Barquín, A. Kvasha, I. Urdampilleta, J.A. Blázquez, Understanding of crucial factors for improving the energy density of lithium-sulfur pouch cells, Front. Chem. 2020, 10, 888750. https://doi.org/10.3389/fchem.2022.888750.

[6] S. Dörfler, H. Althues, P. Härtel, T. Abendroth, B. Schumm, S. Kaskel, Challenges and key parameters of lithium-sulfur batteries on pouch cell level, Joule 2020, 4, 539–554. https://doi.org/10.1016/j.joule.2020.02.006.

[7] Z.X. Chen, M. Zhao, L.P. Hou, X.Q. Zhang, B.Q. Li, J.Q. Huang, Toward practical high-energy-density lithium–sulfur pouch cells: A review, Adv. Mater. 2022, 34, 2201555. https://doi.org/10.1002/adma.202201555.

[8] X.B. Cheng, C. Yan, J.Q. Huang, P. Li, L. Zhu, L. Zhao, Y. Zhang, W. Zhu, S.T. Yang, Q. Zhang, The gap between long lifespan Li-S coin and pouch cells: The importance of lithium metal anode protection, Energy Storage Mater. 2017, 6, 18–25. https://doi.org/10.1016/j.ensm.2016.09.003.

[9] S. Chen, C. Niu, H. Lee, Q. Li, L. Yu, W. Xu, J.G. Zhang, E.J. Dufek, M.S. Whittingham, S. Meng, J. Xiao, J. Liu, Critical parameters for evaluating coin cells and pouch cells of rechargeable Li-metal batteries, Joule 2019, 3, 1094–1105. https://doi.org/10.1016/j.joule.2019.02.004.

[10] Z.X. Chen, L.P. Hou, C.X. Bi, Q. Cheng, X.Q. Zhang, B.Q. Li, J.Q. Huang, Failure

analysis of high-energy-density lithium-sulfur pouch cells, Energy Storage Mater. 2022, 53, 315–321. https://doi.org/10.1016/j.ensm.2022.07.035.

[11] L. Zhang, Y. Jiao, F. Wang, M. Zhou, Y. Hu, Y. Yan, F. Li, T. Lei, B. Chen, W. Chen, Tailoring lithium fluoride interface for dendrite-free lithium anode to prolong the cyclic stability of lithium–sulfur pouch cells, Nanoscale Res. Lett. 2022, 17, 112. https://doi.org/10.1186/s11671-022-03745-w.

[12] Z. Li, Y. Li, C.X. Bi, Q.K. Zhang, L.P. Hou, X.Y. Li, J. Ma, X.Q. Zhang, B.Q. Li, R. Wen, Q. Zhang, Construction of organic-rich solid electrolyte interphase for long-cycling lithium–sulfur batteries, Adv. Funct. Mater. 2023, 2304541. https://doi.org/10.1002/adfm.202304541.

[13] X.Z. Fan, M. Liu, R. Zhang, Y. Zhang, S. Wang, H. Nan, Y. Han, L. Kong, An odyssey of lithium metal anode in liquid lithium–sulfur batteries, Chinese Chem. Lett. 2022, 33, 4421–4427. https://doi.org/10.1016/j.cclet.2021.12.064.

[14] S. Dörfler, S. Walus, J. Locke, A. Fotouhi, D.J. Auger, N. Shateri, T. Abendroth, P. Härtel, H. Althues, S. Kaskel, Recent progress and emerging application areas for lithium–sulfur battery technology, Energy Technol. 2021, 9, 2000694. https://doi.org/10.1002/ente.202000694.

[15] J. Sun, T. Wang, Y. Gao, Z. Pan, R. Hu, J. Wang, Will lithium-sulfur batteries be the next beyond-lithium ion batteries and even much better?, InfoMat 2022, 4, 12359. https://doi.org/10.1002/inf2.12359.

[16] Z. Li, I. Sami, J. Yang, J. Li, R.V. Kumar, M. Chhowalla, Lithiated metallic molybdenum disulfide nanosheets for high-performance lithium–sulfur batteries, Nat. Energy 2023, 8, 84–93. https://doi.org/10.1038/s41560-022-01175-7.

[17] G. Zhou, H. Chen, Y. Cui, Formulating energy density for designing practical lithium–sulfur batteries, Nat. Energy 2022, 7, 312–319. https://doi.org/10.1038/s41560-022-01001-0.

[18] F. Schmidt, S. Ehrling, K. Schönherr, S. Dörfler, T. Abendroth, H. Althues, S. Kaskel, The importance of swelling effects on cathode density and electrochemical performance of lithium−sulfur battery cathodes produced via dry processing, Energy Technol. 10 (2022). https://doi.org/10.1002/ente.202100721.

[19] Y.T. Liu, S. Liu, G.R. Li, X.P. Gao, Strategy of Enhancing the Volumetric Energy Density for Lithium–Sulfur Batteries, Adv. Mater. 2021, 33, 2003955. https://doi.org/10.1002/adma.202003955.

[20] Y.-T. Liu, L. Wang, S. Liu, G.-R. Li, X.-P. Gao, Constructing high gravimetric and volumetric capacity sulfur cathode with LiCoO2 nanofibers as carbon-free sulfur host for lithium-sulfur battery, Sci. China Mater. 2021, 64, 1343–1354. https://doi.org/10.1007/s40843-020-1552-7.

[21] J. Betz, G. Bieker, P. Meister, T. Placke, M. Winter, R. Schmuch, Theoretical versus practical energy: A plea for more transparency in the energy calculation of different rechargeable battery systems, Adv. Energy Mater. 2019, 9, 1803170. https://doi.org/10.1002/aenm.201803170.

[22] T. Liu, H. Li, J. Yue, J. Feng, M. Mao, X. Zhu, Y. sheng Hu, H. Li, X. Huang, L. Chen, L. Suo, Ultralight electrolyte for high-energy lithium–sulfur pouch cells, Angew. Chemie 2021, 60, 17547–17555. https://doi.org/10.1002/anie.202103303.

[23] T. Liu, Z. Shi, H. Li, W. Xue, S. Liu, J. Yue, M. Mao, Y. sheng Hu, H. Li, X. Huang, L. Chen, L. Suo, Low-density fluorinated silane solvent enhancing deep cycle lithium–sulfur batteries' lifetime, Adv. Mater. 2021, 33, 2102034. https://doi.org/10.1002/adma.202102034.

[24] H. Cheng, S. Zhang, B. Zhang, Y. Lu, n -Hexane Diluted Electrolyte with Ultralow Density enables Li–S Pouch Battery Toward >400 Wh kg −1, Small 2023, 19, 2206375. https://doi.org/10.1002/smll.202206375.

[25] R. Fang, K. Chen, Z. Sun, G. Hu, D. Wang, F. Li, Realizing high-energy density for practical lithium–sulfur batteries, Interdiscip. Mater. 2023, 2, 761–770. https://doi.org/10.1002/idm2.12118.

[26] J. Castillo, J.A. Coca-Clemente, J. Rikarte, A. Sáenz De Buruaga, A. Santiago, C. Li, Recent progress on lithium anode protection for lithium-sulfur batteries: Review and perspective, APL Mater. 2023, 11, 010901. https://doi.org/10.1063/5.0107648.

[27] C. Yan, X.Q. Zhang, J.Q. Huang, Q. Liu, Q. Zhang, Lithium-anode protection in lithium–sulfur batteries, Trends Chem. 2019, 1, 693–704. https://doi.org/10.1016/j.trechm.2019.06.007.

[28] X.-B. Cheng, J.-Q. Huang, Q. Zhang, Review—Li Metal Anode in Working Lithium-Sulfur Batteries, J. Electrochem. Soc. 2018, 165, A6058–A6072. https://doi.org/10.1149/2.0111801jes.

[29] A. El Malki, M. Asch, O. Arcelus, A. Shodiev, J. Yu, A.A. Franco, Machine learning for optimal electrode wettability in lithium ion batteries, J. Power Sources Adv. 2023, 20, 100114. https://doi.org/10.1016/j.powera.2023.100114.

[30] D.H. Jeon, Wettability in electrodes and its impact on the performance of lithium-ion batteries, Energy Storage Mater. 2019, 18, 139–147. https://doi.org/10.1016/j.ensm.2019.01.002.

[31] Z. Deng, Z. Huang, Y. Shen, Y. Huang, H. Ding, A. Luscombe, M. Johnson, J.E. Harlow, R. Gauthier, J.R. Dahn, Ultrasonic scanning to observe wetting and "unwetting" in Li-ion pouch cells, Joule 2020, 4, 2017–2029. https://doi.org/10.1016/j.joule.2020.07.014.

[32] A. Davoodabadi, J. Li, Y. Liang, D.L. Wood, T.J. Singler, C. Jin, Analysis of electrolyte imbibition through lithium-ion battery electrodes, J. Power Sources 2019, 424, 193–203. https://doi.org/10.1016/j.jpowsour.2019.03.115.

[33] Y. Huang, M. Shaibani, M.J. Abedin, D.J. Mendoza, Z. Xu, T.D. Gamot, M.C.D. Cooray, M. Lin, G. Garnier, M.R. Hill, M. Majumder, Sulfur cathodes with self-organized cellulose nanofibers in stable Ah-level, >300 Wh kg −1 lithium–sulfur cells, Adv. Energy Mater. 2022, 12, 2202474. https://doi.org/10.1002/aenm.202202474.

[34] C. Weller, S. Thieme, P. Härtel, H. Althues, S. Kaskel, Intrinsic shuttle suppression in lithium-sulfur batteries for pouch cell application, J. Electrochem. Soc. 2017, 164, A3766–A3771. https://doi.org/10.1149/2.0981714jes.

[35] Z. Yu, P.E. Rudnicki, Z. Zhang, Z. Huang, H. Celik, S.T. Oyakhire, Y. Chen, X. Kong, S.C. Kim, X. Xiao, H. Wang, Y. Zheng, G.A. Kamat, M.S. Kim, S.F. Bent, J. Qin, Y. Cui, Z. Bao, Rational solvent molecule tuning for high-performance lithium metal battery electrolytes, Nat. Energy 2022, 7, 94–106. https://doi.org/10.1038/s41560-021-00962-y.

[36] Z. Yu, W. Yu, Y. Chen, L. Mondonico, X. Xiao, Y. Zheng, F. Liu, S.T. Hung, Y. Cui, Z. Bao, Tuning fluorination of linear carbonate for lithium-ion batteries, J. Electrochem. Soc. 2022, 169, 040555. https://doi.org/10.1149/1945-7111/ac67f5.

[37] Y. Lin, S. Huang, M. Xiao, D. Han, Z. Huang, S. Wang, Y. Meng, Excavating anomalous capacity increase of Li-S pouch cells by electrochemical oscillation formation, ACS Appl. Mater. Interfaces. 2022, 14, 22197–22205. https://doi.org/10.1021/acsami.2c04284.

[38] Y. Lin, Y. Zhou, S. Huang, M. Xiao, D. Han, J. Qin, S. Wang, Y. Meng, Catalytic disproportionation for suppressing polysulfide shuttle in Li–S pouch cells: Beyond adsorption interactions, Adv. Energy Mater. 2022, 12, 2201912. https://doi.org/10.1002/aenm.202201912.

Chapter VII

Conclusions

VII. Conclusions

While a detailed discussion of results and main conclusions has been presented in detail at the end of each chapter, the paramount findings are summarized below, emphasizing their significance to the overall cell performance improvement:

1. The transference of knowledge from established technology electrochemical capacitors to the development of carbonaceous materials for use as sulfur host has proven to be highly effective, optimizing the composition of sulfur cathodes.

2. The incorporation of the ResFArGO material has yielded a substantial improvement in the Li-S cell performance compared to the reference employing the commercial carbonaceous material KJ600. Notably, the commendable textural properties, such as a 2D planar-shaped structure, high surface area, and a narrower and smaller pore size distribution, complemented by favorable surface chemistry, exhibiting polar characteristics, exhibited by ResFArGO contributed to its excellent compatibility with LiPS, effectively overcoming a key technological challenge. Furthermore, the synergistic interplay between these distinctive characteristics and the enhanced electronic conductivity provided by the presence of graphene resulted in remarkable LSB performance, manifesting high-capacity values in power conditions (e.g., 950 mAh g^{-1} / 2.5 mAh cm^{-2} at C/2) and high sulfur loading cells (e.g., 1100 mAh g^{-1}/ 4.4 mAh cm^{-2}).

3. The strategic incorporation of ResFArGO as an additive has proven to be effective in ensuring the practical viability of this material. Even at reduced quantities, such as 5 wt.%, when combined with the low-cost commercial KJ600, ResFArGO imparts its intrinsic properties to the mixture. This presence accelerates sulfur redox reaction kinetics, thereby evidencing the role of ResFArGO as an effective catalyst. The outstanding properties exhibited by this blend enable cell performances comparable to those achieved when ResFArGO is the sole carbonaceous material, validating the effectiveness of the additive approach.

4. Despite the improvements implemented in the sulfur cathode, the conventional electrolyte demonstrated inadequate long-term compatibility with the LMA, thus failing to guarantee the long-term cycling of LSBs, a key feature established as part of the thesis objective.

5. Intending to improve the electrolyte, the developed GPE_20 exhibits exceptional individual properties, demonstrating a remarkable balance between structural integrity, electrochemical properties, thermal stability, and safety characteristics. Regrettably, the unregulated dissolution of LiPS, coupled with the uncontrolled reactivity of its fluorinated polymer matrix with the LMA, gave rise to parasitic reactions, ultimately leading to poor LSB performance.

6. While considered as a practical setback within the scope of this thesis, the results associated with the GPE_20 have evidenced and established that mitigating LiPS dissolution and ensuring compatibility with the LMA are fundamental attributes for an electrolyte applied in Li-S technology to ensure optimal performance. Moreover, the surprisingly impressive results obtained in battery technology distinct from Li-S, even at the prototype scale, highlight the potential of the developed electrolyte and unveil a new application niche for its utilization.

7. The SSE developed has proven its efficacy as a Li-S electrolyte in meeting the established targets. The strategic incorporation of the LiFSI salt in its composition leverages the distinctive solvation structure characteristic of this electrolyte family. This tailored composition results in exceptional Li metal deposition and facilitates the formation of an effective LiF-rich protective SEI layer. These fundamental attributes have proven essential in establishing robust long-term compatibility with the LMA.

8. Moreover, the unique solvation structure of the SSEs, characterized by a minimal presence of free solvent molecules, played a pivotal role in mitigating the dissolution of LiPS. In this sense, this characteristic, together with the tailored selection of its components, imparts a non-flammable nature to the electrolyte, ensuring the safety of the system. These achievements align with another essential attribute established for the final target cell.

9. SSE_LiFSI not only fulfilled the requirements for an optimal LSB electrolyte but also forged a synergistic relationship with the graphene-based sulfur cathode. Through the cycling of high sulfur cells, it attained high-capacity values (i.e., 1280 mAh g^{-1} at C/10) and demonstrated stable cycling, completing 100 cycles with a high CE of 99%. Additionally, this electrolyte exhibited outstanding rate capability and enabled high-temperature cycling for 50 cycles, showcasing the excellent versatility of the system.

10. The model for calculating the energy density of LSBs has been successfully developed, enabling the identification of the most influential parameters and the establishment of cycling conditions essential for the development of high energy density Li-S prototype cells.

11. The monolayer pouch cells' performance has yielded valuable insights. On the one hand, it demonstrated the excellent scalability properties of the strategies implemented during the thesis, facilitating the development and operation of prototype cells. On the other hand, it underscored the substantial cycling differences between the results obtained at the laboratory scale in coin cells and those at the prototype scale. This finding illustrated the challenges associated with the upscaling process and the non-trivial transferability of findings from small coin cells to prototype scale, emphasizing the notable gap between these two domains. Within this gap, the holistic system based on SSE_LiFSI and ResFArGO's sulfur cathode demonstrated its effectiveness in ensuring high-performance and stable prototype cell cycling, attaining 100 cycles with a high CE of 99.2% and a capacity retention of 70%, thus reaffirming the efficacy of the overall strategy.

12. Successfully developed, 1.1 Ah prototype cells have reaffirmed the excellent scalability behavior of the proposed strategies, even at conditions closely aligned to practical applications. In this configuration, the ResFArGO-based cathode with conventional electrolyte achieved excellent capacity values, attaining high energy densities of 310 Wh kg^{-1}, surpassing those offered by conventional LIBs. However, the electrolyte's inability to ensure stable cycling was evident from the observed cell swelling cell and substantial degradation in the LMA. The incorporation of the degassing process led to an improvement in stability, reaching high energy density values of 270 Wh kg^{-1} at C/10 for 15

cycles. Conversely, even at the prototype scale, the holistic system boasted superior cell stability, achieving incredibly stable cycling for 45 cycles with high CE values (> 95%). However, the upscaling process to cells close to practical application introduced new challenges that need to be addressed to enhance system prototype cell performance.

In conclusion, the holistic approach presented in this thesis represents an effective and reliable solution for the scientific community focused on developing high-performing, safe, and long-cycle-life prototype LSBs. The comprehensive scalability study conducted in this study yields valuable insights for future advancements, emphasizing the crucial need to intensify scientific efforts in evaluating performances at the pouch cell level. This necessary step is essential for propelling Li-S technology towards commercialization. Building on the findings of this work, the refinement of the SSE formulation through the exploration of new solvents, co-solvents, and lithium salts, along with the implementation of an effective ex-situ LMA protection strategy, emerges as the focal point for future optimization within the conceptual framework proposed in this thesis.

Appendix

A.1. List of variables

A_{anode}	Total area of LMA, cm^2
A_{elec}	Electrolyte area, cm^2
C_{cell}	Capacity of the cell, Ah g^{-1}
C_{ch}	Charge capacity, Ah g^{-1}
C_{dis}	Discharge capacity, Ah g^{-1}
CE	Coulombic efficiency, %
C_{Li^+}	Concentration of lithium ions in the electrolyte, mol L^{-1}
C_S	Specific capacity of the cell, Ah g^{-1}
C_{theo}	Theoretical capacity, Ah g^{-1}
D_{Li^+}	Li^+ diffusion coefficient, cm^2 s^{-1}
E/S	Electrolyte to sulfur, µL mg_S^{-1}
E_{cell}	Energy of a battery, Wh kg^{-1}
E_G	Gravimetric energy density Wh kg^{-1}
F	Faraday's constant
I^0	Initial current, µA
I_{1h}	The current density required to charge/discarge a cell 1 hour, µA
$i_{applied}$	Current density applied to the battery, µA
I_p	Current peak, µA
I^s	Steady-state current, µA
m_{cath}	Mass of the cathode, g
m_{cc_cath}	Mass of the cathode current collector, g
m_{cell}	Overal mass of the cell, g
m_{LE}	Mass of the liquid electrlolyte, g
m_{Li}	Mass of lithium metal anode, g
m_{sep}	Mass of the separator, g

M_w	Molecular weight, g mol^{-1}
n	Charge transfer number
N/P	Negative to positive
n_e	Number of electrons involved in the redox reaction
P_{cell}	Power of the cell, W kg^{-1}
Q_p	Plated Li capacity, mAh cm^{-2}
Q_s	Stripped Li capacity, mAh cm^{-2}
Q_T	Plated Li reservoir capacity, mAh cm^{-2}
R_b^0	Initial bulk resistance, Ω
R_b^s	Steady-state bulk resistance, Ω
R_i^0	Initial interfacial resistance, Ω
R_i^s	Steady-state interfacial resistance, Ω
RT	Room temperature, °C
S	Geometric area of the active electrode, cm^2
t	The time for charge/discharge process to take place, h
t_{elec}	Electrolyte thickness, cm
t_{Li+}	Lithium-ion transference number
U_{nom}	Nomimal voltage, V
v	Scan rate, mV s^{-1}
V_{cell}	Voltage of the cell, V
σ	Ionic conductivity, S cm^{-1}
μ_S	Sulfur utilization

A.2. Experimental details

The subsequent section describes the experimental details employed in materials, cell components preparation, cell fabrication, and characterization techniques used during this thesis work.

A.2.1. Materials

Coffee waste, employed as raw material for synthesizing rGOCaf carbon material, was collected from used capsules of a well-known coffee company. Resorcinol (99 wt.%, Sigma-Aldrich), formaldehyde (37 wt.%, Sigma-Aldrich), phosphoric acid catalyst (≥ 85 wt.%, Sigma-Aldrich), graphene oxide (4 mg mL^{-1}, Graphenea), and potassium hydroxide (KOH, ≥ 85 wt.%, Sigma-Aldrich) were employed as received without further treatment.

Sulfur (powder 99.98%, Sigma-Aldrich), Ketjenblack (EC-600JD, AkzoNobel), multi-walled carbon nanotubes (MWCNTs, Sigma-Aldrich), C-65 conductive carbon black (Imerys), graphene nanoplatelets (Sigma-Aldrich), and sodium carboxymethylcellulose (Sigma-Aldrich) were stored in close containers and employed as received. To maintain their purity, all these materials underwent regular drying at 50 °C under vacuum. sodium carboxymethylcellulose (Sigma-Aldrich) and styrene butadiene rubber (Jingrui) were stored in closed containers and employed as received.

1,2-dimethoxyethane (DME, Anhydrous, 99.5%, Sigma-Aldrich), 1,3-dioxolane (DOL, ≥ 99.5%, Sigma-Aldrich), polyethylene glycol dimethyl ether (PEGDME M_w 500 g mol^{-1}, Sigma-Aldrich 99%), and sulfolane (99%, Sigma-Aldrich) were introduced to the glovebox as received. To avoid the presence of water traces, 1,1,2,2-Tetrafluoroethyl-2,2,3,3-Tetrafluoropropyl Ether (TTE, >95.0%, Fluorochem) was dried in preactivated 4 Å molecular sieves for 48 hours before use. Poly-(vinylidene fluoride-co-hexafluoropropylene) (PVDF-HFP, 2801 Kynar Flex, Arkema) was kindly dried at 120 °C overnight under vacuum, to avoid the presence of moisture traces before being introduced and stored inside an Ar filled glovebox. Lithium bis(trifluomethanerosulfonyl)imide (LiTFSI 99.95%, Sigma-Aldrich), lithium nitrate ($LiNO_3$, battery grade, anhydrous, ≥ 99.9%, Sigma-Aldrich), lithium bis(fluorosulfonyl)imide (LiFSI, battery grade, Nippon Shokubai), and lithium (difluoromethanesulfonyl)-(trifluoromethanesulfonyl)imide (LiDFTFSI, homemade)

were dried at 50 °C overnight under vacuum before being introduced into the glove box.

A.2.2. Preparation of cell components

A.2.2.1. Preparation of positive electrodes

In **Chapter II**, the three sulfur cathodes were prepared following the experimental procedure. These cathodes shared a final composition consisting of 64 wt.% sulfur as active material, 26 wt.% carbon, and 10 wt.% CMC/SBR (in a 1:1 wt.% ratio). The incorporation of sulfur into the three different carbon matrices was conducted through a melt diffusion process at 155 °C for 12 h. The studied carbon materials included KetjenBlack® as the benchmark, and the novel in-house materials rGOCaf and ResFArGO. Concurrently, CMC was dissolved by magnetically stirring in deionized water until complete dissolution. Subsequently, C@S composite powders, previously made after the melt-diffusion process, were introduced and vigorously stirred for 4 hours. Finally, SBR solution was added and magnetically stirred for 20 h. The resulting slurries were coated on carbon-coated aluminum foil, fixing the sulfur loading at 2.5-3 $mg_S\ cm^{-2}$ for medium loading electrodes (denoted as power cells) and 4 $mg_S\ cm^{-2}$ for high loading electrodes (denoted as energy cells). To prevent the cracking process during slurry drying, the electrodes were gently dried at room temperature for 4 hours and then vacuum-dried at 50 °C overnight. Finally, electrodes of 13 mm diameter or 37.5 × 54 mm were punched for coin cell assembly or pouch cell assembly, respectively.

The sulfur electrodes prepared in **Chapter III**, particularly KJ600 + CAs and KJ600 + $ResFArGO_{10}$, maintained the same composition described above. In the case of KJ600 + $ResFArGO_{10}$, the procedure closely mirrored the previously described process, with the only distinction being the use of a mixture of KJ600 (as main carbon) and ResFArGO (as additive) in a ratio of 62:38 wt.% as the carbon-sulfur host. On the contrary, for the KJ600 + CAs cathode, owing to the non-porous characteristics of the carbonaceous materials constituting CAs and to ensure optimal contact between sulfur and the carbonaceous material, the melt diffusion process was exclusively conducted with the KJ600. Subsequently, the carbonaceous materials forming the referred CAs additive were introduced. On the other hand, the KJ600 + ResFArGO5 sulfur cathode followed the same experimental procedure but underwent a

modification in electrode composition. This composition modification consisted of 70 wt.% sulfur, 20 wt.% carbon, and 10 wt.% binder (CMC/SBR mixture).

A.2.2.2. Gel polymer electrolyte preparation

The different GPEs studied in **Chapter IV** were prepared by a solvent-casting manufacturing method, resulting in membranes with an average thickness of 70−80 µm. Initially, the battery-grade LiTFSI was dissolved in PEGDME with an EO:Li molar ratio of 20:1, yielding the PEGDME liquid electrolyte. Subsequently, the PVDF-HFP polymer host was dissolved in 4 mL of acetone, an optimized quantity for ensuring the dissolution of all the components while maintaining an appropriate viscosity for further manipulation. Following this, the liquid PEGDME electrolyte, previously prepared, was incorporated and gently stirred for 4 hours at RT to achieve a homogeneous solution. The resulting solution was then cast in a polytetrafluoroethylene dish for solvent evaporation at RT under vacuum overnight.

Following the solvent-casting process, the membranes were punched into the desired dimensions: a disk with 16 µm diameter for coin cell evaluation and a rectangle sheet with 30.1 cm^2 area for pouch cell analysis. Finally, a final drying step at 50 °C under vacuum overnight was conducted to ensure the complete removal of any residual acetone from the punched membranes.

A.2.2.3. Coin cell assembly

In this thesis, all the electrochemical measurements conducted at coin cell level utilized the CR2032-type coin cell format, and the samples were assembled inside an argon-filled glovebox. Various cell configurations were adopted based on the different electrochemical measurements to be studied. For assessing the ionic conductivity of the GPEs, symmetric stainless steel (SS) coin cells were prepared, incorporating the GPEs between the two SS spacers. In this setup, the GPEs were punched in 8 mm diameter discs and placed in the inner space of the same diameter of a 50 µm thickness Kapton film with an outer diameter of 16 mm. In the Li metal symmetric coin cells, the electrolyte, along with the Celgard® 2500 for liquid systems, was positioned between two Li metal discs. In the case of liquid electrolytes, a fixed volume of 60 µL was employed for all test cycling. To maintain an adequate inert pressure, one SS spacer was introduced in contact with the coin cell case. For the Li/Cu cells, the electrolyte, together with Celgard® 2500 for liquid systems, was placed

between the Cu substrate and Li metal discs. Similar to Li metal symmetric cells, tests with liquid electrolytes were performed with a fixed volume of 60 µL, and two SS spacers were added to ensure optimal pressure inside the cell. Finally, in the Li-S coin cell configuration, the electrolyte, combined with the Celgard® 2500 separator for liquid systems, was positioned between the sulfur cathode and the Li metal disc. In this case, two spacers were added to ensure optimal pressure inside the cell.

A.2.2.4. Monolayer and multilayer pouch cell assembly

Li-S pouch cells were fabricated inside an argon-filled glovebox, using high sulfur cathodes with dimensions of 37.5 × 54 mm and LMA measuring 39 × 55 mm. For monolayer pouch cells, a single sheet of one-layer sulfur cathode and a 500 µm thick LMA were stacked with a Celgard® 2500 separator in between. In contrast, for the multilayer pouch cells fabrication, double side-coated sulfur cathodes and 150 µm thickness LMA (equivalent to 75 µm for each cathode side) were stacked layer-by-layer with Celgard® 2500 separator. In both cases, all the cell components were packed within an aluminum-plastic pouch bag. Aluminum and nickel taps were welded to positive and negative electrodes, respectively, using a welding machine. Subsequently, all sides of the pouch bag were heat-sealed, leaving one side open for the liquid electrolyte filling using a pipette. Finally, the last side was sealed, and the pouch bag was closed under vacuum.

In the case of the SSE_LiFSI prototype cells, an external stacking pressure of 66 kPa was applied during the cell cycling through a two-plate design tool.

A.2.3. Characterization techniques

This section is divided into six parts: computational, thermal, morphological, elemental, chemical, specific sulfur cathode and electrolyte, and electrochemical characterization.

A.2.3.1. Theoretical methods and computational details

Classical Molecular Dynamics (MD) simulations were conducted to theoretically evaluate the solvation structure of different electrolytes in **Chapter V**. These simulations were carried out using Gromacs software [1–3]. The simulation boxes were tailored to encompass an appropriate number of molecules to replicate the experimental concentrations: DME/DOL electrolyte (60 LiTFSI + 60 $LiNO_3$ + 564

DME + 828 DOL); SSE_REF electrolyte (120 LiTFSI + 510 sulfolane + 480 TTE); SSE_LiFSI electrolyte (96 LiTFSI + 24 LiFSI + 510 sulfolane + 480 TTE). The initial simulation boxes were generated directly with Gromacs, with each molecule randomly placed in a larger simulation box with a low density, for all cases. Subsequently, the structures underwent compression at 10 K under a pressure of 10 bar, facilitating the attainment of densities akin to experimental conditions. This compression process was performed using the Berendsen thermostat and the Parrinello−Rahman barostat, with a relaxation time of 1 ps in all cases. Following this, the systems were gradually heated up to 600 K under 1 atm, followed by equilibration at this temperature within an NVT ensemble to break possible metastable configurations. The systems were then cooled to the simulation temperature of 298 K at 1 atm. The resultant configuration underwent an additional equilibration phase for 1 ns at the same temperature and pressure. The production simulation spanned 50 ns within the NVT ensemble to ensure the attainment of a diffusive regime.

For the simulations, a cutoff of 10 Å was applied for the van der Waals force, and the real space of Ewald summation was considered. The fast smooth particle mesh Ewald electrostatics was used to address Coulomb interactions within the periodic system. The force field parameters (bond, angle, torsion angle, and Lennard-Jones potential) for all the molecules were sourced from the OPLS-AA force field and their structures were optimized at the density functional theory level with the Gaussian 16 software [4–6]. Becke's three parameters (B3) exchange functional together with the Lee−Yang−Parr nonlocal correlation functional was adopted, employing the 6-31G basis set and single first polarization functions [7–13]. The DFT approach was further used to compute the partial atomic charges essential for the MD simulations, using the restrain electrostatic potential method. To account for polarizability effects, the calculated partial charges for all the molecules were scaled by a factor of 0.8.

A.2.3.2. Thermal characterization

A.2.3.2.1. Thermogravimetric analysis

Thermogravimetric analysis (TGA) was employed to evaluate the thermal stability of the developed GPEs in **Chapter IV**. TGA measurements were performed on a NETZSCH simultaneous thermal analyzer 209 F1 Libra. The samples underwent heating from RT up to 800 °C at a heating rate of 10 °C min^{-1} under an argon flow. The

degradation temperature was determined when the mass loss reached 5 wt.% of the total weight of the samples.

A.2.3.2.2. Flammability test

The flammability test was used to evaluate the safety properties and flammable characteristics of different electrolytes in both **Chapter IV** and **Chapter V**. In **Chapter IV**, for the liquid electrolytes, a controlled amount of electrolyte was dropped onto a watch glass, and the combustion behavior was examined through direct ignition using a lighter. For the GPEs flammability assessment, a 16 µm disk was ignited to ascertain their combustion characteristics.

In **Chapter V**, the Celgard® 2500 separator was soaked in the electrolyte solution, and subsequent combustion behavior was tested by direct ignition using a lighter. The self-extinguishing time (SET) was measured by measuring the duration it took for the flame to naturally extinguish after ignition of a controlled amount of electrolyte (approximately 500 µL) dropped over onto a watch glass. To ensure robustness and reliability, the test was repeated a minimum of three times for each electrolyte, and the resulting SET values were calculated as an average.

A.2.3.3. Morphological characterization

A.2.3.3.1. Scanning Electron Microscope

The Scanning Electron Microscope (SEM) is a technique employed to analyze the morphology and chemical characteristics of a certain material surface. All the surface and cross-section morphology analyses of the different samples were evaluated using a field emission Gun Quanta 200 FEG (FEI) scanning electron microscope, operated at voltages up to 30 kV. For the evaluation of air-sensitive samples, a specialized air-tight holder was employed to facilitate the direct transfer of these samples from the glovebox to the SEM equipment.

A.2.3.3.2. N_2 adsorption-desorption isotherms

Among the different gas adsorption methods, N_2 adsorption at -195.8 °C (77 K) stands out as the most widely employed technique due to its capacity to cover a broad pore range and its weak interaction with most solids. The evaluation of the resulting adsorption-desorption isotherms from this technique provides valuable

information, allowing for the determination of the specific surface area and pore size distribution of the material. This is particularly useful in the context of analyzing the different carbon sulfur hosts analyzed in this thesis.

Nitrogen adsorption-desorption isotherms were measured using ASAP2020 adsorption analyzer (Micrometrics) at −196 °C. Before the analysis, all the samples underwent outgassing at 250 °C for 12 h under vacuum to remove any adsorbed gasses or contaminants. The specific surface area was calculated using the Brunauer-Emmet-Teller (BET) method, calculated from the nitrogen isotherms in the relative pressure range of 0.05-0.25 [14]. Additionally, the pore size distribution (PSD) was derived from the N_2 isotherm by the 2D-NLDFT heterogeneous surface method and fitting with the SAIEUS software.

A.2.3.4. Elemental characterization

A.2.3.4.1. Energy dispersive X-ray spectroscopy

The Energy dispersive X-ray spectroscopy (EDX) technique provides insights into the elemental chemical composition using the EDX spectrometer. This technique proves particularly valuable for determining the distribution of sulfur active material within the positive electrode, an important feature for achieving an optimal LSB performance. The analysis involves detecting characteristic X-rays generated by the interaction of the electron beam with the sample. The data acquisition for EDX analysis was carried out using the same setting as employed in the SEM.

A.2.3.4.2. X-ray diffraction

X-ray diffraction (XRD) technique was employed to assess the degree of sulfur infiltration within different porous carbonaceous materials. XRD patterns were acquired using a Bruker D8 Discover X-ray diffractometer, utilizing Cu-Kα radiation with a wavelength (λ) of 1.54056 Å. The diffraction measurements were performed in the 2θ range from 15° to 80°, with a step width of 0.0198° and a residence time of 5 seconds.

A.2.3.5. Chemical characterization

A.2.3.5.1. Raman spectroscopy

The Raman spectroscopy technique was used for two main purposes in this thesis. Firstly, it was employed to investigate the structural characteristics and quality of the two graphene-based porous carbonaceous materials developed in **Chapter II**. This involved evaluating features such as the D-band and G-band, providing insights into the material's disorder structure and the vibration of sp^2-bound carbon atoms [15,16]. Secondly, Raman spectroscopy was utilized to evaluate the interaction between lithium salt molecules and solvents in the studied electrolytes in **Chapter V**. This analysis provided valuable information about the experimental solvation structure of the different electrolytes, with a focus on understanding how these structures varied depending on the concentration of lithium salt.

Raman spectra were acquired using a Renishaw spectrometer (Nanonics Multiview 2000) operating with an excitation wavelength of 532 nm. The spectra were obtained with a 10-second exposure time of the laser beam to the samples. For graphene-based materials analysis, the ratio between the integral of D and G peaks was calculated using Origin software by fitting the experimental curve with Gaussian and Lorentz equations. For electrolyte characterization, the laser with a wavelength of 532 nm, exciting from 300-1200 nm, was employed.

A.2.3.5.2. X-ray photoelectron spectroscopy (XPS)

The X-ray photoelectron spectroscopy (XPS) technique was employed to analyze and characterize the chemical composition of different surfaces of components. The measurements were conducted in a Phoibos 150 XPS spectrometer (SPECS Surface Nano Analysis) operating in Fixed Analyzer Transmission (FAT) mode, utilizing a non-monochromatic Mg source (K_α line with h_ν = 1253.6 eV) at 100 W. To ensure the integrity of surface composition, all samples were directly transferred from the GB to the XPS equipment through a specially designed airtight setup. Additionally, a Shirley function was employed to simulate the inelastically scattered electrons background and Voigt functions (70% Gaussian and 30% Lorentzian) as line shapes for fitting the different studied photoelectron peaks using the CasaXPS software.

A.2.3.5.3. Attenuated total reflectance-Fourier transform infrared

To elucidate the degradation mechanism arising from the interaction between LMA and GPE_20, as developed in **Chapter IV**, along with the resulting structural modifications, attenuated total reflectance-Fourier transform infrared (ATR-FTIR) spectrophotometry was used. The ATR-FTIR spectra were collected using a Spectrum 400 DTGS spectrometer (PerkinElmer, Waltham, MA, United States), with infrared measurements spanning from the 400 to 4000 cm^{-1} wavenumber range and a resolution of 2 cm^{-1}.

A.2.3.6. Specific sulfur cathode and electrolyte characterization

A.2.3.6.1. LiPS dissolution adsorption test

The LiPS dissolution visual test was employed to qualitatively evaluate the affinity between the analyzed carbonaceous materials and LiPS. To prepare the LiPS dissolution, stoichiometric amounts of S_8 and Li_2S were mixed into 1,2-dimethoxyethane (DME, anhydrous, Sigma-Aldrich) solvent to obtain a final concentration of 3 mM Li_2S_6. For the LiPS adsorption test 10 mg of each carbonaceous material was incorporated into 2 mL of the aforementioned LiPS dissolution. This specific combination of LiPS concentration and carbonaceous material quantity was determined to provide the most discernible results. Following a brief resting period, the carbons settled at the bottom of the vials, facilitating easy observation of any color changes within the solution.

A.2.3.6.2. UV-Vis spectroscopy of LiPS adsorption test

In conjunction with the qualitative LiPS adsorption test, the UV-Vis technique enabled the quantitative assessment of the LiPS adsorption ability exhibited by the different carbonaceous materials. Following the same procedure outlined earlier, wherein the carbonaceous materials interact with the LiPS dissolution, the resulting solutions were filtered to remove the presence of any solid residues. Subsequently, the quantitative UV-Vis measurements of the filtered solutions were performed using a Cary 5000 UV-vis spectrophotometer (Varian).

A.2.3.6.3. LiPS formation test

The LiPS formation test was conducted to study the differences in the affinity between SSEs and LiPS. This involved attempting to generate LiPS in situ within the electrolyte at different temperatures. To this end, stoichiometric amounts of S_8 and Li_2S were mixed in SSE_LiFSI, to obtain a maximum concentration of 0.5M Li_2S_6. The mixtures were left to react for 3 days at both 25 °C and 60 °C, followed by filtration to obtain clear solutions.

A.2.3.6.4 Viscosity measurement

Viscosity measurements of different electrolytes in **Chapter V** (determined at RT) and **Chapter VI** (determined from 10 °C to 80 °C at 10 °C intervals) were measured using an Anton Paar DMA 4500 M density meter equipped with a Lovis 2000 M rolling ball viscometer module. The equipment ensures precise temperature control with an accuracy of ± 0.02 °C, and equilibrium is achieved after approximately 5 minutes. The viscosity values presented are an average of at least 5 runs of the ball back and forth. Before each set of measurements, the instrument was calibrated and verified with standards to ensure accuracy and reliability.

A.2.3.6.5. Contact angle

The wettability between the developed positive electrodes and Celgard® 2500 separator with the electrolytes was evaluated through contact angle measurements. These measurements were performed using the sessile drop method at room temperature using an LSA100 surface analyzer (Lauda Scientific). A 3 µL electrolyte drop was deposited on top of each electrode and separator, and the process was recorded at a rate of 90 fps. The images used for analysis were captured during the second frame after the drop deposition (at 0.011 seconds).

A.2.3.7. Electrochemical characterization

A.2.3.7.1. Ionic conductivity

Depending on the electrolyte type under examination, whether it be a liquid electrolyte or GPE in this case, two different setups were employed to determine electrolyte conductivity. For GPEs, ionic conductivity was determined using electrochemical impedance spectroscopy (EIS) analysis conducted on CR2032-type

cells. These cells were assembled by sandwiching the GPE between two stainless steel (SS) blocking electrodes (SS | GPE | SS) in an Ar-filled glove box. The measurements were conducted using a VMP3 potentiostat (Biologic), with the frequency ranging from 10^{-1} to 10^{6} Hz and a signal amplitude of 10 mV. Subsequently, after fitting the obtained EIS spectra to the corresponding circuit to determine the bulk resistance (R_b) of the electrolyte, the ionic conductivity (σ) was calculated as follows:

$$\sigma = R_b \frac{t_{elec}}{A_{elec}} \quad \text{(A.2.1)}$$

where t_{elec} and A_{elec} represent the electrolyte thickness and area, respectively. The membrane thickness was determined after cell testing, by direct measurement employing a micrometer (Digimatic Micrometer, Mitutoyo).

In the case of liquid electrolytes, ionic conductivity was measured by analyzing the internal resistance of a 2-pole conductivity cell. This analysis followed the same EIS protocol described earlier in a VMP3 potentiostat. The 2-pole conductivity cell presents a cell characteristic constant, representing the ratio of electrode separation to electrode area. Therefore, upon obtaining the R_b through the fitting of the EIS spectra, the ionic conductivity of the liquid electrolytes is calculated from **Equation A.2.1**.

A.2.3.7.2. Lithium transference number

The Li-ion transference number (t_{Li^+}) of GPE_20 at RT was determined by a combined approach involving AC EIS and DC polarization methods in a symmetric Li metal|GPE|Li metal cell, as proposed by Bruce et al. and Watanabe et al. [17,18]. Initially, a 10 mV DC voltage step was applied using a VMP3 potentiostat until a steady current was achieved. The impedance spectra of the cell were recorded in the frequency range from 10^{-2} to 10^{6} Hz with a voltage oscillation of 10 mV, both before and after the DC polarization. The value of t_{Li^+} was calculated using **Equation A.2.2**:

$$t_{Li^+} = \frac{I^s R_b^s (\Delta V - I^0 R_i^0)}{I^0 R_b^0 (\Delta V - I^s R_i^s)} \quad \text{(A.2.2)}$$

where I^0 and I^s represent the initial and steady-state currents, R_b^0 and R_b^s are the initial and final resistances of the bulk electrolytes, R_i^0 and R_i^s are the initial and

final interfacial resistances of the Li metal electrode/electrolyte, and ΔV is the applied DC voltage.

A.2.3.7.3. Cyclic voltammetry and its associated characterizations

Cyclic voltammetry (CV) analysis emerged as an important characterization technique for evaluating the kinetics of sulfur redox reactions in sulfur cathodes employing different carbonaceous materials. The CV measurements were conducted on a BioLogic VMP3 electrochemical potentiostat, employing a three-electrode setup. The Li metal disk served as both the counter and reference electrode.

In addition to the insights obtained from CV curves, further analysis of individual peaks within these CV curves, which delineate the different redox reactions, was conducted through Tafel plots. This analysis enables the determination of the electrocatalytic effect introduced by the different carbonaceous materials under investigation.

Furthermore, the investigation of CV curves of the cell at different scanning rates, in this case ranging from 0.1 mV s^{-1} to 0.4 mV s^{-1}, facilitated the analysis of the Li^+ diffusion coefficient (D_{Li^+}) for different sulfur cathodes. This analysis was made possible by applying the Randles-Sevick equation based on the above CV results:

$$I_p = 2.69 \times 10^5 n^{1.5} S D_{Li^+}^{0.5} C_{Li^+} v^{0.5} \quad \text{(A.2.3)}$$

here, I_p represents the current peak, n denotes the charge transfer number (where n = 2 for LSBs), S is the geometric area of the active electrode, C_{Li^+} is the concentration of lithium ions in the electrolyte, and v is the potential scan rate. Therefore, by fitting the CV results to the I_p-$v^{0.5}$ curve, the obtained slope can be directly correlated to the D_{Li^+}, as n, S, and C_{Li^+} are constants.

A.2.3.7.4. Li_2S nucleation and dissolution tests

To comprehensively characterize the kinetic properties of different carbon mixtures analyzed in **Chapter III**, Li_2S nucleation and dissolution tests were conducted. The Li_2S_8 solution (0.2 mol L^{-1}) was prepared by stoichiometrically mixing S_8 and Li_2S powder in tetraglyme under vigorous stirring for 3 days. Sulfur-free free-standing cathodes were prepared, serving as working cathodes coupled with the Li metal as the anode and Celgard 2500 as the separator. Subsequently, 20 µL of the Li_2S_8 solution

was added into the cathode part as a catholyte, and 20 µL of control anolyte without Li_2S_8 was dropped on the anode side, completing the assembly of the coin cell.

To carry out the nucleation test, the cells were discharged to 2.06 V under a constant current of 0.112 mA to consume most of the high-order polysulfides and were later maintained at 2.05 V until the current dropped below 10^{-5} A, inducing the nucleation and growth of Li_2S. This nucleation test provides valuable insights into the dynamics of the liquid-solid conversion process.

In the dissolution test, using the same cell configuration described earlier, the cells were initially discharged to 1.7 V using a constant current of 0.112 mA to produce Li_2S. Afterward, they were potentiostatically charged at 2.4 V until the current dropped below 10^{-5} A, intending to observe the dissolution of Li_2S into higher-order LiPS. As opposed to the nucleation test, the dissolution test offers important information into the dynamics of the solid-liquid conversion process.

In both tests, based on Faraday's law, the whole displayed current was used to determine the Li_2S nucleation and dissolution process.

A.2.3.7.6. Electrochemical stability between electrolytes and LMA

The galvanostatic cycling experiments were performed using Li/Li symmetric cells with a Maccor Battery Tester (Series 4000). In this thesis, two different galvanostatic cycling protocols were employed. On one hand, long-term galvanostatic cycling was implemented, applying a fixed current density of 0.1 and 0.3 mA cm^{-2}, and a half-cycle duration of 2 hours. On the other hand, galvanostatic cycling tests at different current densities, ranging from 0.1 mA cm^{-2} to 0.5 or 2 mA cm^{-2} in this case, with a half-cycle duration of 1 hour. During this test, the current was kept constant for 10 hours before transitioning to the subsequent current density.

Based on the same cell configuration and principles applied in the latest galvanostatic cycling test, the critical current density (CCD) evaluation was performed. This assessment yielded key insights into the maximum current density that different electrolytes could withstand without inducing cell failure. In this particular test, the Li symmetric cells were kept at 25 °C for 6 hours of resting before undergoing galvanostatic cycling at different current densities, ranging from 0.1 to 5.0 mA cm^{-2}, keeping one cycle per studied current density.

A.2.3.7.7. Determination of CE in LMAs

To evaluate the compatibility of different electrolytes developed with the LMA, different electrochemical measurements in Li||Cu cells were conducted to determine the Coulombic efficiency (CE). Different methods were employed to gain a detailed understanding of the interaction between lithium anode and electrolyte.

In the initial procedure, a specific capacity of Li metal (Q_P = 0.5 mAh cm^{-2}) was electrodeposited onto the Cu substrate, followed by the galvanostatic cycling of Li metal with a cut-off voltage of 1 V (to remove the available lithium from Cu, denoted as Q_S) for n cycles. The CE in this method was calculated using the following equation:

$$\mathrm{CE} = \frac{\mathrm{Q_S}}{\mathrm{Q_P}} \times 100 \qquad \text{(A.2.4)}$$

In the second test, the modified Aurbach method was employed, incorporating a substrate preconditioning or stabilization step [19]. This step involved the electrodeposition of a high capacity of Li metal onto Cu (5 mAh cm^{-2}) at a current density of 0.5 mA cm^{-2} for 10 hours, followed by stripping the Li up to 1 V. Afterward, the Li reservoir capacity (Q_T = 5 mAh cm^{-2}) was again deposited on Cu at 0.5 mA cm^{-2} for 10 hours and subjected to galvanostatic cycling with a capacity of Q_P = 0.5 mAh cm^{-2} for a specific number of cycles at a current density of 0.5 mA cm^{-2}. Finally, in the last cycle, the remaining Li was stripped at 0.5 mA cm^{-2} to 1 V, and the obtained capacity (Q_S) was measured. In this case, the CE is determined by the following equation:

$$\mathrm{CE} = \frac{(\mathrm{nQ_P} + \mathrm{Q_S})}{(\mathrm{nQ_P} + \mathrm{Q_T})} \times 100 \qquad \text{(A.2.5)}$$

Finally, to evaluate the long-term endurance of the Li deposition morphology, the Aurbach method was employed [20]. This test shares similarities with the previous one, except for the prestabilization process applied to the Cu substrate. In this case, the long-term galvanostatic cycling at 0.5 mA cm^{-2} and 0.5 mAh cm^{-2} was initiated after depositing a Li reservoir of 5 mAh cm^{-2} at a current density of 0.5 mA cm^{-2} for 10 hours.

A.2.3.7.8. Lithium sulfur cell cycling

The battery cycling performance of the approaches implemented in this doctoral thesis was evaluated through galvanostatic cycling at different discharge and charge rates, using a Maccor Series 4000 battery tester. Different cut-off voltages were applied based on the electrolyte type employed. Specifically, when cycling with the conventional DME/DOL electrolyte, the voltage range was set between 2.6-1.7 V. For the GPE, the voltage range varied from 2.8 to 1.6 V, or 1.7 V in the case of GPE with $LiNO_3$ in its composition. Finally, for the SSEs, various cut-off voltages were examined, including 3.0-1.2 V, 2.7-1.4, and 2.5-1.7 V.

Within the galvanostatic cycling of Li-S cells, two different protocols were applied. The first protocol utilized medium sulfur loading cells, also referred to as power cells, evaluating their performance at various cycling rates ranging from modest rates (e.g., C/20) to high rates (e.g., 2C). This test played a fundamental role in understanding the behavior of the proposed strategies under different cycling rates, with particular emphasis on the challenges associated with sluggish kinetics of redox reactions at high C-rates in Li-S technology.

On the other hand, to assess the long-term cycling of high sulfur loading cells, also denoted as energy cells, a cycling protocol incorporating moderate operating rates was applied. This specific cycling protocol was designed to evaluate the capability of the developed strategies in ensuring stable and long-term cycling under sulfur loading conditions aligned with practical requirements.

A.2.3.7.9. LFP-based GPE cell cycling

While not the primary focus of this thesis, galvanostatic cycling of LFP-based LMBs was carried out to examine the performance of the GPE_20 in a different technology than Li-S. Two different cycling protocols were employed based on the operating conditions. For both coin cells and the pouch cell with a thick LMA, a cycling protocol between a voltage of 3.8-2.7 V at different operating rates, including C/20, C/10, C/5, and return to C/10 for long-term, was executed. Conversely, due to the more demanding operating conditions, a moderate rate cycling protocol at C/10, preceded by 5 cycles at C/20 as preconditioning step, was employed for the pouch cell using the thin LMA of 50 µm. This galvanostatic cycling protocol took place within a voltage range of 3.8-2.7 V.

A.3. Supplementary information Chapter III

A.3.1 SEM images of KJ600-based high sulfur loading cathode

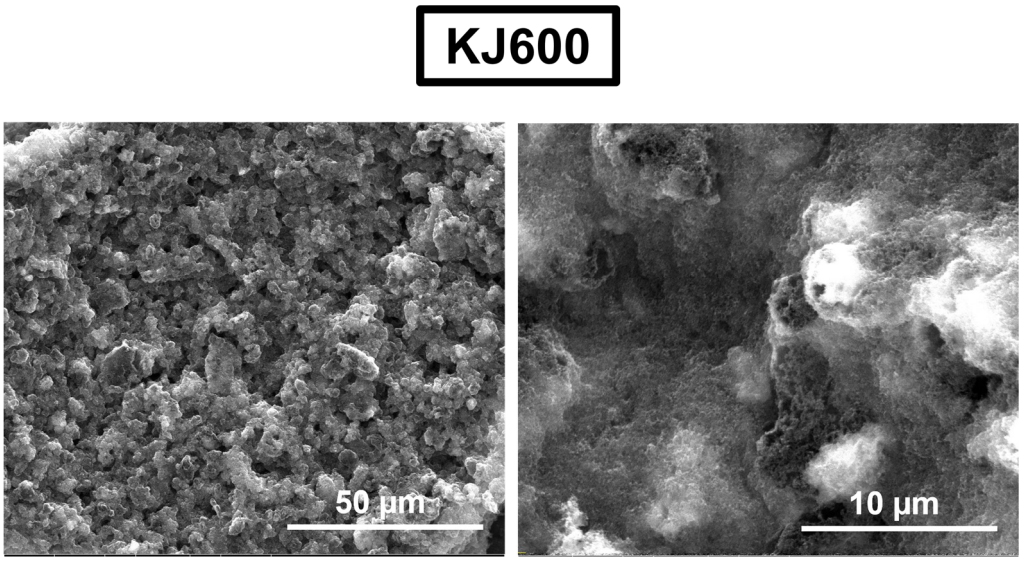

Figure A.3.1. SEM images of the reference KJ600-based high sulfur loading cathode under different magnifications: **a)** × 2000 and **b)** × 10000 magnifications.

A.3.2 SEM images of KJ600 + CAs-based high sulfur loading cathode

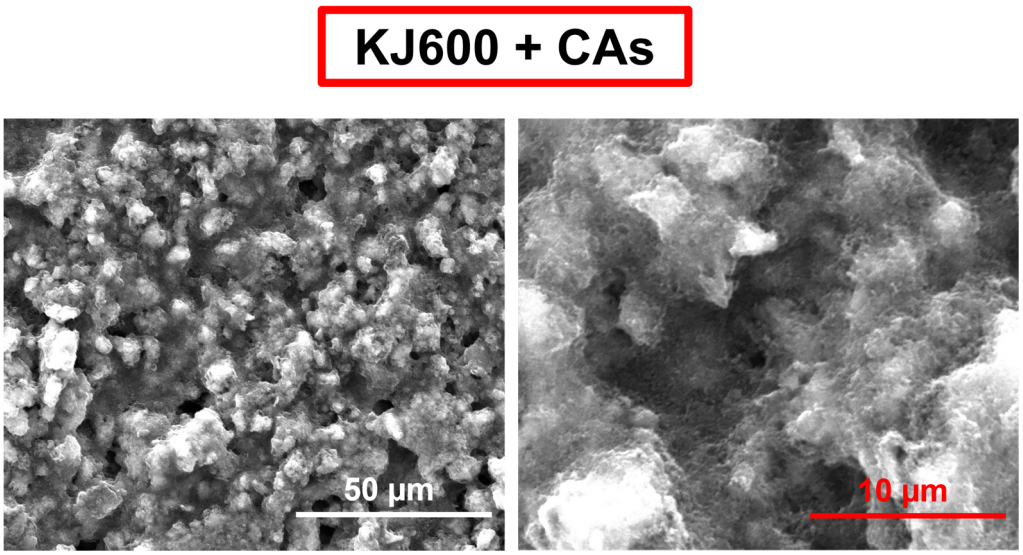

Figure A.3.2. SEM images of the reference KJ600 + CAs-based high sulfur loading cathode under different magnifications: **a)** × 2000 and **b)** × 10000 magnifications.

A.3.3 SEM images of KJ600 + ResFArGO$_{10}$-based high sulfur loading cathode

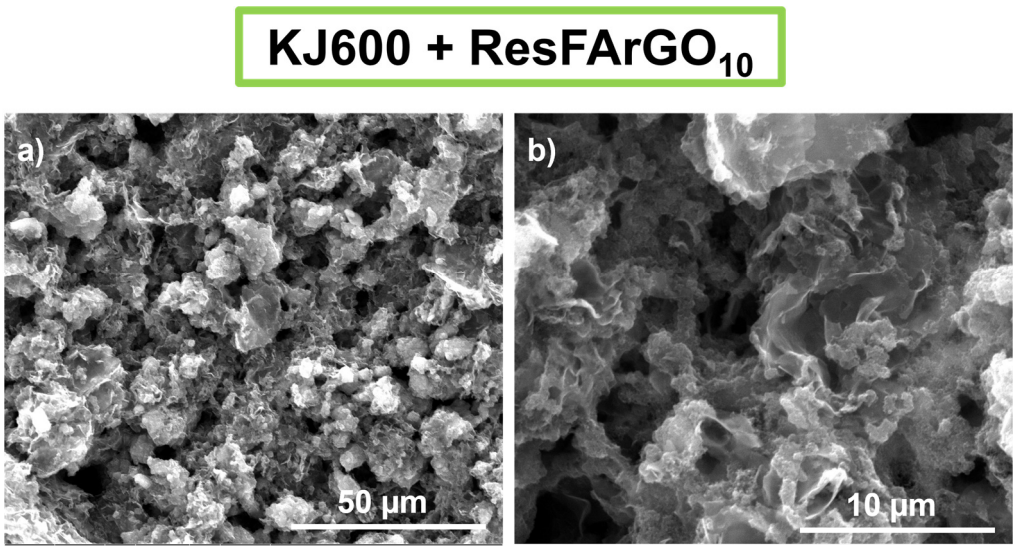

Figure A.3.3. SEM images of the reference KJ600 + ResFArGO$_{10}$-based high sulfur loading cathode under different magnifications: **a)** × 2000 and **b)** × 10000 magnifications.

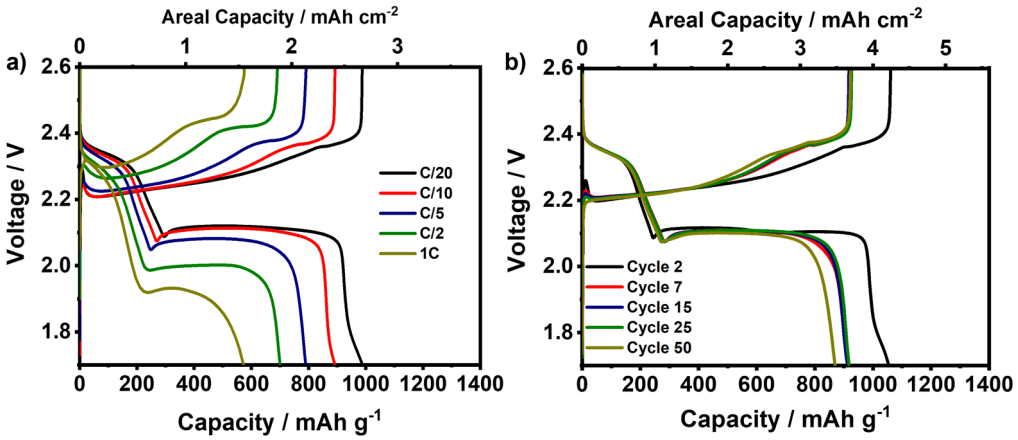

Figure A.3.4. Charge/discharge profiles of KJ600 + ResFArGO$_5$ cathode in **a)** power and **b)** energy cells.

A.4. Supplementary information Chapter IV

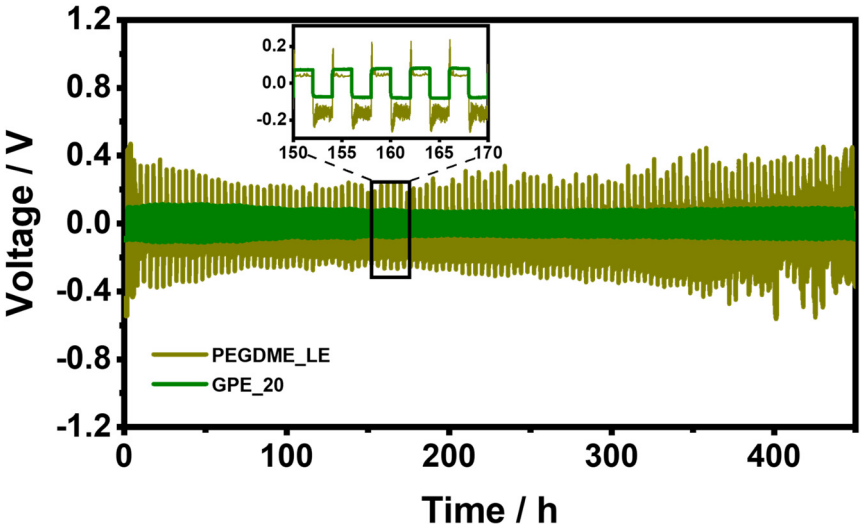

Figure A.4.1. Galvanostatic cycling comparison of the Li metal symmetric cells using PEGDME_LE and GPE_20 at a current density of 0.1 mA cm^{-2}.

A.4.2 LFP-based Lithium-Metal Batteries performance using GPE_20

The performance demonstrated in LSBs introduced significant concerns regarding the applicability of the developed GPE. However, acknowledging the favorable individual properties exhibited by the electrolyte and recognizing the operational challenges associated with the cycling of LSBs, additional battery cycling evaluations were conducted employing different cathode chemistry. In this case, the new investigation employed LMBs based on lithium iron phosphate (LFP) cathode chemistry. This replacement of the active material aims to evaluate the applicability of GPE_20 under more benign operating conditions within an already commercially deployed technology.

A.4.2.1 LFP-based LMB coin cell performance

In the evaluation of the LFP cell performance using the GPE_20 electrolyte, a comprehensive analysis was undertaken employing a cycling protocol that involved different C-rates. Specifically, this protocol encompassed 5 cycles at C/20, succeeded by 5 cycles at C/10, followed by 5 cycles at C/5, ultimately culminating in extended and stable cycling at C/10. As depicted in **Figure A.4.2a**, GPE_20 exhibited remarkable

rate capability with almost no capacity drop from C/20 (156 mAh g^{-1}) to C/5 (140 mAh g^{-1}). Additionally, the cell demonstrated an exceptional capacity recovery upon reverting to the C/10 rate, with an outstanding capacity retention, retaining 98% of its initial capacity after 60 cycles, alongside an impressive Coulombic Efficiency exceeding 99.2%. Importantly, this exceptional performance was achieved without encountering any erratic cycling behavior, reaffirming the system's robust stability. These remarkable outcomes were substantiated by the charge/discharge profiles (**Figure A.4.2b**), where minimal differences in polarization were observed across different cycling C-rates. This observation indicates a low overpotential, approximately 15 mV, attributed to the favorable Li+ conductivity of the prepared GPE ascribed to its high t_{Li+}.

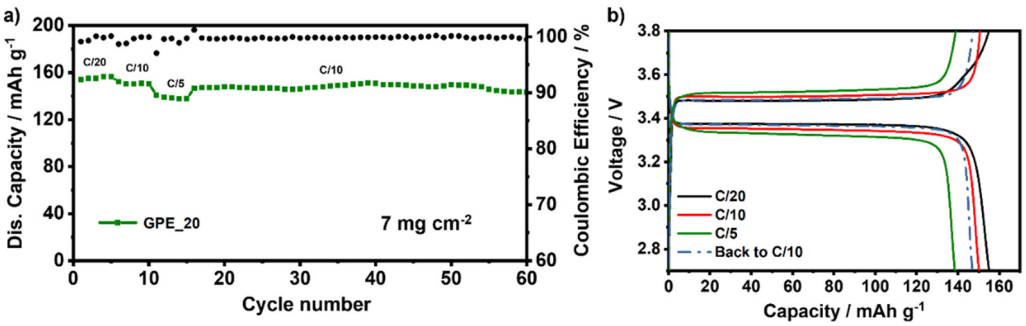

Figure A.4.2. a) Long-term cycling performance and **b)** charge/discharge profiles of the GPE_20 in LMBs at different C-rates (C/20, C/10, C/5, and back to C/10) with LFP as active materials at RT.

4.5.2 LFP-based LMB pouch cell performance

Before delving into the analysis of the causes of Li-S cell failure with GPE_20, it is worth noting that while the central focus of this thesis does not primarily center on the development of LFP technology, the promising potential of the developed GPE in this technology, coupled with the significant emphasis on battery scaling process within the framework of this thesis, prompted to explore the scalability of this system. As in the case of Li-S technology, extensively described in the introduction (**Section 1.4.3.2**), it is important to acknowledge that most of the research works related to the development of GPEs for LMBs primarily involve testing at the coin cell level. This approach poses challenges when attempting to directly translate research findings into practical prototype cells, often overlooking critical aspects of GPE performance under more realistic operating conditions. Consequently, encouraged by the

promising results obtained with the GPE_20 electrolyte at the coin cell level, a comprehensive evaluation of its scalability at the pouch cell was performed, maintaining the same cell configuration, LFP cathode loading of 7 mg cm^{-2} 500 um thick lithium foil. Indeed, 20 cm^2 pouch cells were effectively assembled with an excellent degree of reproducibility, thereby highlighting the scalability, manufacturing feasibility, and remarkable mechanical properties of the larger-sized GPE_20-based electrolyte developed in this study.

To evaluate the potential feasibility, flexibility, and safety of the GPE_20-based LFP pouch cell a comprehensive series of experiments were conducted. Firstly, the performance of the assembled pouch cell was demonstrated by employing it to power a bank of 20 commercial light-emitting diode (LED) lamps. As depicted in **Figures A.4.3a-d**, the assembled pouch cell reliably illuminated the 20 LED lamps, even when subjected to different degrees of bending, emphasizing the exceptional flexibility of the system. Interestingly, even after the physical bisection of the, as illustrated in **Figure A.4.3d**, the GPE_20-based pouch cell continued to power the LED lamps without any observable liquid leakage, smoke generation, or combustion. These rigorous tests unequivocally prove the exceptional safety behavior of this system, aligning with findings from the flammability test outlined in **Chapter IV**. Such results robustly reinforce the potential for the practical and safe application in prototype scale LMBs. Analyzing the electrochemical performance of the pouch cell, as shown in **Figure A.4.3e**, it exhibited capacity values closely mirroring that obtained at the coin cell level, resulting in an impressive total cell capacity of approximately 19 mAh. Additionally, the cell provided several remarkable characteristics, including exceptional rate capability, with capacity values approaching 140 mAh g^{-1} even under the demanding conditions of a high cycling rate of C/5. Furthermore, the cell demonstrated outstanding capacity recovery when reverting to C/10. These encouraging results were reinforced by stable and consistent charge and discharge profiles, marked by a low cell polarization, albeit with a slight increment observed at C/5 (**Figure A.4.3f**).

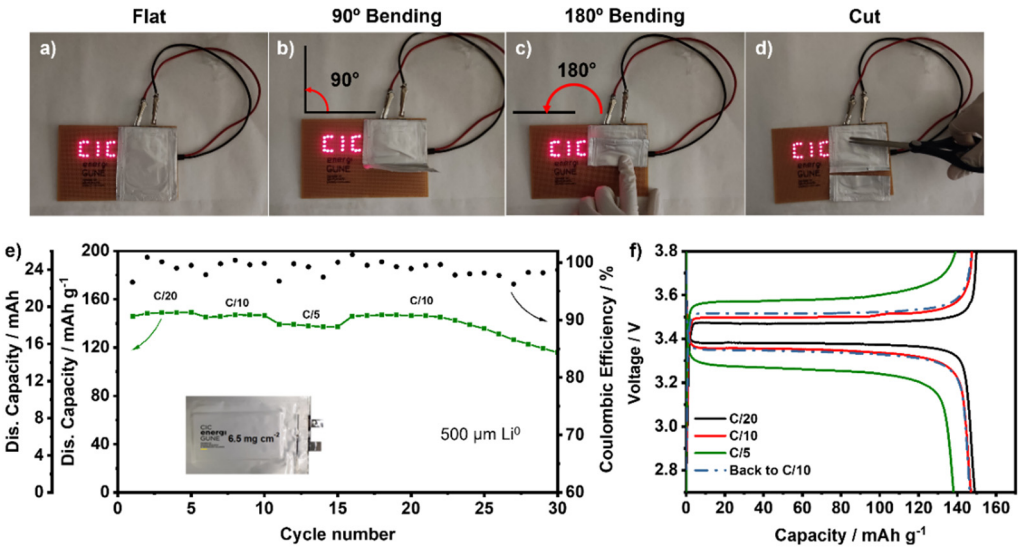

Figure A.4.3. Evaluation of the flexibility and safety of the GPE_20-based LFP pouch cell by lighting LEDs **a)** initial state, **b)** blended at 90°, **c)** folded at 180°, and **d)** after cutting. **e)** Battery test performance and **f)** charge/discharge profiles of the pouch cell at different C-rates.

While the promising results achieved thus far are indeed encouraging, the effort to scale up this system was pushed forward by the integration of a thinner lithium metal anode. This practical adjustment involved reducing the anode thickness from the previous 500 µm to a slenderer 50 µm. This subtle modification aimed to bring the system even closer to practical operating conditions, representing a significant milestone in the ongoing exploration and development of the system. As displayed in **Figure A.4.4a**, the pouch cell employing the thin Li metal anode demonstrated successful cycling for up to 30 cycles, consistently delivering remarkable capacity values. Moreover, the cell exhibited relatively stable capacity values during its cycling at a C-rate of C/10, underscoring the exceptional compatibility of the system even with this thinner anode configuration. Indeed, to the best of the authors' knowledge, these results represented the first study in literature focusing on a high LFP loading GPE-based Li metal cell in a prototype cell format using a thin Li metal anode, underscoring the significance of the obtained findings. However, it is worth noting that the obtained capacity was slightly lower than what was observed with the thicker lithium cell. This difference can be attributed to the reduction of internal cell pressure resulting from the reduced lithium thickness, which may potentially affect the optimal contact between cell components.

It is essential to highlight that both prototype cells exhibited a notable reduction in cycle life compared to the performance observed during coin cell cycling, with a noticeable drop in the capacity occurring after just 25 cycles in both cases. To gain deeper insights into the factors contributing to this observed cell performance degradation, impedance testing during cycling and a post-mortem at the end of the pouch cell's life were conducted.

Figure A.4.4b presents a Nyquist plot presenting the impedance of the pouch cell at different stages of its battery life, including measurements taken after 24 h of rest and after cycles 5, 10, and 25. The resistance of the bulk (R_b), representing the resistance associated with Li^+ mobility through the GPE_20 electrolyte, remained consistently stable throughout the pouch cell cycling, indicating the enduring ionic conductivity properties of the electrolyte. However, a significant increase in the overall resistance of the cell became evident after 25 cycles, mainly attributed to a sharp increase in interfacial resistance. This observation was interpreted as a manifestation of reduced Li^+ diffusion through the Li metal electrode/GPE_20 electrolyte interface, leading to increased resistance and, consequently, directly linked to the observed capacity drop.

The post-mortem analysis conducted after 30 cycles provided additional support for this hypothesis. In **Figure A.4.4c**, an irregular surface and the presence of a thick layer on the surface of the Li metal anode were observed. This finding can be attributed to two different factors. First, the degradation of Li metal anode, which is notably more severe in pouch batteries compared to coin batteries, as established by previous research work focused on the scalability of LMBs. This exacerbated degradation of pouch cells can be ascribed to the considerably higher total current density applied in this cell configuration during cycling, directly resulting in the formation of mossy or dead lithium on the anode surface. Second, this phenomenon may also be related to the potential interaction between the Li metal anode and the GPE_20 electrolyte developed in this chapter. It is worth the ongoing debate concerning the anodic stability of PVdF-based polymers in LMBs. While there is a consensus in the literature regarding the reactivity of these polymers with the Li metal anode, the potential advantages or detriments this interaction may introduce to cell stability have not been comprehensively addressed.

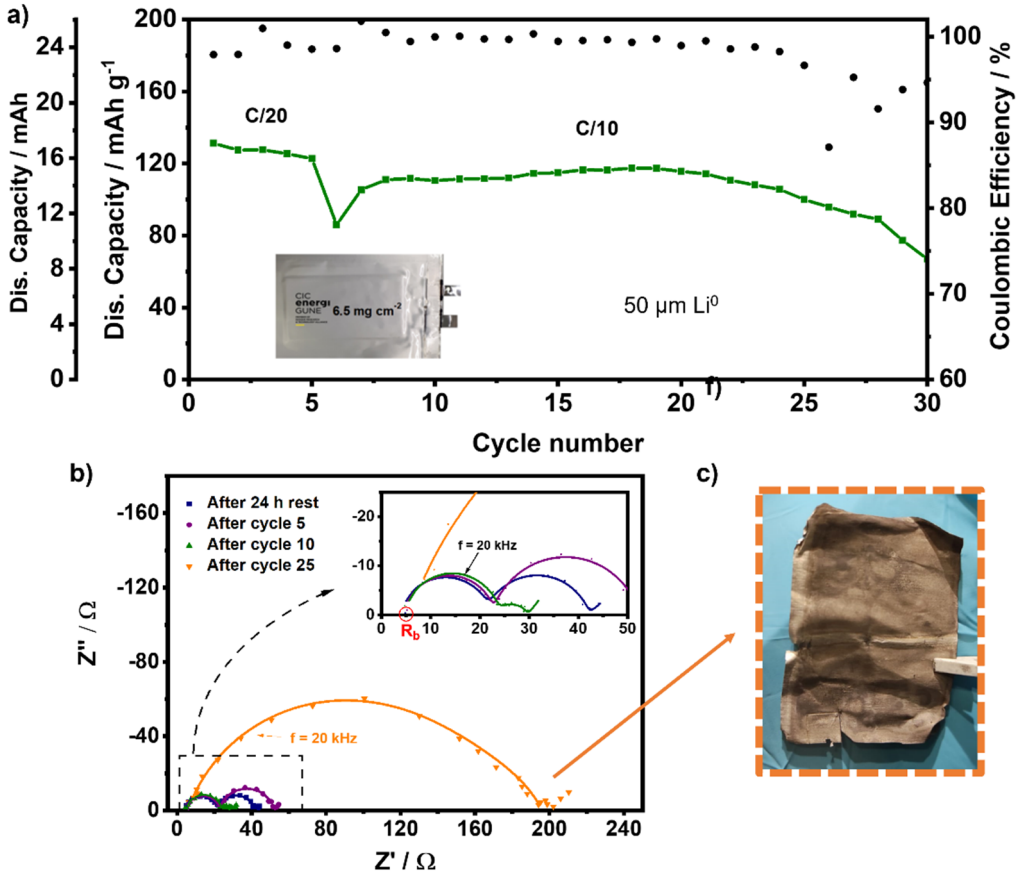

Figure A.4.4. a) Thin lithium-based GPE_20 pouch cell cycling performance, **b)** electrochemical impedance spectroscopy of LFP pouch cell over consecutive cycling, and **c)** optical images of the Li metal anode after 25 cycles.

To contextualize the outstanding results achieved by the GPE developed in this chapter, an extensive review of the current state of research in this field was conducted. The landscape of GPEs for LMBs has experienced significant growth in recent years, as evident from the prolific number of recent publications in this field. However, it is noteworthy that a considerable number of these reported studies remain in the proof-of-concept phase, characterized by low active material loadings in the cathode, typically less than 4 mg cm^{-2}, rendering them far from practical application. Notably, the study performed with the GPE_20 achieves an areal capacity of approximately 1 mAh cm^{-2}, with an LFP loading of around 7 mg cm^{-2}. This achievement surpasses many previously reported works in this domain, as illustrated in **Figure A.4.5**. These findings underscore the potential of the developed GPE in this

study, demonstrating exceptional performance in LFP-based LMBs under practical operating conditions [21]. Consequently, this investigation, which entailed substituting the battery's active material, unequivocally demonstrates that the observed poor performance in Li-S cells of the GPE_20 was attributable to other factors rather than the behavior of the electrolyte. This underscores the imperative need for a comprehensive analysis of the underlying causes behind the lackluster performance observed in the Li-S system.

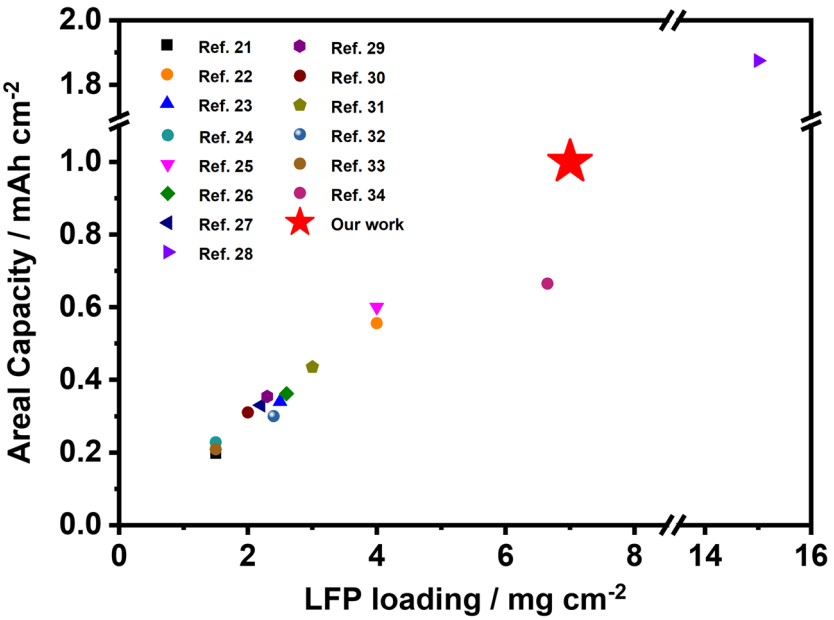

Figure A.4.5. Comparison of GPE_20 performance in LFP-based LMBs with recent relevant publications (until 2021) [22–35] in areal capacity vs LFP loading at RT.

A.5. Supplementary information Chapter V

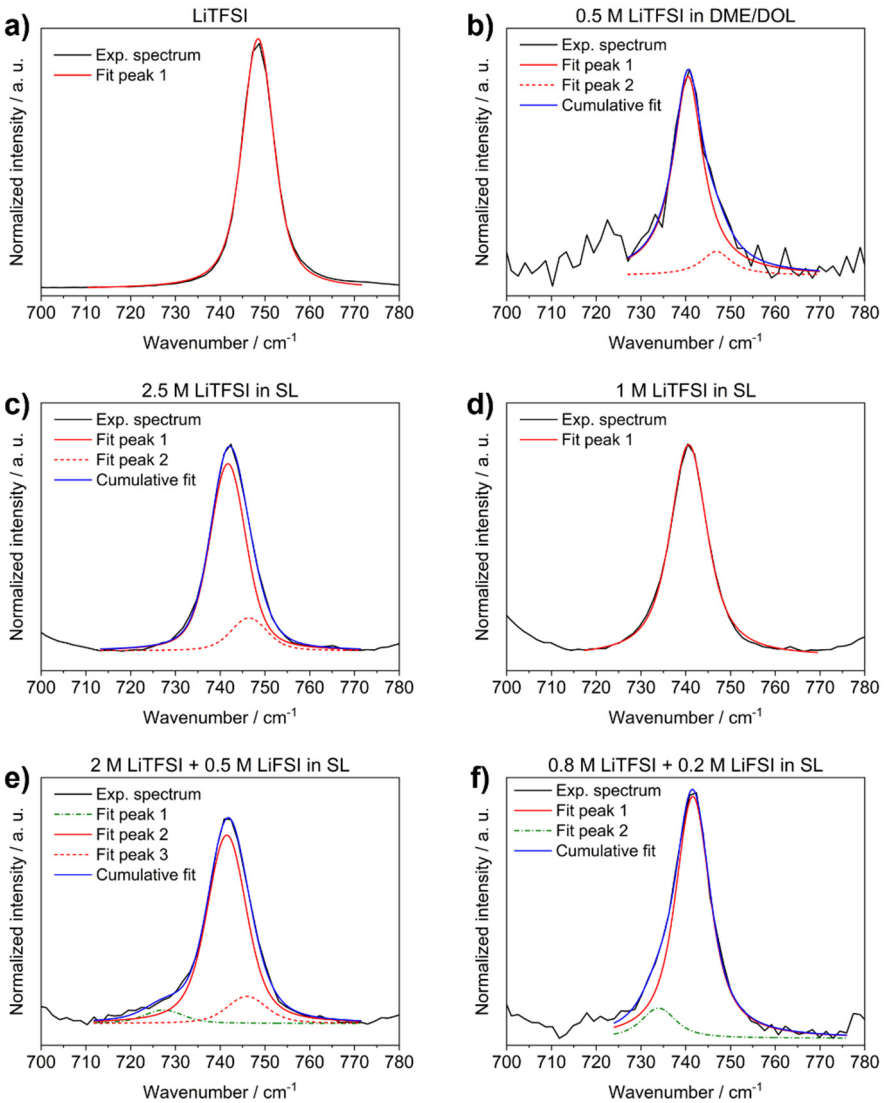

Figure A.5.1. Cumulative and individual fits of the Raman spectra in the region between 700-780 cm^{-1} of the different analyzed electrolytes.

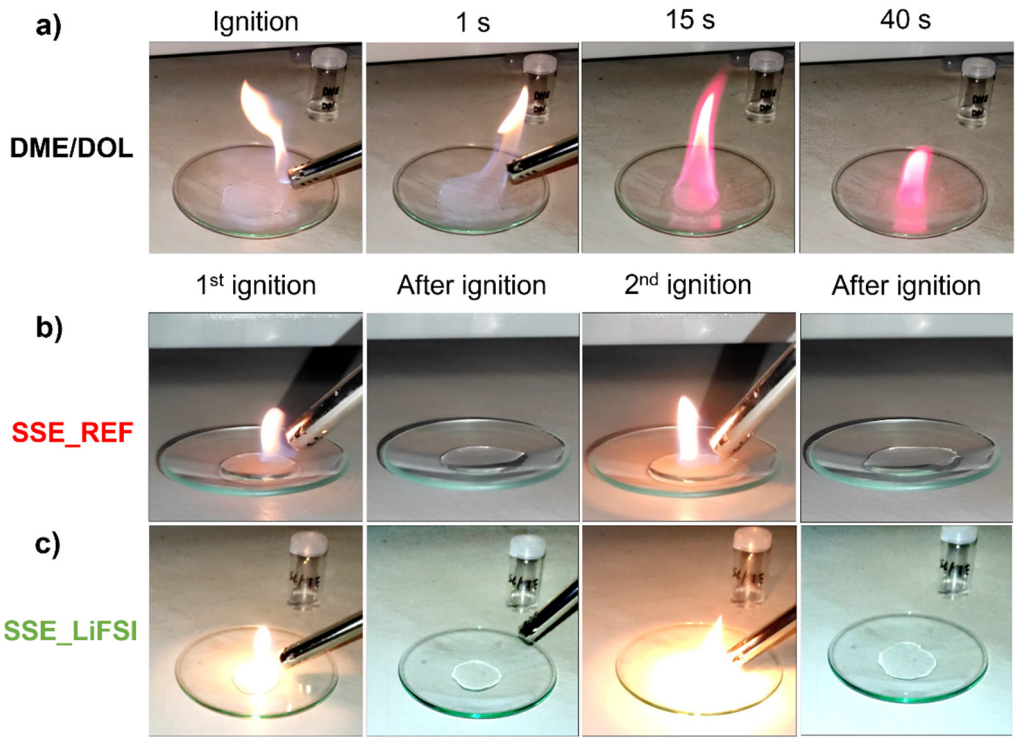

Figure A.5.2. Digital photos of the flammability test carried out to determine the SET value of the **a)** DME/DOL, **b)** SSE_REF, and **c)** SSE_LiFSI electrolytes.

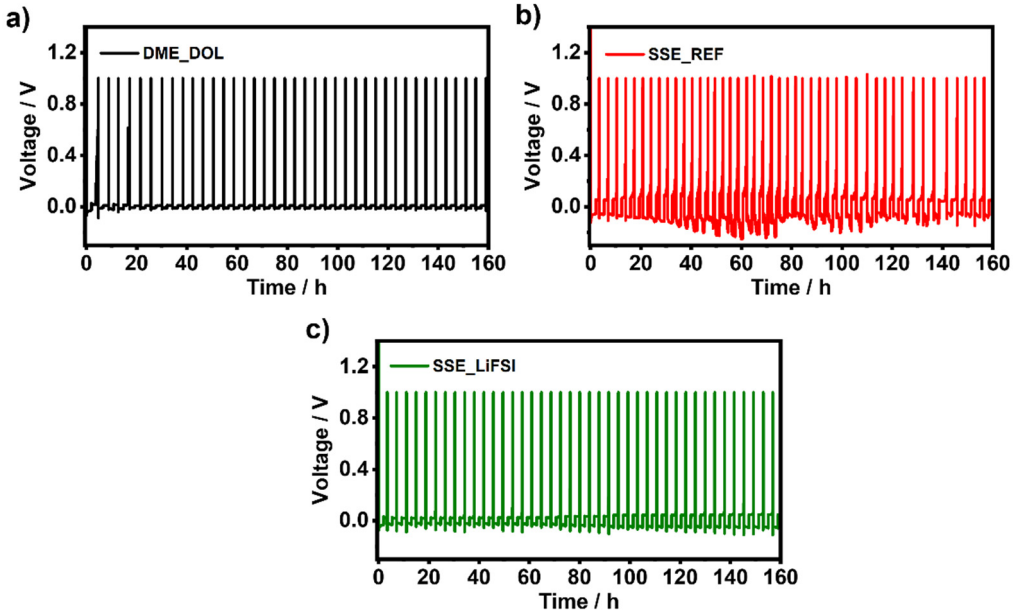

Figure A.5.3. Cycling performance profiles of the Li||Cu cells using **a)** DME/DOL, **b)** SSE_REF, and **c)** SSE_LiFSI electrolytes.

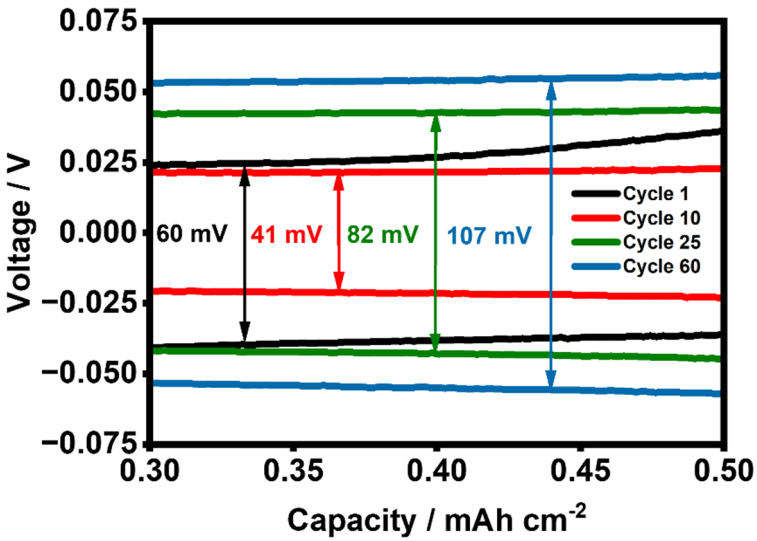

Figure A.5.4. Zoomed polarization of SSE_LiFSI during the Li plating and stripping in Li||Cu cells.

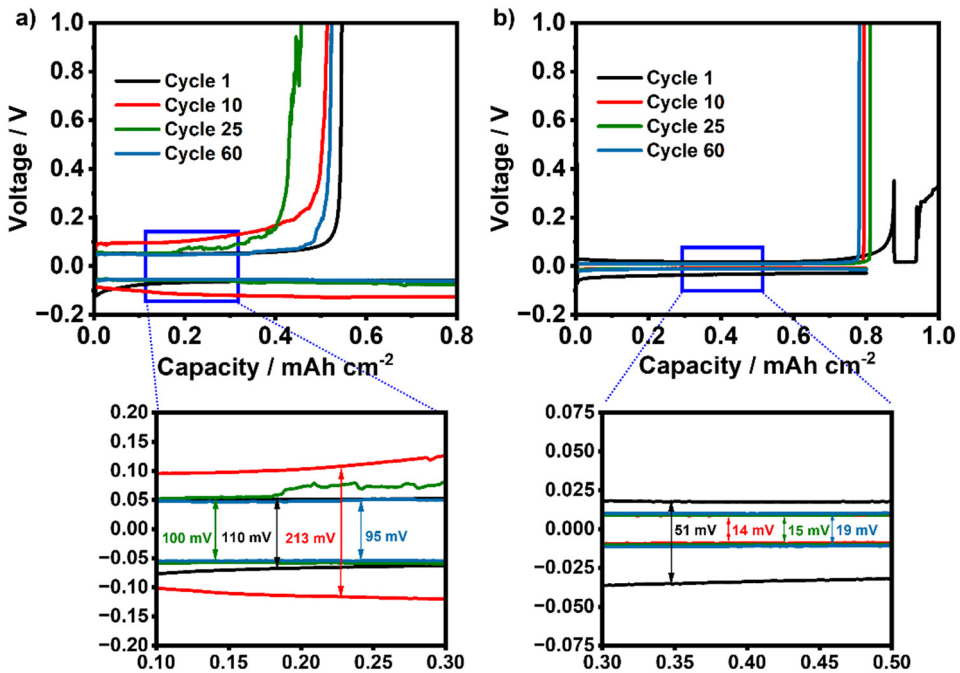

Figure A.5.5. Polarization of Li metal during plating and stripping in **a)** SSE_REF and **b)** DME/DOL electrolytes.

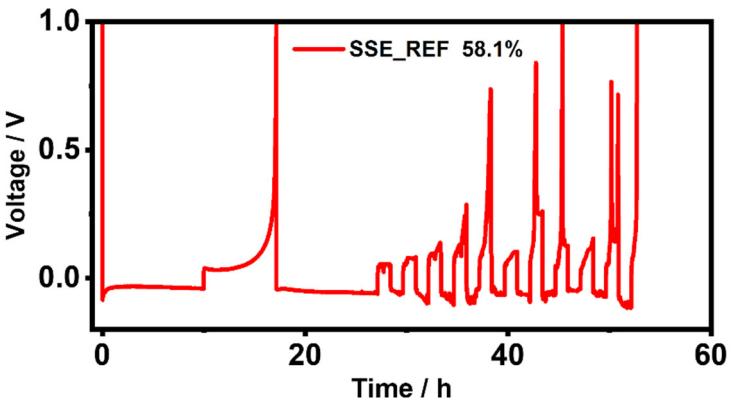

Figure A.5.6. Cycling performance and the obtained CE of the SSE_REF using the Aurbach modified method.

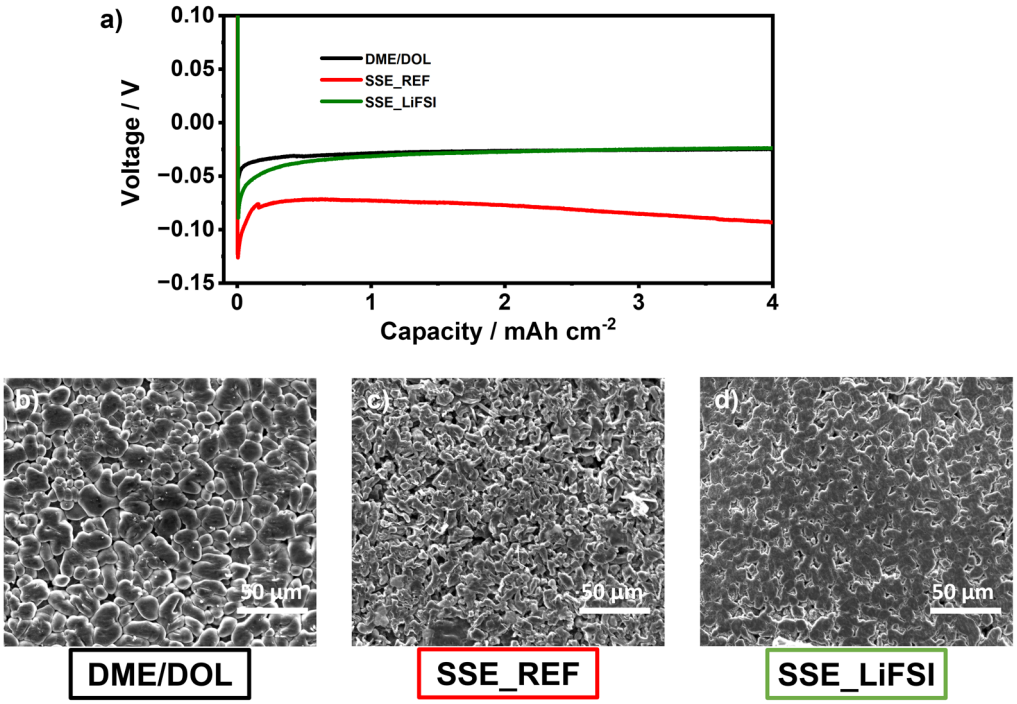

Figure A.5.7. **a)** Voltage-capacity curves of the first lithium deposition using the studied electrolytes. SEM images under lower magnifications of **b)** DME/DOL, **c)** SSE_REF, and **d)** SSE_LiFSI electrolytes.

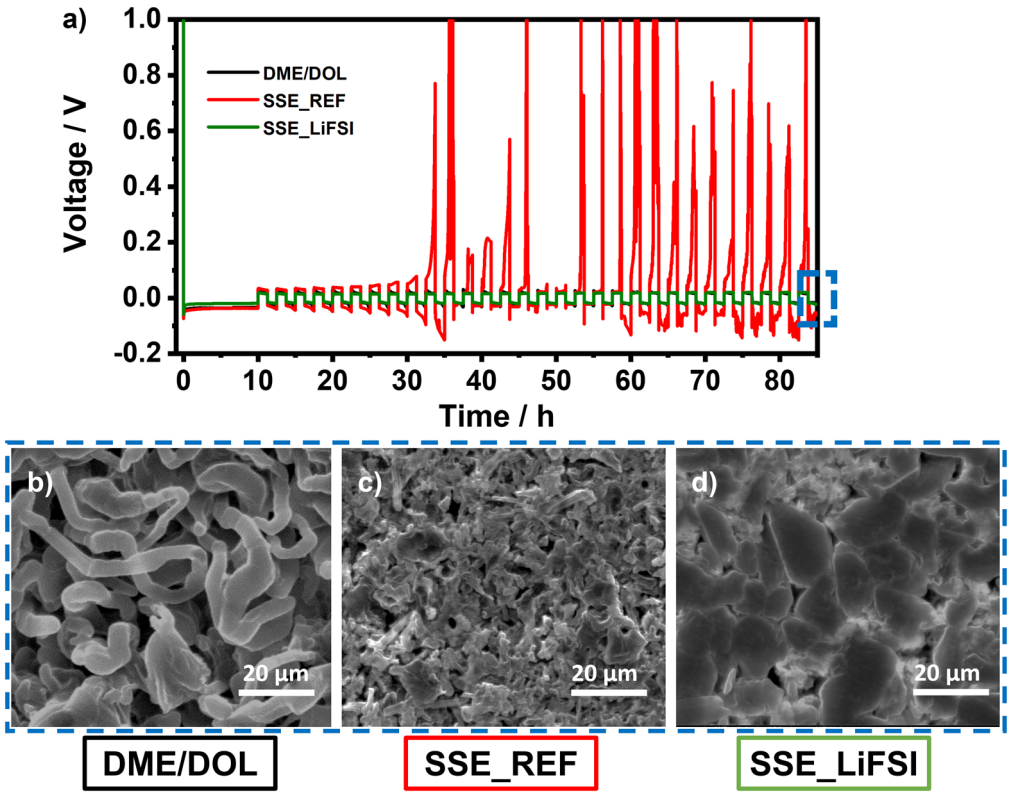

Figure A.5.8. a) Long cycling Li plating and stripping in Li||Cu cells at 0.5 mA cm^{-2} using the prepared electrolytes. SEM images of the lithium deposition after 30 cycles (depicted within the dashed blue square) of **b)** DME/DOL, **c)** SSE_REF, and d) SSE_LiFSI electrolytes.

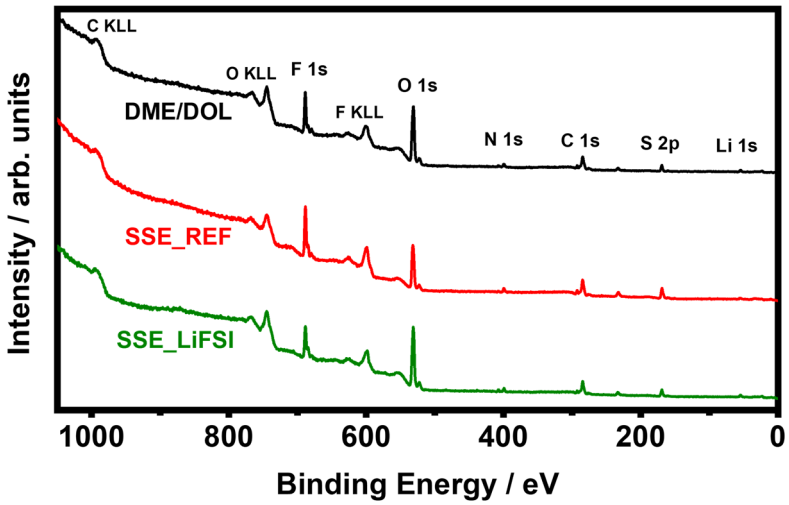

Figure A.5.9. The full XPS spectra of the different lithium deposition on Cu substrates in different electrolytes.

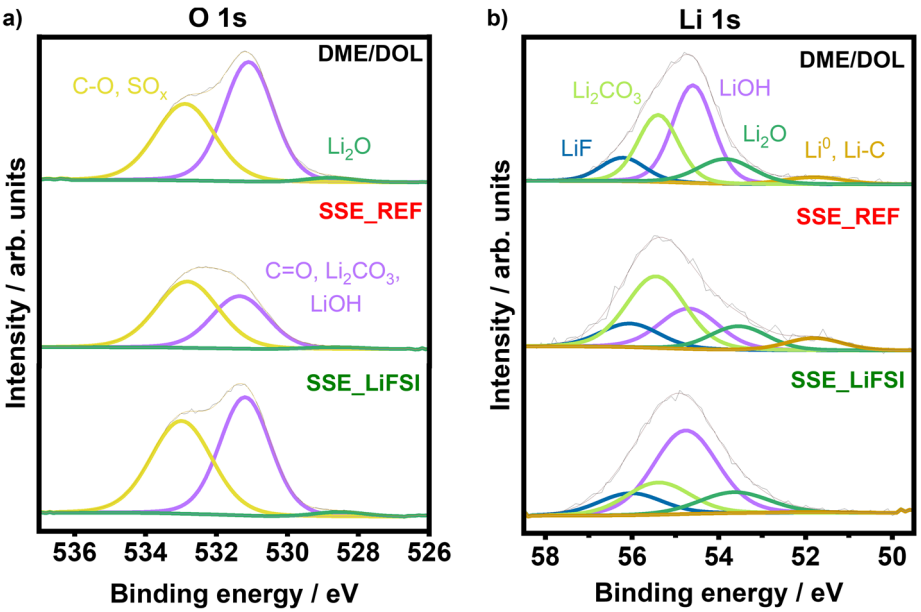

Figure A.5.10. High-resolution XPS spectra of **a)** O 1s and **b)** Li 1s on the lithium deposition on Cu substrate with different electrolytes.

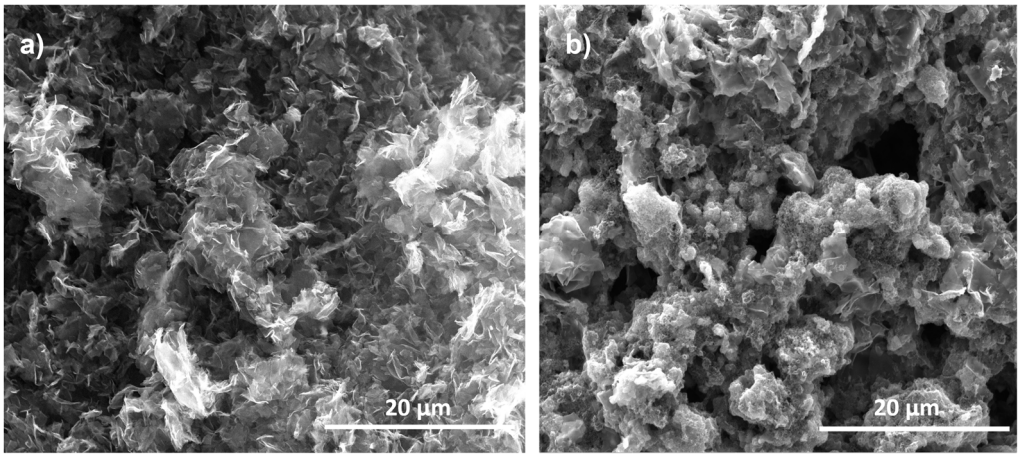

Figure A.5.11. The structural and morphological structure of the **a)** ResFArGO 2D graphene-based carbon material and **b)** its corresponding sulfur cathode.

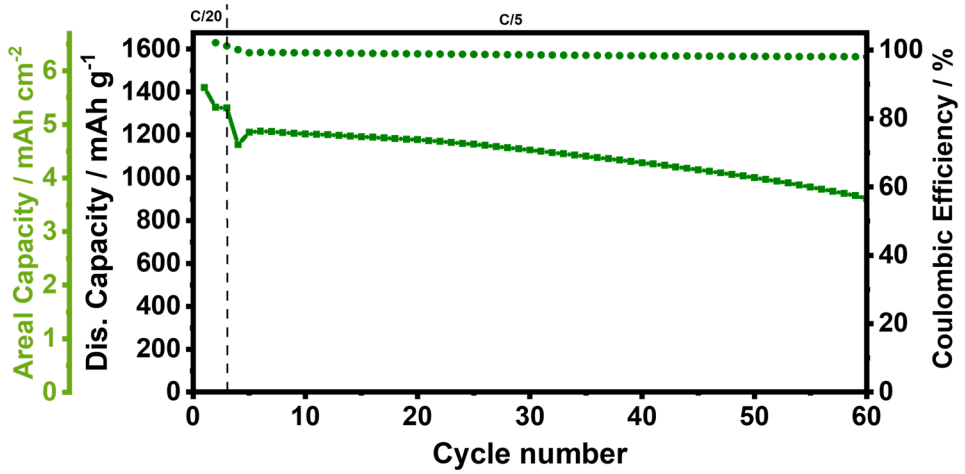

Figure A.5.12. Long cycling performance of high sulfur loading LSB using SSE_LiFSI electrolyte at C/5.

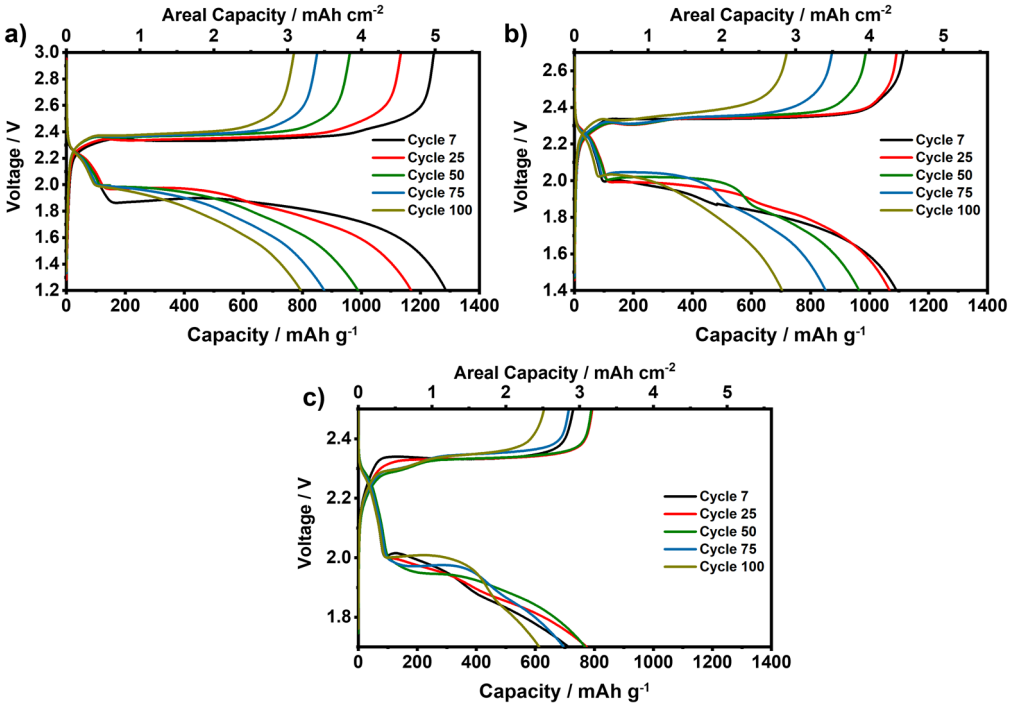

Figure A.5.13. Voltage profiles of the high sulfur loading LSBs using SSE_LiFSI electrolyte under different cut-off voltage: **a)** 1.2-3.0 V, **b)** 1.4-2.7 V, and **c)** 1.7-2.5 V.

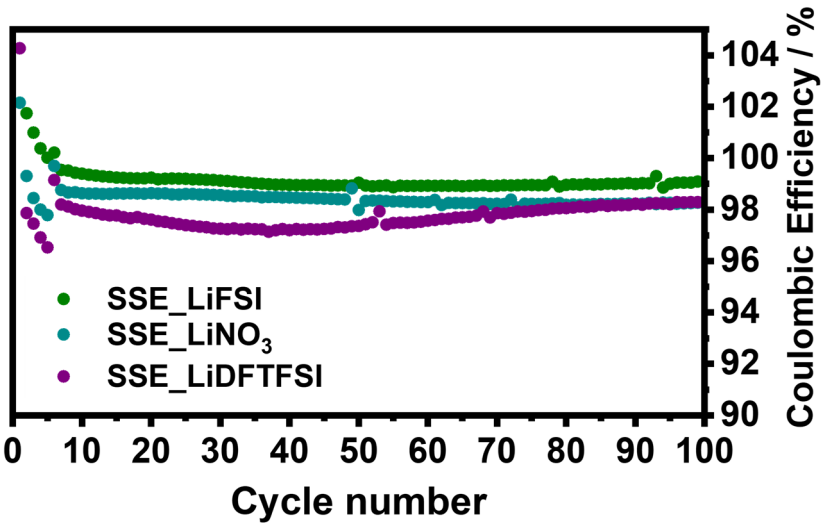

Figure A.5.14. CE comparison between SSE_LiFSI, SSE_$LiNO_3$, and SSE_LiDFTFSI electrolytes.

Table A.5.1. The atomic contents of the different elements present on the surface of the lithium depositions on the Cu substrate using different electrolytes.

Elements	Li	O	C	F	N	S
DME/DOL	33.2%	29.0%	20.6%	11.4%	2.7%	3.1%
SSE_REF	22.3%	23.8%	28.7%	16.3%	2.0%	6.9%
SSE_LiFSI	31.4%	31.2%	19.8%	10.4%	3.4%	3.8%

A.6. Supplementary information Chapter VI

MATLAB code for gravimetric energy density calculations of liquid electrolyte-based LSBs

```
% This function houses the calculations for estimating the energy density of liquid electrolyte Li-S batteries

Function Eg=GravimetricEnergy(rNP,Ls,Cg,Aanode,Csp_Li,Acathode,ws,Acc_cath,ncath,tAl,dAl,Asep,nds,Lsep,rES,dE,Unom)

mLi= rNP*(Ls*10^-3)*Cg*(Aanode/Csp_Li); % Total mass of the lithium metal anode in the cell (g)

mcath=(Acathode*Ls*10^-3)/ws;  % Total mass of the cathode (g)

mcc_cath=Acc_cath*ncath*tAl*dAl; % Total mass of the cathode current collector (g)

msep=Asep*nds*ncath*Lsep;   % Total mass of the separator (g)

mLE=Acathode*(Ls*10^-3)*rES*dLE; % Total mass of the electrolyte (g)

mtot=mLi+mcath+mcc_cath+msep+mLE; % Total mass of the overall cell(g)

Cnom=Cg*(Ls*10^-3)*Acathode; % Nominal capacity of the cell (Ah)

Eg=Cnom*Unom/(mtot*10^-3);  % Gravimetric energy density (Wh kg^-1)

end

% Evaluation of the impact of the N/P ratio and the E/S ratio on the energy density of Li-S cell

function varargout=Energy_Density_Estimation_Liq_IWS_analisisparameters_rNP_vs_rES(varargin)

if nargin==0

clc,close;

% General parameters

Cs_theo=1675*10^-3; % Theoretical capacity of sulfur as active material (in Ah g-1)

uS=0.75;    % Sulfur utilization rate (adimensional)

Unom=2.133; % Nominal voltage of the cell (V)

ncath=4;     % Number of double-side coated cathodes
```

```
A1cath=20.25;    % Surface of one cathode side (cm^2)

Acc_cath=20.7;  % Total surface of one cathode current collector side
(cm^2)

tAl=18*10^-4;      % thickness of the aluminum current collector (um)

dAl=2.7;      % Density of the aluminum cathode current collector (g
cm^-3)

Ls=4;       % Loading of sulfur of the cathode (gs cm^-2),

ws=0.64;    % Sulfur content in the cathode (adimensional)

wc=0.26;     % Carbon content in the cathode (adimensional)

wb=0.1;      % Binder (CMC + SBR) content in the cathode

ds=2;        % Density of sulfur (g cm^-3)

dc=0.12;     % Density of the carbon material (represented by KJ600,
in this case)(g cm^-3)

db=1.5;      % Density of the binder (g cm^-3)

dLi=0.534;  % Density of lithium (g cm^-3)

Csp_Li=3860*10^-3; % Theoretical capacity of lithium (Ah g-1)

rNP_vec=0:1:10;    % N/P ratio // In this case, a vector is created to
analyze the effect of the N/P ratio on the energy density

rES_vec=0.5:0.1:10;      % E/S ratio, (ml gs^-1)// As in the case of
N/P ratio, a vector is created to analyze the effect of E/S ratio in
the energy density

dLE=1.1;    % Electrolyte density (g cm^-3)

Asep=30.08; % Celgard separator sheet surface (cm^2)

Lsep=1.48*10^-3;  % Areal density of separator material (g cm^-2)

tsep=25*10^-4;  % Thickness of the separator (cm)

nds=2;         % This parameter was created to indicate whether the
analyzed cell is monolayer or multilayer, being 1 for the first case
and 2 for the second.

nanode=5;     % Number of lithium metal anodes


else

Unom=varargin{1};ncath=varargin{2};A1cath=varargin{3};Acc_cath=vararg
in{4};tAl=varargin{5};dAl=varargin{6};ws=varargin{7};wc=varargin{8};w
```

```
b=varargin{9};ds=varargin{10};dc=varargin{11};db=varargin{12};dLi=var
argin{13};Csp_Li=varargin{14};rNP_vec=varargin{15};rES_vec=varargin{1
6};dLE=varargin{17};Asep=varargin{18};Lsep=varargin{19};tsep=varargin
{20};esep=varargin{21};nds=varargin{22};nanode=varargin{23};Ls=vararg
in{24};

end

Acathode=nds*A1cath*ncath;  % Total surface of the cathode (cm^2)

Aanode=Acathode;     % Total surface of the anode is equal to the total
surface of the cathode (cm^2)

Cg=Cs_theo*uS; % The specific capacity of the cell linked to the sulfur
utilization parameter

Eg=ones(length(rES_vec),length(rNP_vec));

LIBg=ones(length(rES_vec),1)*250;  % Gravimetrix Energy density of
commercial LIBs

for i=1:length(rES_vec)

  rES=rES_vec(i); % E/S ratio of the cell (ml gs^-1)

    for j=1:length(rNP_vec)

        rNP=rNP_vec(j); % N/P ratio of the cell

Eg(i,j)=GravimetricEnergy(rNP,Ls,Cg,Aanode,Csp_Li,Acathode,ws,Acc_cat
h,ncath,tAl,dAl,Asep,nds,Lsep,rES,dLE,Unom);    %Gravimetric    energy
density (Wh kg^-1)

    end

end
```

A.6.1 Charge/discharge profiles of the DME/DOL-based monolayer pouch cells

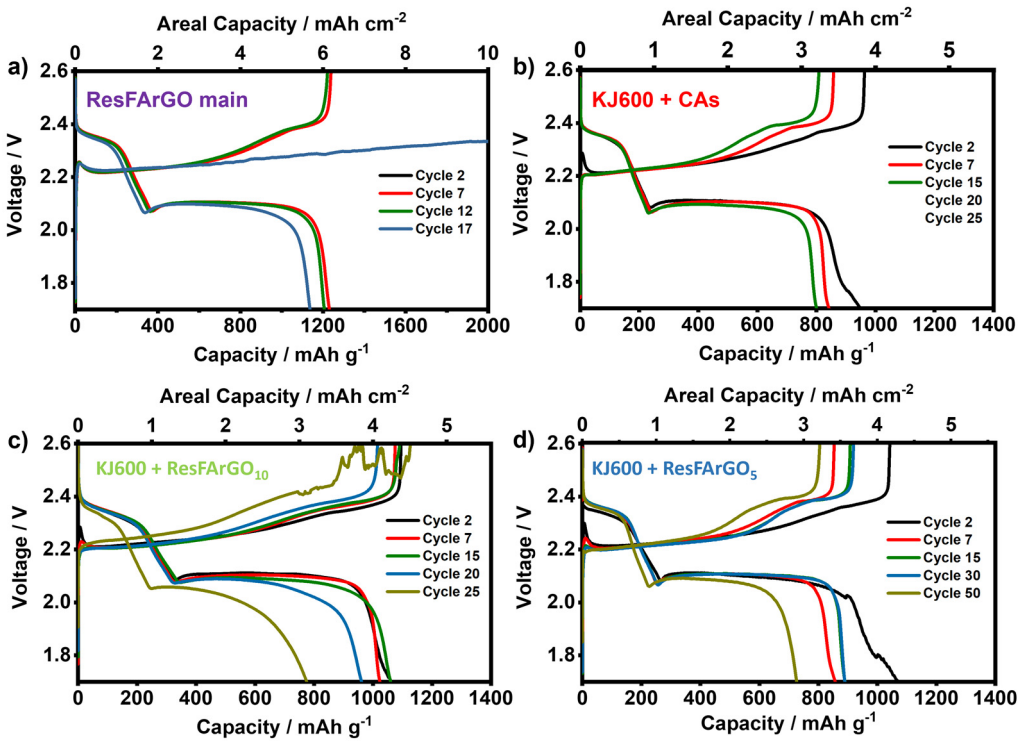

Figure A.6.1. Charge/discharge profiles of the monolayer pouch cells based on the different strategies developed in previous chapters: **a)** ResFArGO as main carbon, **b)** KJ600 + CAs, **c)** KJ600 + ResFArGO$_{10}$, and **d)** KJ600 + ResFArGO$_5$.

A.6.2 Charge/discharge profiles of the SSE_LiFSI-based monolayer pouch cell

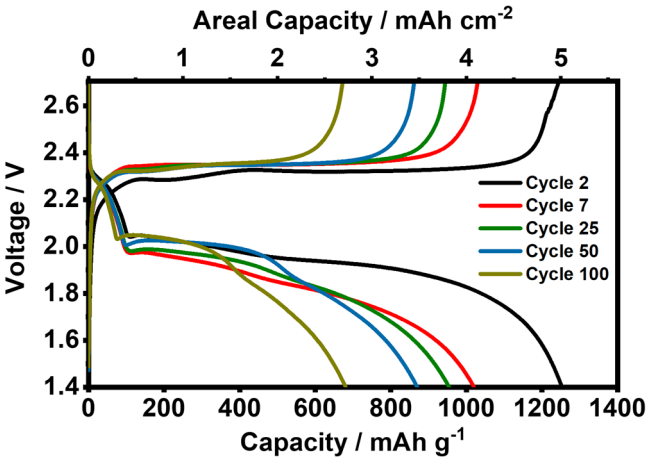

Figure A.6.2. Charge/discharge profiles of the SSE_LiFSI-based monolayer pouch cell.

A.6.3 Post-mortem analysis of disassembled DME/DOL employing prototype cell

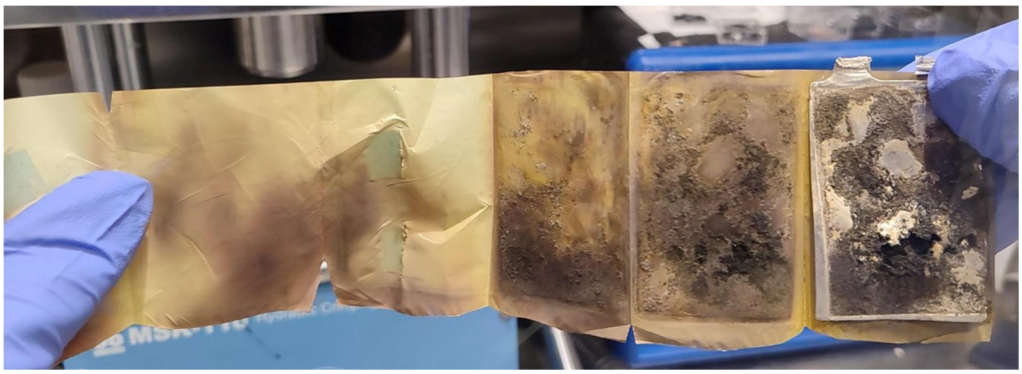

Figure A.6.3. Complete DME/DOL prototype cell status after being disassembled.

A.6.4 Post-mortem analysis of disassembled SSE_LiFSI employing prototype cell

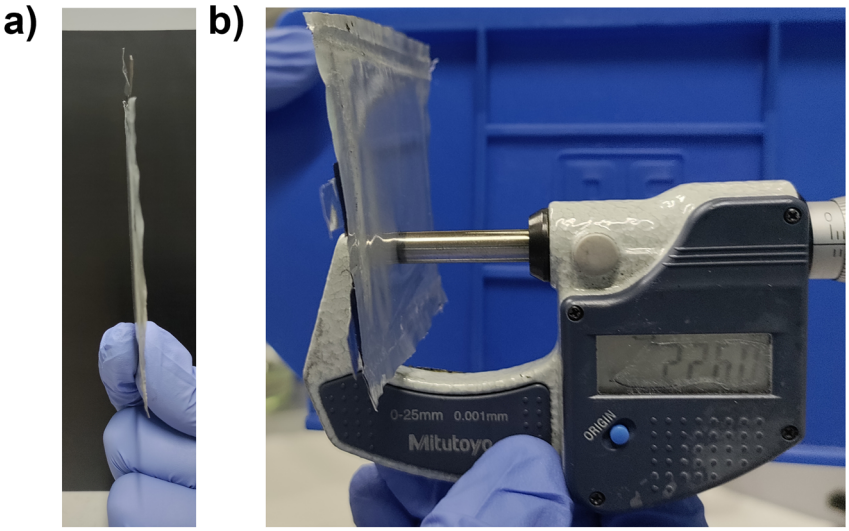

Figure A.6.4. **a)** Cross-section optical image of the SSE_LiFSI-based prototype cell after cycling and **b)** its corresponding cell thickness, corroborating the absence of gas generation.

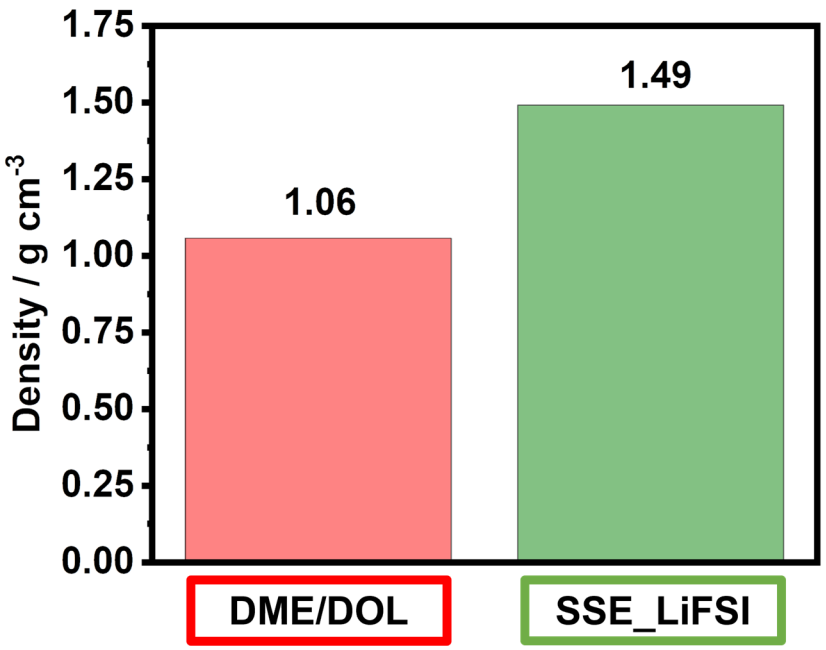

Figure A.6.5. Density comparison between DME/DOL and SSE_LiFSI electrolytes.

Table A.6.1. *Definition of working parameters for the calculations of gravimetric energy density*

Parameter		Value	Unit
Positive electrode	Theoretical capacity of sulfur (C_{S_theo})	1.675	Ah g^{-1}
	Sulfur loading (L_S)	4×10^{-3}	g_S cm^{-2}
	Sulfur utilization rate (μ_S)	0.75	-
	Nominal voltage of the cell (U_{nom})	2.10	V
	Number of double-side cathodes (n_{cath})	4	-
	Area of one cathode coating (A_{1cath})	20.25	cm^2
	Area of one cathode current collector (A_{cc_cath})	20.70	cm^2
	Thickness of the cathode current collector (t_{Al})	18×10^{-4}	cm
	Density of the aluminum current collector (ρ_{Al})	2.7	g cm^{-3}
	Sulfur content in the cathode (ω_S)	0.64	-
	Carbon content in the cathode (ω_C)	0.26	-
	Binder content in the cathode (ω_b)	0.1	-
	Density of sulfur (ρ_S)	2.0	g cm^{-3}
	Density of the carbon material (ρ_C)	0.12	g cm^{-3}
	Density of the binder (ρ_b)	1.5	g cm^{-3}
Electrolyte	E/S ratio (r_{ES})	3	µL mg_S^{-1}
	Density of the liquid electrolyte (ρ_{LE})	1.1	g cm^{-3}
	Area of 1 sheet of separator (A_{sep})	30.1	cm^2
	Areal density of separator material (L_{sep})	1.48×10^{-3}	g cm^{-2}
	Thickness of the separator (t_{sep})	25×10^{-4}	cm
Negative electrode	Theoretical capacity of lithium (C_{Li_theo})	3.860	Ah g^{-1}
	N/P ratio (r_{NP})	3	-
	Density of lithium (ρ_{Li})	0.534	g cm^{-3}

A.7. Bibliography

[1] H.J.C. Berendsen, D. van der Spoel, R. van Drunen, GROMACS: A message-passing parallel molecular dynamics implementation, Comput. Phys. Commun. 1995, 91, 43–56. https://doi.org/10.1016/0010-4655(95)00042-E.

[2] D. Van Der Spoel, E. Lindahl, B. Hess, G. Groenhof, A.E. Mark, H.J.C. Berendsen, GROMACS: Fast, flexible, and free, J. Comput. Chem. 2005, 26, 1701–1718. https://doi.org/10.1002/jcc.20291.

[3] M.J. Abraham, T. Murtola, R. Schulz, S. Páll, J.C. Smith, B. Hess, E. Lindah, Gromacs: High performance molecular simulations through multi-level parallelism from laptops to supercomputers, SoftwareX. 2015, 1–2, 19–25. https://doi.org/10.1016/j.softx.2015.06.001.

[4] G.A. Kaminski, R.A. Friesner, J. Tirado-rives, W.L. Jorgensen, Comparison with accurate quantum chemical calculations on peptides, Quantum. 2021, 2, 6474–6487.

[5] W.L. Jorgensen, D.S. Maxwell, J. Tirado-Rives, Development and testing of the OPLS all-atom force field on conformational energetics and properties of organic liquids, J. Am. Chem. Soc. 1996, 118, 11225–11236. https://doi.org/10.1021/ja9621760.

[6] W.L. Jorgensen, J. Tirado-Rives, The OPLS [optimized potentials for liquid simulations] potential functions for proteins, energy minimizations for crystals of cyclic peptides and crambin, J. Am. Chem. Soc. 1998, 110, 1657–1666. https://doi.org/10.1021/ja00214a001.

[7] C. Lee, W. Yang, R.G. Parr, Development of the Colle-Salvetti correlation-energy formula into a functional of the electron density, Phys. Rev. B. 1988, 37, 785–789. https://doi.org/10.1103/PhysRevB.37.785.

[8] A.D. Becke, Density-functional thermochemistry. III. The role of exact exchange, J. Chem. Phys. 1993, 98, 5648–5652. https://doi.org/10.1063/1.464913.

[9] R. Ditchfield, W.J. Hehre, J.A. Pople, Self-consistent molecular-orbital methods. IX. An extended gaussian-type basis for molecular-orbital studies of organic molecules, J. Chem. Phys. 1971, 54, 724–728. https://doi.org/10.1063/1.1674902.

[10] W.J. Hehre, K. Ditchfield, J.A. Pople, Self-consistent molecular orbital methods. XII. Further extensions of gaussian-type basis sets for use in molecular orbital studies of organic molecules, J. Chem. Phys. 1972, 56, 2257–2261. https://doi.org/10.1063/1.1677527.

[11] P.C. Hariharan, J.A. Pople, The influence of polarization functions on molecular orbital hydrogenation energies, Theor. Chim. Acta 1973, 28, 213–222. https://doi.org/10.1007/BF00533485.

[12] P.C. Hariharan, J.A. Pople, Accuracy of AH n equilibrium geometries by single determinant molecular orbital theory, Mol. Phys. 1974, 27, 209–214. https://doi.org/10.1080/00268977400100171.

[13] M.M. Francl, W.J. Pietro, W.J. Hehre, J.S. Binkley, M.S. Gordon, D.J. DeFrees, J.A. Pople, Self-consistent molecular orbital methods. XXIII. A polarization-type basis set for second-row elements, J. Chem. Phys. 1982, 77, 3654–3665. https://doi.org/10.1063/1.444267.

[14] P. Sinha, A. Datar, C. Jeong, X. Deng, Y.G. Chung, L.C. Lin, Surface area determination of porous materials using the Brunauer-Emmett-Teller (BET) method: Limitations and improvements, J. Phys. Chem. C. 2019, 123, 20195–20209. https://doi.org/10.1021/acs.jpcc.9b02116.

[15] M. Sethi, H. Bantawal, U.S. Shenoy, D.K. Bhat, Eco-friendly synthesis of porous graphene and its utilization as high performance supercapacitor electrode material, J. Alloys Compd. 2019, 799, 256–266. https://doi.org/10.1016/j.jallcom.2019.05.302.

[16] J. Bin Wu, M.L. Lin, X. Cong, H.N. Liu, P.H. Tan, Raman spectroscopy of graphene-based materials and its applications in related devices, Chem. Soc. Rev. 2018, 47, 1822–1873. https://doi.org/10.1039/c6cs00915h.

[17] M. Watanabe, S. Nagano, K. Sanui, N. Ogata, Estimation of Li^+ transport number in polymer electrolytes by the combination of complex impedance and potentiostatic polarization measurements, Solid State Ion. 1988, 28-30, 911–917.

[18] J. Evans, C.A. Vincent, P.G. Bruce, Electrochemical measurement of transference numbers in polymer electrolytes, Polym. 1987, 28, 2324–2328. https://doi.org/10.1016/0032-3861(87)90394-6.

[19] B.D. Adams, J. Zheng, X. Ren, W. Xu, J.G. Zhang, Accurate determination of Coulombic efficiency for lithium metal anodes and lithium metal batteries, Adv. Energy Mater. 2018, 8, 1702097. https://doi.org/10.1002/aenm.201702097.

[20] D. Aurbach, E. Granot, The study of electrolyte solutions based on solvents from the “glyme” family (linear polyethers) for secondary Li battery systems, Electrochim. Acta 1997, 42, 697–718. https://doi.org/10.1016/S0013-4686(96)00231-9.

[21] J. Castillo, A. Santiago, X. Judez, J.A. Coca-Clemente, A. Saenz de Buruaga, J.L. Gomez-Urbano, J. González-Marcos, M. Armand, C. Li, D. Carriazo, High energy density lithium–sulfur batteries based on carbonaceous two-dimensional additive cathodes, ACS Appl. Energy Mater. 2023, 6, 3579–3589. https://doi.org/10.1021/acsaem.3c00177.

[22] W. Fan, X. Zhang, C. Li, S. Zhao, J. Wang, UV-Initiated Soft-Tough Multifunctional gel polymer electrolyte achieves stable-cycling Li-metal battery, ACS Appl. Energy Mater. 2019, 2, 4513–4520. https://doi.org/10.1021/acsaem.9b00766.

[23] R. Liu, Z. Wu, P. He, H. Fan, Z. Huang, L. Zhang, X. Chang, H. Liu, C. an Wang, Y. Li, A self-standing, UV-cured semi-interpenetrating polymer network reinforced composite gel electrolytes for dendrite-suppressing lithium ion batteries, J. Mater. 2019, 5, 185–194. https://doi.org/10.1016/j.jmat.2018.12.006.

[24] L. Balo, H. Gupta, S.K. Singh, V.K. Singh, A.K. Tripathi, N. Srivastava, R.K. Tiwari, R. Mishra, D. Meghnani, R.K. Singh, Development of gel polymer electrolyte based on LiTFSI and EMIMFSI for application in rechargeable lithium metal battery with GO-LFP and NCA cathodes, J. Solid State Electrochem. 2019, 23, 2507–2518. https://doi.org/10.1007/s10008-019-04321-6.

[25] X. Zhao, C. an Tao, Y. Li, X. Chen, J. Wang, H. Gong, Preparation of gel polymer electrolyte with high lithium ion transference number using GO as filler and application in lithium battery, Ionics 2020, 26, 4299–4309. https://doi.org/10.1007/s11581-020-03628-z.

[26] S.Z. Zhang, X.H. Xia, D. Xie, R.C. Xu, Y.J. Xu, Y. Xia, J.B. Wu, Z.J. Yao, X.L. Wang, J.P. Tu, Facile interfacial modification via in-situ ultraviolet solidified gel polymer electrolyte for high-performance solid-state lithium ion batteries, J. Power Sources 2019, 409, 31–37. https://doi.org/10.1016/j.jpowsour.2018.10.088.

[27] M. Ravi, S. Kim, F. Ran, D.S. Kim, Y.M. Lee, M.H. Ryou, Hybrid gel polymer electrolyte based on 1-methyl-1-Propylpyrrolidinium Bis(Trifluoromethanesulfonyl) imide for flexible and shape-variant lithium secondary batteries, J. Memb. Sci. 2021, 621, 119018. https://doi.org/10.1016/j.memsci.2020.119018.

[28] H. Fan, C. Yang, X. Wang, L. Liu, Z. Wu, J. Luo, R. Liu, UV-curable PVdF-HFP-based gel electrolytes with semi-interpenetrating polymer network for dendrite-free Lithium metal batteries, J. Electroanal. Chem. 2020, 871, 114308. https://doi.org/10.1016/j.jelechem.2020.114308.

[29] J. Jie, Y. Liu, L. Cong, B. Zhang, W. Lu, X. Zhang, J. Liu, H. Xie, L. Sun, High-performance PVDF-HFP based gel polymer electrolyte with a safe solvent in Li metal

polymer battery, J. Energy Chem. 2020, 49, 80–88. https://doi.org/10.1016/j.jechem.2020.01.019.

[30] Y. Tong, Y. Xu, D. Chen, Y. Xie, L. Chen, M. Que, Y. Hou, Deformable and flexible electrospun nanofiber-supported cross-linked gel polymer electrolyte membranes for high safety lithium-ion batteries, RSC Adv. 2017, 7, 22728–22734. https://doi.org/10.1039/c7ra00112f.

[31] D. Shao, X. Wang, X. Li, K. Luo, L. Yang, L. Liu, H. Liu, Internal in situ gel polymer electrolytes for high-performance quasi-solid-state lithium ion batteries, J. Solid State Electrochem. 2019, 23, 2785–2792. https://doi.org/10.1007/s10008-019-04382-7.

[32] S. Li, N. Li, C. Sun, A flexible three-dimensional composite nanofiber enhanced quasi-solid electrolyte for high-performance lithium metal batteries, Inorg. Chem. Front. 2021, 8, 361–367. https://doi.org/10.1039/d0qi01159b.

[33] J. Chen, Z. Yang, G. Liu, C. Li, J. Yi, M. Fan, H. Tan, Z. Lu, C. Yang, Reinforcing concentrated phosphate electrolytes with in-situ polymerized skeletons for robust quasi-solid lithium metal batteries, Energy Storage Mater. 2020, 25, 305–312. https://doi.org/10.1016/j.ensm.2019.10.008.

[34] X. Pan, T. Liu, D.J. Kautz, L. Mu, C. Tian, T.E. Long, P. Yang, F. Lin, High-performance N-methyl-N-propylpiperidinium bis(trifluoromethanesulfonyl)imide/poly(vinylidene fluoride-hexafluoropropylene) gel polymer electrolytes for lithium metal batteries, J. Power Sources 2018, 403, 127–136. https://doi.org/10.1016/j.jpowsour.2018.09.080.

[35] G. Zhou, X. Lin, J. Liu, J. Yu, J. Wu, H.M. Law, Z. Wang, F. Ciucci, In situ formation of poly(butyl acrylate)-based non-flammable elastic quasi-solid electrolyte for dendrite-free flexible lithium metal batteries with long cycle life for wearable devices, Energy Storage Mater. 2021, 34, 629–639. https://doi.org/10.1016/j.ensm.2020.10.012.

LIST OF CONTRIBUTIONS

Publications

The following articles were published in indexed in Q1 journals during this PhD work.

[1] A. Santiago, A. Robles-Fernández, A. Soria-Fernández, J. L. Lopez-Morales, **J. Castillo**, D. Fraile-Insagurbe, N. Casado, M. Armand, E. J. Garcia-Suarez, and D. Carriazo, Polymeric ionic liquid as binder: A promising strategy for enhancing Li-S battery performance, J. Energy Storage, 2024, 80, 110285. https://doi.org/10.1016/j.est.2023.110285.

[2] **J. Castillo**, A. Soria-Fernández, S. Rodriguez-Peña, J. Rikarte, A. Robles-Fernández, I. Aldalur, R. Cid, J.A. González-Marcos, J. Carrasco, M. Armand, A. Santiago, D. Carriazo, Graphene-based sulfur cathodes and dual salt-based sparingly solvating electrolytes: A perfect marriage for high performing, safe, and long cycle life lithium-sulfur prototype batteries, Adv. Energy Mater. 2023, 14, 2302378. https://doi.org/10.1002/aenm.202302378.

[3] **J. Castillo**, A. Robles-Fernandez, R. Cid, J.A. González-Marcos, M. Armand, D. Carriazo, H. Zhang, A. Santiago, Dehydrofluorination process of poly(vinylidene difluoride) PVdF-based gel polymer electrolytes and its effect on lithium-sulfur batteries, Gels 2023, 9, 336. https://doi.org/10.3390/gels9040336.

[4] **J. Castillo**, A. Santiago, X. Judez, J.A. Coca-Clemente, A. Saenz de Buruaga, J.L. Gómez-Urbano, J.A. González-Marcos, M. Armand, C. Li, D. Carriazo, High energy density lithium-sulfur batteries based on carbonaceous two-dimensional additive cathodes, ACS Appl. Energy Mater. 2023, 6, 3579–3589. https://doi.org/10.1021/acsaem.3c00177.

[5] L. Fernandez-Diaz, **J. Castillo**, E. Sasieta-Barrutia, M. Arnaiz, M. Cabello, X. Judez, A. Terry, L. Otaegui, M.C. Morant-Miñana, A. Villaverde, Mixing methods for solid state electrodes: Techniques, fundamentals, recent advances, and perspectives, Chem. Eng. J. 2023, 464, 142469. https://doi.org/10.1016/j.cej.2023.142469.

[6] **J. Castillo**, J.A. Coca-Clemente, J. Rikarte, A. Sáenz De Buruaga, A. Santiago, C. Li, Recent progress on lithium anode protection for lithium-sulfur batteries: Review and perspective, APL Mater. 2023, 11, 010901. https://doi.org/10.1063/5.0107648.

[7] G. Jiménez-Martín, **J. Castillo**, X. Judez, J.L. Gómez-Urbano, G. Moreno-Fernández, A. Santiago, A. Saenz de Buruaga, I. Garbayo, J.A. Coca-Clemente, A. Villaverde, M. Armand, C. Li, D. Carriazo, Graphene-based activated carbon composites for high performance lithium-sulfur batteries, Batter. Supercaps 2022, 5,

202200167. https://doi.org/10.1002/batt.202200167.

[8] **J. Castillo**, L. Qiao, A. Santiago, X. Judez, A.S. de Buruaga, G. Jimenez, M. Armand, H. Zhang, C. Li, Perspective of polymer-based solid-state Li-S batteries, Energy Mater. 2022, 2, 200003. https://doi.org/10.20517/energymater.2021.25.

[9] **J. Castillo**, A. Santiago, X. Judez, I. Garbayo, J.A. Coca Clemente, M.C. Morant-Miñana, A. Villaverde, J.A. González-Marcos, H. Zhang, M. Armand, C. Li, Safe, flexible, and high-performing gel-polymer electrolyte for rechargeable lithium metal batteries, Chem. Mater. 2021, 33, 8812–8821. https://doi.org/10.1021/acs.chemmater.1c02952.

[10] A. Santiago, **J. Castillo**, I. Garbayo, A. Saenz De Buruaga, J.A. Coca Clemente, L. Qiao, R. Cid Barreno, M. Martinez-Ibañez, M. Armand, H. Zhang, C. Li, Salt additives for improving cyclability of polymer-based all-solid-state lithium-sulfur batteries, ACS Appl. Energy Mater. 2021, 4, 4459–4464. https://doi.org/10.1021/acsaem.1c00091.

[11] I. Garbayo, A. Santiago, X. Judez, A.S. De Buruaga, **J. Castillo**, M.A. Muñoz-Márquez, Alumina Nanofilms As Active Barriers for polysulfides in high-performance all-solid-state lithium-sulfur batteries, ACS Appl. Energy Mater. 2021, 4, 2463–2470. https://doi.org/10.1021/acsaem.0c03032.

[12] A. Santiago, X. Judez, **J. Castillo**, I. Garbayo, A. Saénz De Buruaga, L. Qiao, G. Baraldi, J.A. Coca-Clemente, M. Armand, C. Li, H. Zhang, Improvement of lithium metal polymer batteries through a small dose of fluorinated salt, J. Phys. Chem. Lett. 2020, 11, 6133–6138. https://doi.org/10.1021/acs.jpclett.0c01883.

Patent

J. Castillo, D. Carriazo, M.A. Moreno-Fernández, X. Judez, J.L. Gómez-Urbano, C. Li, A. Villaverde, A. Santiago. P23141EP00, 2023.

Works presented at conferences

[1] **J. Castillo**, A. Santiago, X. Judez, I. Garbayo, J.A. Coca Clemente, M.C. J.A. González-Marcos, H. Zhang, M. Armand, C. Li, Safe Electrolytes for Lithium-Sulfur Batteries, Int. Conference on Lithium-Sulfur Batteries, 2021 (ICLSB) (Online).

[2] **J. Castillo**, A. Santiago, X. Judez, I. Garbayo, J.A. Coca Clemente, M.C. Morant-Miñana, A. Villaverde, J.A. González-Marcos, H. Zhang, M. Armand, C. Li, Safe, Flexible, and High-Performing Gel-Polymer Electrolyte for Rechargeable Lithium Metal Batteries, Advance Materials Science, 2022 (Online).

[3] **J. Castillo**, X. Judez, J.L. Gómez-Urbano, G. Moreno-Fernández, A. Santiago, A. Saenz de Buruaga, I. Garbayo, M. Armand, C. Li, D. Carriazo, Graphene-based Activated Carbon Composites for High Performance Lithium-Sulfur Batteries, Power of Future 2022 (POF). 2022. Vitoria-Gasteiz, Spain.

[4] **J. Castillo**, X. Judez, J.L. Gómez-Urbano, G. Moreno-Fernández, A. Santiago, A. Saenz de Buruaga, I. Garbayo, M. Armand, C. Li, D. Carriazo, High-Performing Lithium-Sulfur Cathode Development Through Rationally Incorporated Graphene-Derived Carbon Materials, Int. Conference on Lithium-Sulfur Batteries, 2022 (ICLSB) (Online).

[5] **J. Castillo**, X. Judez, J.L. Gómez-Urbano, G. Moreno-Fernández, A. Santiago, A. Saenz de Buruaga, I. Garbayo, M. Armand, C. Li, D. Carriazo, Graphene-based Activated Carbon Composites for High Performance Lithium-Sulfur Batteries, International Battery Association (IBA). 2022. Bled, Slovenia.

[6] A. Santiago, **J. Castillo**, X. Judez, I. Garbayo, J.A Coca-Clemente, M.C. Morant-Miñana, A. Villaverde, H. Zhang, M. Armand, C. Li, Safe, Flexible, and High-Performing Gel-Polymer Electrolyte for Rechargeable Lithium Metal Batteries, International Battery Association (IBA). 2022. Bled, Slovenia.

[7] A. Santiago, **J. Castillo**, A. Robles-Fernandez, A. Soria, M. Armand, D. Carriazo, 2D graphene-based activated carbon-containing sulfur cathode and: a perfect marriage for the development of high energy density, safe and long cycle life lithium-sulfur batteries, Int. Conference on Lithium-Sulfur Batteries, 2023 (ICLSB), Dresden (Germany).

[8] A. Robles-Fernández, Gelines Moreno-Fernández, Asier Soria-Fernández, **Julen Castillo**, Alexander Santiago and Daniel Carriazo, Graphene-containing cathodes

for high-performing lithium-sulfur batteries, Carbon for Energy Storage and Environmental Protection (CESEP), 2023, Budapest (Hungary).